UNIVERSITY OF CALIFORNIA SAN DIEGO

Properties and Impact of Active Galactic Nuclei-driven Outflows through Cosmic Time

A dissertation submitted in partial satisfaction of the
requirements for the degree
Doctor of Philosophy

in

Physics

by

Gene Chun Kwan Leung

Committee in charge:

Professor Alison L. Coil, Chair
Professor Farhat N. Beg
Professor Patrick H. Diamond
Professor Karin M. Sandstrom
Professor Shelley A. Wright

2020

The dissertation of Gene Chun Kwan Leung is approved, and it is acceptable in quality and form for publication on microfilm and electronically:

_____

_____

_____

_____

_____

Chair

University of California San Diego

2020

DEDICATION

To my parents

EPIGRAPH

Once we overcome our fear of being tiny, we find ourselves on the threshold of a vast and awesome Universe that utterly dwarfs – in time, in space, and in potential – the tidy anthropocentric proscenium of our ancestors.

—Carl Edward Sagan

TABLE OF CONTENTS

LIST OF FIGURES

LIST OF TABLES

ACKNOWLEDGEMENTS

I thank my advisor Alison Coil for her guidance and support throughout my graduate studies. She is an outstanding scientist, mentor and role model. She is highly dedicated to ensuring the academic and personal success of her students. I also thank Mojegan Azadi for her help and support as a senior graduate student, office-mate, and friend. I am grateful to David Rupke for his insights and discussions on my research projects. I would also like to thank Serena Perrotta for her input and suggestions on my work. It is a pleasure working with the former and current members of our research group, Brooke Simmons, Angela Berti, Erin George and Nancy Ning. I wish to show my gratitude to my committee members Farhat Beg, Patrick Diamond, Karin Sandstrom, Shelley Wright for their feedback on my research projects and reading of this dissertation.

I thank my friends who have helped make my graduate experience more enjoyable. It is a true pleasure sharing a home with Jonathan, Luna and Sol Lam for most of my graduate years. I enjoy the countless lunch and dinner conversations with Manho Tang.

Finally, I thank my family for all things big and small. I am particularly grateful to my parents and brother for providing a nurturing childhood, and for their encouragement and support for me to pursue my dream far away from home.

Chapter 2, in full, is a reprint of the material as it appears in The Astrophysical Journal 2017. Leung, Gene C. K., Coil, A. L., Aird, J., Azadi, M., Kriek, M., Mobasher, B., Reddy, N., Shapley, A., Siana, B., Fetherolf, T., Fornasini, F. M., Freeman, W. R., Price, S. H., Sanders, R. L., Shivaei, I., and Zick, T. 2017. The dissertation author was the primary investigator and author of this paper.

Chapter 3, in full, is a reprint of the material as it appears in The Astrophysical Journal 2019. Leung, Gene C. K., Coil, A. L., Azadi, M., Aird, J., Shapley, A., Kriek, M., Mobasher, B., Reddy, N., Siana, B., Freeman, W. R., Price, S. H., Sanders, R. L., Shivaei, I. 2019. The dissertation author was the primary investigator and author of this paper.

Chapter 4, in full, is currently being prepared for submission for publication of the material. Leung, Gene C. K., Coil, A. L., Rupke, D. S. N. and Perrotta, S. The dissertation author was the primary investigator and author of this paper.

VITA

2012	Bachelor of Science, University of Hong Kong
2014	Master of Philosophy, University of Hong Kong
2020	Doctor of Philosophy, University of California San Diego

PUBLICATIONS

Sanders, R. L., Shapley, A. E., Reddy, N. A., Kriek, M., Siana, B., Coil, A. L., Mobasher, B., Shivaei, I., Freeman, W. R., Azadi, M., Price, S. H., **Leung, G.**, Fetherolf, T., de Groot, L., Zick, T., Fornasini, F. M., and Barro, G. 2020, *"The MOSDEF survey: direct-method metallicities and ISM conditions at* $z \sim 1.5-3.5$*"*, MNRAS, 491, 1427

Leung, G. C. K., Coil, A. L., Aird, J., Azadi, M., Kriek, M., Mobasher, B., Reddy, N., Shapley, A., Siana, B., Fetherolf, T., Fornasini, F. M., Freeman, W. R., Price, S. H., Sanders, R. L., Shivaei, I., and Zick, T. 2019, *"The MOSDEF survey: a census of AGN-driven ionized outflows at* $z = 1.4-3.8$*"*, ApJ, 886, 11

Fornasini, F. M., Kriek, M., Sanders, R. L., Shivaei, I., Civano, F., Reddy, N. A., Shapley, A. E., Coil, A. L., Mobasher, B., Siana, B., Aird, J., Azadi, M., Freeman, W. R., **Leung, G. C. K.**, Price, S. H., Fetherolf, T., Zick, T., and Barro, G. 2019, *"The MOSDEF Survey: The Metallicity Dependence of X-Ray Binary Populations at* $z \sim 2$*"*, ApJ, 885, 65

Rupke, D. S. N., Coil, A., Geach, J. E., Tremonti, C., Diamond-Stanic, A. M., George, E. R., Hickox, R. C., Kepley, A. A., **Leung, G.**, Moustakas, J., Rudnick, G., and Sell, P. H. 2019, *"A 100-kiloparsec wind feeding the circumgalactic medium of a massive compact galaxy"*, Natur, 574, 643

Shapley, A. E., Sanders, R. L., Shao, P., Reddy, N. A., Kriek, M., Coil, A. L., Mobasher, B., Siana, B., Shivaei, I., Freeman, W. R., Azadi, M., Price, S. H., **Leung, G. C. K.**, Fetherolf, T., de Groot, L., Zick, T., Fornasini, F. M., and Barro, G. 2019, *"The MOSDEF Survey: Sulfur Emission-line Ratios Provide New Insights into Evolving Interstellar Medium Conditions at High Redshift"*, ApJL, 881, L35

Wilson, T. J., Shapley, A. E., Sanders, R. L., Reddy, N. A., Freeman, W. R., Kriek, M., Shivaei, I., Coil, A. L., Siana, B., Mobasher, B., Price, S. H., Azadi, M., Barro, G., de Groot, L., Fetherolf, T., Fornasini, F. M., **Leung, G. C. K.**, and Zick, T. O. 2019, *"The MOSDEF Survey: No Significant Enhancement in Star Formation or Deficit in Metallicity in Merging Galaxy Pairs at* $1.5 \lesssim z \lesssim 3.5$*"*, ApJ, 874, 18

Freeman, W. R., Siana, B., Kriek, M., Shapley, A. E., Reddy, N., Coil, A. L., Mobasher, B., Muratov, A. L., Azadi, M., **Leung, G.**, Sanders, R., Shivaei, I., Price, S. H., DeGroot, L., and Kereš, D. 2019, *"The MOSDEF Survey: Broad Emission Lines at* $z = 1.4-3.8$*"*, ApJ, 873, 102

Reddy, N. A., Shapley, A. E., Sanders, R. L., Kriek, M., Coil, A. L., Shivaei, I., Freeman, W. R., Mobasher, B., Siana, B., Azadi, M., Fetherolf, T., Fornasini, F. M., **Leung, G.**, Price, S. H., Zick, T., and Barro, G. 2018, *"The MOSDEF Survey: Significant Evolution in the Rest-frame Optical Emission Line Equivalent Widths of Star-forming Galaxies at* $z = 1.4 - 3.8$*"*, ApJ, 869, 92

Zick, T. O., Kriek, M., Shapley, A. E., Reddy, N. A., Freeman, W. R., Siana, B., Coil, A. L., Azadi, M., Barro, G., Fetherolf, T., Fornasini, F. M., de Groot, L., **Leung, G.**, Mobasher, B., Price, S. H., Sanders, R. L., and Shivaei, I. 2018, *"The MOSDEF Survey: Stellar Continuum Spectra and Star Formation Histories of Active, Transitional, and Quiescent Galaxies at* $1.4 < z < 2.6$*"*, ApJL, 867, L16

Azadi, M., Coil, A., Aird, J., Shivaei, I., Reddy, N., Shapley, A., Kriek, M., Freeman, W. R., **Leung, G. C. K.**, Mobasher, B., Price, S. H., Sanders, R. L., Siana, B., and Zick, T. 2018, *"The MOSDEF Survey: The Nature of Mid-infrared Excess Galaxies and a Comparison of IR and UV Star Formation Tracers at* $z \sim 2$*"*, ApJ, 866, 63

Sanders, R. L., Shapley, A. E., Kriek, M., Freeman, W. R., Reddy, N. A., Siana, B., Coil, A. L., Mobasher, B., Davé, R., Shivaei, I., Azadi, M., Price, S. H., **Leung, G.**, Fetherolf, T., de Groot, L., Zick, T., Fornasini, F. M., and Barro, G. 2018, *"The MOSDEF Survey: A Stellar Mass-SFR-Metallicity Relation Exists at* $z \sim 2.3$*"*, ApJ, 858, 99

Shivaei, I., Reddy, N. A., Siana, B., Shapley, A. E., Kriek, M., Mobasher, B., Freeman, W. R., Sanders, R. L., Coil, A. L., Price, S. H., Fetherolf, T., Azadi, M., **Leung, G.**, and Zick, T. 2018, *"The MOSDEF Survey: Direct Observational Constraints on the Ionizing Photon Production Efficiency,* $\xi_{\rm ion}$*, at* $z \sim 2$*"*, ApJ, 855, 42

Leung, G. C. K., Coil, A. L., Azadi, M., Aird, J., Shapley, A., Kriek, M., Mobasher, B., Reddy, N., Siana, B., Freeman, W. R., Price, S. H., Sanders, R. L., Shivaei, I. 2017, *"The MOSDEF Survey: The Prevalence and Properties of Galaxy-wide AGN-driven Outflows at* $z \sim 2$*"*, ApJ, 849, 48

Krumpe, M., Husemann, B., Tremblay, G. R., Urrutia, T., Powell, M., Davis, T. A., Scharwächter, J., Dexter, J., Busch, G., Combes, F., Croom, S. M., Eckart, A., McElroy, R. E., Perez-Torres, M., **Leung, G.** 2017, *"The Close AGN Reference Survey (CARS). Mrk 1018 halts dimming and experiences strong short-term variability"*, A& A, 607, 9

Shapley, A. E., Sanders, R. L., Reddy, N. A., Kriek, M., Freeman, W. R., Mobasher, B., Siana, B., Coil, A. L., **Leung, G. C. K.**, deGroot, L., Shivaei, I., Price, S. H., Azadi, M., Aird, J. 2017, *"The MOSDEF Survey: First Measurement of Nebular Oxygen Abundance at* $z > 4$*"*, ApJ, 846, 30

Azadi, M., Coil, A. L., Aird, J., Reddy, N., Shapley, A., Freeman, W. R., Kriek, M., **Leung, G. C. K.**, Mobasher, B., Price, S. H., Sanders, R. L., Shivaei, I., Siana, B. 2017, *"The MOSDEF Survey: AGN Multi-wavelength Identification, Selection Biases, and Host Galaxy Properties"*, ApJ, 835, 27

Leung, G. C. K., Takata, J., Ng, C. W., Kong, A. K. H., Tam, P. H. T., Hui, C. Y. and Cheng, K. S. 2014, *"Fermi-LAT Detection of Pulsed Gamma-rays Above 50 GeV from the Vela Pulsar"*, ApJ, 797, L13

Wang, Y., Ng, C. W., Takata, J., **Leung, G. C. K.** and Cheng, K. S. 2014, *"Emission Mechanism of GeV-quiet Soft Gamma-ray Pulsars: A Case for Peculiar Geometry?"*, MNRAS, 445, 604

Takata, J., **Leung, G. C. K.**, Cheng, K. S., Kong, A. K. H., Tam, P. H. T., Hui, C. Y. 2014, *"High-energy Emission from the Gamma-ray Binary LS 5039"*, ApJ, 790, 18

Ng C.-Y., Takata J., **Leung, G. C. K.**, Cheng K. S., Philippopoulos P., 2014, *"High-energy Emission of the First Millisecond Pulsar"*, ApJ, 787, 167

Takata, J., Li, K. L., **Leung, G. C. K.**, Kong, A. K. H., Tam, P. H. T., Hui, C. Y., Wu, E. M. H., Xing, Y., Cheng, K. S., Cao, Y., Tang, S., Prince, T. A., Wang, Z. 2014, *"Multi-wavelength Emissions from the Millisecond Pulsar Binary PSR J1023+0038 during an Accretion Active State"*, ApJ, 785, 131

Leung, G. C. K. and Lee, Man Hoi 2013, *"An Analytic Theory for the Orbits of Circumbinary Planets"*, ApJ, 763, 107

ABSTRACT OF THE DISSERTATION

Properties and Impact of Active Galactic Nuclei-driven Outflows through Cosmic Time

by

Gene Chun Kwan Leung

Doctor of Philosophy in Physics

University of California San Diego, 2020

Professor Alison L. Coil, Chair

This dissertation studies the properties of outflows driven by active galactic nuclei (AGNs) and their impact on the evolution of galaxies. AGNs are predicted by theoretical models of galaxy formation to provide the necessary feedback to produce realistic galaxies. In theoretical models, AGNs provide feedback by driving outflows that remove gas from the host galaxy, thereby quenching star formation in massive galaxies and producing scaling relations between supermassive black holes and galaxies. Despite being indispensable in theory, critical open questions remain for AGN-driven outflows from an observational perspective.

This dissertation first presents two studies using data from the MOSDEF survey, a large spectroscopic survey of galaxies when the Universe was about 3.5 billions years old ($z \sim 2$). The

first study focuses on the incidence and physical properties of AGN-driven outflows at $z \sim 2$. We show that AGN-drive outflows are at least as prevalent at $z \sim 2$ as they are in the local Universe. They are fast and extend to distances comparable to the size of the host galaxy. Using emission line ratio diagnostics, we find our data consistent with the picture of negative AGN feedback, where AGN-driven outflows suppress star formation, and find no evidence of galaxy-wide positive AGN feedback.

The second study focuses on the demographics of galaxies hosting AGN-driven outflows and the relation between outflow properties and the galaxy and AGN population at $z \sim 2$. We show that AGN-driven outflows are a ubiquitous phenomenon occurring across the galaxy population and in different phases of galaxy evolution, both before and after quenching. By measuring the energetics and correlations of AGN-driven outflows, we find that the outflows are more energetic at $z \sim 2$ than in the local Universe, where AGNs are more powerful on average. We find that the outflows remove gas at a rate comparable to or faster than gas is being converted into stars. This shows that AGN-driven outflows at $z \sim 2$ are capable of regulating star formation in the host galaxy.

The third study in this dissertation presents integral field spectroscopy of a nearby ultraluminous infrared galaxy (ULIRG) and AGN Mrk 273. The study focuses on the extended ionized gas on scales of ~ 20 kpc. We detect for the first time highly ionized gas in one of the extended nebula surrounding the galaxy. From this, we show that shocks contribute significantly to the ionization of the gas in the extended nebulae, mixed with AGN photoionization. Our data is compatible with theoretical models in which AGNs drive a multiphase outflow, and slower-moving extended cold gas filaments form out of a more spatially confined but faster warm outflow. Our data suggests that AGNs play an important role in ejecting gas in the ULIRG phase of galaxy evolution.

Chapter 1

Introduction

One hundred years ago, on 26 April 1920, a debate took place between the astronomers Harlow Shapley and Heber Curtis at the Smithsonian Museum of Natural History. The debate, now known as the Great Debate, concerned the size of the Universe and the nature of the perplexing objects known as "spiral nebulae". Shapley argued that the spiral nebulae were gas clouds that were part of our own Milky Way Galaxy, which alone comprised the entire observable Universe. Curtis proposed that these spiral nebulae were each a galaxy like our own, and the Universe was composed of many such galaxies, which he called "island universes". The debate ended without a clear consensus. Four years later, a breakthrough occurred when Edwin Hubble used variable stars to measure the distance to the Andromeda Galaxy, classified as a spiral nebula then. His measurements showed that Andromeda was located at a distance far exceeding the size of the Milky Way, and thus had to be a galaxy of its own. This momentous discovery represented another great leap in humankind's ancient quest to understand our place in the Universe, just as when the likes of Galileo Galilei and Johannes Kepler showed in the seventeenth century that Earth was only one of the several planets orbiting the Sun. Importantly, it also marked the birth of the field of extragalactic astronomy, opening the door to the study of galaxy evolution in the century that followed.

1.1 Galaxies

Galaxies are collections of stars, gas, dust and dark matter bound by gravitational force. The dark matter of a galaxy resides in a halo, which embeds the ordinary matter, or baryons, that make up the stars, gas and dust. Galaxies come in a variety of physical properties and environments in which they reside, and there are a large number of methods to classify them accordingly. As one of the most readily observable properties of a galaxy, morphology has been used to classify galaxies since the earliest galaxy studies. Hubble (1926) classified 400 galaxies by their observed structures, producing the well-known Hubble tuning-fork diagram. This diagram classifies galaxies into two broad categories - *spiral galaxies* with dominant spiral arm features and a disk-like morphology and *elliptical galaxies* with a smooth and ellipsoidal morphology. Finer classification of galaxies were based on how tightly wound the spiral arms are, whether a bar is presence at the galactic center, and the ellipticity of elliptical galaxies. In reality, galaxies can exhibit a combination of both spiral and elliptical features along a sequence, ranging from purely disk-dominated spiral galaxies, to galaxies consisting of a rotating disk around a spheroidal bulge, to purely bulge-dominated galaxies. Nevertheless, this broadly bimodal behavior of galaxy morphology remains a useful tool to classify galaxies in the local Universe.

The bimodality of galaxies extends to aspects well beyond their morphology. A vital quantity regarding the physical condition of a galaxy is the rate at which it is growing, measured by the star formation rate (SFR). As young stars are known to emit high energy photons in the bluer wavelengths, the color of a galaxy reflects the stellar population and the recent star formation history of the galaxy. Large photometric surveys of galaxies revealed two major distinct populations of galaxies by their colors (Strateva et al. 2001; Blanton et al. 2003). One group of galaxies, named the “red sequence”, demonstrate redder color and slightly fainter magnitude. Another group of galaxies, named the “blue cloud”, demonstrate bluer color and slightly brighter magnitude. Remarkably, galaxies in the red sequence are dominated by elliptical galaxies, while

galaxies in the blue cloud are dominated by spiral galaxies. This indicates that the morphological bimodality of galaxies reflects an intrinsic difference in their physical properties. The color bimodality shows that the redder elliptical galaxies consist of older stellar populations with little recent star formation and low SFR, while the bluer spiral galaxies consist of younger stellar populations which point to recent star formation and higher SFR. Additionally, red elliptical galaxies are found to have higher stellar masses and a more compact structure than blue spiral galaxies (e.g. Kauffmann et al. 2003a; Baldry et al. 2004) This bimodality in stellar mass, SFR and morphology suggests an evolutionary picture in which quiescent, elliptical galaxies evolve from star-forming, spiral galaxies (See Madau & Dickinson 2014, for a detailed review).

Surveys of galaxies through cosmic time revealed more information on the evolution of galaxies. While only a small fraction of all galaxies are quiescent at the early epoch of $z \sim 3$, or 11 billion years ago, the number of quiescent galaxies exceed that of star-forming galaxies at the present (e.g. Borch et al. 2006; Fontana et al. 2009; Brennan et al. 2015). Moreover, examination of the stellar populations through cosmic time shows that the stellar mass of galaxies in the blue cloud have been substantially constant, while the stellar mass of the galaxies in the red sequence has been significantly rising from the early Universe to the present (e.g. Faber et al. 2007). These temporal trends together suggest that some process "quenches" the star formation in the blue cloud galaxies, transforming them into the quiescent red sequence galaxies. The mechanism of the quenching of star formation in galaxies is a critical process to be understood in galaxy evolution.

1.2 Active Galactic Nuclei

One of the greatest discoveries in astronomy in the last 30 years is that virtually every galaxy hosts a supermassive black hole (SMBH) at its center. The notion that a compact and massive object can exist at the center of at least some galaxies, however, dates back to the 1960s.

In 1963, a peculiar starlike object was identified with a powerful source 3C 273 (Schmidt 1963). Remarkably, spectroscopy of the object revealed that it was at a high resdhift of $z = 0.158$, making it the second-most-distant object known at the time. The (then) vast distance to 3C 273 implied that it was located in a distant galaxy and was ~ 10 times more luminous than the brightest galaxy known then (Kormendy & Ho 2013). This discovery was soon followed by others, leading to a new class of objects called "qusai-stellar radio source", or "quasars". It was soon realized that some quasars exhibit variations in short timescales, indicating that they have a compact size (Matthews & Sandage 1963). Subsequently, an array of theoretical work pushed forward the idea that quasars are powered by the accretion of gas onto SMBHs at distant galactic centers (e.g Salpeter 1964; Zel'dovich 1964; Lynden-Bell 1969; Lynden-Bell & Rees 1971).

This picture indeed provides an energetic feasible source for quasars. Gas falling onto a SMBH releases an enormous amount of gravitational potential energy, and the luminosity of an accreting SMBH is given by

$$L = \varepsilon \dot{M}_\bullet c^2, \tag{1.1}$$

where $\dot{M}_\bullet$ is the accretion rate onto the SMBH and ε is the radiative efficiency, which is typically ~ 0.1 (e.g. Yu & Tremaine 2002; Marconi et al. 2004). It was only realized subsequently that qualitatively similar objects, albeit with lower luminosity, had been discovered much earlier in the nuclei of relatively nearby galaxies (Seyfert 1943). These Seyfert galaxies, along with quasars, are nowadays understood to belong to the the same class of phenomenon known as active galactic nuclei (AGNs).

An AGN is the bright central region of a galaxy that results when gas falls onto a SMBH and releases strong radiation in the process. While the full structure of AGNs is complicated, most AGNs consist of several of the following components producing radiation throughout the electromagnetic spectrum (Heckman & Best 2014; Netzer 2015).

- *SMBH*: The SMBH is located at the center of an AGN. The SMBH, with a mass of

$10^6 - 10^{10}\ M_\odot$, is the central engine of an AGN.

- *Accretion disk*: Gas inflow onto the SMBH occurs through the accretion disk. Gas is heated up to emit thermal radiation from the far ultraviolet to visible wavelengths.

- *Hot corona*: The hot corona surrounds the accretion disk. The thermal photons from the accretion disk are up-scattered by the corona through inverse-Compton scattering, resulting in X-ray emission.

- *Broad line region*: The broad line region (BLR) is a dense cloud of ionized gas at around light days to light years from the SMBH. It travels in roughly Keplerian motion around the SMBH. Its proximity to the SMBH results in very high velocity of > 5000 km s^{-1}, producing very broad emission lines.

- *Torus*: The torus is a dusty molecular gas structure surrounding the BLR, corona and accretion disk. The visible to X-ray emission from the inner regions is absorbed and re-emitted in the mid-infrared. It also obscures the view of the BLR from some lines of sight.

- *Narrow line region*: The narrow line region (NLR) is a cloud of lower density ionized gas located at hundreds to thousands of parsecs away from the SMBH. Its larger distance from the SMBH results in lower velocity, producing narrow emission lines.

- *Jets*: In AGNs with lower accretion rates, the accretion flow is altered, resulting in a configuration capable of launching two-sided jets extending from several parsecs to the Mpc scale. The jets produce synchrotron radiation most easily detected in radio.

1.3 Co-evolution of Galaxies and SMBHs

For several decades since the discovery of AGNs, the study of galaxies and AGNs remained largely separate from each other. AGN research primarily focused on high energy phenomena in extreme conditions. While AGNs demonstrated the existence of SMBHs at the centers of at least some galaxies, it was unclear whether these AGN host galaxies represent a rare subclass of galaxies or SMBHs (and AGNs) are a widespread phenomenon in the galaxy population. Definitive evidence of the widespread existence of SMBHs came from the measurement of the movement of stars near the center of a galaxy in the form of a rotation curve. Since stars move under the influence of gravity, one can deduce the mass around which the stars orbit by measuring their velocity. The first such measurement was made in the nearby M32 galaxy, where a central black hole mass of $3 - 10 \times 10^6\ M_\odot$ was inferred (Tonry 1984, 1987). The launch of the *Hubble Space Telescope*, which is free from the blurring effects of the atmosphere, opened the way to a wealth of detections of SMBHs in nearby galaxies. Nowadays, it is understood that virtually every galaxy hosts a SMBH at its center (Kormendy & Richstone 1995; Kormendy & Ho 2013). For these SMBHs to be almost ubiquitous, AGNs are likely an integral part of the lifecycle of typical galaxies.

With measurements of SMBHs becoming increasingly abundant, the close connection between galaxies and SMBHs started to gain substantial attention at the turn of the century. A series of seminal work by Magorrian et al. (1998), Ferrarese & Merritt (2000) and Gebhardt et al. (2000) showed that the mass of the central SMBH is tightly correlated with various properties of the host galaxy, such as the velocity dispersion, luminosity and stellar mass of their host galaxy bulge bulge. In particular, the correlation between the SMBH mass and the velocity dispersion of the galactic bulge is thought to be one of the most fundamental correlations observed, with a scatter of only 0.3 dex, or a factor of two, over three orders of magnitude in SMBH mass (Gebhardt et al. 2000). This far-reaching influence of the SMBH on the host galaxy is remarkable

given that the mass of the SMBH is typically only $\sim 0.001 - 0.002$ times that of the galactic bulge (Kormendy & Ho 2013). These tight correlations between SMBH and host galaxy properties on a galaxy-by-galaxy basis were the first strong evidence suggesting that galaxies and SMBHs *co-evolve*.

The co-evolution of galaxies and SMBHs also manifests itself on substantially larger scales, both in space and time. A striking example of such co-evolution comes from tracing the overall buildup history of the populations of galaxies and of SMBHs through cosmic time. The former is traced by the SFR density of galaxies, while the latter is traced by the AGN luminosity density. Large galaxies surveys such as the Sloan Digital Sky Survey (SDSS, e.g. Baldry et al. 2005) and the *Galaxy Evolution Explorer* (GALEX) mission (e.g. Arnouts et al. 2005) in the UV wavelengths, and results from the *Spitzer Space Telescope* (e.g. Le Floc'h et al. 2005) in the far-infrared wavelengths enabled the accurate mapping of the cosmic star formation history (SFH) up to $z \sim 1$. The famous *Hubble Ultra-Deep Field* measured the cosmic SFH up to the redshift of $z \sim 6$, when the Universe was less than one billion year old (Bunker et al. 2004). On the whole, the Universe reached a phase of the most active star formation when it was about 2.5 billion years old at $z \sim 2 - 3$, during which galaxies were assembling at about 10 times the rate they are nowadays (Hopkins & Beacom 2006).

On the other hand, cosmic X-ray surveys of AGNs provide a powerful tool to trace SMBH growth through cosmic time, as X-ray emission is relatively unaffected by absorption, and provides a reliable probe of the accretion rate of the SMBH (Brandt & Alexander 2015). The hard X-ray AGN luminosity function measured by telescopes such as the *Chandra X-ray Observatory* shows that the density of the most luminous X-ray AGNs peaks at $z \sim 2 - 3$, although less luminous AGNs are more prevalent at later epochs (Ueda et al. 2003; Aird et al. 2010). Nonetheless, the overall growth of SMBHs combining the effects of AGNs of all luminosities peaks at $z \sim 2$, when SMBHs were accreting about ten times the mass they are nowadays (Aird et al. 2015). Comparing the global SFR density and AGN luminosity density, the buildup history of galaxies and SMBHs

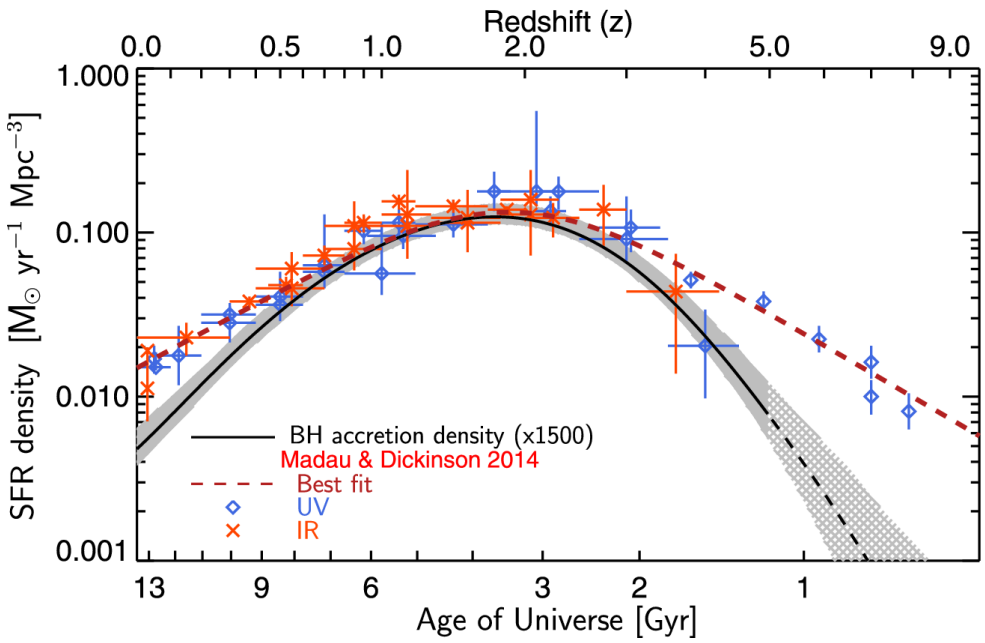

Figure 1.1: Global SFR density and SMBH accretion rate density through cosmic time. The blue points show the SFR density measured by UV observations, while the orange points show that measured by IR observations. The red dashed line shows the best fit SFR density trend of Madau & Dickinson (2014). The black solid line shows the SMBH accretion density traced by X-ray surveys. The buildup history of galaxies and SMBHs followed a strikingly similar trend for 12 billion years through cosmic time and reached a common peak at $z \sim 2$. The ratio of the two remaining roughly constant at ~ 1500. The figure is adapted from Aird et al. (2015) with permission.

followed a strikingly similar trend for 12 billion years through cosmic time, with the ratio of the two remaining roughly constant at ~ 1500 (Figure 1.1). Galaxies and SMBHs, despite having different physical extents by ~ 10000 times, seem to "know of" each other and evolve at the same rate.

The ubiquity of SMBHs in galaxies, the tight correlations between SMBHs and the host galaxy on a galaxy-by-galaxy basis, and the synchronized growth of SMBHs and galaxies through cosmic time all indicate the co-evolution of SMBHs and galaxies over vastly different scales. Such strong empirical evidence points to some underlying mechanism linking the evolution of galaxies and SMBHs.

1.4 AGN Feedback

The first theoretical study of the impact of a SMBH on the host galaxy during an AGN event was explored in Silk & Rees (1998), which proposed that only a few percent of the radiative energy of an AGN is needed to drive a wind that creates a galaxy-wide outflow. The power of such an outflow depends on the mass of the SMBH, and if the SMBH grows above a critical mass, the wind becomes powerful enough to remove all its surrounding gas, preventing further growth of the SMBH. The critical mass depends on the velocity dispersion of the surrounding materials, therefore a growing SMBH will stabilize at the critical mass, establishing the observed correlation between SMBH mass and velocity dispersion, as well as other host galactic bulge properties. The accretion of gas onto an AGN is known as *AGN feeding*, and the process of the AGN releasing energy into and affecting the surroundings is known as *AGN feedback*.

A more direct and far-reaching effect connecting AGNs and their host galaxies can be inferred from the comparison of theoretical models of galaxy evolution and observations. An intriguing observational result of galaxies is that the stellar mass to dark matter ratio in galaxies varies with the mass of the dark matter halo the galaxy resides in. Galaxies residing in massive ($> 10^{12}\ M_{\odot}$) dark matter halos have a lower stellar mass to dark matter mass ratio than those in intermediate-mass halos, indicating that massive galaxies are less efficient in converting baryons into stars (e.g. Behroozi et al. 2013a,b). Most theoretical models of galaxy formation invoke AGN feedback to reduce the star formation efficiency in massive galaxies (e.g. Di Matteo et al. 2005; Croton et al. 2006; Hopkins et al. 2006). In such models, the AGN drives a galaxy-wide outflow which expels gas, the raw ingredient of stars, from the galaxy, thereby quenching or regulating star formation in the galaxy. In addition, AGN feedback is indispensable to theoretical models in order to produce the observed bimodality of galaxies, and match the large number of red, elliptical galaxies at the present. Without invoking AGN feedback to quench star formation in galaxies, theoretical models produce unrealistic galaxies that are too massive, blue, compact

and disk-like (e.g Hopkins et al. 2008; Dubois et al. 2013).

While AGN feedback by AGN-driven outflows is theoretically attractive in producing the observed galaxy properties, it has to be tested by observations. Several questions are key to understanding whether AGN-driven outflows can indeed regulate star formation in massive galaxies.

1. *How common are AGN-driven outflows?* To be able to affect the galaxy population, they have to be sufficiently prevalent.

2. *What are their velocity and physical extent?* To be able to expel gas and quench star formation throughout the entire galaxy, they have to be fast and extended enough, so the gas is expelled to a sufficiently large distance that it can no longer be used to form stars.

3. *How much mass do they contain?* To be able to regulate star formation, a sufficient amount of gas has to be expelled. Outflows removing gas at rate equal to or faster than gas is being turned into stars are expected to have a substantial impact on star formation.

4. *What kind of galaxies do they live in?* To put them in the context of the galaxy population, they have to exist in the right galaxies. It is also crucial to measure how their properties differ in different galaxies. AGN feedback is expected to reduce the star formation efficiency of massive galaxies in particular.

We have partial answers to some of these questions. In the local Universe ($z \sim 0$), outflows associated with AGNs have been detected as a blueshifted wing in emission line spectra since the early work of Burbidge & Burbidge (1965). Using large spectroscopic surveys such as SDSS, AGN-driven outflows with high velocity of $\gtrsim 500$ km s^{-1} have been observed to be fairly common at $z \sim 0$, occurring in at least 25% of AGNs (e.g Mullaney et al. 2013; Woo et al. 2016). The physical extent of AGN-driven outflows is still an open questions. The physical extent outflows are most commonly measured by integral field spectrographs (IFS) or long-slit

spectrographs. While some observations showed that outflows in very luminous AGNs can extend to sizes comparable to the galaxy (e.g. Liu et al. 2013a,b; Rupke & Veilleux 2013a; Harrison et al. 2014; Rupke et al. 2017), others have reported much more compact sizes of $\lesssim 1.5$ kpc using different observation or analysis techniques, and in different samples of AGNs (e.g Husemann et al. 2016; Karouzos et al. 2016a,b; Baron & Netzer 2019a,b). The physical extent, and thus the mass, of AGN-driven outflows remains an open question.

Despite the observational results at $z \sim 0$, critical questions remain unanswered for the role of AGN-driven outflows in the early Universe, when the present-day galaxies were being built, and AGN feedback may be in the process of shaping the present-day galaxy properties that theoretical models attempt to reproduce. Galaxies and SMBHs were growing the most actively at the earlier epoch of $z \sim 2$, so AGNs were the most powerful at this epoch, and could potentially have the largest impact on the evolution of the host galaxy. Observing AGN-driven outflows at $z \sim 2$ is also crucial in understanding the role of AGN feedback in building the increasingly quiescent galaxy population from the early Universe to the present.

Existing observations of AGN-driven outflows at $z \sim 2$ have been limited. Several observational studies have focused on a small number of objects carefully selected to maximize the chance of detecting an outflow (e.g. Nesvadba et al. 2008; Cano-Díaz et al. 2012; Harrison et al. 2012; Brusa et al. 2015; Perna et al. 2015). While these studies demonstrate that AGN-driven outflows exist at $z \sim 2$, we cannot answer the critical questions of how common AGN-driven outflows are, and what kind of galaxies they live in. We are also unable to generalize the findings about the velocity, physical extents and mass of the outflows to the majority of AGN-driven outflows at $z \sim 2$. The above-mentioned key questions about AGN-driven outflows remain largely unanswered at $z \sim 2$.

1.5 Overview

An overview of this dissertation is as follows. Chapter 2 presents a study using data from the first two years of the MOSDEF survey, focusing on the incidence and physical properties AGN-driven outflows at $z \sim 2$. Chapter 3 presents a study using the full dataset of the MOSDEF survey, focusing on the demographics of AGN-dricen outflows and the relation between outflows and the galaxy and AGN populations at $z \sim 2$. Chapter 4 presents a study of the extended warm gas associated with the AGN and ultraluminous infrared galaxy Mrk 273, and its relation with the AGN, using observations with the new KCWI IFS. Chapter 5 summarizes the main findings of this dissertation and describes future research directions.

Chapter 2

The MOSDEF survey: the prevalence and properties of galaxy-wide AGN-driven outflows at $z \sim 2$

2.1 Abstract

Using observations from the first two years of the MOSFIRE Deep Evolution Field (MOSDEF) survey, we study 13 AGN-driven outflows detected from a sample of 67 X-ray, IR and/or optically-selected AGN at $z \sim 2$. The AGN have bolometric luminosities of $\sim 10^{44} - 10^{46}$ erg s^{-1}, including both quasars and moderate-luminosity AGN. We detect blueshifted, ionized gas outflows in the Hβ, [OIII], Hα and/or [NII] emission lines of 19% of the AGN, while only 1.8% of the MOSDEF galaxies have similarly-detected outflows. The outflow velocities span $\sim$300 to 1000 km s^{-1}. Eight of the 13 outflows are spatially extended on similar scales as the host galaxies, with spatial extents of 2.5 to 11.0 kpc. Outflows are detected uniformly across the star-forming main sequence, showing little trend with the host galaxy SFR. Line ratio diagnostics indicate that the outflowing gas is photoionized by the AGN. We do not find evidence

for positive AGN feedback, in either our small MOSDEF sample or a much larger SDSS sample, using the BPT diagram. Given that a galaxy with an AGN is ten times more likely to have a detected outflow, the outflowing gas is photoionzed by the AGN, and estimates of the mass and energy outflow rates indicate that stellar feedback is insufficient to drive at least some of these outflows, they are very likely to be AGN-driven. The outflows have mass-loading factors of the order of unity, suggesting that they help regulate star formation in their host galaxies, though they may be insufficient to fully quench it.

2.2 Introduction

Perhaps one of the most remarkable discoveries in astronomy over the last two decades is that supermassive black holes (mass greater than $\sim 10^6\ M_\odot$) exist in the nuclei of virtually all galaxies (e.g. Magorrian et al. 1998; Heckman & Best 2014). Supermassive black holes grow by accreting gas from the centers of their galaxies, which are observed as active galactic nuclei (AGN, e.g., Antonucci 1993; Netzer 2015). The growth rates of supermassive black holes and galaxies over cosmic time, traced by black hole accretion density and star formation density respectively, follow a strikingly similar pattern for the last ~ 11 billion years (e.g. Ueda et al. 2003; Hopkins & Beacom 2006; Aird et al. 2015). Furthermore, a tight relation exists between the masses of central supermassive black holes and various properties of their galactic bulges (e.g., Ferrarese & Merritt 2000; Gebhardt et al. 2000). Such empirical evidence clearly indicates a co-evolution between galaxies and their supermassive black holes.

An important theoretical connection between AGN and galaxies is inferred from the comparison between models of galaxy formation and observed galaxy properties. The observed stellar mass function of galaxies, which traces the distribution of galaxies by stellar mass, shows a sharp cutoff at the high mass end relative to the dark matter halo mass function. Without some kind of feedback mechanism(s) releasing energy into the galaxy in the theoretical models, strong

gas cooling in massive, luminous galaxies would lead to more galaxies being formed at the high mass / high luminosity end of the luminosity function than are observed (e.g., Benson et al. 2003).

Most of the current successful models of galaxy formation (e.g. Di Matteo et al. 2005; Hopkins et al. 2006, 2008; Debuhr et al. 2012) invoke AGN as the primary source of feedback in massive galaxies, in order to inject energy into the interstellar medium, regulate or quench star formation, and slow black hole growth. A key process for AGN feedback is AGN-driven outflows, in which the AGN produces a high-velocity wind that heats or sweeps up gas and drives them into the interstellar medium over distances comparable to the size of the galaxy, leading to the regulation and/or quenching of star formation. Although these models successfully produce the observed galaxy stellar mass function, they must be verified with observations. Therefore, it is a critical area of on-going research to observe and characterize AGN-driven outflows.

It is now evident that AGN-driven outflows are common in the local Universe ($z \lesssim 1$). Ionized outflows have long been known to manifest themselves in a blueshifted wing in the emission lines of AGN spectra (e.g. Weedman 1970). The prevalence of these outflows are revealed by large spectroscopic surveys such as the Sloan Digital Sky Survey (SDSS). Using $>$ 24000 AGN ($L_{[\mathrm{OIII}]} \sim 10^{40} - 10^{44}$ erg s^{-1}) from SDSS, Mullaney et al. (2013) find signs of ionized outflows in the [OIII]λ5007 emission line profile in 17% of AGN, with outflow velocities between 600 and 2000 km s^{-1}. Zakamska & Greene (2014) also find widespread ionized outflows in $>$500 luminous AGN ($L_{[\mathrm{OIII}]} \sim 10^{42} - 10^{43}$ erg s^{-1}) in SDSS, with outflow velocities of 400 to 4800 km s^{-1}.

The fiber spectroscopy provided by SDSS does not allow for measurements of the physical extent of the outflows, which can be determined by follow-up integral field spectroscopy (IFS) observations. Using IFS, the physical extent of the outflows in very luminous AGN ($L_{[\mathrm{OIII}]} \gtrsim 10^{42}$ erg s^{-1}) are shown to be $\sim$ 6 to 19 kpc, comparable to the size of the host galaxies (e.g. Liu et al. 2013a; Harrison et al. 2014). These studies show that galaxy-wide ionized outflows are relatively common among the most luminous AGN in the local Universe.

However, the crucial epoch to observe AGN-driven outflows is $z \sim 2$, when the Universe was only a quarter of its current age. The cosmic black hole accretion and star formation densities both reach a maximum at $z \sim 2$, before gradually declining by about a factor of 10 to the present-day values (e.g. Aird et al. 2015). Not only are AGN-driven outflows expected to be more prevalent at this epoch of peak black hole accretion activity, their relation to the subsequent decline of cosmic star formation density is of particular interest in understanding the role of AGN feedback in the regulation and quenching of star formation. Therefore, it is a key cosmic time to observe and characterize AGN-driven outflows and investigate their impact on their host galaxies.

Observations of AGN-driven outflows at this epoch of peak activity level in the Universe remain limited. Many of the studies in the existing literature at $z \sim 2$ are focused on small samples of extreme sources. Some early results include Nesvadba et al. (2008), which finds outflows in three powerful radio-loud AGN in very massive galaxies. Harrison et al. (2012) finds energetic galaxy-wide outflows in a sample of 8 $z \sim 2$ AGN-hosting ultraluminous infrared galaxies (ULIRGs), which are galaxies with elevated star formation activity. Powerful outflows have also been found in a study of 10 $z \sim 1.5$ luminous quasars (Brusa et al. 2015; Perna et al. 2015), which are the most luminous members of the AGN population ($L_{\rm bol} \gtrsim 10^{45}$ erg s^{-1}). These studies consist of special subclasses of AGN, which are not representative of the much larger AGN population. In order to investigate how AGN feedback affects galaxy evolution in the wider picture, a study using a more complete sample of AGN is necessary.

Recent studies using larger samples of a few tens of AGN report evidence of prevalent AGN-driven outflows. Harrison et al. (2016) study [OIII] in a sample of 54 X-ray selected AGN ($L_{\rm X} \sim 10^{42} - 10^{45}$ erg s^{-1}) at somewhat lower redshifts of $z \sim 1.1 - 1.7$ and find that a second kinematic component is detected in 35% of the [OIII]-detected AGN, while $\sim 50\%$ have line widths > 600km s^{-1}, with a maximum line width of $\sim$1000 km s^{-1}. The largest sample at $z \sim 2$ to date is from Genzel et al. (2014), where the Hα and [NII] line profiles are used to find signs of outflows in the nuclear region (radius < 2.5 kpc) of 34 out of 110 star-forming galaxies at

$z \sim 1-3$, 18 of which are confirmed AGN ($L_{\rm AGN} \sim 10^{44}-10^{46}$ erg s^{-1}). With outflow velocities of 300 to 1300 km s^{-1}, the estimated mass outflow rates (though very uncertain) are comparable to the star formation rates (SFR) of the host galaxies, suggesting the outflows may be capable of ejecting sufficient gas to quench star formation in the host galaxies.

It is important to test these results with a larger and more representative sample of AGN at $z \sim 2$. Moreover, to better constrain and characterize the kinematics of the outflows, it is important to have simultaneous measurement of Hβ, [OIII], Hα and [NII]; [OIII] is especially useful, as it is unlikely affected by any potential AGN broad line emission. The commissioning of the MOSFIRE multi-object spectrograph (McLean et al. 2010a,b) on the 10-meter Keck I telescope provides great opportunities to systematically study AGN-driven outflows at high redshift. It is now possible to simultaneously obtain rest-frame optical spectra for a large number of sources at high redshift. In this study, we make use of data from the MOSFIRE Deep Evolution Field (MOSDEF) survey (Kriek et al. 2015), a recently-completed four year near-infrared spectroscopic survey using MOSFIRE. With MOSDEF, we have obtained rest-frame optical spectra of ~ 1500 galaxies in $1.4 < z < 3.8$, including more than 100 AGN. These rest-frame optical spectra cover important emission lines for characterising AGN and AGN-driven outflows, including Hβ, [OIII], Hα and [NII]. The spectroscopic targets in the survey are selected to a fixed H-band magnitude, roughly corresponding to a threshold in stellar mass. These selection criteria result in a more representative sample of galaxies that is not biased towards high SFRs. Moreover, AGN in this study are identified using multi-wavelength data (see Section 3.3), which minimizes AGN selection biases (Coil et al. 2015; Azadi et al. 2017). This provides us with a large sample consisting of more typical AGN in more representative galaxies, allowing us to investigate the effects of AGN-driven outflows in the general AGN population.

In this paper we present the results using data from the first two years of the MOSDEF survey. In Section 3.3 we describe the survey and our AGN sample; in Section 3.4 we report our detection and analysis of outflows among our AGN; in Section 2.5 we discuss the implications of

our results. We conclude in Section 2.6.

2.3 Observations and AGN Sample

In this section we describe the dataset used in this study and the methods employed to identify AGN at various wavelengths. We also outline how we estimate host galaxy properties using SED fitting.

2.3.1 The MOSDEF Survey

In this study we use data from the first two years of the MOSDEF survey (Kriek et al. 2015), which makes use of the MOSFIRE spectrograph (McLean et al. 2010a,b) on the Keck I telescope. In the first two years of observations, a total of 713 targets were observed, 555 of which yielded a reliable redshift. With the complete MOSDEF survey, we have obtained moderate-resolution ($R = 3000 - 3650$) rest-frame optical spectra of ~ 1500 galaxies and AGN at $1.4 \lesssim z \lesssim 3.8$ in three well-studied CANDELS fields (Grogin et al. 2011; Koekemoer et al. 2011): AEGIS, COSMOS and GOODS-N. Data were obtained for three masks in two additional CANDELS fields, GOODS-S and UDS, because our primary target fields were not visible during a portion of a few of the observed nights. All of the MOSDEF targets are covered by the 3D-*HST* survey (Skelton et al. 2014). Full technical details of the design and observations of the MOSDEF survey can be found in Kriek et al. (2015). MOSDEF targets are selected within three redshift intervals, $1.37 \leq z \leq 1.70$, $2.09 \leq z \leq 2.61$ and $2.95 \leq z \leq 3.80$, such that the brightest rest-frame optical emission lines lie within atmospheric windows. This allows coverage of the Hβ, [OIII], Hα and [NII] emission lines in the lower and middle redshift intervals, and Hβ and [OIII] in the higher redshift interval.

Targets are prioritized according to weights determined by their H-band (F160W) magnitudes and redshifts in the 3D-*HST* catalogs (Skelton et al. 2014), with emphasis given to brighter

galaxies and galaxies within the middle redshift interval ($2.09 \leq z \leq 2.61$). Targets are selected down to limiting H-band magnitudes of 24.0, 24.5 and 25.0 for the lower, middle and higher redshift intervals, respectively. We assign higher targeting priority to galaxies that are known to host AGN, identified in advance by X-ray emission and/or red IRAC colors. In addition, AGN are identified in the MOSDEF spectra using rest-frame optical diagnostics. The identification of AGN in the MOSDEF survey is described below; full details are discussed in Azadi et al. (2017).

2.3.2 X-ray AGN Sample

X-ray AGN were identified prior to the MOSDEF slitmasks design using deep *Chandra* X-ray imaging in the survey fields. The depth of the *Chandra* data used is 160 ks in COSMOS, 2 Ms in GOODS-N, 4 Ms in GOODS-S and 800 ks in AEGIS. These correspond to hard band (2-10 keV) flux limits of 1.8×10^{-15}, 2.8×10^{-16}, 1.6×10^{-16} and 5.0×10^{-16} ergs s^{-1} cm^{-2}, respectively.

The X-ray data from all the fields were reduced and analyzed according to the prescription in Laird et al. (2009, see also Georgakakis et al. 2014; Nandra et al. 2015). For point source detection, a false probability threshold of 4×10^{-6} was adopted. Each source must be detected in at least one of the four bands: soft (0.5-2 keV), hard (2-7 keV), ultrahard (4-7 keV) and full (0.5-7 keV). Then the X-ray sources were matched to sources detected at IRAC, NIR and optical wavelengths using the likelihood ratio method (see Ciliegi et al. 2003, 2005; Brusa et al. 2007; Luo et al. 2010) to identify secure multiwavelength counterparts. (See Aird et al. 2015 for details.) The resulting catalogs were then matched to the closest source within $1''$ in the 3D-*HST* catalogs used for MOSDEF target selection. These X-ray sources were given higher priority in MOSDEF target selection.

For the X-ray sources observed by MOSDEF and for which a redshift was determined, the 2-10 keV rest-frame X-ray luminosity was estimated from the hard or soft band fluxes. Luminosity estimates assume a simple power-law spectrum with photon index $\Gamma = 1.9$ and Galactic absorption

only. Our hard band detection threshold approximately corresponds to an X-ray luminosity limit of $L_{2-10\mathrm{keV}} \approx 1.3 - 15.1 \times 10^{42}$ erg s^{-1} across the four fields. The luminosity estimates should be reasonable since at the MOSDEF redshift range ($z > 1.4$), a relatively large absorption column density ($N_H \gtrsim 10^{23}$ cm^{-2}) is required to significantly suppress the observed flux, even in the soft band. Of the 28 X-ray AGN observed in the first two years of the MOSDEF survey with a secure derived redshift, 22 are detected in the hard band, with $L_{2-10\mathrm{keV}}$ spanning $\sim 10^{43} - 10^{45}$ erg s^{-1}. All 28 X-ray AGN are included in this study.

2.3.3 IR AGN Sample

Although deep X-ray surveys are a highly reliable means of selecting AGN, X-ray photons can be significantly absorbed at high column densities (e.g. $N_H \gtrsim 10^{23}$ cm^{-2}), weakening their efficiency in identifying heavily obscured AGN. The MIR wavelengths can potentially be used to identify such AGN, as high-energy photons from the AGN are absorbed and re-radiated by dust at the MIR wavelengths.

It is common to use the unique MIR colors of AGN to identify infrared AGN (IR AGN) using IRAC data from *Spitzer* (e.g. Lacy et al. 2004; Stern et al. 2005). For MOSDEF, we make use of the IRAC color criteria from Donley et al. (2012) to select IR AGN. These criteria were designed to limit contamination from star forming galaxies at high redshift ($z \sim 3$), resulting in a pure AGN sample, and were used by Azadi et al. (2017) for the MOSDEF survey.

We use IRAC fluxes reported in the 3D-*HST* catalogs (Skelton et al. 2014), and select IR

AGN following the Donley et al. (2012) criteria in IRAC color-color space:

$$x = \log_{10}\left(\frac{f_{5.8\mu\mathrm{m}}}{f_{3.6\mu\mathrm{m}}}\right), \quad y = \log_{10}\left(\frac{f_{8.0\mu\mathrm{m}}}{f_{4.5\mu\mathrm{m}}}\right) \tag{2.1}$$

$$x \geq 0.08 \text{ and } y \geq 0.15 \tag{2.2}$$

$$y \geq (1.21 \times x) - 0.27 \tag{2.3}$$

$$y \leq (1.21 \times x) + 0.27 \tag{2.4}$$

$$f_{4.5\mu\mathrm{m}} > f_{3.6\mu\mathrm{m}} \tag{2.5}$$

$$f_{5.8\mu\mathrm{m}} > f_{4.5\mu\mathrm{m}} \tag{2.6}$$

$$f_{8.0\mu\mathrm{m}} > f_{5.8\mu\mathrm{m}}. \tag{2.7}$$

Conditions 3.5, 3.6 and 3.7 are slightly relaxed to include sources satisfying these conditions within 1σ uncertainties of their IRAC fluxes. Condition 3.4 is also relaxed to include one source falling marginally outside this condition but satisfying all the others and having colors far from any star-forming galaxies in the MOSDEF sample. 27 IR AGN are selected in the data from the first two years of MOSDEF in this way; 9 of these IR AGN are also identified through X-ray imaging as described in Section 2.3.2.

2.3.4 Optical AGN Sample

Apart from the 46 X-ray and/or IR AGN identified prior to target selection as described in Sections 2.3.2 and 2.3.3, we additionally identify AGN optically using emission line ratios derived from the MOSDEF rest-frame optical spectra. For the 555 MOSDEF sources from the first two years that have a reliable redshift, as described in Azadi et al. (2017), we simultaneously fit the Hβ, [OIII], [NII] and Hα emission lines using a χ^2-minimization method by the `MPFIT` (Markwardt 2009) routine in `IDL`. For sources in the highest redshift interval of $2.95 \leq z \leq 3.80$, we fit only the Hβ and [OIII] emission lines, as the spectra do not cover the [NII] and Hα lines.

We fit the spectra with a continuum near the emission lines with zero slope and a maximum of three Gaussian components for each line:

1. A Gaussian function with FWHM < 2000 km s^{-1}, one each for the Hβ, [OIII], [NII] and Hα emission lines, representing the narrow-line emission from the AGN and/or host galaxy;

2. A broad Gaussian function with FWHM > 2000 km s^{-1}, one each for Hβ and Hα only, representing the broad line emission from the AGN;

3. An additional Gaussian function with FWHM < 2000 km s^{-1} and a velocity offset between -500 and 0 km s^{-1}, one each for the Hβ, [OIII], [NII] and Hα emission lines, representing a potential blueshifted outflow component.

The FWHM of each Gaussian function is set to be equal for all of the lines of interest. The flux ratios between [OIII]λ4960 and [OIII]λ5008 and between [NII]λ6550 and [NII]λ6585 are fixed at 1:3 for each Gaussian function. We determine the minimum width of the Gaussian functions by randomly selecting unblended sky lines in different wavelength intervals and fitting them with a single Gaussian function. From the average width of the sky lines, we determine a minimum width (Gaussian sigma) in observed wavelength of 2.5Å for Hβ and [OIII] and 3.5Å for Hα and [NII]. We first perform fits and evaluate the χ^2 with a model consisting of the narrow-line component (component 1) alone, then only accept additional components when the resulting decrease in χ^2 implies a p-value of < 0.01 for the simpler model.

Based on the results from the emission line fits, we use the diagnostic BPT diagram (Baldwin et al. 1981; Veilleux & Osterbrock 1987) to identify optical AGN in the MOSDEF sample. For this diagnostic we sum the non-broad component fluxes of the Hβ, [OIII], [NII] and Hα emission lines, applying Balmer absorption corrections to the Hβ and Hα fluxes.

Sources above the Kauffmann et al. (2003b) demarcation line in the BPT diagram are selected as optical AGN for the purposes of this study, as at low redshift sources above this line are considered likely to have an AGN contribution to their optical spectra. At high redshifts,

star-forming galaxies are known to be offset from SDSS star-forming galaxies in the BPT diagram (e.g. Shapley et al. 2015; Sanders et al. 2016). In the MOSDEF survey, this offset is observed only for galaxies in the lower stellar mass half of the sample ($M_* < 10^{10}\,M_\odot$) (Shapley et al. 2015), while most of the AGN identified in the MOSDEF have stellar masses of $M_* > 10^{10}\,M_\odot$. Previous MOSDEF AGN papers (Coil et al. 2015; Azadi et al. 2017) used the Meléndez et al. (2014) demarcation line in the BPT digram to identify optical AGN, as it balances contamination by star-forming galaxies and completeness of the AGN sample in our survey. In this study, the aim is to select sources with at least some AGN contribution instead of pure AGN, as the presence of any AGN activity may suffice to drive an outflow and provide feedback. Therefore, an AGN sample as complete as possible is preferred, even if it has some contamination. The use of the Kauffmann et al. (2003b) line instead of the Meléndez et al. (2014) line results in nine additional sources being identified as potential AGN. This relative increase in the total number of AGN is consistent with the initial MOSDEF sample presented in Coil et al. (2015), who show that at $z \sim 2$ sources in the BPT diagram on average are offset high by ~ 0.1 dex compared to low redshift samples. This small shift implies that the Kauffmann et al. (2003b) demarcation line should be fairly reliable for our sample, if possibly somewhat contaminated.

Using this criterion, we have selected 21 optical-only AGN in addition to the 46 AGN selected through X-ray and/or IR emission. This results in a total of 67 X-ray, IR and/or optical AGN in our sample. Details of the overlap and uniqueness of AGN identified at each wavelength in our sample are given in Azadi et al. (2017). The detection rates of outflows in AGN subsamples detected at different wavelengths are discussed below in Section 2.5.4. We note that only two of the 13 AGN for which we detect outflows (presented below) are identified as AGN solely using the BPT diagram.

Table 2.1: Outflow Host Properties

ID	Field	R.A. (J2000)	Decl. (J2000)	z	Identification Method	SFR ($M_\odot$ yr^{-1})	$\log(M_*/M_\odot)$	$\log(L_{[\mathrm{OIII}]}/\mathrm{erg\ s^{-1}})$
6055	UDS	02:17:34	-05:14:48	2.3	IR	3	10.58	43.03
20891	COSMOS	10:00:14	+02:22:57	2.19	Opt	129	10.55	43.38
15286	COSMOS	10:00:15	+02:19:44	2.45	X-ray/IR/Opt	2399	10.63	42.39
20979	COSMOS	10:00:16	+02:23:00	2.19	Opt	85	10.6	43.20
11223	COSMOS	10:00:20	+02:17:25	2.1	X-ray/Opt	209	11.2	42.55
9367	GOODS-N	12:37:04	+62:14:46	2.21	IR/Opt	6	10.49	43.39
8482	GOODS-N	12:37:07	+62:14:08	2.49	X-ray/Opt	83	11.24	42.22
6976	GOODS-N	12:37:23	+62:13:04	1.59	X-ray/Opt	2	10.59	42.92
10421	GOODS-N	12:37:23	+62:15:38	2.24	X-ray/IR/Opt	11	10.57	42.94
30014	AEGIS	14:19:21	+52:51:36	2.29	X-ray/Opt	4	10.56	41.51
31250	AEGIS	14:18:33	+52:43:13	2.14	IR	129	10.14	42.38
17754	AEGIS	14:19:35	+52:51:09	2.3	X-ray	45	11.35	42.30
17664	AEGIS	14:19:38	+52:51:38	2.19	X-ray	26	10.93	42.64

2.3.5 Stellar Masses and Star Formation Rates

We estimate the stellar masses and SFR of our sources by fitting their spectral energy distributions (SED, full details are described in Azadi et al. 2017). We use multi-wavelength photometric data from the 3D-*HST* catalogs (Skelton et al. 2014) and fit the data with the FAST SED fitting code (Kriek et al. 2009), adopting the FSPS stellar population synthesis model (Conroy et al. 2009) and the Chabrier (2003) initial mass function. The star formation history is parametrized by a delayed exponentially declining model, where $\mathrm{SFR}(t) \propto te^{-t/\tau}$, τ being the characteristic star formation timescale. Dust attenuation is described by the Calzetti et al. (2000) attenuation curve.

The SEDs of AGN may include a red power law in the MIR and/or a blue power law in the UV (e.g. Koratkar & Blaes 1999; Donley et al. 2012). The majority of the AGN in our sample are type 2 (only six have a broad component), such that the optical light is dominated by the host galaxy. To account for the potential contribution to the SED from the AGN, we subtract a UV and/or an IR power law from the observed photometric data, as described in Azadi et al. (2017). Power law templates spanning a range of slopes and normalizations are created and subtracted from the observed photometric data before fitting the power-law subtracted photometry

with FAST. We accept the fit with the smallest χ^2 as the best fit. We create a blue power law at rest-frame wavelengths < 1 μm and a red power law at rest-frame wavelengths > 1 μm. The normalization of the blue and red power laws can vary from 0 to 1 times of the fluxes in the U and IRAC channel 3 (5.8μm) bands, respectively. The spectral indices of the blue and red power laws can vary from 0 to 0.5 and -5 to -0.5, respectively (slightly modified from values in Ivezić et al. 2002; Donley et al. 2012). The power law subtraction results in an average 0.13 dex decrease in the SFR and an average 0.03 dex decrease in the stellar mass of the AGN host galaxies.

2.4 Outflow Detection and Analysis

In this section we report the methods used to detect outflows and their properties, including their kinematics, optical line ratios, and physical extent in the MOSDEF data.

2.4.1 Detection of Outflows in AGN

First, we identify AGN with *potential* outflows in our sample. For 25 of the 67 AGN in our sample, the best fit emission line model with an outflow component is preferred, with the null hypothesis of a single component rejected at a p-value less than 0.01. Of the six AGN with a broad-line component, we detect a significant outflow component in only one source, COSMOS 15286.

To reduce the chance of a false detection potentially due to overfitting noise in the spectra, we further tighten our outflow selection criteria by selecting only those AGN satisfying the following conditions:

1. S/N $>$ 3 for both the narrow-line and outflow components for at least one of the Hβ, [OIII]λ5008, [NII]λ6585 and/or Hα emission lines;

2. a velocity shift between the outflow and narrow-line components of > 20 km s^{-1}, roughly

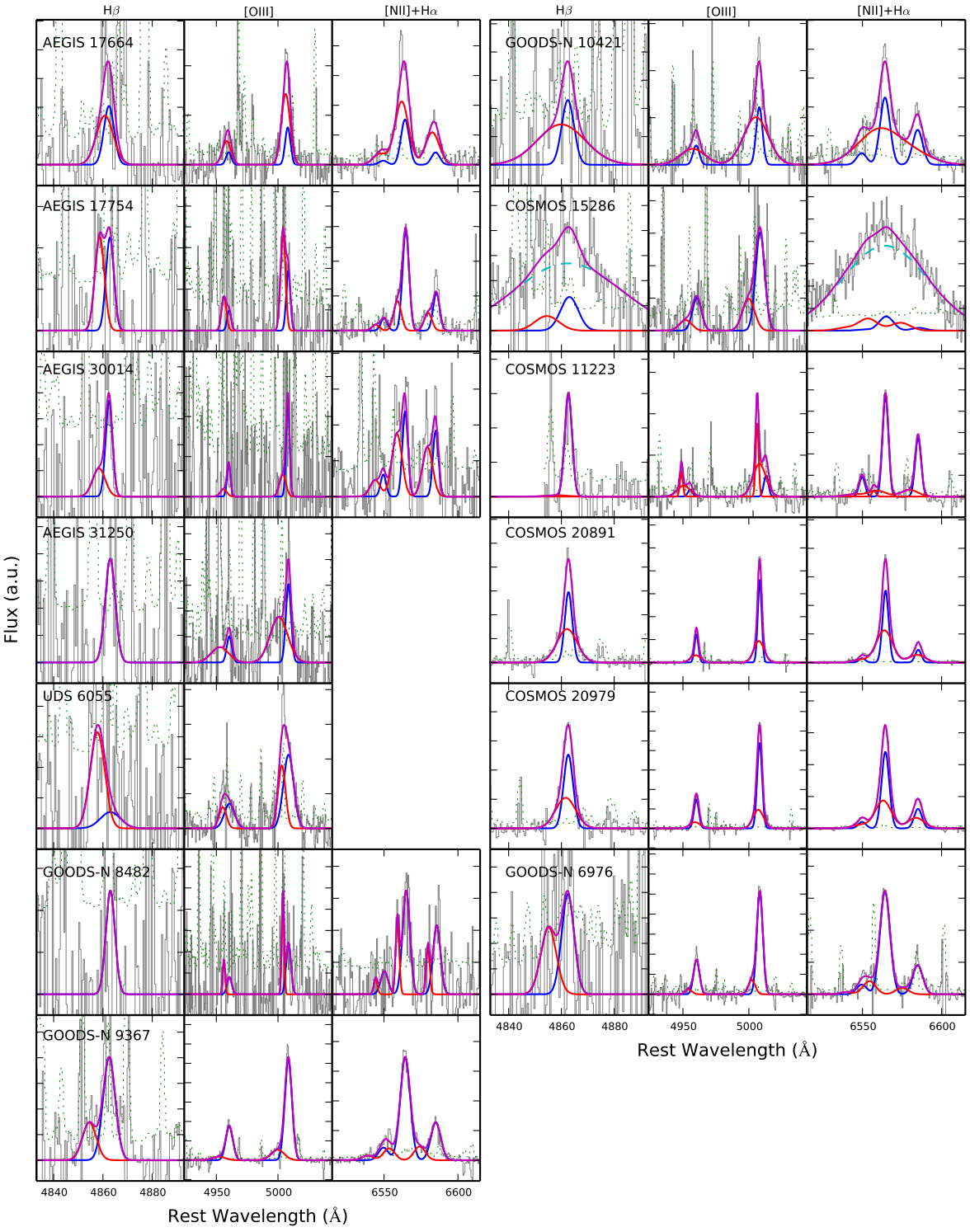

Figure 2.1: 1D spectra showing the Hβ (left), [OIII] (middle), and Hα and [NII] (right) emission lines of all 13 AGN outflows not identified as potential mergers. The thin gray lines show the observed spectra; the solid blue curves show the best-fit narrow-line components; the dashed cyan curves show the best-fit broad-line components; the red curves show the best-fit outflow components; and the thick magenta curves show the best-fit total emission line profiles. Each panel is scaled to arbitrary units.

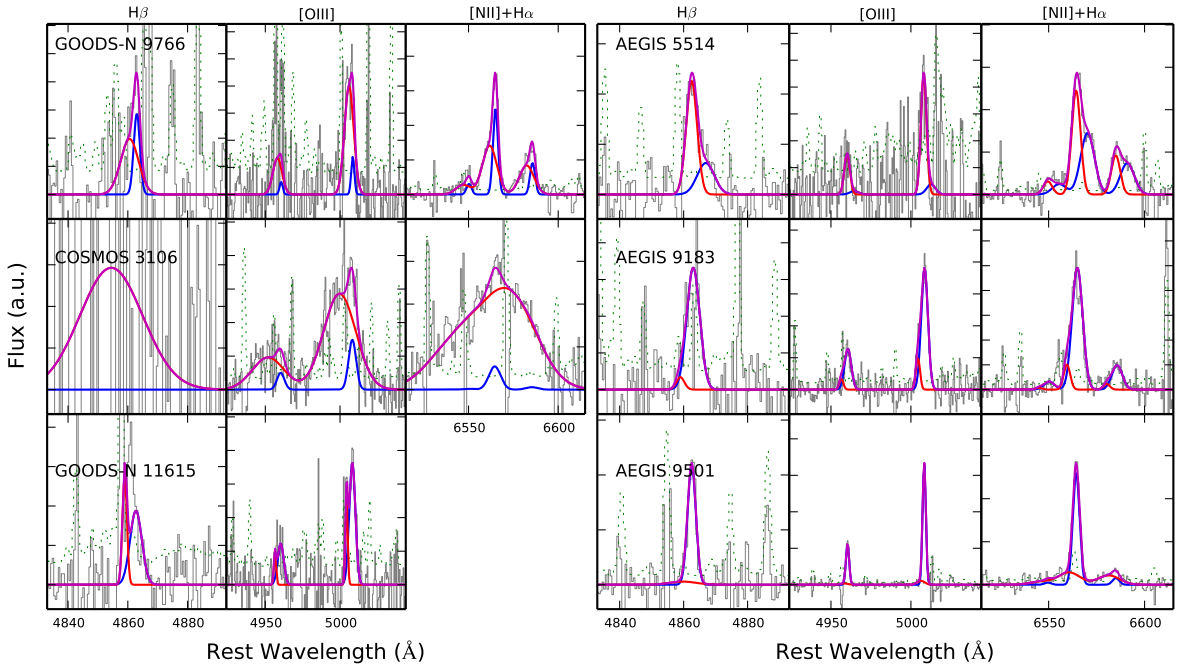

Figure 2.2: Same as Figure 2.1 but for outflow candidates identified as potential mergers.

corresponding to the spectral resolution.

The first criterion is required because of the larger number of sky lines in our observed NIR wavelengths, so it is common for one or more sky lines to affect these emission lines. A total of 19 outflow candidates satisfy these more stringent criteria; their 1D spectra are shown in Figures 2.1 and 2.2, with the best-fit models overlaid.

On-going galaxy merger events can disturb the gas kinematics in galaxies and could result in a second kinematic component in the spectra that appear similar to that from an outflow. While it is entirely possible that outflows can happen during a merger phase, kinematically-disturbed gas from the merger event can contaminate the measurement of the kinematics of the outflows in mergers. As our aim is to use the MOSDEF spectra to characterize the outflowing gas, we remove sources which are potentially undergoing merger events from our sample, in order to avoid potential contamination from disturbed gas that is not outflowing. The study of outflows in

galaxy mergers is better served using integral field spectroscopy, which is beyond the scope of this paper.

We identify potential mergers in the sample using the *HST* images of each source observed in the F160W and F606W bands. Source features suggesting the presence of double nuclei are considered potential mergers. We consider a source to have indication of double nuclei when two distinct peaks in brightness are separated by less than $\sim 1''$ (corresponding to ~ 8 kpc at $z \sim 2$).

13 of the 19 outflow candidates are classified as non-mergers, and their *HST* images in the F160W band are shown in Figure 2.3. Most of these outflow candidates exhibit a round morphology, without multiple distinct peaks in brightness. The morphology of AEGIS 17664 is highly elongated with some brightness variation but is not separable into multiple distinct peaks. This specific morphology is likely produced by an edge-on disk, therefore we include this source in our outflow sample. The elongated morphology of AEGIS 17754 also suggests an edge-on disk. A total of six sources are found to contain possible double nuclei and are excluded from our outflow sample; the F160W *HST* images of these sources are shown in Figure 2.4. Although the F160W image of GOODS-N 9766 shows a point-like morphology, its F606W image clearly shows a ring morphology (see Coil et al. 2015), so it is considered a potential merger. After excluding potential mergers, there are 13 AGN with identified outflows, out of a total of 67 AGN, corresponding to 19% of the full AGN sample.

2.4.2 Detection of Outflows in Galaxies

As all MOSDEF targets with a reliable redshift have been fit using the same emission line fitting procedure described above to identify optical AGN, we can compare the incidence of outflows detected in the emission line spectra of AGN and galaxies in our sample. A significant outflow component satisfying the criteria detailed in Section 2.4.1 is detected in 21 out of the 457 galaxies used in this study. After excluding potential mergers upon inspection of their *HST* images, there are a total of 8 galaxies with outflows detected in emission, corresponding to 1.8%

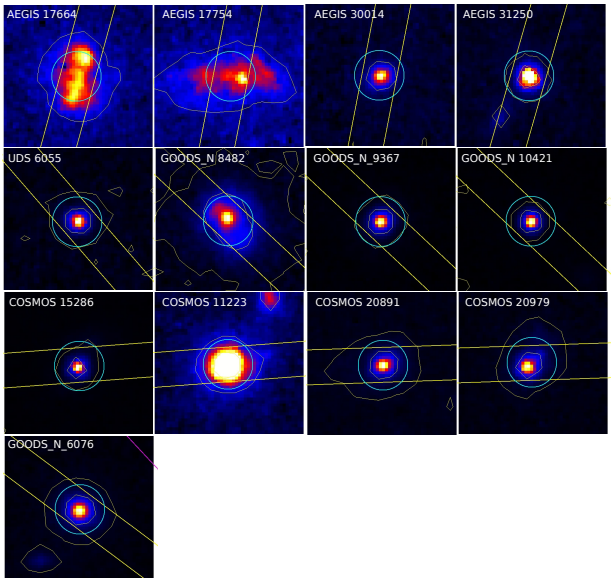

Figure 2.3: *HST* F160W band images of all 13 AGN outflows not identified as potential mergers. The MOSFIRE slit is shown in yellow lines, and a green circle of radius 0.5' centered at the source position is shown for reference. Note that the F606W band images, which are not shown here, are also inspected.

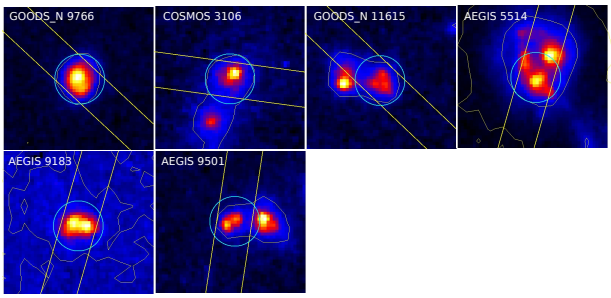

Figure 2.4: Same as Figure 2.3 but for AGN outflow candidates identified as potential mergers.

of the total galaxy sample. These sources could potentially be AGN which are missed by our identification. In particular, two of the galaxies with outflows do not have coverage of Hα and [NII], preventing us from performing optical AGN identification. With an incidence rate of 19%, outflows detected in emission are therefore identified in MOSDEF at a rate $\sim$10 times higher for galaxies with a detected AGN than for inactive galaxies. While outflows are commonly detected in absorption in star-forming galaxies at similar redshifts (e.g. Steidel et al. 2010), our results here provide a direct comparison of the detection rate of outflows in emission in AGN and inactive

galaxies. This factor of 10 difference indicates that the outflows are likely AGN-driven (we return to this point in Section 2.5.5). A detailed study of outflows detected in emission in MOSDEF galaxies is presented in Freeman et al. (2019). The slight difference in the number of galaxy outflow detections in that paper compared to here is likely due to small differences in the fitting procedures used in the studies.

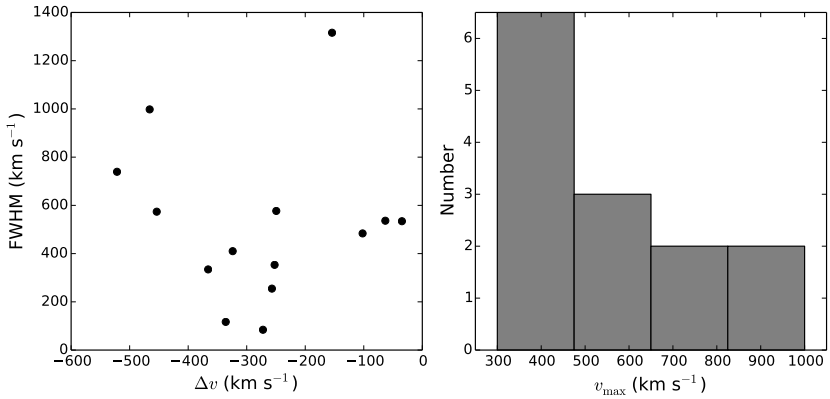

Figure 2.5: Left: Distribution of the velocity widths (FWHM$_v$) and velocity offsets (Δv) for the AGN outflows. Right: Distribution of the maximum velocity ($v_{\rm max}$) of the AGN outflows.

2.4.3 Kinematics

By definition in our detection algorithm, all of the outflow components have a velocity centroid that is blueshifted relative to the narrow-line component (though the outflow may have some emission that is redshifted relative to the narrow-line emission, e.g., COSMOS 10421). The velocity offset between the centroids of the narrow-line and outflow components Δv ranges from ~ -30 to -500 km s^{-1}, with a median of ~ -270 km s^{-1}, while the FWHM of the outflow components ranges from $\sim$100 to 1300 km s^{-1}, with a median of $\sim$ 500 km s^{-1}. The FWHM values reported are deconvolved with the instrumental resolution, as determined from sky lines (see Section 2.3.4). Figure 2.5 (left panel) shows the distribution of FWHM versus Δv. In general, outflows with high velocity shifts (Δv) have relatively high FWHM, though outflows with high FWHM do not necessarily have high velocity shifts. Similar findings in SDSS AGN are also

reported in Woo et al. (2016).

The velocity shift Δv, which shows the average projected line-of-sight velocity of the outflowing gas, depends on the geometry of the outflow and the extinction by dust in the galaxy, and does not directly reflect the average bulk velocity of the outflowing gas. The average velocity of the outflow is better represented by the maximum projected velocity observed, corresponding to the most blueshifted part of the emission line profile. As the S/N of the spectrum at this location may be low, we estimate this maximum velocity by $v_{\rm max} = |\Delta v| + {\rm FWHM}/2$ (e.g. Rupke et al. 2005; Harrison et al. 2012). Figure 2.5 (right panel) shows the distribution of maximum velocity in our sample, which ranges from $\sim$ 300 to 1000 km s^{-1}, with a median of $\sim$ 540 km s^{-1}.

We have also considered other kinematic measures such as the non-parametric line width containing 80% of the flux (w_{80}, see e.g. Zakamska & Greene 2014; Harrison et al. 2016). However, this measure depends on the flux ratio between the narrow-line and outflow components, which can vary among different emission lines, giving different results for different lines. While studies that use this measure often have only one emission line available, we simultaneously fit the [OIII], Hα, [NII] and Hβ emission lines in this study. For our dataset, the kinematic measures from our simultaneous fit results, utilizing information in all the emission lines, provide a more consistent and better constrained measurement of the gas kinematics. For completeness, we compare the ratio of w_{80} in [OIII] to $v_{\rm max}$ in our outflow sample. Using our simultaneous fit results to calculate w_{80} in [OIII], it is very consistent with $v_{\rm max}$, having a ratio of 1.05 ± 0.28. If we calculate w_{80} in [OIII] by fitting the [OIII] line alone, the ratio slightly increases to 1.35 ± 0.47, but is still consistent with unity given the variance.

2.4.4 Line Ratios

The unique dataset obtained by the MOSDEF survey, which provides simultaneous coverage of all of the required optical emission lines at $z \sim 2$, allows us to probe the excitation mechanism of the narrow-line and outflow emission with the optical diagnostic BPT diagram

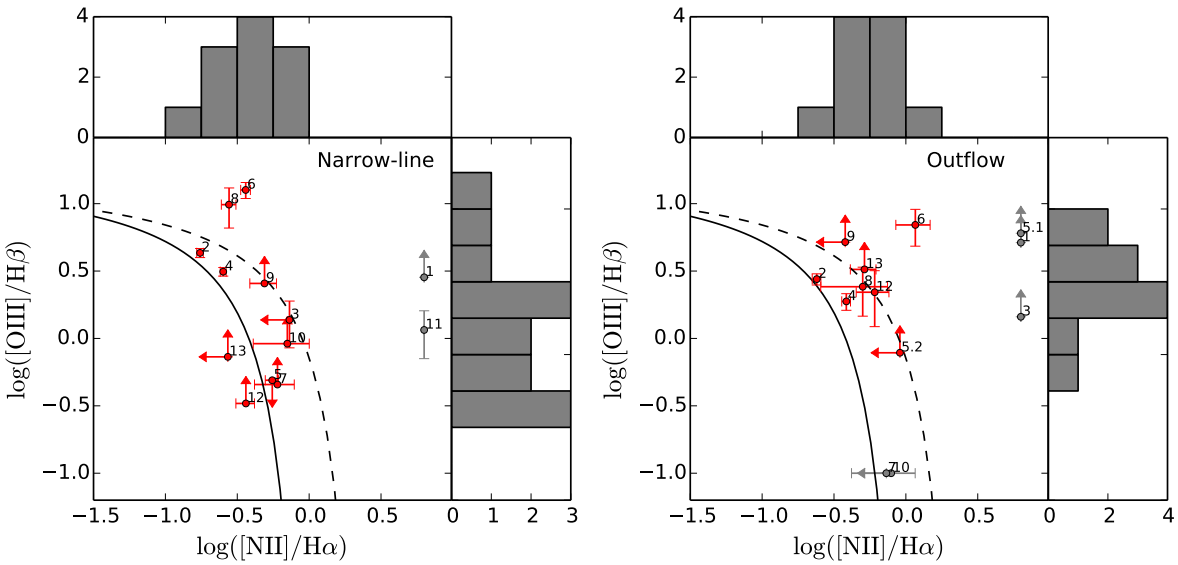

Figure 2.6: [NII] BPT diagrams for gas in the narrow-line component (left) and outflow component (right) of the AGN with outflows in our sample. The solid lines show the Kauffmann et al. (2003b) demarcation line, while the dashed line show the Kewley et al. (2013b) demarcation line at $z = 2.3$. The gray points show sources where only one line ratio is measured. Upper and lower limits are also included in the histograms. The outflow component line ratios are generally shifted towards the AGN region compared with the narrow line component. The sources in each panel are labelled with the same numbers, which correspond to the row numbers in Table 2.1.

(Baldwin et al. 1981; Veilleux & Osterbrock 1987). The excitation mechanism of the individual gas components allows us to test the picture of the quenching of star formation by AGN-driven outflows. If there is increased excitation by star formation in the outflowing gas component, it will argue against the idea that the outflows are AGN-driven and these outflows quench star formation. Figure 3.2 shows the [NII] BPT diagrams for the narrow-line (left) and outflow (right) components of each of our AGN with outflows. The Hα and Hβ fluxes of the narrow-line emission are corrected for Balmer absorption in the galaxy. Sources with S/N$<$3 in one or both of the line ratios are shown with 3σ limits. Also shown are histograms for $\log([\mathrm{OIII}]/\mathrm{H}\beta)$ and $\log([\mathrm{NII}]/\mathrm{H}\alpha)$, which include sources where only one of the line ratios is significant.

Compared with the narrow-line components, the line ratios for the outflow components are shifted towards the AGN region in this diagram. All of the outflow component line ratios lie above the Kauffmann et al. (2003b) line, indicating a likely contribution from AGN in their excitation. For the narrow-line ratios, only two sources lie above the maximum starburst line of Kewley et al. (2013b), in contrast to four sources using the outflow components. This indicates that the excitation of the outflow emission is dominated by AGN rather than star formation for the bulk of the AGN outflows. The outflows are unlikely excited by shocks alone, but it is possible to explain the observed line ratios with a combination of shocks and stellar radiation (e.g. Kewley et al. 2013a; Newman et al. 2014). Given that these sources have known AGN, it is most likely that the gas is photoionized by the AGN. It is worth noting that many of the narrow line components are in the "composite" region between the Kauffmann et al. (2003b) and Kewley et al. (2013b) lines. We will return to the BPT diagram in Section 2.5.7 to discuss the lack of positive AGN feedback observed.

2.4.5 Physical Extent

One of the key properties of AGN-driven outflows is their physical extent, which is crucial information needed to determine the impact outflows have on their host galaxies and whether

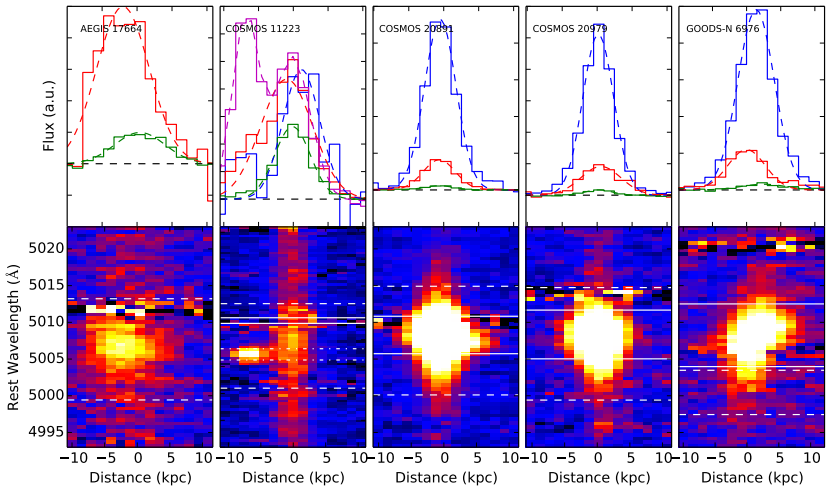

Figure 2.7: Spatial profiles (upper) derived from 2D spectra (lower) of the [OIII]λ5008 emission line for AGN outflows with significant spatial extent detected in this emission line. In the 2D spectra the solid white lines show the wavelength range used to extract the narrow-line spatial profile, while the dashed white lines show the wavelength range used to extract the outflow spatial profile. For COSMOS 11223, the wavelength range dominated by the additional, faster outflow component is shown with dashed-dotted white lines. If two wavelength ranges overlap, the overlapped region is excluded from the wider wavelength range during the extraction. (See text for details.) In the spatial profiles the narrow-line, outflow, and continuum profiles are shown in blue, red and green, respectively; the second, faster outflow component of COSMOS 11223 is shown in magenta. Dashed curves show the best-fit Gaussian function to each spatial profile.

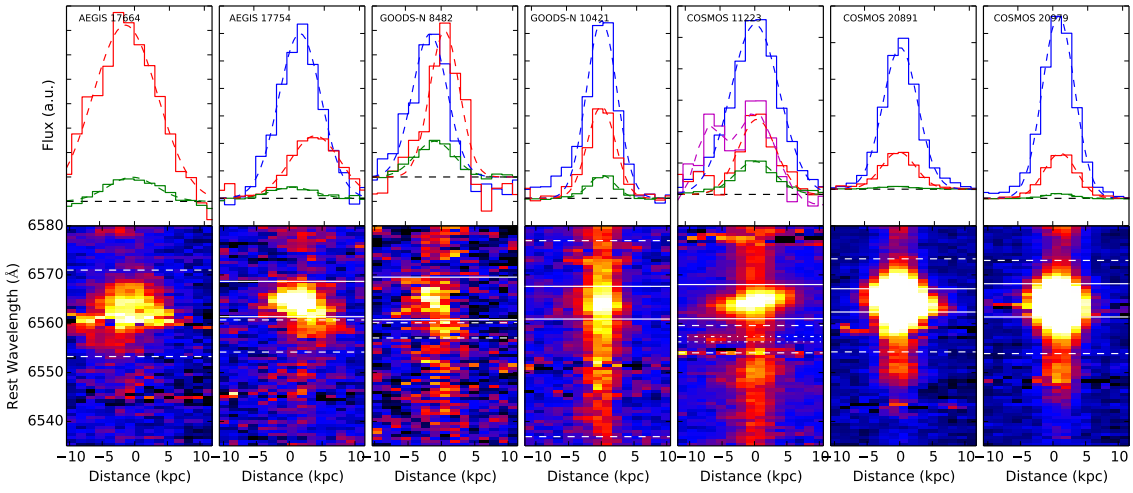

Figure 2.8: Same as Figure 2.7 but for the Hα emission line.

they can successfully expel gas out of the halo of the galaxy and quench star formation. With the slit spectra from MOSDEF, we have spatial information along the slit direction, allowing us to determine the physical extent of the outflows in one spatial direction. To investigate the potential presence of physically-extended emission, we create spatial profiles from the 2D spectra for the narrow-line and outflow components for the [OIII]λ5008 and Hα emission lines, as well as for the continuum. We first select narrow-line or outflow dominated wavelength ranges, over which the narrow-line or outflow flux from the 1D Gaussian fit is higher than the sum of all of the other components. We also limit the wavelength range to be within 2σ of the central wavelength of the respective component.

For AEGIS 17664, the narrow-line component is weaker than the outflow component in all wavelengths, so only an outflow wavelength range is selected according to the criteria above. For sources where the narrow-line wavelength range is enclosed within the outflow wavelength range, such as COSMOS 20891, the narrow-line wavelength range is excluded from the outflow wavelength range according to the criteria above, since it is weaker than the outflow flux. The continuum is selected in wavelength ranges far from emission lines. We then sum the fluxes in the 2D spectra along the wavelength axis within the specific wavelength range to create spatial profiles for each component: narrow-line, outflow, and continuum.

To quantify the physical extent of the emission in each component, we fit a single Gaussian function to each spatial profile. The difference between the Gaussian centroids of the narrow-line and outflow components, $|\Delta x|$, will give the projected spatial offset between the narrow-line region and the outflows. The width of each Gaussian is deconvolved from the seeing, measured from the star observed on every MOSDEF mask. An outflow is resolved if the deconvolved width of the outflow component is significantly non-zero (more than three times its uncertainty). We combine these two measurements to estimate the full physical extent of the outflow from the center of the narrow-line region. We define r_{10} as $|\Delta x| + \mathrm{FWTM}/2$, where FWTM is the full width at 1/10 of the maximum of the outflow component.

The spatial profile measurements are shown in Table 2.2. Six sources have their outflow component spatially offset from the narrow-line component in at least one of the emission lines while seven are resolved. Eight sources have a significantly non-zero r_{10}, ranging from 2.5 to 11.0 kpc. Figures 2.7 and 2.8 show the 2D spectra and spatial profiles of the [OIII]λ5008 and Hα emission lines for the sources with significantly non-zero r_{10}. We measure r_{10} for both the [OIII] and Hα emission lines because often one of the lines is impacted by a sky line. In the cases where r_{10} is well measured in both lines, the spatial extent in the two lines generally agrees, with the [OIII] extent ranging from $\sim 0.7 - 1.5$ that in Hα.

2.4.6 COSMOS 11223

Among the AGN with outflows, COSMOS 11223 is particularly interesting, as this source has *two* significant outflow components at different velocities. It is the only source in our sample where the best fit requires more than one outflow component. Figure 2.9 shows the 1D and 2D spectra of this source, along with the *HST* F160W image and the spatial profile.

The slower outflow has a velocity offset of -253 km $s^{-1}$and a FWHM of 580 km s^{-1}. It is detected in Hα (S/N=3) and at high S/N in the [OIII] lines (S/N=5 for both lines combined). [NII] has a marginal S/N of 2.6. The faster outflow has a velocity offset of -340 km $s^{-1}$and a FWHM of 136 km s^{-1}. It is detected at very high S/N in the [OIII] lines (S/N=13 for both lines combined) and can be seen clearly in each of the [OIII] lines. The detection at two wavelengths indicates that it is not a chance projection of a single emission line from a source at another redshift. This outflow is not detected at [NII], as there is a sky line at this wavelength, but it is detected at Hα (S/N=5). On the BPT diagram, the slower outflow is not detected in either Hβ or [NII], such that it can not be placed on the BPT diagram. The faster outflow is detected in one of the lines in both line ratios, resulting in a limit that lies just below the Kewley et al. (2013b) demarcation line, and is labelled "14" in Figure 3.2.

In terms of spatial extent, the slower outflow is not significantly resolved or offset from

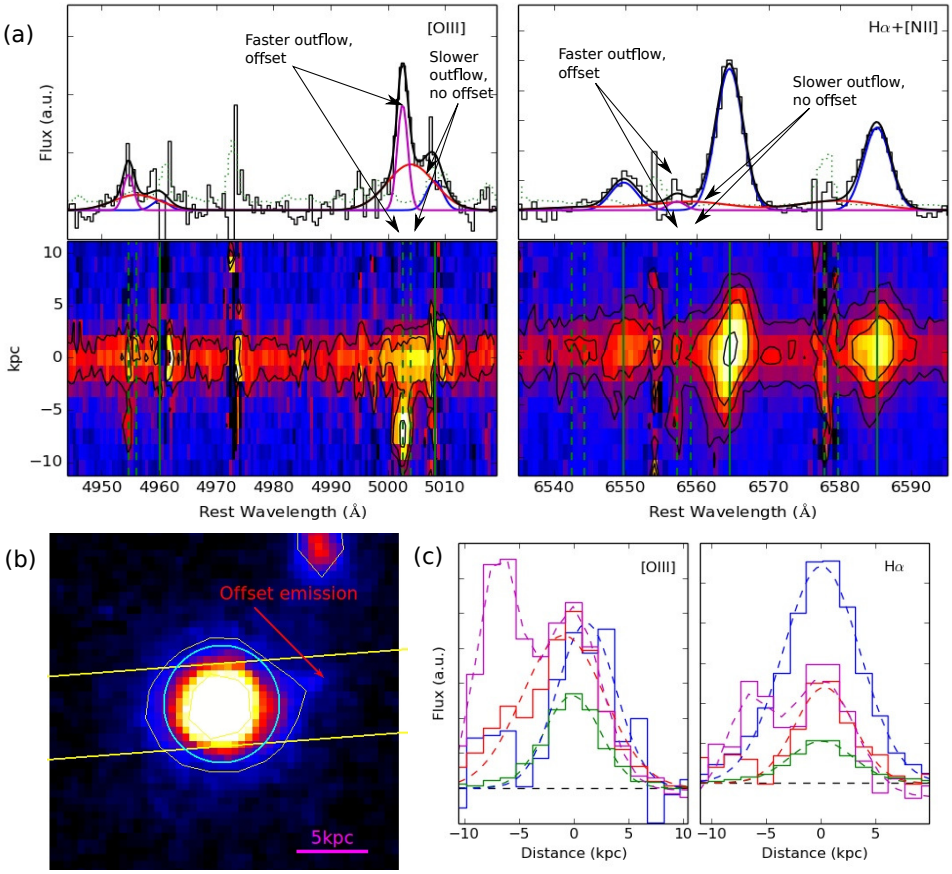

Figure 2.9: (a) 1D (top) and 2D (bottom) spectra of COSMOS 11223. The 1D spectrum is extracted from the central 13 spatial pixels. The thin black line shows the observed spectra; the blue curve shows the best-fit narrow-line component; the red curves shows the best-fit for the slower outflow; the red curve shows the best-fit for the faster outflow; and the thick black curve shows the best-fit total emission line profile. (b) *HST* F160W band images of COSMOS 11223. Note the nearby source at the top-right corner at a similar projected position with the offset emission. The MOSFIRE slit is shown in yellow lines, and a green circle of radius 0.5' centered at the source position is shown for reference. (c) Spatial profiles for the [OIII]λ5008 (left) and Hα (right) emission lines. Two outflow components at different velocities are detected in this source. The faster outflow is spatially offset from the narrow-line region by 6.8 kpc while the slower outflow is not. The spatially offset outflow is seen in the *HST* image as a faint emission along the MOSDEF slit.

Table 2.2: Kinematic and Spatial Measurements

ID	Δv (km s^{-1})	FWHM (km s^{-1})	v_{max} (km s^{-1})	Offset ([OIII]) (kpc)	FWHM ([OIII]) (kpc)	r_{10} ([OIII]) (kpc)	Offset (Hα) (kpc)	FWHM (Hα) (kpc)	r_{10} (Hα) (kpc)
6055	-324	410	529	0.3 ± 0.4	[a]	0.3 ± 0.4	[b]	[b]	[b]
20891	-35	534	302	0.2 ± 0.1	**2.8 ± 0.2**[c]	**2.7 ± 0.2**	**0.3 ± 0.1**	**4.0 ± 0.2**	**3.9 ± 0.2**
15286	-454	574	741	0.1 ± 0.1	1.6 ± 0.7	1.6 ± 0.7	[b]	[b]	[b]
20979	-63	536	331	0.4 ± 0.3	**4.8 ± 0.9**	**4.8 ± 0.9**	0.2 ± 0.1	**3.6 ± 0.1**	**3.5 ± 0.1**
11223a	-250	577	538	2.1 ± 0.7	**7.4 ± 0.6**	**8.8 ± 0.9**	0.3 ± 0.5	3.6 ± 2.8	3.5 ± 2.6
11223b	-335	117	394	**6.8 ± 0.1**	**4.5 ± 0.3**	**11.0 ± 0.3**	**6.7 ± 0.7**	4.5 ± 2.0	**10.7 ± 1.2**
9367	-522	739	891	0.5 ± 0.3	3.4 ± 1.5	3.5 ± 1.4	0.2 ± 0.3	3.5 ± 1.3	3.4 ± 1.2
8482	-272	84	314	3.5 ± 3.5	9.2 ± 12.3	11.8 ± 11.8	**2.0 ± 0.4**	2.9 ± 1.3	**4.7 ± 1.3**
6976	-366	334	533	**1.4 ± 0.2**	**4.4 ± 0.9**	**5.4 ± 0.8**	1.5 ± 0.5	[a]	1.5 ± 0.5
10421	-154	1316	812	0.0 ± 0.3	2.3 ± 1.4	2.1 ± 1.3	0.1 ± 0.1	**2.6 ± 0.5**	**2.5 ± 0.5**
30014	-252	353	429	2.1 ± 1.1	[a]	2.1 ± 1.1	1.6 ± 0.7	[a]	1.6 ± 0.7
31250	-466	998	965	0.4 ± 0.6	3.7 ± 2.2	3.8 ± 2.1	[b]	[b]	[b]
17754	-257	255	384	1.2 ± 1.0	2.0 ± 4.6	3.1 ± 4.3	**2.1 ± 0.3**	**5.7 ± 1.0**	**7.3 ± 1.0**
17664	-102	484	344	**2.4 ± 0.5**	**6.1 ± 1.0**	**7.9 ± 1.1**	**1.0 ± 0.3**	**8.6 ± 0.6**	**8.8 ± 0.6**

[a] FWHM is not larger than seeing.
[b] Hα measurements are unavailable in 31250, 6055 and 15286.
[c] Spatial measurement which are significantly non-zero are shown in bold.

the narrow-line region in this source, but the faster outflow is both resolved and offset. It has the largest physical extent of any outflow in our sample, r_{10}=11.0 kpc in [OIII]. The *HST* F160W, F814W, and F606W images all show faint extended emission in the direction of the outflow as detected on the MOSDEF slit. The *HST* images show a faint nearby source (COSMOS 10856) located $1.6''$ away from COSMOS 11223 (see Figure 2.9). This nearby source is outside of the MOSDEF slit, but its projected position along the MOSDEF slit is somewhat similar to the position of the spatially extended outflow component. In the 3D-*HST* catalog (Momcheva et al. 2016; Brammer et al. 2012), this nearby source has a grism redshift estimate of $z = 0.52 - 0.63$ and a photometric redshift estimate of $z = 0.81 - 0.90$, within the 95% confidence intervals. There is no current spectroscopic redshift available for this source, such that we can not strictly rule out the possibility of a tidal interaction between this source and COSMOS 11223, if they are at the same redshift. We are in the process of conducting Keck/OSIRIS integral field spectroscopy follow-up of this source, to better determine the nature of this very extended outflow.

2.5 Discussion

2.5.1 Outflow Incidence

In our sample of 67 X-ray, IR, and/or optically-selected AGN at $z \sim 2$, outflows are identified in 13 (19%) of the AGN (after removing likely on-going mergers). In the 457 non-AGN MOSDEF galaxies, only 8 (1.8%) outflows are detected. The outflow incidence detected in the MOSDEF AGN sample is similar to that found at $z \sim 0$ by Mullaney et al. (2013) using broad [OIII] emission, who find outflow signatures in 17% of $>$ 24000 optically-selected AGN in SDSS. The incidence of outflows in AGN at $z \sim 2$ is at least as high as that at $z \sim 0$. As shown below in Section 2.5.3, the detection rate of outflows in our sample correlates with the signal-to-noise ratio of the [OIII] emission line. Therefore, in general, the incidence rate found here should be treated as a lower limit on the true outflow incidence.

Harrison et al. (2016) analyze the [OIII] spectra of 54 X-ray AGN at $z \sim 1.1 - 1.7$, detecting a second kinematic component in 14 of the AGN, corresponding to 26% of their AGN sample. This is comparable to the outflow incidence found in our study at $z \sim 2$. If only X-ray AGN are considered in our sample, the outflow incidence is 25%, in very good agreement with Harrison et al. (2016). At $z \sim 2$, Genzel et al. (2014) finds 34 outflows in 110 star-forming galaxies, while 18 of the star-forming galaxies are confirmed AGN. While our study first defines a sample of AGN and searches for outflows in it, Genzel et al. (2014) searches for outflows in a sample of galaxies. Due to the difference in the nature of the parent sample, one cannot directly compare the outflow incidence in this study with that in Genzel et al. (2014). In particular, one cannot directly determine the incidence of outflows among AGN at $z \sim 2$ using the results of Genzel et al. (2014).

2.5.2 Correlation with Host Galaxy Properties

AGN-driven outflows are commonly believed to affect the evolution of their host galaxies, in particular by quenching star formation in galaxies in the high mass end of the stellar mass function (Di Matteo et al. 2005; Hopkins et al. 2006, 2008; Debuhr et al. 2012). Therefore, it is informative to study the correlation between the incidence of AGN outflows with their host galaxy properties such as stellar mass and SFR.

Figure 2.10 (left panel) shows the distribution of SFR versus stellar mass (see Section 3.3.4) for all of the galaxies (shown in contours), AGN (blue filled circles), and AGN with outflows (red filled circles) in the sample used here. The star formation main sequence for MOSDEF galaxies found by Shivaei et al. (2015):

$$\log\left(\mathrm{SFR}/M_{\odot}\ \mathrm{yr}^{-1}\right) = 0.8\ \log(M_{*}/M_{\odot}) - 6.79 \tag{2.8}$$

is also shown (magenta line). The upper right and lower right panels of Figure 2.10 show the distributions of stellar mass and SFR, respectively, of all AGN and AGN with outflows in our sample. Outflows are detected in AGN spanning stellar masses of $10^{10} - 10^{11.5}\,\mathrm{M}_{\odot}$. A two-sample KS test on the distributions of stellar masses for AGN with and without outflows returns a p-value of 0.4 for the null hypothesis that the two distributions are the same. Therefore, no significant trend of outflow incidence with host stellar mass is observed. Similarly, the distribution of SFR with respect to the main sequence is similar for AGN with and without detected outflows.

Genzel et al. (2014) use a sample of 44 star-forming galaxies at $z \sim 2$ to report a strong stellar mass-dependent incidence of detected outflows observed in emission that increases with stellar mass at least as much as the incidence of AGN within the galaxy sample. They imply that the outflows are predominantly driven by AGN and that there is therefore a strong stellar mass-dependence to the incidence of AGN-driven outflows. However, Genzel et al. (2014) do not first create a sample of AGN and then identify outflows within that AGN sample; they start

with a sample of star-forming galaxies and identify outflows and AGN within that galaxy sample. This means that they cannot measure the incidence of AGN-driven outflows within the AGN population, as we do here.

Additionally, there is a well-known selection bias that leads to AGN in higher mass galaxies being more likely to be identified, while the true incidence of AGN in galaxies is independent of stellar mass to first order (Aird et al. 2012). This implies that if outflows are more likely to be identified in AGN (as we find here), which are preferentially identified in higher mass galaxies (and seen by both Genzel et al. 2014 and in MOSDEF by Azadi et al. 2017), then it will *appear* that outflows are more common in higher mass galaxies, many of which host AGN (as seen by Genzel et al. 2014). However, it does not mean that AGN-driven outflows are actually more common in high mass galaxies, and it does not imply that there is a stellar mass dependence to the incidence of AGN-driven outflows. Therefore our result that the incidence of detected outflows within a sample of AGN does *not* show a strong mass dependence is not in conflict with the data presented in Genzel et al. (2014).

It is also interesting to note that we find that the incidence AGN outflows at $z \sim 2$ does not appear to depend on the host SFR with respect to the main sequence. This suggests that the incidence of AGN-driven outflows is uniform among high mass galaxies ($M_* > 10^{10} \mathrm{M}_\odot$) regardless of their SFR, and could be taken to imply that the presence of AGN-driven outflows does not quench star formation. However, different methods used to estimate SFR are sensitive to star formation on different timescales, and the method of SED fitting used in this study reflects star formation over the relatively long timescale of the *past* 10^8 years (e.g. Kennicutt 1998), such that the instantaneous SFR could differ. Therefore, the measured SFR may reflect the SFR in the past rather than the immediate effect of the outflows on the galaxies.

On the other hand, theoretical work (e.g. Di Matteo et al. 2005; Antonuccio-Delogu & Silk 2010) predicts that the timescale for quenching due to AGN outflows is $\sim 10^8$ yrs, such that there can be a time delay for the effect of the AGN outflow on the host galaxy to become observable

on the SFR. Moreover, AGN are known to vary significantly over a range of timescales (e.g. Hickox et al. 2014; Gabor & Bournaud 2014), such that the AGN may not be detectable when its effects due to feedback become observable. Such AGN variability can also introduce scatter in any underlying correlations between outflow properties and the AGN bolometric luminosity.

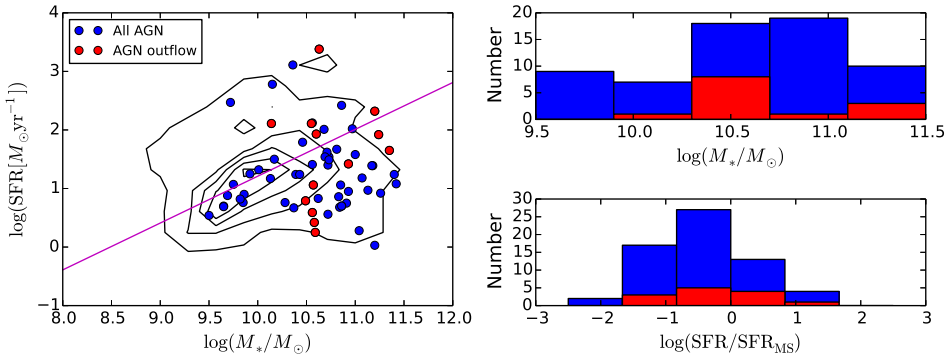

Figure 2.10: Left: SFR versus stellar mass for all galaxies (black contour), AGN (blue points) and AGN with outflows (red points) in the current sample. The magenta solid line shows the star formation main sequence. Upper right: Distribution of stellar mass for all AGN (blue) and AGN with outflows (red). Lower right: Distribution of SFR/SFR$_{MS}$ for all AGN (blue) and AGN with outflows (red). Outflows are detected in AGN spanning the main sequence of star formation, with no clear dependence on the stellar mass or SFR of the host galaxy.

2.5.3 Correlation with [OIII] Luminosity and S/N

One method that may provide hints of the driving mechanism of the outflows is to look for correlations between outflow properties and the AGN luminosity. A common proxy for the AGN bolometric luminosity (L_{AGN}) is the [OIII] luminosity ($L_{[OIII]}$), where L_{AGN} and $L_{[OIII]}$ are related by a constant bolometric correction factor (e.g. 600 in Kauffmann & Heckman 2009). As we have [OIII] luminosities for all AGN in our sample, but we do not necessarily have X-ray luminosities or IR luminosities that are dominated by light from the AGN itself (as opposed to the host galaxy), we compare the incidence of outflows with $L_{[OIII]}$. While $L_{[OIII]}$ can be affected by contamination from star formation in the host galaxy, Azadi et al. (2017) estimate that on average only $\sim 30\%$ of the [OIII] light in AGN in the MOSDEF sample may be due to star formation.

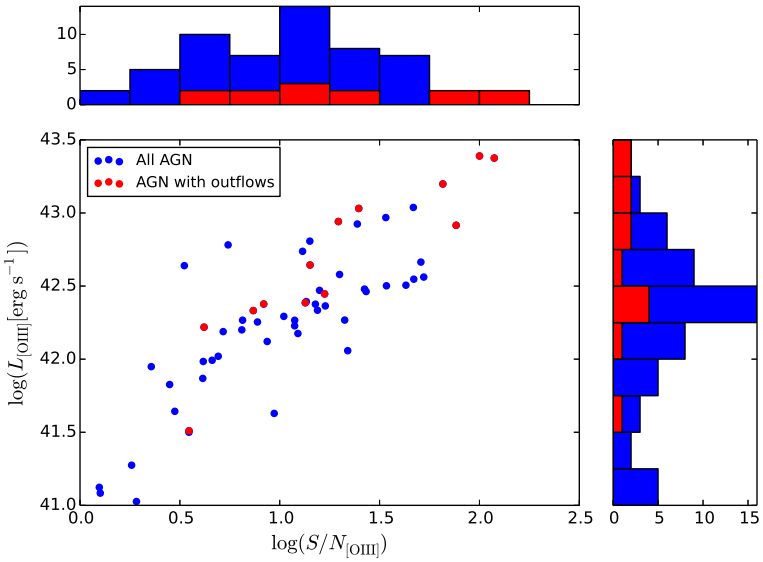

Figure 2.11: Distribution of $L_{[OIII]}$ versus the signal-to-noise ratio in [OIII] for all AGN (blue) and AGN with outflows (red). While outflows are more often found for sources with high $L_{[OIII]}$, the same trend is also observed for the signal-to-noise of the spectra as well.

However, the comparison between outflow incidence and $L_{[OIII]}$ may be complicated by the fact that sources with a higher $L_{[OIII]}$ also tend to have a higher signal-to-noise ratio, which could potentially lead to an easier detection of an outflow in the spectra. As a result, one must take into account the signal-to-noise ratio when looking for any such correlations with $L_{[OIII]}$.

The values of $L_{[OIII]}$ we use are corrected for dust reddening. To determine the correction factor, we calculate the color excess from the Balmer decrement and combine this with the value of the MOSDEF dust attenuation curve at 5008Å (Reddy et al. 2015). The corrected $L_{[OIII]}$ is on average increased by ~ 0.17 dex for the AGN in our sample (see Azadi et al. 2017).

Figure 2.11 shows the distribution of $L_{[OIII]}$ versus signal-to-noise ratio in the [OIII] line, for all AGN and for AGN with outflows. There is a higher incidence rate of detected outflows in AGN with higher $L_{[OIII]}$, but a similar trend is also observed in the signal-to-noise ratio. At a given signal-to-noise ratio, outflows appear to be observed slightly more commonly in those with higher $L_{[OIII]}$, but the difference is not significant. Therefore, the correlation of the incidence of AGN outflows with $L_{[OIII]}$ cannot be tested in our sample due to its coupling with the signal-to-noise

ratio. We also compare the outflow velocity with $L_{[OIII]}$ with no clear trend observed, which is consistent with other AGN outflow studies (e.g. Harrison et al. 2014).

Our results show that the signal-to-noise ratio is an important factor in the detection of outflows, which must be taken into account when comparing outflow incidence with $L_{[OIII]}$. Moreover, high velocity (~ 1000 km s^{-1}) outflows are found to occur in AGN across a range of $L_{[OIII]}$.

2.5.4 Correlation with X-ray, IR and Optical AGN Identification

In the MOSDEF survey, AGN are identified through X-ray, IR and optical selection techniques, which are described in detail in Section 3.3. It is known that different identification methods present biases in both the AGN and host properties, and such biases in the MOSDEF sample are discussed in Azadi et al. (2017). In particular, they show that optical AGN identification is possibly biased towards galaxies with higher dust content, while IR AGN identification may be biased towards galaxies with lower dust content in the MOSDEF sample. This selection bias may help constrain the driver of the outflow since it has been proposed that the radiation pressure on dust grains can lead to galaxy-wide outflows and boost the outflow velocity to $\sim 1000-2000$ km s^{-1}for both AGN or starburst-driven winds (e.g. Murray et al. 2005; Thompson et al. 2015). Therefore, the incidence of outflows in AGN identified at different wavelengths may reveal information about the potential mechanism(s) driving these outflows.

We analyze the dependence of the incidence of outflows detected in our sample and the identification wavelength of the AGN. Outflows are somewhat more commonly detected among X-ray AGN (9/36, $25\% \pm 8\%$), compared to non-X-ray AGN (4/31, $13\% \pm 6\%$). Similarly, the outflow detection rate is higher among optical AGN (11/45, $24\% \pm 7\%$) than non-optical AGN (2/22, $9\% \pm 6\%$). There is no difference in the outflow detection rate between IR AGN (5/27, $19\% \pm 8\%$) and non-IR AGN (8/40, $20\% \pm 7\%$). We note that AGN can be identified at multiple wavelengths; Azadi et al. (2017) report the overlap and uniqueness of AGN selection at each

wavelength in the MOSDEF survey.

The slightly higher outflow incidence in X-ray and/or optical AGN may be due to their bias towards being detected more often in higher mass galaxies. It is interesting to note that optically-selected AGN, which reside in more dusty host galaxies in the MOSDEF survey, have a slightly higher outflow incidence than non-optical AGN. However, no difference is observed between IR AGN and non-IR AGN. Therefore, we cannot establish a significant relation between the incidence of outflows and the dust content of the galaxy or near the AGN, which may be expected if radiation pressure on dust grains is a key component of the physical driving mechanism of these winds. We note that IR AGN in MOSDEF are found to reside in host galaxies which are less dusty on the whole, although there may be more dust in the vicinity of the AGN to allow for IR detection. Nevertheless, one should be cautious about these conclusions as the current sample size is small. The full MOSDEF sample will provide better statistics to further investigate these questions.

2.5.5 Mass and Energy Outflow Rates

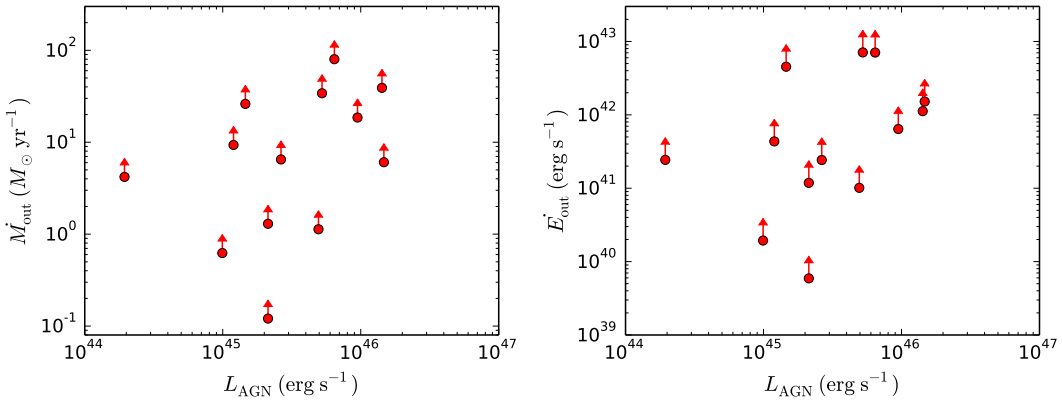

Figure 2.12: Left: Mass outflow rates estimated for the ionized gas (shown as lower limits on the total mass outflow rate) versus the bolometric AGN luminosity. Right: Energy outflow rate of the ionized gas (shown as lower limits on the total energy outflow rate) versus the bolometric AGN luminosity.

To understand the drivers of these outflows and their potential impact on the evolution of their host galaxies, it is crucial to estimate the mass and energy carried by the outflows. Unfortunately, deriving accurate estimates of the mass and energy of the outflows can be challenging as it requires precise knowledge of the outflow geometry and kinematics, as well as the properties of the interstellar medium and the physical state of the gas in the outflow. Nevertheless, first-order estimates of the mass and energy of the outflows are informative to verify the consistency of the proposed picture of AGN-driven outflows quenching star formation.

We estimate the mass of the ionized outflowing gas by counting the number of recombining hydrogen atoms. Assuming purely photoionized gas with 'Case B' recombination with an intrinsic line ratio of Hα/Hβ= 2.9 and an electron temperature of $T = 10^4$K, following Osterbrock & Ferland (2006) and Nesvadba et al. (2017), the mass of the ionized gas in the outflow can be expressed as

$$\frac{M_{\rm ion}}{3.3\times10^8\,{\rm M}_\odot} = \left(\frac{L_{\rm H\alpha,out}}{10^{43}\ {\rm erg\ s^{-1}}}\right)\left(\frac{n_e}{100\ {\rm cm^{-3}}}\right)^{-1}, \tag{2.9}$$

where $L_{\rm H\alpha,out}$ is the outflow Hα luminosity and n_e is the electron density of the ionized gas. Equivalently, the mass of the ionized gas in the outflow can be expressed in terms of the Hβ luminosity as

$$\frac{M_{\rm ion}}{9.5\times10^8\,{\rm M}_\odot} = \left(\frac{L_{\rm H\beta,out}}{10^{43}\ {\rm erg\ s^{-1}}}\right)\left(\frac{n_e}{100\ {\rm cm^{-3}}}\right)^{-1}, \tag{2.10}$$

where $L_{\rm H\beta,out}$ is the outflow Hβ luminosity. As noted in Nesvadba et al. (2017), these updated equations are a factor of 3 smaller than in some previous studies (e.g. Nesvadba et al. 2006, 2011). In 11 of the 14 outflows (we separate the two outflows detected in COSMOS 11223, such that we have a total of 14 outflows), both Hα and Hβ are measured. For all of these outflows, the signal-to-noise in Hα is higher than that in Hβ, so Equation 3.8 is used. Equation 3.8 is also used for GOODS-N 8482, where only Hα is measured. Only Hβ is available in UDS 6055, and equation 3.9 is used. Neither Hα nor Hβ is measured in AEGIS 31250, so no mass estimate is calculated. In our sample, the ionized masses for the same source obtained from Equations 3.8

and 3.9 are in good agreement, differing by at most a factor of five.

The electron density of the *outflow* is not directly measured in MOSDEF as the outflow component is not detectable in the relatively faint [SII] doublet. However, the median electron density in the *star-forming regions* of MOSDEF galaxies at $z \sim 2.3$ is $n_e = 250^{+128}_{-29}$ cm^{-3} (Sanders et al. 2016). A recent study (Newman et al. 2012) suggests that the outflowing gas density is probably a factor of a few smaller than that of the star-forming gas. Therefore, we take the electron density of the outflow as $n_e = 100$ cm^{-3} when calculating the ionized outflow mass in Equations 3.8 and 3.9. While there is uncertainty in this value, this is similar to the electron densities used in other studies of AGN outflows (e.g. Nesvadba et al. 2006, 2008; Liu et al. 2013b; Genzel et al. 2014; Harrison et al. 2014), which lie between 80 and 500 cm^{-3}. Using this method, we obtain ionized outflowing gas masses of $M_{\rm ion} = (0.5-34) \times 10^7\,{\rm M}_\odot$, with a median mass of $4.3 \times 10^7\,{\rm M}_\odot$.

The kinetic energy of the ionized outflow can be estimated by

$$E_{\rm kin} = \frac{1}{2} M_{\rm out} v_{\rm out}^2. \tag{2.11}$$

We use $v_{\rm out} = v_{\rm max}$ as defined in Section 3.4.3 for the outflow velocity. And from here onwards, we use $M_{\rm out} = M_{\rm ion}$. For our sources we find $E_{\rm kin} = (0.07-5.6) \times 10^{56}$ erg, with a median energy of 1.2×10^{56} erg.

Then the mass outflow rate is obtained by

$$\dot{M}_{\rm out} = M_{\rm out} \times \frac{v_{\rm out}}{R_{\rm out}}. \tag{2.12}$$

The value of $R_{\rm out}$ is taken to be r_{10} as defined in Section 3.4.5, which is the distance where the flux of the outflow as seen in emission drops to one tenth of the maximum value. The kinetic

energy outflow rate and momentum flux are then given by

$$\dot{E}_{\rm kin} = \frac{1}{2}\dot{M}_{\rm out} v_{\rm out}^2 \tag{2.13}$$

and

$$\dot{P}_{\rm out} = \dot{M}_{\rm out} v_{\rm out}, \tag{2.14}$$

respectively. We find $\dot{M}_{\rm out} = 0.1 - 80.0$ $M_\odot$ yr^{-1}, with a median mass outflow rate of 6.5 $M_\odot$ yr^{-1}. The kinetic energy outflow rate is $\dot{E}_{\rm kin} = (0.06 - 70.9) \times 10^{41}$ erg s^{-1}, with a median of 4.3×10^{41} erg s^{-1}. The momentum flux is $\dot{P}_{\rm out} = (0.03 - 27) \times 10^{34}$ dyn, with a median of 2.3×10^{34} dyn. Values of the mass and energy outflow rates as a function of bolometric AGN luminosity are shown in Figure 2.12 and listed in Table 2.3.

These estimates provide lower limits on the actual outflow rates as they consider only the ionized phase of the outflowing gas, ignoring outflowing gas in other phases (e.g. molecular and neutral). For example, Nesvadba et al. (2017) find that that there is $\sim 5 - 50$ times more molecular gas than ionized gas in high-redshift radio galaxies with outflows. Moreover, the observed Hα or Hβ flux does not account for the entire mass of the ionized outflows, since we observe only the blueshifted wing in the emission line. Additionally, our estimates are derived assuming $n_e = 100$ cm^{-3}. Since the ionized gas mass is inversely proportional to the value of n_e, any change in the value of n_e will inversely change both the mass and energy outflow rates. For example, if the value of n_e decreases by a factor of ten, the mass and energy outflow rates will increase by a factor of ten. Therefore, it is reasonable that the actual outflow mass is a factor of at least a few to ten times larger the the ionized gas mass estimated here, and these number can serve as a conservative lower limit.

Another method commonly used in the literature to estimate mass and energy outflow rates is to consider an energy conserving bubble expanding into a uniform medium (e.g. Heckman et al. 1990; Veilleux et al. 2005; Nesvadba et al. 2006, 2008; Harrison et al. 2012, 2014). In this

Table 2.3: Ionized Outflow Energetics Measurements

ID	$\dot{M}$[a]	$\dot{M}/\dot{M}_{\rm stellar,max}$[b]	$\dot{M}/{\rm SFR}$[c]	$\dot{E}$[d]	$\dot{E}/L_{\rm AGN}$[e]	$\dot{P}$[f]	$\dot{P}c/L_{\rm AGN}$[g]
6055	80.04	13.56	30.43	7.06×10^{42}	0.11%	2.67×10^{35}	1.24
20891	39.04	0.43	0.30	1.12×10^{42}	0.01%	7.43×10^{34}	0.16
15286	26.13	0.04	0.01	4.52×10^{42}	0.31%	1.22×10^{35}	2.51
20979	18.56	0.28	0.22	6.41×10^{41}	0.01%	3.87×10^{34}	0.12
11223.2	1.30	0.01	0.01	1.18×10^{41}	0.01%	4.40×10^{33}	0.06
11223.3	0.12	0.00	0.00	5.91×10^{39}	0.00%	3.00×10^{32}	0.00
9367	6.06	0.57	0.98	1.52×10^{42}	0.01%	3.41×10^{34}	0.07
8482	0.62	0.01	0.01	1.94×10^{40}	0.00%	1.23×10^{33}	0.04
6976	1.13	0.25	0.64	1.01×10^{41}	0.00%	3.80×10^{33}	0.02
10421	34.12	2.06	2.97	7.09×10^{42}	0.14%	1.75×10^{35}	1.00
30014	4.20	0.54	1.08	2.44×10^{41}	0.13%	1.14×10^{34}	1.75
17754	9.34	0.22	0.21	4.34×10^{41}	0.04%	2.26×10^{34}	0.57
17664	6.50	0.22	0.25	2.42×10^{41}	0.01%	1.41×10^{34}	0.16

[a] Ionized mass outflow rates, in units of $M_\odot$ yr^{-1}.
[b] Ratios of the estimated ionized mass outflow rate to the maximum theoretically-predicted value from stellar feedback.
[c] Ionized mass-loading factors of the outflows.
[d] Energy outflow rates of the ionized outflow, in units of erg s^{-1}.
[e] Ratios of the measured energy outflow rate to the bolometric luminosity of the AGN.
[f] Momentum flux, in units of dyn.
[g] Ratios of the measured momentum flux to the radiation pressure of the AGN.

scenario, the energy outflow rate is estimated by

$$\dot{E}_{\rm out} = 1.5\times10^{35}\left(\frac{r}{\rm kpc}\right)^2\left(\frac{v}{\rm km\ s^{-1}}\right)^3 n_{0.5}\ {\rm erg\ s^{-1}}, \tag{2.15}$$

where $n_{0.5}$ is the ambient density in units of 0.5 cm^{-3}. If we use the observed values of r and v for our outflows and assume $n_{0.5}$ to be unity, we obtain energy injection rates that are ~ 200 times higher than those obtained above by counting recombining hydrogen atoms. As this energy-conserving method results in unreasonably large estimates of the mass and energy outflow rates, we do not employ it further in this paper.

As a sanity check of the outflow masses estimated above by counting recombining

hydrogen atoms, we compare the derived cooling luminosity of the outflows ($L_{\rm cool}$) to the AGN luminosity. A realistic outflow mass should produce a cooling luminosity that does not exceed the AGN luminosity, if the gas in the outflows is indeed photoionized by the AGN. The cooling luminosity is given by

$$\begin{aligned} L_{\rm cool} &= \int \Lambda(T) n_e^2 dV \\ &= 1.19 \times 10^{44}\ {\rm erg\ s^{-1}} n_{e,2} M_{\rm out,8} \Lambda_{-23}(T), \end{aligned} \tag{2.16}$$

where $n_{e,2}$ is the electron density in units of 100 cm^{-3}, $M_{\rm out,8}$ is the outflow mass in units of $10^8\,{\rm M}_\odot$ and $\Lambda_{-23}(T)$ is the cooling function in units of 10^{-23} erg cm^3 s^{-1}, taken to be 1 at 10^4 K, the likely temperature of the ionized gas. We find that the cooling luminosity is much less than the AGN luminosity for all the outflows from our estimates, with an average ratio of $\gtrsim 0.03$. The ratios obtained using the energy conserving approximation (Eq. 2.15), however, have a median value of ~ 60, indicating that the mass outflow rates estimated using this method are physically unrealistic.

2.5.6 Physical Driver of Outflows and Impact on Host Galaxies

To investigate the possible drivers of the outflows, it is common to compare the mass and energy available from potential drivers with that carried by the outflows. The bolometric luminosity of the AGN ($L_{\rm AGN}$) provides a measurement of the energy available from the AGN to drive the outflows. The bolometric luminosity of the AGN is estimated by applying a bolometric correction of 600 times the [OIII]λ5008 luminosity (Kauffmann & Heckman 2009). We also consider another important driver of galaxy-wide outflows, stellar feedback, and the mass potentially available from it. Hopkins et al. (2012) provides a mass loss rate by stellar feedback as a function

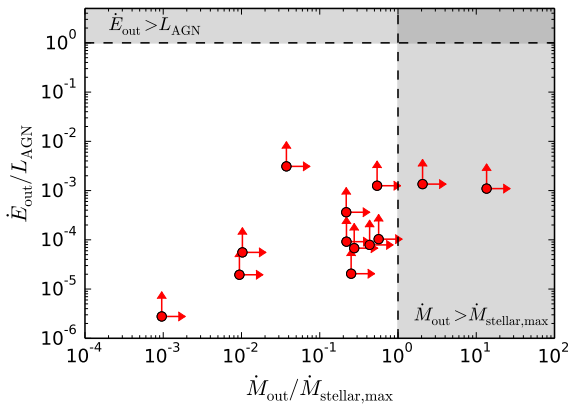

Figure 2.13: The ratio of the kinetic energy rates in the outflow to the AGN luminosity versus the ratio of the observed mass outflow rates to the maximum mass outflow rates that could be provided by stellar feedback, given the SFR of the host galaxy (see Hopkins et al. 2012). The shaded area at the top indicates where the kinetic energy outflow rates exceed the AGN luminosity (such that AGN could not drive the outflows), while the shaded area on the right indicates where the observed mass outflow rates exceed the maximum mass outflow rates that could be due to stellar feedback (such that stars could not drive the outflows).

of star formation rate given by

$$\dot{M}_{\rm stellar,max} = 3\,{\rm M}_\odot\ {\rm yr}^{-1} \left(\frac{\rm SFR}{{\rm M}_\odot\ {\rm yr}^{-1}} \right)^{0.7}. \tag{2.17}$$

This mass loss rate improves on earlier work, in that it considers not only direct mass loss from supernovae and stellar winds, but also the subsequent entrainment of the interstellar medium. Moreover, it includes all material that is being ejected out of the galaxy, in all phases, locations and directions, which tends to overestimate what is actually observed. Therefore, it can be considered as an upper limit to the observed mass outflow rates. This maximum mass loading factors of stellar feedback ($\dot{M}_{\rm stellar,max}/{\rm SFR}$) for our AGN host galaxies are of the order of unity.

In Figure 2.13 we compare the kinetic energy rates of the ionized outflows with $L_{\rm AGN}$ and the ionized mass outflow rates to the maximum possible from stellar feedback. The energy outflow rates range from $> 0.0003 - 0.3\%$ of $L_{\rm AGN}$, with a median of $> 0.009\%$. This shows that the AGN are energetically capable of driving the outflows. The ionized mass outflow rates

range from $> 0.1 - 1400\%$ of the maximum mass loss rate from stellar feedback, with a median of $> 25\%$. Two of the outflows have mass outflow rates lower limits exceeding the maximum mass loss rates of stellar feedback, indicating that stellar feedback must not be the sole driver of these two outflows, and an alternative driver is required. It is important to note that the value of $\dot{M}_{\rm stellar,max}$ represents an upper limit to the observed mass outflow rate from stellar feedback, while the value of $\dot{M}_{\rm out}$ is a strict lower limit to the total mass outflow rate. The actual values of $\dot{M}_{\rm out}/\dot{M}_{\rm stellar,max}$ are likely larger by an order of magnitude; this is a conservative indicator of the need of an alternative driver. Therefore, stellar feedback is likely not the sole driver of these outflows, and an alternative driver, such as AGN, is required.

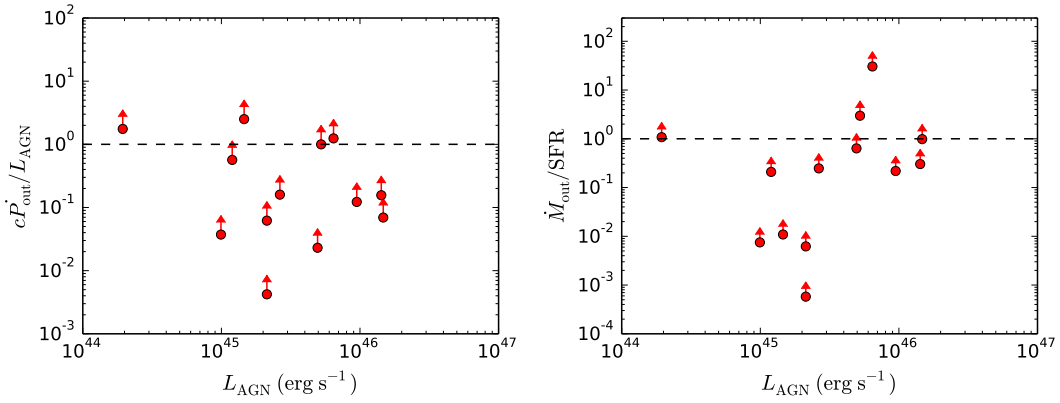

Figure 2.14: The ratio of the momentum flux of the outflow to the radiation pressure of the AGN versus the luminosity of the AGN. The outflow momentum flux exceeds the radiation pressure of the AGN for a considerable number of sources, suggesting radiation pressure alone is insufficient to drive the outflows. The mass loading factors of the outflows versus the bolometric AGN luminosity. The median mass loading factor lower limit is > 0.24.

One possible mechanism for the AGN to drive the outflow is by its radiation pressure on dust grains in the surrounding material (e.g. Murray et al. 2005; Thompson et al. 2015). In this case, the outflow is momentum-driven, and it is useful to compare the momentum flux of the outflow to the radiation pressure of the AGN to test this scenario. In the left panel of Figure 2.14, we plot the ratio of the momentum flux of the outflow ($\dot{P} = \dot{M}v$) to the radiation pressure of the AGN ($L_{\rm AGN}/c$) as a function of the AGN bolometric luminosity. Three of the outflows have lower

limits of the momentum ratio greater than unity, with a median momentum ratio of > 0.16. This shows that most of these outflows can be driven by radiation pressure alone. However, given that the measured momentum fluxes are strict lower limits, as we are observing the ionized phase only, if the total values are an order of magnitude higher then another mechanism must be involved. Additionally, the momentum flux of the outflows could be boosted by a factor of ~ 15 by work done by the hot post-shock gas during the energy-conserving phase (Faucher-Giguère & Quataert 2012). This suggests that for at least some of these sources, radiation pressure on dust grains may be insufficient to drive these outflows.

An important measure of the power and impact of the outflow on the host galaxy is the mass loading factor, $\eta = \dot{M}_{\rm out}/{\rm SFR}$, which compares the mass outflow rate of gas being ejected from the galaxy to the rate at which gas is being converted into stars within the galaxy. For our soures, lower limits on η range from > 0.01 to > 30, with a median of > 0.24. The large mass loading factor for UDS 6055 is due to the low SFR measured for this galaxy. The mass loading factors of the outflows are shown in the right panel of Figure 2.14. Given that these estimates are strict lower limits, the actual mass loading factor is likely a factor of a few to ten times higher, equal to or higher than unity. Such high mass loading factors imply that these outflows are at least capable of regulating star formation in the host galaxies, although it is unclear whether they can remove sufficient gas to quench star formation. This figure shows that there may by an AGN luminosity threshold of $10^{45.5}$ erg s^{-1}, above which the mass loading factor is greater than unity, though a larger sample is required to determine whether this is significant.

2.5.7 Positive AGN Feedback in MOSDEF and SDSS

AGN feedback is typically invoked as a possible mechanism to quench star formation in galaxies. This is referred to as "negative" feedback, in that star formation is reduced or shut off entirely. Another possibility has been raised, which is that AGN feedback may instead *trigger* star formation; this is referred to as "positive" feedback, as it leads to an enhancement in star

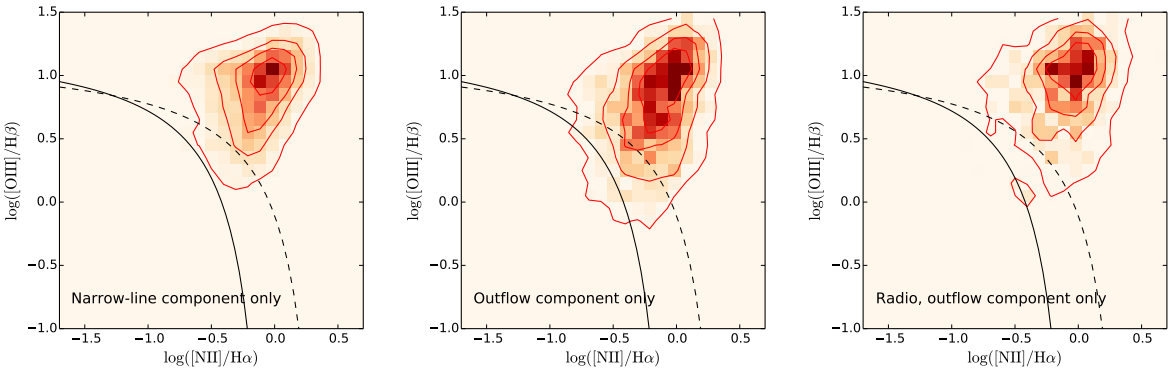

Figure 2.15: BPT diagrams for optically-selected AGN with outflows in SDSS using line ratios from Mullaney et al. (2013). Only sources with signal-to-noise greater than 3 in all four of the relevant lines used for this diagram are shown here. The left panel shows the line ratios for the narrow-line component only, containing 4881 sources. The middle panel shows the line ratios for gas in the outflow component only, containing 2705 sources. The right panel shows the line ratios for the outflow component only for sources from the middle panel which are also detected in the radio, using the FIRST survey, containing 759 sources. There is no increase in the fraction of sources below the Kauffmann et al. (2003b) line for the outflow component in radio-loud sources compared with the middle panel, as may be expected if positive AGN feedback is a widespread phenomenon.

formation.

The motivation for positive AGN feedback originated in observations of a handful of elliptical galaxies at low redshift that have clear radio jets from AGN, for which regions of star formation are clearly seen along the jet (e.g., Croton et al. 2006; Feain et al. 2007; Inskip et al. 2008). Additionally, at high redshift it has been observed that the axis of radio AGN jets was often aligned with an elongation in the surface density of star formation (e.g., Bicknell et al. 2000, and references therein). Recently, several theoretical papers have studied this idea using hydrodynamical simulations of galaxies, in which an AGN-driven jet is seen to be able to induce star formation in a ring in the host galaxy, which propagates outward (e.g., Silk 2005; Gaibler et al. 2012; Ishibashi & Fabian 2012). It has been speculated that such triggered star formation could substantially affect the growth of galaxies (Ishibashi et al. 2013).

A clear observational signature of such positive AGN feedback would be investigating radio AGN with jets and using the BPT diagram to detect star formation in the outflowing gas,

along the jet. Indeed, for the well-studied source known as Minkowski's Object, the gas that appears to be compressed by the jet does have line ratios in the BPT diagram in the location of the star-forming sequence, well below the AGN region of the diagram (Croton et al. 2006). This argues that the jet has induced star formation in this gas.

In the MOSDEF sample, we present the locations of outflowing gas from eight sources in the right panel of Figure 3.2 and find that the locations lie in the AGN region; this outflowing gas does not appear to be photoionized by star formation. This would argue against positive AGN feedback being a widespread phenomenon at $z \sim 2$. However, our sample size is very small, and only two of our sources are known to be radio-loud, which in the observations at both low and high redshift appears to be a prerequisite for positive AGN feedback. Clearly, a much larger sample of radio AGN would be required to robustly test this scenario.

The SDSS provides such a sample at low redshift. To investigate this, we use the publicly-available optical AGN sample of Mullaney et al. (2013), who use the BPT diagram to identify $\sim$25,000 AGN in SDSS, using the line ratios from the SDSS spectral pipeline. This pipeline does not include multiple kinematic components for each line, which Mullaney et al. (2013) subsequently perform. They identify 9,637 sources with a significant (S/N$>$3) blueshifted kinematic component in the [OIII] 5007 Å line, in addition to the narrow line observed at the systemic redshift of the galaxy.

In Figure 2.15, we show in the left panel the *narrow-line* only line ratios for these optical AGN with outflows, while the middle panel shows the line ratios for the *outflow* component only. The narrow-line ratios almost exclusively lie above the Kauffmann et al. (2003b) line (only 3% of sources are below this), while the outflow component line ratios lie somewhat lower, with 6% of the outflow line ratios below the Kauffmann et al. (2003b) line. The difference between these panels may argue that positive AGN feedback occurs in a few percent of these sources, however, the more important test is whether the line ratios shift downward for AGN with jets, i.e., radio AGN. In the right panel, therefore, we show the line ratios for the AGN in the Mullaney et al.

(2013) sample that have outflows detected in the [OIII] line and are also detected in the FIRST survey (Becker et al. 1995). Here we find that only 3% of these sources lie below the Kauffmann et al. (2003b) line, consistent with the left panel. This argues that positive AGN feedback is not observed to be a widespread phenomenon at $z \sim 0.1$. For it to be a common phenomenon, it must then occur only over a relatively short timescale, or it may just be a rare phenomenon.

2.6 Conclusions

Using data from the first two years of the MOSDEF survey, we analyze the rest frame optical spectra of 67 X-ray, IR and/or optically-selected AGN at $z \sim 2$ to identify and characterize AGN-driven outflows at $z \sim 2$. We identify outflows from the presence of an additional blueshifted component in the profiles of the Hβ, [OIII], Hα and [NII] emission lines, and we remove sources which appear to be ongoing mergers from their *HST* morphologies. The bolometric luminosities of the AGN in this study span $10^{44} - 10^{46}$ erg s^{-1}, including both quasars and more common, moderate-luminosity AGN. Our main conclusions are as follows.

1. The velocities of the outflows range from 300 to 1000 km s^{-1}. Eight out of the 13 detected outflows are spatially extended, having spatial extents of 2.5 to 11.0 kpc along the MOSFIRE slits.

2. Outflows are detected in 13 (19%) out of 67 AGN. This can be considered a lower limit on the true incidence as relatively high signal-to-noise spectra are required to detect the outflows. By contrast, using the same analysis procedures, outflows are detected in only eight (1.8%) out of the 457 MOSDEF galaxies. The outflow detection rate increases with the [OIII] luminosity of the AGN, but the same trend is also observed as the signal-to-noise ratio of the spectra increases, as there is a strong correlation between $L_{[\mathrm{OIII}]}$ and the signal-to-noise of the spectra.

3. Outflows are detected across the galaxy star forming main sequence spanning stellar masses of $10^{10} - 10^{11.5}\,M_{\odot}$. No significant trend of incidence with stellar mass is observed. The incidence of outflows also does not depend on the SFR of the host galaxy with respect to the main sequence.

4. Using line ratio diagnostics in the BPT diagram for the narrow-line and outflow components separately, we find that the line ratios of the outflowing gas are shifted towards the AGN region of the BPT diagram. This indicates the the outflowing gas is photoionized by the AGN.

5. The line ratio diagnostics in the outflows argues against "positive" AGN feedback, in which the presence of the outflow triggers, as opposed to suppresses, star formation. As the MOSDEF AGN outflow sample is small, we also analyzed line ratios for AGN outflows in SDSS, specifically investigating radio-loud AGN, and again found little evidence for positive AGN feedback being a widespread or long-lasting phenomenon.

6. The typical ionized mass outflow rate of our sources is $\gtrsim 10\,M_{\odot}$ yr^{-1}, while the typical energy rate of the ionzied gas is $\gtrsim 10^{42}$ erg s^{-1}. These lower limits on the total mass outflow rates are typically at least comparable to the theoretically-predicted maximum values from stellar feedback, while the energy outflow rates are $\sim 0.01\%$ the bolometric AGN luminosities. This indicates the stellar feedback is likely insufficient to drive all of these outflows, while the energetic output of the AGN is more than sufficient to drive them. Taken together with our finding that a galaxy is 10 times more likely to have a detected outflow if it hosts an AGN, it appears very likely that these outflows are AGN-driven.

7. The mass loading factors of these outflows are on the order of unity, which suggests that the outflows likely help to regulate star formation in the host galaxies but may not be sufficient to fully quench star formation.

Our results show that galaxy-wide AGN-driven outflows are common not only for quasars but also for moderate-luminosity AGN at $z \sim 2$. Theoretical studies of galaxy formation and evolution should therefore account for AGN feedback from moderate-luminosity AGN, in addition to feedback from quasars. In the future, the full MOSDEF data will provide a larger sample to better study correlations between AGN outflow properties and host galaxy or AGN properties at $z \sim 2$. This study and future similar AGN outflow studies from large galaxy samples also provide targets for more detailed IFU investigations into the physical nature of AGN-driven outflows at the peak of cosmic galaxy growth.

2.7 Acknowledgements

We thank Norm Murray, Patrick Diamond and Claude-Andrè Faucher-Giguère for useful discussions. We also thank the anonymous referee for helping to improve the paper. This work would not have been possible without the 3D-*HST* collaboration, who provided us the spectroscopic and photometric catalogs used to select our targets and to derive stellar population parameters. This work is partially supported by NSF CAREER grant 1055081, awarded to A. Coil. Funding for the MOSDEF survey is provided by NSF AAG grants AST-1312780, 1312547, 1312764, and 1313171, and archival grant AR-13907, provided by NASA through a grant from the Space Telescope Science Institute. The data presented herein were obtained at the W.M. Keck Observatory, which is operated as a scientific partnership among the California Institute of Technology, the University of California and the National Aeronautics and Space Administration. The Observatory was made possible by the generous financial support of the W.M. Keck Foundation. The authors wish to recognize and acknowledge the very significant cultural role and reverence that the summit of Mauna Kea has always had within the indigenous Hawaiian community. We are most fortunate to have the opportunity to conduct observations from this mountain.

Chapter 2, in full, is a reprint of the material as it appears in The Astrophysical Journal 2017. Leung, Gene C. K., Coil, A. L., Aird, J., Azadi, M., Kriek, M., Mobasher, B., Reddy, N., Shapley, A., Siana, B., Fetherolf, T., Fornasini, F. M., Freeman, W. R., Price, S. H., Sanders, R. L., Shivaei, I., and Zick, T. 2017. The dissertation author was the primary investigator and author of this paper.

Chapter 3

The MOSDEF survey: a census of AGN-driven ionized outflows at $z = 1.4 - 3.8$

3.1 Abstract

Using data from the MOSFIRE Deep Evolution Field (MOSDEF) survey, we present a census of AGN-driven ionized outflows in a sample of 159 AGNs at $1.4 \leq z \leq 3.8$. The sample spans AGN bolometric luminosities of 10^{44-47} erg s^{-1} and includes both quiescent and star-forming galaxies extending across three orders of magnitude in stellar mass. We identify and characterize outflows from the Hβ, [OIII], Hα and [NII] emission line spectra. We detect outflows in 17% of the AGNs, seven times more often than in a mass-matched sample of inactive galaxies in MOSDEF. The outflows are fast and galaxy-wide, with velocities of $\sim 400 - 3500$ km s^{-1}and spatial extents of $0.3 - 11.0$ kpc. The incidence of outflows among AGNs is independent of the stellar mass of the host galaxy, with outflows detected in both star-forming and quiescent galaxies. This suggests that outflows exist across different phases in galaxy evolution. We investigate

relations between outflow kinematic, spatial, and energetic properties and both AGN and host galaxy properties. Our results show that AGN-driven outflows are widespread in galaxies along the star-forming main sequence. The mass-loading factors of the outflows are typically $0.1-1$ and increase with AGN luminosity, capable of exceeding unity at $L_{\rm AGN} \gtrsim 10^{46}$ erg s^{-1}. In these more luminous sources the ionized outflow alone is likely sufficient to regulate star formation, and when combined with outflowing neutral and molecular gas may be able to quench star formation in their host galaxies.

3.2 Introduction

It is well established that supermassive black holes (SMBHs) are virtually ubiquitous at the centers of galaxies (e.g. Magorrian et al. 1998; Heckman & Best 2014; Aird et al. 2018). When SMBHs accrete, they are observed as active galactic nuclei (AGNs) (e.g. Antonucci 1993; Netzer 2015). AGNs are believed to play a crucial role in galaxy evolution as various properties of host galaxies and their SMBHs are observed to be closely connected. Locally, the mass of the central SMBH and the velocity dispersion of the bulge of the host galaxy are found to follow a tight correlation, even though the SMBH is typically only less than one percent of the mass of the bulge (e.g. Ferrarese & Merritt 2000; Gebhardt et al. 2000). Globally, the growth rates of galaxies and SMBHs, traced by the total star formation rate (SFR) density and the total SMBH accretion density, respectively, followed a very similar trend with cosmic time, both reach a peak at the "cosmic high noon" of $z \sim 1-3$ (e.g. Madau & Dickinson 2014; Aird et al. 2015; Azadi et al. 2015; Yang et al. 2018; Aird et al. 2019).

While such empirical evidence strongly suggests that the evolution of SMBHs and their host galaxies are intimately related, theoretical models of galaxy formation point to a more direct connection between AGNs and their host galaxies. It has been observed that galaxies are inefficient in converting baryons into stars in the low ($< 10^{12} M_{\odot}$) and high ($> 10^{12} M_{\odot}$) mass ends

of the halo mass distribution, as they have significantly lower stellar mass to halo mass ratios (e.g. Madau et al. 1996; Baldry et al. 2012; Behroozi et al. 2013a). The star formation inefficiency in low mass halos is satisfactorily explained by stellar feedback (e.g. Bouché et al. 2010; Dutton et al. 2010; Hopkins et al. 2012). Most galaxy formation models have to invoke AGNs to inject energy and/or momentum into the surrounding gas in high mass galaxies in order for their results to match the observed galaxy population (e.g. Benson et al. 2003; Di Matteo et al. 2005; Croton et al. 2006; Hopkins et al. 2006; Kaviraj et al. 2017; Pillepich et al. 2018). Additionally, cosmological simulations have to invoke AGN feedback to produce quiescent bulge-dominated massive red galaxies that are no longer actively forming stars (e.g. Hopkins et al. 2008; Schaye et al. 2015).

AGN feedback provides an energetically feasible mechanism to remove cool gas in a galaxy or heat up cool gas to prevent further accretion of cool gas onto the galaxy to keep new stars from forming. A commonly invoked AGN feedback process is large-scale outflows, in which an AGN produces a high velocity wind that heats or sweeps up gas over distances comparable to the size of the galaxy (e.g. King et al. 2011; Debuhr et al. 2012; Faucher-Giguère & Quataert 2012). This has sparked a wealth of observational studies aiming to characterize AGN outflows and test this picture.

In the local Universe ($z \lesssim 1$), outflows in AGNs have been observed to be ubiquitous and extend to kpc scales in ionized, atomic, and molecular gas (e.g. Liu et al. 2013a,b; Veilleux et al. 2013; Mullaney et al. 2013; Cicone et al. 2014; Harrison et al. 2014; Zakamska & Greene 2014; McElroy et al. 2015; Woo et al. 2016; Rupke et al. 2017; Perna et al. 2017b,a; Mingozzi et al. 2019), though some studies suggest that outflows are more compact (Husemann et al. 2016; Karouzos et al. 2016a,b; Baron & Netzer 2019a,b). While AGN-driven outflows are found to be a widespread phenomenon at low redshift, a crucial epoch to study AGN-driven outflows is at higher redshifts of $z \sim 1-3$. This epoch is known as the "cosmic high noon", when both the global SFR and AGN accretion rate are at their peaks across cosmic time, before declining by about an order of magnitude to the present day values (e.g. Madau & Dickinson 2014; Aird et al.

2015). Therefore, AGN-driven outflows should be most prevalent and powerful at this epoch, which is also when galaxies are undergoing peak growth. This is therefore a crucial era to test models of AGN feedback.

Current observations at $z \sim 1-3$ of a statistical sample of AGNs with complete spectroscopic coverage of the brightest rest-frame optical emission lines are limited. Early results at this redshift (e.g. Nesvadba et al. 2008; Cano-Díaz et al. 2012; Harrison et al. 2012; Perna et al. 2015; Brusa et al. 2015) are often focused on special, extreme subclasses of AGNs such as ULIRGs or luminous quasars and were limited to small sample sizes.

More recent studies of outflows using statistical samples of AGNs at $z \sim 1-3$ have been made possible by the commissioning of multi-object near-infrared (NIR) spectrographs such as MOSFIRE (McLean et al. 2010b) and KMOS (Sharples et al. 2013). The observed NIR waveband covers several important rest-frame optical emission lines, such as Hβ, [OIII], Hα, [NII] and [SII], at this redshift. Of specific relevance to the study of AGN-driven outflows is the [OIII] emission line, which is a bright forbidden emission line that is traditionally used to trace the narrow-line region gas around AGNs and ionized outflows (e.g. Bennert et al. 2002; Schmitt et al. 2003; Mullaney et al. 2013; Zakamska & Greene 2014; Woo et al. 2016). Moreover, Hβ, [OIII], Hα and [NII] are used in emission line ratio diagnostics of the ionized gas using the BPT diagram (Baldwin et al. 1981; Veilleux & Osterbrock 1987). NIR spectroscopic observations are therefore the ideal tool to study ionized AGN outflows at $z \sim 1-3$.

Harrison et al. (2016) study a sample of 89 AGNs up to $z = 1.7$ and detect ionized outflows in $\sim 35-50\%$ of the AGNs, indicating that outflows are quite prevalent in AGN at this epoch. Fiore et al. (2017) study scaling relations of AGN-driven outflows with AGN and host galaxy properties in a meta-analysis of published outflow studies spanning ionized, atomic, and molecular gas, which includes 29 ionized outflows in AGNs at $z \sim 1-3$. Because of the nature of a meta-analysis, AGN and host galaxy properties are calculated by different authors using non-homogeneous recipes, which can affect the scaling relations obtained. Selection biases can

also exist since the sample is compiled from multiple studies.

A larger sample of ionized outflows in AGNs at $z \sim 1-3$ is presented in Förster Schreiber et al. (2019), who study 152 AGNs found in a sample of 599 galaxies using integral field spectra (IFS) covering the Hα, [NII], and [SII] emission lines. While the IFS data provide two-dimensional measurements of the physical size of the outflows, the [OIII] and Hβ emission lines are not covered. These emission lines are required to perform diagnostics using the BPT diagram. The [OIII] forbidden line in particular provides an excellent tracer of narrow-line region gas and ionized outflows, as it is far from other bright emission lines and suffers from less contamination than the [NII] forbidden line. More recently, Coatman et al. (2019) study an even larger sample of luminous $z = 1-4$ quasars in detail, using the [OIII] and CIV line profiles to investigate how small scale outflows correlate with larger scale winds.

To better understand the role of AGN-driven outflows in galaxy evolution and explore their physical characteristics as a function of AGN and host galaxy properties, it is necessary to have a statistical sample of AGNs selected *from a uniform sample of galaxies* with complete spectroscopic coverage of the important rest-frame optical emission lines. We achieve this using data from the recently-completed MOSFIRE Deep Evolution Field (MOSDEF) survey (Kriek et al. 2015). Targets in the MOSDEF survey are selected to a threshold in NIR flux, which roughly corresponds to a stellar mass limit. This results in a more uniform and representative census of the population of "typical" star-forming galaxies, as well as some quiescent galaxies. The spectroscopic data of the MOSDEF survey provides simultaneous coverage of important optical emission lines, including the [OIII] emission line, which is particularly important in tracing the narrow-line region gas and ionized outflows around AGNs. Furthermore, a homogeneous method is employed in this study to determine AGN and host galaxy properties.

In Leung et al. (2017), we presented early results using data from the first 2 years of the MOSDEF survey and found that fast and galaxy-wide AGN-driven outflows are common at $z \sim 2$. In this study, we take advantage of the full data set of the now completed MOSDEF survey, which

contains $\sim$ 1500 galaxies and $\sim$ 160 AGNs. We revisit the incidence and physical characteristics of AGN-driven outflows with a sample that almost triples that in Leung et al. (2017). This allows us to investigate in more detail the trends in the incidence of AGN-driven outflows and make more robust conclusions. Furthermore, now equipped with a statistical sample of AGN-driven outflows, we study their physical properties as a function of AGN and host galaxy properties to better understand the impact of these outflows on their host galaxies and their role in galaxy evolution.

This paper is organized as follows. Section 3.3 describes the MOSDEF survey and the AGN sample. Section 3.4 presents methods used for detection and characterization of the outflows. Section 3.5 discusses the relation between the incidence of outflows and AGN and host galaxy properties. Section 3.6 presents the relation between the physical properties of the outflows and properties of the AGN and host galaxies. We summarize our conclusions in Section 3.7.

3.3 Observations and AGN Sample

In this section we describe the dataset used in this study and the methods employed to identify AGN at various wavelengths. We also outline how we estimate host galaxy properties using SED fitting.

3.3.1 The MOSDEF Survey

The MOSDEF survey was a four and a half year program using the MOSFIRE spectrograph (McLean et al. 2010b) on the Keck I telescope to obtain near-infrared (rest-frame optical) spectra of $\sim$ 1500 galaxies and AGNs at $1.4 \leq z \leq 3.8$ Targets were selected from the photometric catalogs of the 3D-HST survey (Skelton et al. 2014) in the five CANDELS fields: AEGIS, COSMOS, GOODS-N, GOODS-S and UDS. Targets were selected by their H-band magnitudes, down to $H = 24.0, 24.5$ and 25.0 at $z = 1.37 - 1.70, 2.09 - 2.61$ and $2.95 - 3.80$, respectively,

with brighter sources and known AGNs given higher weights in targeting. The Hβ and [OIII] emission lines are covered in the J, H and K bands for the lower, middle and higher redshift intervals, respectively. The Hα, [NII] and [SII] emission lines are covered in the H and K bands for only the lower and middle redshift intervals, respectively. With the full survey, 1824 spectra of galaxies and AGNs were acquired, yielding a reliable redshift for 1415 of them. Full technical details of the MOSDEF survey can be found in Kriek et al. (2015).

3.3.2 Emission Line Measurements

In this section, we describe the procedures to measure emission line fluxes and kinematics in this study. We perform the procedures described in Azadi et al. (2017) and Azadi et al. (2018) to simultaneously fit the Hβ, [OIII], [NII] and Hα emission lines using the `MPFIT` (Markwardt 2009) routine in `IDL`. For sources in the highest redshift interval of $2.95 \leq z \leq 3.80$, we fit only the Hβ and [OIII] emission lines, as the [NII] and Hα lines are not covered in the spectra. The spectra are fitted with a continuum near the emission lines with zero slope and a maximum of three Gaussian components for each line:

1. A Gaussian function with FWHM < 2000 km s^{-1}, one each for the Hβ, [OIII], [NII] and Hα emission lines, representing the narrow-line emission from the AGN and/or host galaxy;

2. A broad Gaussian function with FWHM > 2000 km s^{-1}, one each for Hβ and Hα only, representing the broad line emission from the AGN;

3. An additional Gaussian function with FWHM < 2000 km s^{-1}, one each for the Hβ, [OIII], [NII] and Hα emission lines, representing a potential outflow component.

The FWHM and velocity shift of each set of Gaussian functions are held equal for all of the lines of interest. Tying the kinematics among different lines is a requirement of the restricted signal-noise ratio (S/N) in observations at high redshifts. It assumes that the emission lines

originate from the same gas, undergoing the same kinematics, which is not necessarily true. Nonetheless, it is a common practice in studies of high-redshift galaxies and AGN due to limited S/N (see Harrison et al. 2016 and references therein). The flux ratios between [OIII]λ4960 and [OIII]λ5008 and between [NII]λ6550 and [NII]λ6585 are fixed at 1:3 for each Gaussian function.

We adopt the model with the narrow-line component (component 1) alone unless the addition of more components results in a decrease in χ^2 corresponding to a p-value of < 0.01 for the null hypothesis that the simpler model is true. We further require that all the components have S/N greater than 3 in at least one line.

3.3.3 AGN Sample

AGNs were identified before targeting by X-ray imaging data from *Chandra* and/or IR imaging data from *Spitzer*/IRAC. In addition, AGNs were identified in the MOSDEF spectra using rest-frame optical diagnostics. The identification of AGNs in the MOSDEF survey is described below; full details are discussed in Azadi et al. (2017) and Leung et al. (2017).

We identified X-ray AGNs prior to the MOSDEF target selection using *Chandra* X-ray imaging data with depths of 160 ks in COSMOS, 2 Ms in GOODS-N, 4 Ms in GOODS-S and 800 ks in AEGIS, corresponding to hard band (2-10 keV) flux limits of 1.8×10^{-15}, 2.8×10^{-16}, 1.6×10^{-16} and 5.0×10^{-16} ergs s^{-1} cm^{-2}, respectively. The X-ray catalogs were constructed according to the prescription in Laird et al. (2009), Nandra et al. (2015) and Aird et al. (2015). The X-ray sources were matched to counterparts detected at IRAC, NIR and optical wavelengths using the likelihood ratio method (e.g. Brusa et al. 2007; Luo et al. 2010; Aird et al. 2015), which were then matched with the 3D-HST catalogs for MOSDEF target selection. These X-ray sources were given higher priority in MOSDEF target selection. The 2-10 keV rest-frame X-ray luminosity was estimated by assuming a simple power-law spectrum with photon index $\Gamma = 1.9$ and Galactic absorption only.

To identify highly obscured and Compton-thick AGNs which are not as effectively selected

through X-ray imaging, we also made use of MIR colors to identify AGNs in the MOSDEF survey, since high-energy photons from the AGN absorbed by dust are re-radiated at the MIR wavelengths. We adopt the IRAC color criteria from Donley et al. (2012), with slight modifications, to select IR AGN using fluxes in the 3D-HST catalogs (Skelton et al. 2014). The criteria are:

$$x = \log_{10}\left(\frac{f_{5.8\mu\mathrm{m}}}{f_{3.6\mu\mathrm{m}}}\right), \quad y = \log_{10}\left(\frac{f_{8.0\mu\mathrm{m}}}{f_{4.5\mu\mathrm{m}}}\right) \tag{3.1}$$

$$x \geq 0.08 \ \text{ and } \ y \geq 0.15 \tag{3.2}$$

$$y \geq (1.21 \times x) - 0.27 \tag{3.3}$$

$$y \leq (1.21 \times x) + 0.27 \tag{3.4}$$

$$f_{4.5\mu\mathrm{m}} > f_{3.6\mu\mathrm{m}} \tag{3.5}$$

$$f_{5.8\mu\mathrm{m}} > f_{4.5\mu\mathrm{m}} \tag{3.6}$$

$$f_{8.0\mu\mathrm{m}} > f_{5.8\mu\mathrm{m}}. \tag{3.7}$$

In our modification, we do not require Equation 3.4 and include sources within 1σ uncertainties of Equations 3.5, 3.6 and 3.7. This is because the Donley et al. (2012) criteria are designed to select luminous unobscured and obscured AGNs, but are incomplete to low-luminosity and host-dominated AGNs. These slight modifications allow for the inclusion of a handful of additional sources close to the boundaries and are highly likely to be AGNs due to other properties (see Azadi et al. 2017, for more details).

We also use emission line ratio diagnostics with the BPT diagram (Baldwin et al. 1981; Veilleux & Osterbrock 1987) to identify optical AGN. Emission line fluxes are obtained in the procedures described in Section 3.3.2. As discussed in Coil et al. (2015) and Azadi et al. (2017), the theoretical demarcation line in Meléndez et al. (2014) can satisfactorily balance contamination by star-forming galaxies and completeness of the MOSDEF AGN sample at $z \sim 2$. The Meléndez et al. (2014) line asymptotically approaches $\log([\mathrm{NII}]/\mathrm{H}\alpha) = -0.34$ for low $\log([\mathrm{OIII}]/\mathrm{H}\beta)$.

We adopt a more restrictive criterion of $\log([\mathrm{NII}]/\mathrm{H}\alpha) > -0.3$ to identify optical AGNs in this study to reduce contamination from star formation. In addition, we identify sources above the redshift-dependent maximum starburst demarcation line in Kewley et al. (2013a) at $z = 2.3$ as optical AGNs, as star formation alone cannot produce such high line ratios.

Among sources with a robust redshift measurement in MOSDEF, the procedures above result in 52 AGNs identified at X-ray wavelengths only and 41 AGNs identified at IR wavelengths only. In addition, 25 sources satisfy both the X-ray and IR AGN identification criteria, resulting in a total of 118 AGNs identified in X-ray and/or IR. 79 sources are found to satisfy the optical AGN identification criteria, among which 41 were not previously identified in either X-ray or IR emission. This results in a total number of 159 AGNs identified at X-ray, IR, and/or optical wavelengths.

3.3.4 Stellar Masses and Star Formation Rates

Stellar masses and SFR are measured by spectral energy distribution (SED) fitting using photometric data from the 3D-HST catalogs (Skelton et al. 2014) and the MOSDEF spectroscopic redshifts. In this study, we perform SED fitting using the FAST stellar population fitting code (Kriek et al. 2009) with an additional AGN component (see Aird et al. 2018). We assume the FSPS stellar population synthesis model (Conroy et al. 2009), the Chabrier (2003) initial mass function, a delayed exponentially declining star formation history and the Calzetti et al. (2000) dust attenuation curve. Combined AGN templates taken from the SWIRE template library (Polletta et al. 2007) and Silva et al. (2004) are used (see Aird et al. 2018, for details).

3.4 Outflow Detection and Characterization

In this section we report the methods used to detect outflows and characterize their properties, including kinematics, optical emission line ratios, physical extent, and mass and

energy outflow rates in the MOSDEF dataset.

3.4.1 Detection of Outflows in AGNs

We identify potential outflows in the AGN sample using the emission line fitting procedures described in Section 3.3.2. An outflow component is included in the best fit if the p-value is less than 0.01 for the null hypothesis of the absence of an outflow. In addition, we require that both the narrow and outflow components to have S/N ratios greater than 3 to reduce false detections due to noise. Among the 159 AGNs with a robust measurement of their redshifts, 43 host potential outflows satisfying these requirements.

We then exclude any potential outflows that have signs of on-going merger activity from our sample, as merger activity can produce similar kinematic signatures as outflows (i.e., a second kinematic component). While outflows can be present in and triggered by mergers, we aim to measure and characterize the outflowing gas due to AGN activity in this study. We therefore do not include mergers in our sample. We identify mergers by visually inspecting the *HST* images of each source in the F160W and F606W bands. Sources that have features suggesting double nuclei are considered potential mergers. We define double nuclei as having two distinct peaks in brightness separated by less than $1''$ (corresponding to ~ 8 kpc at $z \sim 2$). 16 of the 43 potential outflows show features satisfying this criteria, and they are removed from the outflow sample. This results in a final sample of 27 AGNs with robustly-identified outflows, corresponding to 17% of a total of 159 AGNs in the full sample. The emission line spectra with best-fit models and properties of these 27 AGNs with outflows are provided in the Appendix. Among these 27 AGNs, 14 are identified in both X-ray and IR emission, 10 are identified in X-ray emission only, one is identified in IR emission only, and two are identified in optical emission only.

While we identify outflows from the decomposition of an asymmetric emission line profile, outflows can potentially result in single broad symmetric line profiles with widths $\gtrsim 600$ km s^{-1} (e.g. Mullaney et al. 2013; Harrison et al. 2016; Woo et al. 2016). In this study, we only

include sources with an asymmetric line profile decomposed into two Gaussian components as outflows because many of the derived quantities used in our analysis, such as velocity, spatial extent, and outflow mass, require the detection of a separate outflow component. The outflow mass, in particular, requires measuring the luminosity of the outflow component alone. This cannot be achieved with sources modelled with a single broad line profile. Among the AGNs that are modelled as a well-constrained single Gaussian component, only three have a FWHM of 600 km s^{-1} or greater. These three sources with broad symmetric line profiles are not identified as outflows in the analysis below, and are very unlikely to affect the conclusions about outflow incidence in this study.

3.4.2 Detection of Outflows in Inactive Galaxies

In this study all MOSDEF targets with a reliable redshift have been fit using the emission-line fitting procedures described in Section 3.3.2. We can therefore compare the incidence of outflows detected in the emission-line spectra of AGNs and of inactive galaxies in our sample. Out of a total of 1179 inactive galaxies with reliable redshifts, a significant outflow component is detected in 70 sources satisfying the spectroscopic criteria in Section 3.4.1. After excluding potential mergers by inspecting their *HST* images, there are 37 inactive galaxies with outflows detected, corresponding to 3.1% of the inactive galaxy sample.

To compare this result directly with the detection rate of outflows in AGNs, we need to account for the difference in the stellar mass distributions of the AGNs and galaxies in our sample. Since AGNs at a given Eddington ratio will be more luminous in more massive galaxies, AGNs will be detected more frequently in galaxies with higher stellar masses (Aird et al. 2012), due to an observational selection bias. As a result, the samples of AGNs and inactive galaxies have fairly different stellar mass distributions (see Azadi et al. 2017). Moreover, the higher luminosities of higher mass galaxies can yield higher S/N spectra, which can potentially contribute to more frequent detection of outflows. Therefore, it is necessary to match the stellar mass distributions of

inactive galaxies to that of AGNs when comparing their outflow detection rates.

To do this, we construct histograms of the stellar mass distributions of the galaxies and AGNs, respectively, in bins of 0.25 dex. Weights in stellar mass bins are computed by the ratio of the number of AGNs to the number of galaxies in the corresponding entries of the histograms, and are normalized to conserve the total number of galaxies. Applying these weights to the inactive galaxy sample leads to a total of 30 outflows, corresponding to 2.5% of inactive galaxies. We also explore the effect of SFR on outflow detection in inactive galaxies by applying the same procedures above to SFR instead of stellar mass. The weighted outflow incidence in inactive galaxies after accounting for their SFR distribution is 3.2%. This is very similar to the unweighted value, showing that the SFR distributions of the AGN and inactive galaxy sample are sufficiently alike that weighting by SFR is not necessary.

With an incidence rate of 17%, ionized outflows are six to seven times more frequently detected in emission in AGNs than in a mass-matched sample of inactive galaxies. While outflows are known to be detected in absorption in star-forming galaxies at similar redshifts (Steidel et al. 2010), here we directly compare the incidence rate of outflows detected in emission in both AGNs and inactive galaxies using the same methodology for both samples. This factor of seven difference in outflow incidence rates between AGNs and galaxies strongly suggests that these AGN outflows are AGN-driven. A detailed study of outflows detected as broad emission lines in inactive star-forming galaxies in MOSDEF is presented in Freeman et al. (2019). There is a small difference in the numbers of outflow detections between this study and Freeman et al. (2019), which is likely due to different constraints and criteria in the emission line fitting procedures, while the difference in outflow detection rate is primarily driven by different selection criteria of the samples.

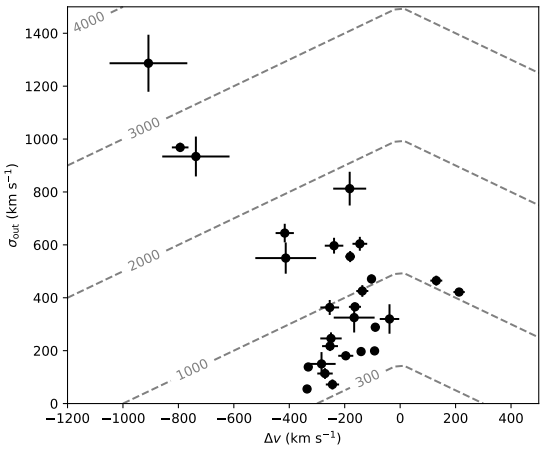

Figure 3.1: Velocity dispersion versus velocity shift for the detected AGN outflows in our sample. The gray dashed lines show constant $v_{\rm max}$ in units of km s^{-1}, where $v_{\rm max} = |\Delta v| + 2\sigma_{\rm out}$ as defined in Rupke & Veilleux (2013b). Sources with large velocity offset have large velocity dispersions, while sources with large velocity dispersions can have small velocity offsets, resulting in the fan-shaped distribution observed in nearby AGNs Woo et al. (2016).

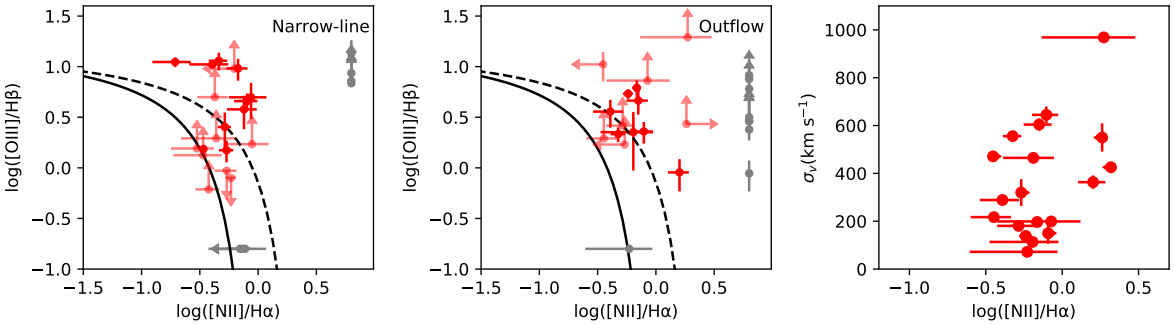

Figure 3.2: Left: BPT diagram for the narrow-line component of each AGN with an outflow in our sample. 3σ limits are shown when one emission line flux is not significant above 3σ. Sources where only one line ratio is available are shown as gray points. Middle: Same as left panel, but for the outflow components in our sample. The line ratios of the outflow components are shifted systematically away from the star formation excitation region. The black solid and dashed lines show the Kauffmann et al. (2003b) and Kewley et al. (2013a) demarcation lines, respectively. Right: Velocity dispersion of the outflow component versus the [NII] to Hα line ratio. If shock excitation is present, a positive correlation should be expected (e.g. Ho et al. 2014; McElroy et al. 2015; Perna et al. 2017a). This is not observed in our sample, suggesting that the ouflowing gas is excited by the photoionizing radiation of the AGN rather than shocks.

3.4.3 Outflow Kinematics

We measure kinematic parameters of the outflows in AGNs using results from the multi-component emission line fitting procedures. One of the outflow signatures is the velocity shift (Δv) between the centroids of the outflow component and the narrow line component. 29 out of the 31 detected outflows have a negative velocity shift, meaning that they are blueshifted, while only 2 outflows are redshifted. The magnitudes of the velocity shift range from $\sim 40-910$ km s^{-1}, with a median value of 230 km s^{-1} and a median 1σ error of 30 km s^{-1}. The fact that the majority of the outflows are blueshifted is consistent with an outflow model with dust extinction (e.g. Crenshaw et al. 2003; Bae & Woo 2016), where dust extinction in the galaxy reduces the flux of the receding outflowing material on the far side of the galaxy.

We also measure the velocity dispersion of the outflow component, $\sigma_{\rm out}$. The outflow velocity dispersions range from $\sim 60-1300$ km s^{-1}, with a median value of 360 km s^{-1} and a median 1σ error of 20 km s^{-1}. Figure 3.1 shows the distribution of the velocity dispersions of the outflows versus their velocity shifts. Sources with high velocity shifts also have high velocity dispersions, while sources with relatively high velocity dispersions ($\sim$600 km s^{-1}) do not always have high velocity shifts. This is similar to findings for nearby AGNs (Woo et al. 2016).

As both the velocity shift and velocity dispersion account only for the component of the outflow velocity along the line of sight, outflows with a non-negligible opening angle will have a spread of observed radial velocities that are lower than the actual bulk outflow velocity. The actual outflow velocity in three dimensions will therefore be closer to the highest or maximum radial velocity in the observed velocity distribution. A common parameter to measure the actual velocity of the outflow is the maximum velocity ($v_{\rm max}$), which is defined as the velocity shift between the narrow and outflow components plus two times the dispersion of the outflow component, i.e. $v_{\rm max} = |\Delta v| + 2\sigma_{\rm out}$ (Rupke & Veilleux 2013b). The maximum velocity of the outflows in our sample ranges from $\sim 400-3500$ km s^{-1}, with a median value of 940 km s^{-1} and a median 1σ error of 50 km s^{-1}.

Another kinematic measure widely used in the literature is the non-parametric line width that contains 80% of the total flux (w_{80}) (e.g. Zakamska & Greene 2014). However, this measure depends on the relative flux ratios of the narrow and outflow components of the emission line. While studies that make use of this measure often have only one emission line, we simultaneously fit the Hβ, [OIII], Hα and [NII] emission lines and utilize them to provide constraints on a single set of kinematic parameters. This non-parametric measure can give rise to different results for different emission lines, due to differences in the relative flux ratios between the narrow and outflow components in different lines. Using a single set of kinematic parameters obtained from all the available strong emission lines provides more consistent and better constrained results for this study. For comparison, we calculated the values of w_{80} for [OIII] in the outflows in our sample, and they are highly correlated with $v_{\rm max}$, with $w_{80} = (0.77 \pm 0.06) \times v_{\rm max}$.

3.4.4 Emission Line Ratios

Emission line ratio diagnostics, such as the BPT diagram (Baldwin et al. 1981; Veilleux & Osterbrock 1987), provide crucial information about the excitation mechanisms of the gas producing the emission. The unique data set in the MOSDEF survey at $z \sim 2$ provides coverage for all the required optical emission lines for the BPT diagram. Our multi-component emission line fitting procedure allows us to simultaneously measure the fluxes of both the narrow and outflow components for all the required emission lines. Therefore, we can study the excitation mechanisms of the narrow and outflowing gas with the BPT diagram separately, allowing us to address important questions about the physical properties and impact of these outflows. For example, we can test the picture of positive AGN feedback stimulating star formation, if we observe increased excitation by star formation in the outflow components compared with the narrow-line components (Leung et al. 2017).

Figure 3.2 shows [NII] BPT diagrams for the narrow-line (left) and outflow (middle) components for the AGNs with a detected outflow. The Hα and Hβ fluxes for the narrow-line

components are corrected for Balmer absorption as determined by SED modelling (see Reddy et al. 2015). Sources with S/N < 3 in one or both of the line ratios are shown with 3σ limits. Sources where only one of the two line ratios is available are shown as gray points.

The line ratios of the outflow components are shifted towards the AGN region in the BPT diagram (upper right) compared with the narrow-line components. Three of the narrow-line component line ratios lie below the Kauffmann et al. (2003b) demarcation line, while all the outflow component line ratios are above this line, indicating a contribution from AGNs in the photoionization of the outflowing gas. In addition, two more outflow component line ratios lie above the Kewley et al. (2013a) demarcation line of a maximum starburst compared to the narrow-line component line ratios. This trend of the outflowing gas shifting to the AGN region of this diagram is also observed in Leung et al. (2017). This shows that there is an increased contribution from AGNs to the excitation of the outflowing gas rather than from star formation.

We also consider the possibility of shock excitation by examining the relationship between the velocity dispersion and the [NII]/Hα line ratio of the outflow component, as a positive correlation between the two is often interpreted as a strong tracer for shock excitation (e.g. Ho et al. 2014; McElroy et al. 2015; Perna et al. 2017a). Figure 3.2 (right panel) shows the distribution of velocity dispersion and the [NII]/Hα line ratio for the outflows in our sample. We compute the Spearman's rank correlation coefficient in this space for sources with S/N > 3 in both line fluxes in the outflow component, and cannot reject the null hypothesis that there is no correlation between the two quantities, with a p-value of 0.35 for the null hypothesis of non-correlation. The absence of a significant correlation between velocity dispersion and the [NII]/Hα line ratio suggests that as there is no evidence for shock excitation in these outflows, they are likely photoionized by the AGNs. The increased relative contribution from AGN rather than star formation in the outflow component also suggests there is no evidence for positive AGN feedback on the galaxy scale in our sample.

3.4.5 Physical Extent

The physical extent of the outflows is a crucial measurement, needed to determine both the impact of AGN-driven outflows on the future SFR of the host galaxy and whether these outflows can expel gas over the scale of the host galaxy. With the long-slit spectroscopic data in the MOSDEF survey, we can measure the physical extent of these AGN outflows along the slit direction. From the 2D spectra, we create spatial profiles for the narrow-line and outflow components for the [OIII] and Hα emission lines, as well as for the continuum emission. Using results from the 1D emission line fitting, we select narrow-line or outflow dominated wavelength ranges where the narrow-line or outflow component flux is higher than the sum of all of the other components. We also limit the wavelength ranges to be within 2σ of the central wavelength of the respective component. The continuum range is selected far from emission lines. We then sum the fluxes in the 2D spectra along the wavelength axis within each wavelength range to create spatial profiles for the narrow-line, outflow, and continuum components. If the flux of one component is weaker than other components in all wavelengths, no spatial profile is created for the weaker component.

To measure the physical extent of the emission in each component, we fit a Gaussian function to each of the spatial profiles. We take the centroid of the narrow-line component as the fiducial location of the central black hole, and take the difference between the centroids of the narrow-line and outflow components, $|\Delta x|$, as the projected spatial offset between the bulk of the outflow and the central black hole. While a broad-line component can provide an accurate measurement of the location of the central black hole (e.g. Husemann et al. 2016), most of the AGNs in our sample are Type II (with no very broad components in the Hα or Hβ emission lines) so this approach is not applicable here. The centroid of the continuum component can also provide an approximate location of the center of the galaxy, but the continuum emission in our sample is substantially weaker than the narrow-line emission, providing a less accurate measurement than the narrow-line component. If we, instead, use the centroid of the continuum

to calculate the spatial offset, the resulting values only differ by 0.15 kpc on average, with a maximum of 1.05 kpc. This difference is within the 1σ uncertainty of $|\Delta x|$ for 79% of the sources. Therefore, the centroid of the narrow-line component is a reliable proxy for the location of the central black hole in our sample.

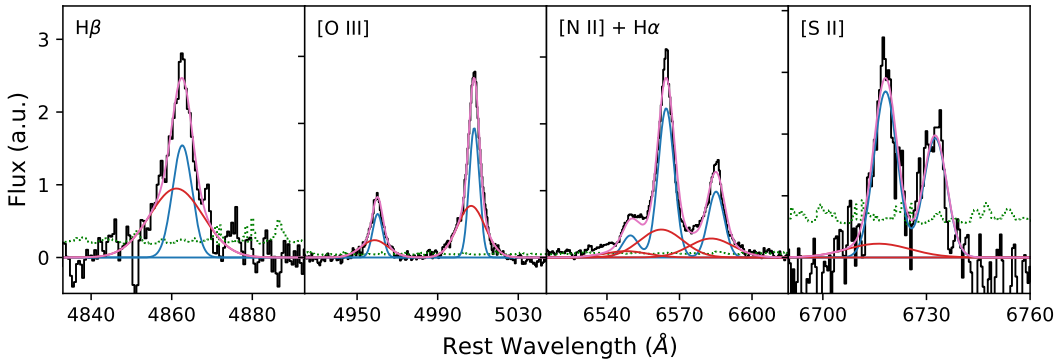

Figure 3.3: Stacked emission line spectrum of 23 AGNs with blueshifted outflows and no BLR emission, weighted by $v_{\rm max}$. The flux is shown in arbitrary units. The black line shows the observed spectrum and the green dotted line shows the error spectrum. The magenta line shows the best-fit model, while the blue and red lines show the best-fit narrow-line and outflow components, respectively. The [SII] doublet is undetected in the outflow component, with S/N of 1.1 and 0.0 for [SII]λ6716 and [SII]λ6731, respectively.

In the MOSDEF survey, a star was observed simultaneously with galaxies on every slitmask, providing a real-time measurement of the seeing for each target. We deconvolve the width of the Gaussian of each spatial profile from the seeing for that slitmask in quadrature. The deconvolved width of the spatial profile of the outflow component (σ_x) is significant (greater than three times the uncertainty) in [OIII] and/or Hα in 17 out of the 27 outflows in our sample.

We then combine these two measurements, the spatial offset and width of the spatial profile, to estimate the full physical extent of the outflow from the central black hole. We define the radius of the outflow as the distance between the central black hole to the edge of the outflow where the outflow emission flux is $1/10$ the strength of the maximum, i.e. $r_{10} = |\Delta x| + 2.146\sigma_x$ or $|\Delta x| + 0.911$ FWHM$_x$. 19 of the 27 outflows are significantly extended in [OIII] and/or Hα with r_{10} ranging from 0.3 to 11.0 kpc, with a median of 4.5 kpc. We measure r_{10} for both [OIII] and

Hα as often one of the lines is impacted by a sky line. A robust measurement of r_{10} is obtained in both lines in three sources. The spatial extents in [OIII] and Hα differ by 0.1, 0.3 and 2.3 kpc in these sources, corresponding to 1.2%, 2.8% and 29.6% of the radius in Hα, respectively.

Our outflow size measurements of a few kpc are consistent with multiple studies in the local Universe (e.g. Greene et al. 2011; Harrison et al. 2014; McElroy et al. 2015; Rupke et al. 2017; Mingozzi et al. 2019) and are larger than those of some recent studies reporting outflow sizes $\lesssim 1$ kpc (e.g. Rose et al. 2018; Baron & Netzer 2019a).

We note that certain caveats exist with the measurement of outflow extents. The actual outflows almost certainly have complex three dimensional structures (e.g. Rupke et al. 2017) and representing the spatial extent of the outflow with a single number such as r_{10} is likely incomplete. Moreover, projection effects can on average affect the measured extent by a factor of $2/\pi \approx 0.64$. Nonetheless, r_{10} provides a lower limit to the actual spatial extent of the outflows.

3.4.6 Mass and Energy Outflow Rates

The mass and energy carried by the outflows are crucial parameters that determine the impact these AGN-driven outflows have on their host galaxies. Correlations between the mass and energy outflow rates with both AGN and host galaxy properties reveal their effects on the galaxy population as a whole, as well as constrain the physical mechanisms driving the outflows.

We estimate the mass of the ionized outflowing gas by calculating the mass of recombining hydrogen atoms. Assuming purely photoionized gas with Case B recombination with an intrinsic line ratio of Hα/Hβ= 2.9 and an electron temperature of $T = 10^4$K, following Osterbrock & Ferland (2006) and Nesvadba et al. (2017), the mass of the ionized gas in the outflow can be expressed as

$$\frac{M_{\rm ion}}{3.3\times10^8\,{\rm M}_\odot} = \left(\frac{L_{\rm H\alpha,out}}{10^{43}\ {\rm erg\ s^{-1}}}\right)\left(\frac{n_e}{100\ {\rm cm^{-3}}}\right)^{-1}, \tag{3.8}$$

where $L_{\rm H\alpha,out}$ is the outflow Hα luminosity and n_e is the electron density of the ionized out-

flowing gas. The electron density is taken to be 150 cm^{-3}; the rationale for this is discussed below. Equivalently, the mass of the ionized gas in the outflow can be expressed in terms of the Hβ luminosity as

$$\frac{M_{\rm ion}}{9.5\times10^8\,{\rm M}_\odot} = \left(\frac{L_{\rm H\beta,out}}{10^{43}\ {\rm erg\ s^{-1}}}\right)\left(\frac{n_e}{100\ {\rm cm^{-3}}}\right)^{-1}, \tag{3.9}$$

where $L_{\rm H\beta,out}$ is the outflow Hβ luminosity.

To calculate the intrinsic Hα and Hβ luminosity of the outflow corrected for extinction, we use the Balmer correction for the narrow line luminosity determined by SED modelling (see Reddy et al. 2015) and apply this correction factor to compute the intrinsic outflow luminosity, preserving the observed outflow to narrow flux ratio. This introduces a source of uncertainty due to differential extinction in the outflowing and narrow line gas, but very likely provides a conservative lower limit to the intrinsic luminosity (see Förster Schreiber et al. 2019). For the rest of this paper we use $M_{\rm out} = M_{\rm ion}$, while noting that this is a strict lower limit as the total mass in the outflow will include molecular and neutral gas as well, which can be substantial (e.g. Vayner et al. 2017; Brusa et al. 2018; Herrera-Camus et al. 2019).

Then the mass outflow rate is obtained by

$$\dot{M}_{\rm out} = B\frac{M_{\rm out}v_{\rm out}}{R_{\rm out}}. \tag{3.10}$$

The value of $v_{\rm out}$ is taken to be $v_{\rm max}$ as defined in Section 3.4.3 for the outflow velocity, while $R_{\rm out}$ is taken to be r_{10} as defined in Section 3.4.5. An overall factor B of $1-3$ is typically applied (Harrison et al. 2018) depending on the assumed geometry of the outflows. A spherical outflow implies a factor of 3 while an outflow covering 1/3 of the entire sphere gives a factor of 1. In this study, we use a fiducial value of $B = 1$. Using a different factor would simply change the overall mass and energy outflow rates by that factor. In our sample, we find $\dot{M}_{\rm out} \sim 0.1 - 10^4$ M$_\odot$ yr^{-1}, with a median of 13 M$_\odot$ yr^{-1}.

The kinetic energy outflow rate and momentum flux are then given by

$$\dot{E}_{\rm out} = \frac{1}{2}\dot{M}_{\rm out} v_{\rm out}^2 \tag{3.11}$$

and

$$\dot{P}_{\rm out} = \dot{M}_{\rm out} v_{\rm out}, \tag{3.12}$$

respectively. We find $\dot{E}_{\rm out} \sim 10^{40} - 10^{46}$ erg s^{-1}, with a median of 4×10^{42} erg s^{-1}, and $\dot{P}_{\rm out} \sim 10^{32} - 10^{38}$ dyn, with a median of 8×10^{34} dyn.

The largest systematic uncertainty in the calculation of the mass and energy outflow rates is the electron density n_e. The value of n_e is difficult to measure as it typically requires detection of the outflow in a density-sensitive line such as the [SII] doublet. This doublet is not detected in the outflows in MOSDEF (see Section 3.4.7). Measurements of n_e in AGN-driven outflows in the literature span a wide range of values and often have very large uncertainties. Harrison et al. (2014) find $n_e \approx 200 - 1000$ cm^{-3} in a sample of $z < 0.2$ luminous AGNs, Kakkad et al. (2018) find spatially-resolved electron densities of $\approx 50 - 2000$ cm^{-3} in $z < 0.02$ radio AGNs, and Rupke et al. (2017) find spatially-averaged electron densities of $50 - 400$ cm^{-3}, with a median of 150 cm^{-3} in a sample of $z < 0.3$ quasars. Mingozzi et al. (2019) present a high resolution map of electron density in nearby AGNs with outflows and find a wide range of densities from 50 to 1000 cm^{-3}, with a median of 250 cm^{-3} in the outflow. At higher redshifts, Förster Schreiber et al. (2019) report $n_e \sim 1000$ cm^{-3} in a stacked analysis of the spatially integrated spectra of AGN outflows at $z = 0.6 - 2.7$, while Vayner et al. (2017) report a lower n_e of 272 cm^{-3} in the outflow of a $z = 1.5$ quasar. Measurements using other diagnostics yield an even wider range of values. Studies of extended AGN scattered light infer very low densities of < 1 cm^{-3} (Zakamska et al. 2006; Greene et al. 2011). Diagnostics with trans-auroral [SII] and [OII] emission line ratios yield densities of $10^{3-4.8}$ cm^{-3} (Holt et al. 2011; Rose et al. 2018), while SED and photoionization modelling infers density estimates of $\sim 10^{4.5}$ cm^{-3} (Baron & Netzer 2019a,b).

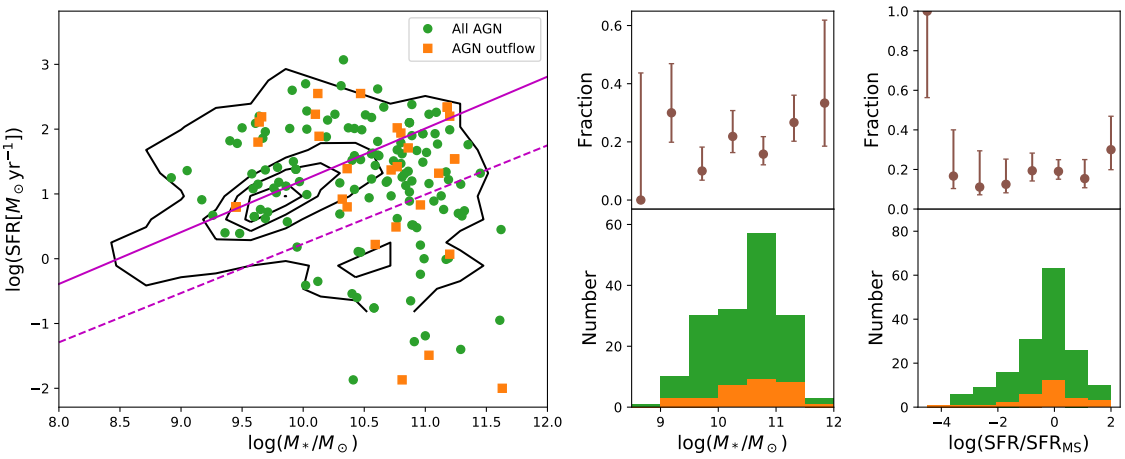

Figure 3.4: Left panel: Distribution of SFR and M_* for all AGNs in the MOSDEF survey (blue points) and the AGNS with detected outflows in our sample (red points). Black contours show the distribution of all galaxies in the MOSDEF survey. The solid magenta line is the best-fit star-forming main sequence by Shivaei et al. (2015), while the dashed magenta line shows the redshift-dependent demarcation line between star-forming and quiescent galaxies by Aird et al. (2018), shown here for $z = 2.3$. Lower middle panel: Histogram of M_* for all AGNs (green) and AGNs with outflows (orange). Lower right panel: Same as the lower middle panel, but for SFR relative to the main sequence. Upper middle panel: Fraction of AGNs that host an outflow as a function of M_*. Outflows are found to be distributed uniformly with M_* among AGNs. However, the incidence of outflows among all galaxies can be different, since AGNs are detected more easily in higher mass galaxies (see text for details). Upper right panel: Same as the upper middle panel, but for SFR/SFR$_{MS}$. Outflows are detected uniformly with SFR/SFR$_{MS}$ among AGNs.

Additionally, spatially-resolved analyses of electron density show that regions of elevated electron densities ($\gtrsim 1000$ cm^{-3}) are concentrated in very localized regions, while most of the other regions have much lower electron densities ($\lesssim 100$ cm^{-3}, e.g. Rupke et al. 2017; Kakkad et al. 2018; Mingozzi et al. 2019). For instance, electron density maps of the outflowing gas in Kakkad et al. (2018) show that regions of dense gas are located in small spatial regions at radii < 0.5 kpc, while the electron density drops quickly with radius, reaching < 50 cm^{-3} beyond 1 kpc from the AGN. Therefore, higher values of n_e near ~ 1000 cm^{-3} reported from spatially-averaged analyses can be biased towards high density regions which dominates the total flux, as shown in Mingozzi et al. (2019). This bias can potentially lead to overestimation of the electron density over the large spatial volume of the outflows present in this study, which extend over several kpc in physical size. While most of the high density gas in the outflows is concentrated in the most luminous compact region, substantial mass can reside in lower density regions with a much higher volume filling factors. For instance, in a spherically symmetric mass-conserving free wind, i.e. the mass outflow rate and velocity is conserved at any radius, the density profile has to follow $n(r) \propto r^{-2}$ (e.g. Rupke et al. 2005; Liu et al. 2013a; Genzel et al. 2014; Förster Schreiber et al. 2019). In such a profile, a compact inner region dominates the density and luminosity, but the mass, which is distributed uniformly in radius, resides mostly in low density regions over a much larger volume outside this compact inner region. Therefore, in our calculation, we take r_{10} as the radius of the outflow and $n_e = 150$ cm^{-3}. r_{10} represents the maximum extent of the outflow including the most extended but low surface brightness region, and the choice of n_e is similar to the median electron densities in the spatially-resolved maps of Rupke et al. (2017) and Kakkad et al. (2018).

Furthermore, $\dot{M}_{\rm out}$ scales with $(n_e R_{\rm out})^{-1}$. If, alternatively, a small radius and a high electron density is adopted to represent the densest compact region, one will obtain a similar outflow rate. For example, the $0.5-1$ kpc radius of the dense compact region in Kakkad et al. (2018) is a factor of a few lower than the typical r_{10} of 4.5 kpc in our outflows, while the electron

density therein of ~ 1000 cm^{-3} is a factor of a few higher than the adopted median value of 150 cm^{-3} here, such that the product $n_e R_{\rm out}$, and thus $\dot{M}_{\rm out}$, is largely consistent with our value. As these two sets of values represent the outflow rates at two different radii, this result is to be expected if the mass-conserving free wind scenario is a good approximation over the range of radius concerned. We note that outflow rate estimates based on different assumptions of the distribution of the outflowing gas can lead to different results.

3.4.7 Stacked Spectrum Analysis

We attempt to constrain the electron density in the outflow through measurements of the [SII] doublet using a stacking analysis of the outflow emission line spectra. We select from our outflow sample sources with no BLR emission in Hα and Hβ in order to avoid contamination to the [SII] doublet. Seven outflows are excluded by this criterion. We also exclude two outflows with a positive Δv, i.e. a redshifted outflow component, to boost the blueshifted outflow signal in the stacked spectrum. These criteria result in a sample of 23 AGN outflows. We then assign weights to each source according to the magnitude of the measured $v_{\rm max}$. A stacked spectrum is constructed using the method described in Shivaei et al. (2018). We perform the same line-fitting procedures described in Section 3.3.2 to the stacked spectrum. The resulting stacked spectrum and its best-fit model are shown in Figure 3.3. The Hβ, [OIII], Hα and [NII] emission lines all display a significant outflow component. For the [SII] doublet, a narrow-line component is detected at S/N of 8.8 and 9.9 for [SII]λ6718 and [SII]λ6732, respectively. However, the outflow component is undetected in both lines, yielding S/N of 1.1 and 0.0 in the best-fit model for the two emission [SII] lines. No meaningful line ratios can be calculated from the line fluxes to place constraints on the electron density of these outflows. We also construct stacked spectra using different weighting algorithms, including weighting by Δv and outflow fluxes in [OIII] or Hα. The outflow component of the [SII] doublet is undetected in all of these stacked spectra.

3.5 Outflow Incidence and Host Properties

In this section we study the relation between outflow incidence and the properties of the AGN or host galaxy.

3.5.1 Host Galaxy Properties

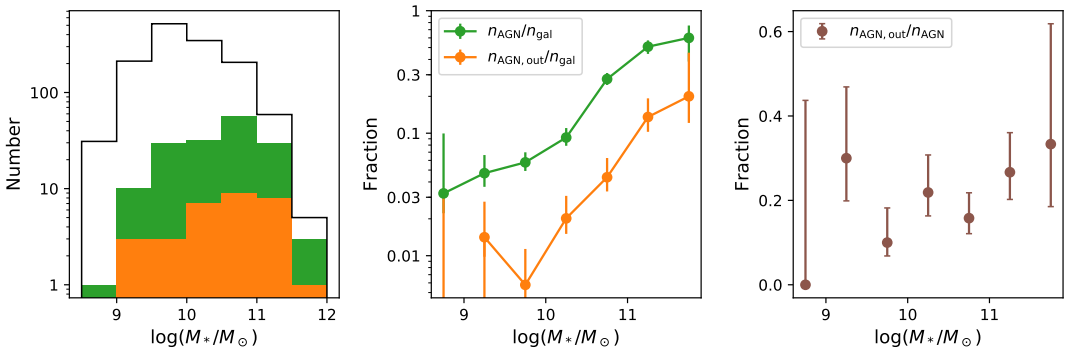

Figure 3.5: Left panel: Stellar mass histogram for all galaxies (black), all AGNs (green), and AGNs with outflows (orange) in the MOSDEF survey. Middle panel: The fraction of galaxies that host an AGN (green) and the fraction of galaxies that host an AGN and an outflow as a function of stellar mass. Right panel: the fraction of AGNs that host an outflow as a function of stellar mass. Both the fraction of galaxies that host an AGN and the fraction of galaxies that host an AGN and an outflow increase with M_*. However, the fraction of AGNs that host an outflow is uniform with M_*. The increasing trend seen in the middle panel is due to an observational AGN selection bias (see text for details). The right panel shows that given the presence of an AGN, the presence of an outflow is independent of stellar mass. The intrinsic incidence of AGN outflows is thus also independent of M_*.

Since AGN-driven outflows are widely believed to impact the evolution of their host galaxies, especially as a form of AGN feedback appears to be needed to quench or regulate star formation in high mass galaxies, here we examine the relation between the incidence rate of AGN-driven outflows and the properties of their host galaxies.

Figure 3.4 shows the distribution of SFR versus stellar mass for all MOSDEF galaxies (black contours), all MOSDEF AGNs (green points) and all AGNs with a detected outflow (orange points). The star-forming main sequence for SED-based SFR in MOSDEF galaxies found by

Shivaei et al. (2015):

$$\log \mathrm{SFR}[\mathrm{M}_\odot\ \mathrm{yr}^{-1}] = 0.8\ \log(M_*/M_\odot) - 6.79 \tag{3.13}$$

is shown with a solid magenta line. We adopt the redshift-dependent minimum SFR relative to the main sequence defined in Aird et al. (2018):

$$\begin{aligned} &\log\ \mathrm{SFR}_{\mathrm{min}}[\mathrm{M}_\odot\ \mathrm{yr}^{-1}] \\ &\quad = 0.76\ \log(M_*/M_\odot) - 8.9 + 2.95\ \log(1+z), \end{aligned} \tag{3.14}$$

where $z = 2.3$, shown with a dashed magenta line. In this study we classify galaxies that lie below this line as quiescent and galaxies above the line as star-forming. The lower and upper right panels of Figure 3.4 show the distributions and fractions with stellar mass and SFR, respectively, for all AGNs and AGNs with outflows in our sample.

AGNs in MOSDEF are detected in galaxies with stellar masses of $10^{8.5-12}\,\mathrm{M}_\odot$, while outflows are detected in AGN host galaxies with $10^{9-12}\,\mathrm{M}_\odot$. A two-sample KS test of the stellar mass distributions of all AGNs and AGNs with outflows results in a KS statistic of 0.11 and a p-value of 0.89 for the null hypothesis of identical distributions. This shows that there is no significant difference between the two distributions. The incidence of AGN-driven outflows is independent of stellar mass, within the errors (upper middle panel). Outflows are detected in AGNs above and below the star forming main sequence, in both star forming galaxies and quiescent galaxies. There is no significant difference between the distributions of $\log(\mathrm{SFR}/\mathrm{SFR}_{\mathrm{MS}})$ (defined as the SFR relative to the main sequence) of AGNs with outflows and all AGNs, with a KS statistic of 0.11 and a p-value of 0.90.

It should be noted that, as discussed in Leung et al. (2017), the independence of outflow incidence with SFR should not be interpreted as a it lack of negative AGN feedback. The SFR in this study are obtained by SED fitting, which reflects the SFR over the past 10^8 years (Kennicutt

1998). The outflows in our sample have dynamical timescales, defined by $r_{10}/v_{\rm max}$, of 10^{5-7} years. Therefore, the currently observed outflows are not expected to have an impact on the measured SFR. The independence of outflow incidence rate with both stellar mass and SFR, shows that AGN-driven outflows are a widespread and common phenomenon that occur uniformly among galaxies both along and across the star-forming main sequence, and across different phases of galaxy evolution.

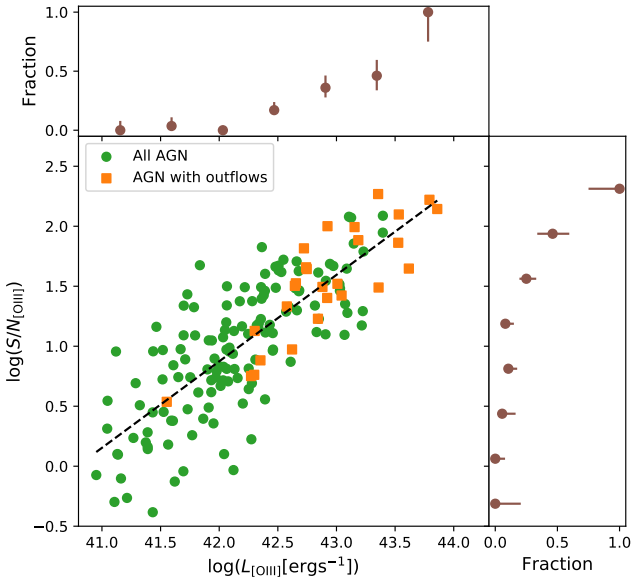

Figure 3.6: Distribution of signal to noise (S/N) in [OIII] and $L_{[\rm OIII]}$ for all AGNs in the MOSDEF survey (green points) and AGNs with outflows (orange squares). Upper panel: The fraction of AGNs which host an outflow as a function of $L_{[\rm OIII]}$. Right panel: Same as the upper panel, but as a function of S/N in [OIII]. The distribution of $L_{[\rm OIII]}$ and S/N$_{[\rm OIII]}$ are strongly correlated, and the fraction of AGNs with an outflow increases with both $L_{[\rm OIII]}$ and S/N$_{[\rm OIII]}$. The increasing fraction cannot be independently associated with either $L_{[\rm OIII]}$ or S/N$_{[\rm OIII]}$ in this sample.

There has been reported in the literature an increasing incidence of AGN outflows with stellar mass (Genzel et al. 2014; Förster Schreiber et al. 2019), which appears to be contradictory to our results. However, Genzel et al. (2014) and Förster Schreiber et al. (2019) show that the incidence of AGN outflows *among all galaxies* increases with stellar mass, while here we are

showing that the incidence of outflows *among AGNs* is independent of stellar mass. In Figure 3.5, the left panel shows the stellar mass distribution of galaxies, AGNs, and AGNs with outflows in the MOSDEF survey, while the middle panel shows the fraction of galaxies that host an AGN and the fraction of galaxies that host an AGN and an outflow. Both of these fractions show a strong increasing trend with stellar mass, which is consistent with the findings of Genzel et al. (2014) and Förster Schreiber et al. (2019). While less than 10% of galaxies host an AGN at $M_* \sim 10^9\,M_\odot$, this fraction increases to over 60% at $M_* \sim 10^{11.5}\,M_\odot$. This is a well-known selection effect, as AGNs of the same Eddington ratio are more luminous at higher stellar mass and thus are more likely to be detected (Aird et al. 2012). The intrinsic probability that a galaxy hosts an AGN does rise with increasing stellar mass but is not nearly as steep as the observed fraction shown here (Aird et al. 2018). The fraction of galaxies that host an AGN and an outflow shows a similar increasing trend as the trend caused by AGN selection effects. However, the fraction *of AGNs* that host an outflow, shown in the right panel of Figure 3.5, is constant with stellar mass, showing that given the presence of an AGN, the presence of an outflow is independent of stellar mass. Our results indicate that after removing the selection bias of AGN identification, the underlying incidence of AGN outflows is independent of stellar mass, and that AGN-driven outflows are equally probable in galaxies across the stellar mass range probed here.

3.5.2 [OIII] Luminosity

The [OIII] luminosity ($L_{[\mathrm{OIII}]}$) is a common proxy for the AGN bolometric luminosity (L_{AGN}) (e.g. Heckman & Best 2014), where L_{AGN} is estimated by a constant factor times $L_{[\mathrm{OIII}]}$ (a constant of 600 is found in Kauffmann & Heckman 2009). A correlation between the incidence rate of outflows and $L_{[\mathrm{OIII}]}$ may therefore be interpreted as evidence that more powerful AGNs drive outflows more frequently. However, as noted in Leung et al. (2017), $L_{[\mathrm{OIII}]}$ scales directly with the S/N of the [OIII] emission line ($\mathrm{S/N}_{[\mathrm{OIII}]}$), which directly determines whether an outflow is detectable in emission. We note that the AGN [OIII] luminosity in our sample is corrected

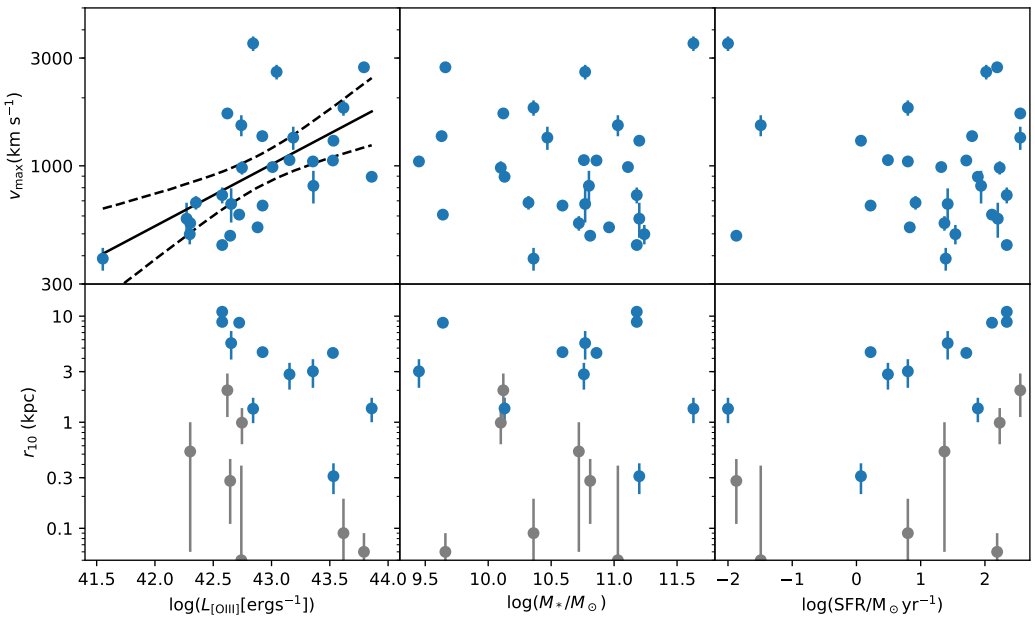

Figure 3.7: l
uminosity (left), galaxy stellar mass (middle) and SFR (right).] Top: Maximum outflow velocity ($v_{\rm max}$) versus [OIII] luminosity (left), galaxy stellar mass (middle) and SFR (right). Bottom: Outflow radius (r_{10}) versus [OIII] luminosity (left), galaxy stellar mass (middle) and SFR (right). Radius measurements with high significance (S/N $>$ 3) are shown in blue while those with an absolute uncertainty $<$ 1 kpc are shown in gray. The solid line shows the best-fit log-linear relation for significant correlations, while the dashed lines show the 90% confidence intervals. $v_{\rm max}$ is significantly correlated with $L_{[\rm OIII]}$. Although the high significance measurements of r_{10} are anti-correlated with $L_{[\rm OIII]}$, this is a selection effect, and this trend is absent if measurements with an absolute uncertainty $<$ 1 kpc are included (see text for details). There are no significant correlations with stellar mass or SFR.

for dust reddening. To determine the correction factor, we calculate the color excess from the Balmer decrement and combine this with the value of the MOSDEF dust attenuation curve at 5008 Å(Reddy et al. 2015). This correction results in an average increase of ~ 0.17 dex in [OIII] luminosity for the AGNs in our sample.

Figure 3.6 shows the the distribution of $L_{[OIII]}$ and S/N$_{[OIII]}$ of all AGNs and AGNs with a detected outflow in our sample. $L_{[OIII]}$ here includes emission from both the narrow-line and outflow components, which are both photoionized by the AGN. There is an obvious correlation between $L_{[OIII]}$ and S/N$_{[OIII]}$, as expected. The fraction of AGNs with a detected outflow increases with both $L_{[OIII]}$ and S/N$_{[OIII]}$. More than 50% of the AGNs have an outflow component detected at $L_{[OIII]}$ above $\sim 10^{43}$ ergs^{-1}, which corresponds to S/N$_{[OIII]}$ above ~ 100. The fraction of AGNs with a detected outflow approaches 100% at $L_{[OIII]} \sim 10^{43.8}$ ergs^{-1} and at S/N$_{[OIII]} \sim 250$. On the other hand, no AGNs have an outflow detected with S/N$_{[OIII]}$ below 3, corresponding to $L_{[OIII]} \sim 10^{41.5}$ ergs^{-1}. In our analysis, we require a S/N of > 3 in both the narrow-line and outflow components individually, so any potential outflows in AGNs below this threshold are undetectable by definition.

A similar increasing trend between the fraction of AGNs with a detected outflow and $L_{[OIII]}$ was reported in the study of $\sim 39,000$ nearby Type II AGNs at $z < 0.3$ in Woo et al. (2016). They detect an outflow component in over 50% of the AGN and composite sources at $L_{[OIII]}$ above $\sim 10^{40.5}$ ergs^{-1}, while the fraction approaches unity at $\sim 10^{42}$ ergs^{-1}. At the latter luminosity, AGNs in our sample at $z \sim 2$ have a typical S/N$_{[OIII]}$ of only ~ 5, such that detecting an outflow is challenging. Their trend is similar to ours, except that the luminosity thresholds for outflow detection have been shifted to lower values in the lower redshift sample of Woo et al. (2016). Similar results among X-ray AGN in SDSS are also reported in Perna et al. (2017b).

We note that among the three sources without an outflow detection at S/N above 100 in our sample, two of them have a second kinematic component detected but are removed from our outflow sample as they are identified as potential mergers in HST imaging, following the

procedures described in Section 3.4.1. Taking this into account, a second kinematic component is detected in 7 out of 8 of the AGNs with S/N $>$ 100 in our sample. As noted above, the lower overall incidence of AGN outflows we report here is in part due to the removal of potential mergers in our analysis.

In an effort to distinguish whether the trend seen in Figure 3.6 is primarily driven by S/N or $L_{[OIII]}$, we perform a linear regression analysis to the S/N-$L_{[OIII]}$ diagram. We fit a linear function in logarithmic space to the AGNs with outflows, AGNs without outflows, and all AGNs separately, and obtained slopes of 0.75 ± 0.11, 0.72 ± 0.05 and 0.72 ± 0.04, respectively. There is no difference between the distributions of AGNs with and without outflows within uncertainties. We also use the best-fit model for all AGNs to obtain the mean $L_{[OIII]}$ as a function of S/N, and compare the offset of $L_{[OIII]}$ from the mean for AGNs with and without outflows, and find no significant difference in the distribution of $L_{[OIII]}$ offset between the two samples. Our results show that $L_{[OIII]}$ is highly correlated with S/N in our sample, which directly affects the detection of outflows. The effects of $L_{[OIII]}$ and S/N cannot be separated in the correlation between outflow incidence rate and $L_{[OIII]}$ seen here.

3.6 Outflow Parameters and Host Galaxy Properties

With our statistical sample of AGN outflows at $z \sim 1-3$, it is possible to study the relationship between outflow properties and AGN or host galaxy properties at these high redshifts. Such analysis can potentially reveal crucial information about the impact these outflows have on their host galaxies and help clarify their role in galaxy evolution. As discussed in Section 3.4.6, the calculation of the mass and energy outflow rates contains a systematic uncertainty due to the assumption of the electron density in the outflows; however, this does not affect the trends studied in this section, as all sources are affected uniformly.

3.6.1 Outflow Velocity and Radius

First we study the relationship between the outflow velocity $v_{\rm max}$ and outflow radius r_{10} and properties of the AGN and host galaxy. In Figure 3.7, the top row shows $v_{\rm max}$ against $L_{\rm [OIII]}$, M_* and SFR. We search for correlations between the outflow parameters and AGN or host galaxy parameters by computing the Spearman rank correlation coefficient and the associated p-value for the null hypothesis of non-correlation. For correlations with a p-value of $< 5\%$, we perform a Bayesian linear regression analysis as described in Kelly (2007) to fit a linear function with an intrinsic scatter in logarithmic space and obtain the best-fit slope and its error. The results are shown in Table 3.1.

Table 3.1: Correlations of Outflow Velocity and Radius with AGN and Host Galaxy Properties

Correlation	Spearman rank	p-value	Slope
$v_{\rm max}$vs $L_{\rm [OIII]}$	0.624	0.04 %	0.27 ± 0.09
σ_v vs $L_{\rm [OIII]}$	0.667	0.01 %	0.41 ± 0.11
Δv vs $L_{\rm [OIII]}$	0.227	25 %	-
$v_{\rm max}$vs M_*	-0.186	34 %	-
$v_{\rm max}$vs SFR	-0.030	88 %	-
r_{10} vs $L_{\rm [OIII]}$	-0.361	14 %	-
r_{10} vs M_*	0.045	86 %	-
r_{10} vs SFR	0.447	6.3 %	-
$v_{\rm max}$vs r_{10}	-0.521	2.7 %	-0.24 ± 0.12
σ_v vs r_{10}	-0.569	1.4 %	-0.33 ± 0.16
Δv vs r_{10}	0.253	31 %	-

The maximum velocity $v_{\rm max}$ is correlated with $L_{\rm [OIII]}$, with a p-value of 0.04% and a best-fit relation of $v_{\rm max} \propto L_{\rm [OIII]}^{0.27\pm0.09}$. Our results agree with the findings of Fiore et al. (2017), who report a common scaling between $L_{\rm AGN}$ and $v_{\rm max}$ in an analysis of AGN-driven outflows across different phases, namely ionized, molecular, and ultrafast outflows, of $L_{\rm AGN} \propto v_{\rm max}^{4.6\pm1.5}$, i.e. $v_{\rm max} \propto L_{\rm AGN}^{0.22\pm0.07}$. Moreover, these results are consistent with the theoretical model for an energy conserving outflow in Costa et al. (2014), which predicts a relation between $L_{\rm AGN}$ and $v_{\rm max}$ with a power to the fifth order. There is no significant correlation between $v_{\rm max}$ and M_* or SFR in our

sample.

The bottom panels of Figure 3.7 show outflow radius r_{10} in [OIII] versus $L_{[\mathrm{OIII}]}$, M_*, and SFR. The blue points show radius measurements with S/N > 3, while the grey points show radius measurements with S/N < 3 and an absolute uncertainty < 1 kpc. The reason for showing the grey points is that while some of these measurements have fairly large relative uncertainties, if we only show measurements with S/N > 3 (blue points), then we introduce a selection effect which results in an artificial negative correlation between outflow radius and $L_{[\mathrm{OIII}]}$(lower left panel). There is a selection effect because small radius measurements with high S/N would imply a very small absolute uncertainty, which is only achievable with very high $L_{[\mathrm{OIII}]}$. It is therefore not possible to observe high S/N (blue) points in the lower left region of this plot. Including the grey points, which have an absolute uncertainty < 1 kpc, we do not find a significant correlation between radius and $L_{[\mathrm{OIII}]}$. Similarly, no significant correlation is found between outflow radius and host galaxy M_* or SFR.

Studies of AGN-driven outflows (and extended narrow-line regions) in low-redshift galaxies have revealed a positive size-luminosity relation between outflow radius and L_{AGN} (e.g. Kang & Woo 2018). This is not observed in our sample. However, it has also been reported that an upper limit in radius may exist above a certain luminosity, likely due to insufficient gas beyond such a radius or the over-ionization of gas, which reduces [OIII] emission (e.g. Hainline et al. 2013, 2014; Sun et al. 2017). For example, Sun et al. (2017) report a flattening in the size-luminosity relation at $R \sim 10$ kpc and $L_{\mathrm{AGN}} > 10^{46}$ ergs^{-1}, corresponding to $L_{[\mathrm{OIII}]} \sim 10^{43}$ erg s^{-1}, while Hainline et al. (2013) and Hainline et al. (2014) suggest that this limit can be as low as $6-8$ kpc and $L_{[\mathrm{OIII}]} \sim 10^{42}$ erg s^{-1}. Our sample only spans $L_{[\mathrm{OIII}]} > 10^{42}$ erg s^{-1}, therefore we are likely probing the flattened part of the size-luminosity relation. Our results support the existence of an upper limit in outflow size of $\sim$5-10 kpc at high luminosities.

While v_{max} depends on $L_{[\mathrm{OIII}]}$, the definition of v_{max} encompasses two different kinematic parameters, namely the velocity shift (Δv) and the outflow velocity dispersion (σ_{out}). We next

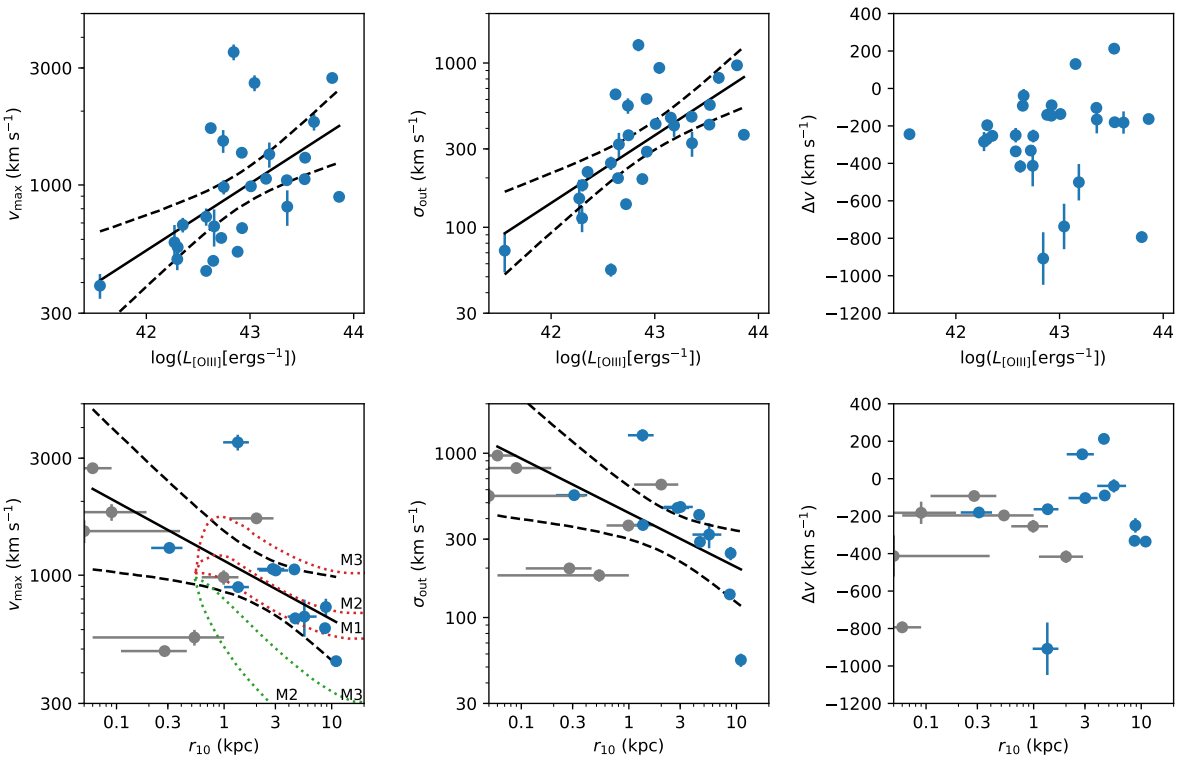

Figure 3.8: Top: The outflow maximum velocity ($v_{\rm max}$, left), velocity dispersion ($\sigma_{\rm out}$, middle), and velocity offset (Δv, right) versus [OIII] luminosity. Bottom: The same kinematic parameters as the top panel plotted against the outflow radius r_{10}. Radius measurements with S/N > 3 are shown in blue while those with lower S/N and an absolute uncertainty < 1 kpc are shown in grey. The solid black line is the best-fit log-linear relation, while the dashed lines show the 90% confidence intervals. Both $v_{\rm max}$and σ_v are correlated with $L_{[\rm OIII]}$, though the correlation is stronger with $\sigma_{\rm out}$ than with $v_{\rm max}$. Both $v_{\rm max}$and $\sigma_{\rm out}$ are anti-correlated with r_{10}. The dotted lines in the lower left panel show the analytic solutions of Costa et al. (2014) for energy-driven (red) and momentum-driven (green) outflows for three different black hole masses, $5 \times 10^7\,{\rm M}_\odot$ (M1), $10^8\,{\rm M}_\odot$ (M2), and $3 \times 10^8\,{\rm M}_\odot$ (M3).

study the relation between $L_{[OIII]}$ and Δv and σ_{out} separately. The results are shown in the top panels of Figure 3.8 and in Table 3.1. We find that σ_{out} is significantly correlated with $L_{[OIII]}$, with the Spearman rank correlation coefficient giving a p-value of 0.01%. Interestingly, the correlation between σ_{out} and $L_{[OIII]}$ is more significant than that between v_{max} and $L_{[OIII]}$. The best-fit relation is $L_{[OIII]} \propto \sigma_{out}^{0.41\pm0.11}$, which is steeper than the relation between v_{max} and $L_{[OIII]}$. There is no correlation between Δv or $|\Delta v|$ and $L_{[OIII]}$. We consider the absolute value of Δv since it can have negative or positive values. While a monotonic correlation is not observed, it does appear that only AGNs with higher $L_{[OIII]}$ are capable of producing higher $|\Delta v|$, while AGNs with any $L_{[OIII]}$ can produce small $|\Delta v|$. Since v_{max} is the sum of Δv and σ_{out}, the monotonic relation between v_{max} and $L_{[OIII]}$ is mainly driven by σ_{out}.

We also examine the relation between these outflow kinematic parameters and the outflow radius r_{10} in [OIII]. The results are shown in the bottom panels of Figure 3.8 and in Table 3.1. With the inclusion of radius measurements with a threshold in absolute uncertainty of < 1 kpc (grey points), there is a weak anti-correlation between radius and v_{max} as well as radius and σ_{out}, with the Spearman rank correlation coefficient giving a p-value of 2.7% and 1.4%, respectively. The best-fit relations are $v_{max} \propto r_{10}^{-0.24\pm0.12}$ and $\sigma_{out} \propto r_{10}^{-0.33\pm0.16}$. When studying the relation between radius and $L_{[OIII]}$, using only radius measurements with S/N > 3 results in a significant anti-correlation which is due to a selection effect. However, doing the same with radius and v_{max} or σ_{out} does not lead to a significantly different result in terms of either the Spearman rank correlation coefficient or the log-linear slope. This suggests that the weak correlation seen here between radius and v_{max} or σ_{out} is unlikely due to the same selection effect, and is more likely a genuine correlation. There is no significant correlation between radius and Δv.

Bae & Woo (2016) study a biconical outflow model that includes dust extinction and show that σ_{out} is mostly driven by the intrinsic velocity and inclination of the outflow, while Δv is primarily produced by extinction. Using this model, our results show that either the intrinsic velocity or the inclination of the outflow, or both, is anti-correlated with the outflow radius. The

former can be explained by a deceleration of the outflowing gas as it expands, while the latter can potentially be understood as a projection effect, since the velocity is measured along the line of sight while the radius is measured perpendicular to it. On the other hand, our data show that there is, reasonably, no correlation between extinction and outflow radius. We explore the possibility of a deceleration of the outflowing gas as an explanation to our observed anti-correlation between radius and velocity. Costa et al. (2014) present analytic solutions to the velocity and radius of an energy- or momentum-driven outflow for three different black hole masses, $5 \times 10^7\,M_\odot$, $10^8\,M_\odot$, and $3 \times 10^8\,M_\odot$. In Figure 3.8, we overlay these analytic solutions on our observed relation between $v_{\rm max}$ and radius. The energy-driven solutions for all three black hole masses and the momentum-driven solutions for the two highest black hole masses all produce a velocity that decreases with radius between 1 and 10 kpc. The energy-driven solutions for black hole masses of $5 \times 10^7\,M_\odot$ and $10^8\,M_\odot$ are the most consistent with the observed data, lying within the 90% confidence interval of the best-fit observed relation of $v_{\rm max}$ and radius. The energy-driven solution for a black hole mass of $3 \times 10^8\,M_\odot$ is higher than the observed relation, while the momentum-driven solutions for all the black hole masses are lower than the observed velocity.

To summarize, in this section we explored correlations between outflow velocity, outflow size, and AGN and host galaxy properties. We find that the outflow velocity is proportional to $L_{\rm [OIII]}^{0.27\pm0.09}$, in agreement with theoretical models of an energy-conserving outflow. The outflow size is independent of $L_{\rm [OIII]}$, supporting the existence of an upper limit in outflow size of $\sim 5-10$ kpc at $L_{\rm [OIII]} > 10^{42}$erg s^{-1}. The outflow velocity is inversely correlated with the outflow size, and the observed relation is consistent with analytic solutions of an energy-conserving outflow, while that of a momentum-conserving outflow predicts lower velocities than observed.

3.6.2 Mass and Energy Outflow Rates

Figure 3.9 shows the mass and energy outflow rates of the outflows in the sample versus $L_{\rm AGN}$, M_*, and SFR. The error bars are the combined 1σ uncertainties from the errors on the

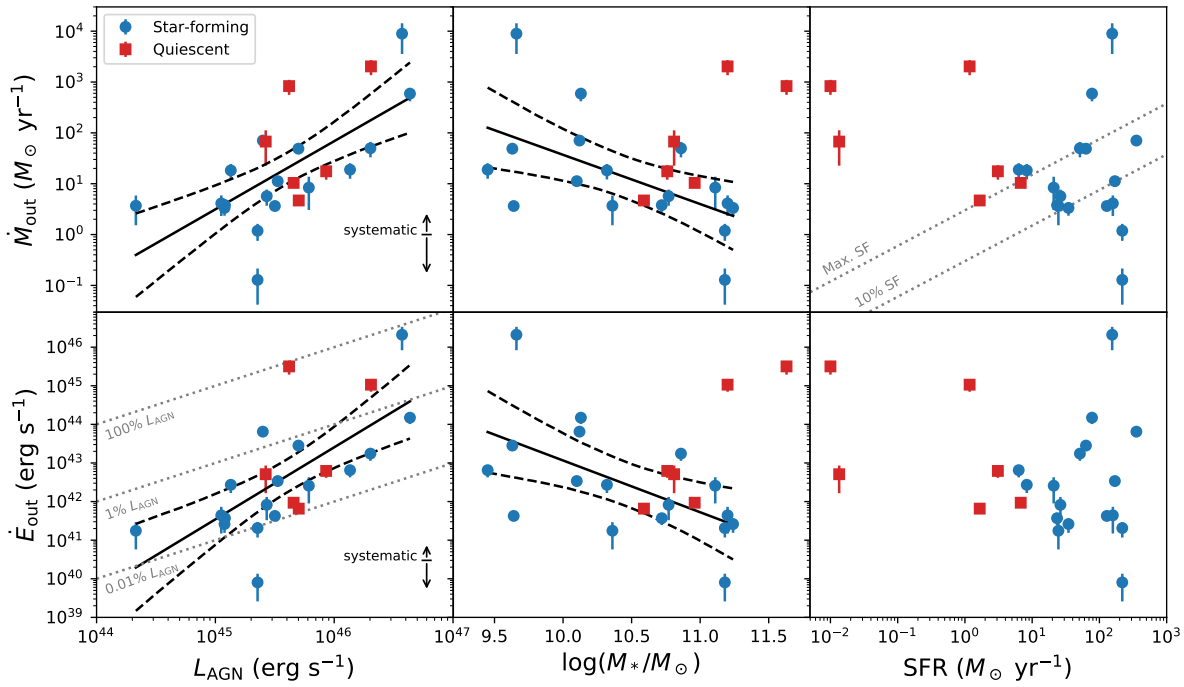

Figure 3.9: Top: Mass outflow rates versus $L_{\rm AGN}$ (left), M_* (middle), and SFR (right). Star-forming galaxies are shown in blue points while quiescent galaxies are shown in red points. Bottom: Same as the top panel but for the kinetic power of the outflow. The solid lines show the best-fit log-linear slopes for significant correlations with p-values $< 1\%$. The black arrows in the left panels show the systematic effect due to the uncertainty in the value of n_e, which can range from $50 - 1000{\rm cm}^{-3}$. The dotted lines in the top right panel show 100% and 10% of the expected maximum mass-loss rate from stellar feedback by Hopkins et al. (2012). This includes mass loss in all phases, including ionized, neutral and molecular gas, while the measurements in this study only include ionized gas. The dotted lines in the bottom left panel show the kinetic power equating 100%, 1% and 0.01% of $L_{\rm AGN}$. The kinetic power of all the outflows are below 100% of $L_{\rm AGN}$, and are energetically consistent with being AGN-driven. The mass outflow rates of most AGNs exceed are above 10% of expected maximum mass-loss rate from stellar feedback. Assuming 10% of the total outflow mass is ionized, these outflows cannot be produced by stellar feedback.

velocity, radius, and flux. We search for correlations between the outflow rates and $L_{\rm AGN}$, M_*, and SFR by computing the Spearman rank correlation coefficient. $L_{\rm AGN}$ is obtained by applying a bolometric correction factor of 600 to the total [OIII] luminosity (Kauffmann & Heckman 2009). For correlations with a p-value of $< 5\%$, we fit a log-linear relation with an intrinsic scatter and obtain the best-fit slope and its error. Six of the outflow host galaxies in our sample lie far enough below the star-forming main sequence to be classified as quiescent galaxies (see Section 3.5.1) and are shown as red points, while star-forming galaxies are shown as blue points. Since quiescent galaxies have very different SFR, and therefore potentially different physical properties, from the rest of the sample, we perform the correlation analysis on the entire outflow sample containing both star-forming and quiescent galaxies, as well as on the sub-sample of outflows in star-forming galaxies only. Table 3.2 shows the Spearman rank correlation coefficients, p-value, and the best-fit slope in the case of a p-value $< 5\%$.

Both the mass outflow rate and energy outflow rate are significantly correlated with the AGN bolometric luminosity, with p-values of 0.05% and 0.006%, respectively. The best-fit relations are $\dot{M}_{\rm out} \propto L_{\rm AGN}^{1.34\pm0.37}$ and $\dot{E}_{\rm out} \propto L_{\rm AGN}^{1.87\pm0.51}$. The typical value of $\dot{E}_{\rm out}$ is between $0.01-1\%$ of $L_{\rm AGN}$, with a median of 0.1%. Such kinetic coupling efficiencies are similar to those in low redshift studies (Harrison et al. 2018, and references therein). The log-linear slope of $\dot{E}_{\rm out}$ versus $L_{\rm AGN}$ is > 1, meaning outflows in higher luminosity AGNs have a higher kinetic coupling efficiency. This finding is consistent with that of Fiore et al. (2017), who find a somewhat lower but greater than unity log-normal slope of 1.29 ± 0.38 in ionized outflows in AGNs. The similarity of the kinetic coupling efficiency with that at low redshift and the luminosity dependence of $\dot{E}_{\rm out}$ suggest that outflows can be more energetic at $z \sim 2$, where luminous AGNs are more prevalent. The marginally steeper dependence of $\dot{E}_{\rm out}$ on $L_{\rm AGN}$ may hint that the efficiency of very luminous AGNs in driving outflows are slightly enhanced at $z \sim 2$. Outflows in both star-forming and quiescent galaxies follow the same trend with $L_{\rm AGN}$. This shows that at a given $L_{\rm AGN}$ outflows are not significantly more powerful in either quiescent or star-forming galaxies.

There is no significant correlation between mass or energy outflow rate and stellar mass for the full sample, which includes both star-forming and quiescent galaxies. However, in the sub-sample of star-forming galaxies only, there is a marginally significant negative correlation between $\dot{M}_{\rm out}$ and M_* with a p-value of 1.57%. We note that this correlation could potentially be driven by two outlying points with the highest and lowest mass outflow rates. If we remove those two points, we obtain a weak negative correlation with a p-value of 6.4%. There is also a negative correlation between $\dot{E}_{\rm out}$ and M_* with a p-value of 1.0%. The best-fit relations for star-forming galaxies are $\dot{M}_{\rm out} \propto M_*^{-0.97\pm0.41}$ and $\dot{E}_{\rm out} \propto M_*^{-1.34\pm0.56}$. If these two correlations are robust, the negative slope indicates that along the star-forming main sequence, higher mass galaxies produce less powerful AGN outflows. On the other hand, this trend is not observed in quiescent galaxies, where higher mass galaxies appear to have more powerful outflows at a given stellar mass. However, the small number of outflows in quiescent galaxies in our sample prevents the detection of any potential correlations. This correlation could imply that at higher stellar masses ($M_* > 10^{10.5}\,{\rm M}_\odot$), quiescent galaxies host more powerful AGN-driven outflows than star-forming galaxies. There is no significant correlation between the outflow rates and SFR of the host galaxy.

Table 3.2: Correlations of Outflow Parameters with AGN and Host Galaxy Properties

	Star-forming and quiescent galaxies			Star-forming galaxies only		
Correlation	Spearman rank	p-value	Slope	Spearman rank	p-value	Slope
$\dot{M}_{\rm out}$ vs $L_{\rm AGN}$	0.666	0.053 %	1.34 ± 0.37	0.703	0.17 %	1.26 ± 0.38
$\dot{E}_{\rm out}$ vs $L_{\rm AGN}$	0.735	0.006 %	1.87 ± 0.51	0.765	0.034 %	1.78 ± 0.50
$\dot{M}_{\rm out}$ vs M_*	-0.217	32 %	-	-0.575	1.57 %	-0.97 ± 0.41
$\dot{E}_{\rm out}$ vs M_*	-0.242	27 %	-	-0.606	1.00 %	-1.34 ± 0.56
$\dot{M}_{\rm out}$ vs SFR	-0.303	16 %	-	-0.070	79 %	-
$\dot{E}_{\rm out}$ vs SFR	-0.236	28 %	-	0.025	93 %	-
η vs $L_{\rm AGN}$	0.655	0.070 %	1.83 ± 0.94	0.658	0.41 %	1.46 ± 0.55
η vs M_*	-0.067	76 %	-	-0.514	3.5 %	-1.08 ± 0.51
η vs SFR	-0.723	0.010 %	-1.35 ± 0.21	-0.499	4.1 %	-1.09 ± 0.70
$\widetilde{\eta}$ vs $L_{\rm AGN}$	0.641	0.10 %	1.89 ± 0.50	0.690	0.22 %	1.93 ± 0.60
$\widetilde{\eta}$ vs M_*	-0.507	1.35 %	-1.19 ± 0.46	-0.798	0.012 %	-1.84 ± 0.44
$\widetilde{\eta}$ vs SFR	-0.173	43 %	-	-0.075	78 %	-

3.6.3 Physical Driver of the Outflows

Our measurements of mass and energy outflow rates allow us to constrain the physical drivers of these outflows. For example, the ratio of $\dot{E}_{\rm out}/L_{\rm AGN}$ compares the kinetic energy carried by the outflows to the bolometric luminosity of the AGN. For all of the outflows in our sample, $\dot{E}_{\rm out}$ is less than 100% of $L_{\rm AGN}$, while most are between $0.01-1\%$ of $L_{\rm AGN}$, meaning that the AGN is energetically sufficient to drive these outflows.

On the other hand, another possible driver of galactic outflows is stellar feedback. Hopkins et al. (2012) estimate a mass loss rate in outflows driven by stellar feedback as a function of SFR given by

$$\dot{M}_{\rm stellar,max} = 3\,{\rm M}_\odot\ {\rm yr}^{-1}\left(\frac{\rm SFR}{{\rm M}_\odot\ {\rm yr}^{-1}}\right)^{0.7}. \tag{3.15}$$

This mass loss rate includes not only direct mass loss from supernovae and stellar winds but also the subsequent entrainment of the interstellar medium. Moreover, it includes all material that is being ejected out of the galaxy, in all phases, locations, and directions, which will generally be larger than what is directly observed. Therefore it can be considered as an upper limit on the observed mass outflow rates that could be due to stellar feedback alone. This maximum mass loss rate as a function of SFR is shown in the upper right panel of Figure 3.9 in the gray dashed line.

Nine of the outflows have mass outflow rates exceeding the predicted maximum mass loss rate from stellar feedback, meaning that stellar feedback is decidedly insufficient to drive these ten outflows. Moreover, it should be noted that the observed $\dot{M}_{\rm out}$ here only includes ionized outflows, while $\dot{M}_{\rm stellar,max}$ accounts for mass loss in all phases, such that more sources could potentially have a total mass loss rate greater than $\dot{M}_{\rm stellar,max}$. In particular, the molecular gas mass can easily be an order of magnitude greater than the ionized gas mass in AGN outflows (e.g. Herrera-Camus et al. 2019). 17 of the 22 outflows have mass outflow rates exceeding 10% of the expected maximum mass-loss rate from stellar feedback. Assuming ionized gas makes up 10% of the total outflowing mass, the majority of the outflows in our sample cannot be driven by stellar

feedback. Combined with the fact that the kinetic power of all the outflows is less than $L_{\rm AGN}$, the outflows lie in the AGN region in the BPT diagram, and the seven-fold increase in outflow incidence among AGNs relative to inactive galaxies, AGN are the likely drivers of the outflows in our sample.

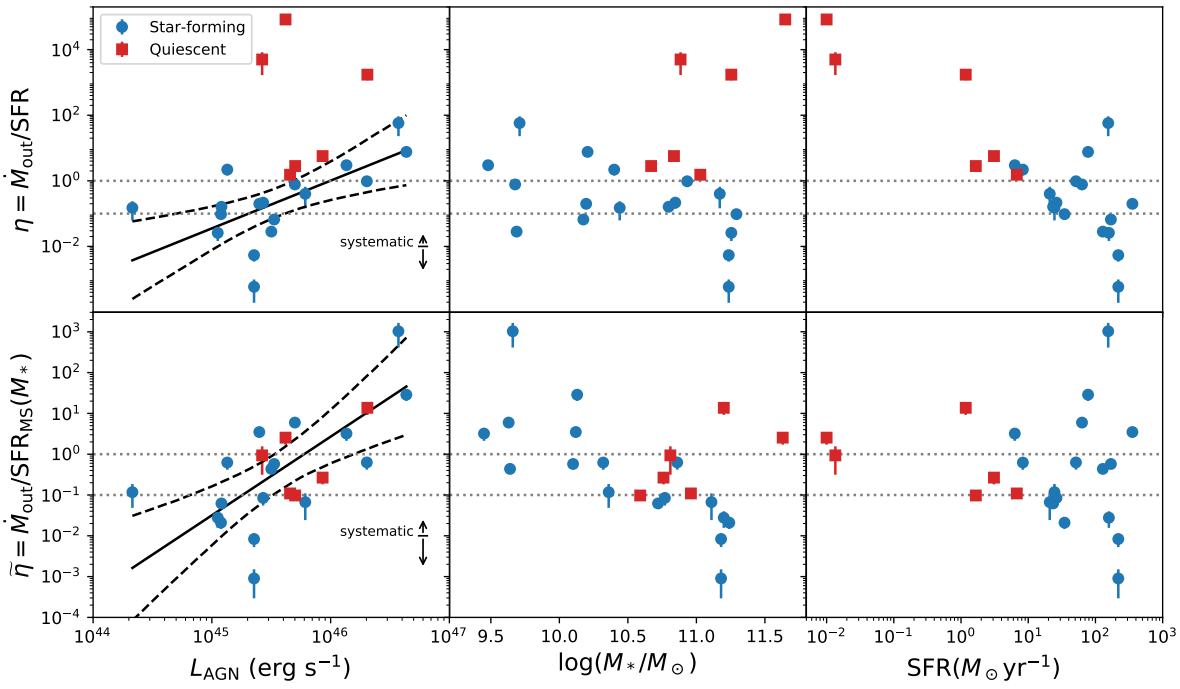

Figure 3.10: Top: Mass-loading factors of the outflows versus $L_{\rm AGN}$ (left), M_* (middle), and SFR (right). Star-forming galaxies are shown in blue points while quiescent galaxies are shown in red points. Bottom: Same as the top panel but for a re-scaled mass-loading factor $\widetilde{\eta} = \dot{M}_{\rm out}/{\rm SFR}_{\rm MS}$, which represents the mass-loading factor of the outflow if the galaxy is on the star-forming main sequence. The dotted lines show mass-loading factors of unity and 0.1. The mass-loading factors are greater than 0.1 for most of the outflows. If 10% of the outflowing mass is ionized, these outflows would have significant impact on the star formation of the host galaxy. The re-scaled mass-loading factor of quiescent galaxies are $\gtrsim 0.1$, showing that the current outflows would be sufficient to regulate the past SFR of the host galaxy.

3.6.4 Mass Loading Factor

To quantify the potential impact of the outflows in the context of their host galaxies, it is common to calculate the mass-loading factor of the outflows, defined as $\eta = \dot{M}_{\rm out}/{\rm SFR}$. The

mass-loading factors of outflows in our sample span a wide range from $\sim 10^{-3} - 10^{5}$, with a median of 0.8. Outflows residing in quiescent galaxies have systematically elevated mass-loading factors due to their very small SFRs and the fact that η is defined as $\dot{M}_{\rm out}/{\rm SFR}$. Among the outflows in star-forming galaxies, the maximum mass-loading factor is ~ 50, and the median is ≈ 0.2.

Figure 3.10 (upper panel) shows the mass-loading factors of the outflows versus $L_{\rm AGN}$, M_*, and SFR. A strong correlation is observed in η versus $L_{\rm AGN}$ with a p-value of 0.07% for all galaxies and 0.41% for star-forming galaxies only. While the mass-loading factor in star-forming galaxies follows a tight correlation with $\eta \propto L_{\rm AGN}^{1.46\pm0.55}$, the values in quiescent galaxies deviate systematically upward of this trend, and the best-fit relation for quiescent and star-forming galaxies combined is $\eta \propto L_{\rm AGN}^{1.83\pm0.94}$. This is due to the systematically lower SFR of quiescent galaxies which elevate their mass-loading factors. In star-forming galaxies, the mass-loading factor reveals the impact of the outflows on the host galaxy while it is still in the process of forming stars, and can therefore provide information on whether the outflow can quench or regulate star formation. However, in quiescent galaxies the mass-loading factor reveals the impact of the outflows after star formation in the host galaxies has been quenched, and therefore can only indicate whether the outflow can keep the host galaxy quenched. Therefore, the correlation observed in star-forming galaxies alone is more relevant to the potential role of the outflows in the initial quenching of star formation in the host galaxy.

There is a weak negative correlation in star-forming galaxies between η and M_*, with a p-value of 3.5%. The best-fit relation is $\eta \propto M_*^{-1.08\pm0.51}$. There is no correlation between η and M_* when combining star-forming and quiescent galaxies. This is similar to the trend observed between $\dot{M}_{\rm out}$ and M_*. However, the correlation in η is less significant, and the slope is somewhat lower, though it is within the 1σ uncertainty of the slope with $\dot{M}_{\rm out}$. Fiore et al. (2017) also find a weak negative correlation between the mass-loading factor and stellar mass in outflows in their sample.

A strong artifact is observed in the plot of η and SFR, as η is proportional to $1/\mathrm{SFR}$ by definition. This artifact makes it apparent that η is heavily affected by the SFR of the host galaxy, and any interpretation of correlations between η and other quantities must take into account any potential underlying correlation with SFR. In particular, this makes it clear that star-forming and quiescent galaxies should generally be separated in such analyses, which is not often done. Figure 3.11 shows the distribution of L_{AGN} versus M_* and SFR for our outflow sample. We do not observe any correlations between L_{AGN} and either M_* or SFR. There is also no correlation between M_* and SFR among the outflow host galaxies in our sample (see Figure 3.4). Therefore, the correlations between η and L_{AGN} and M_* are not driven by underlying correlations with SFR.

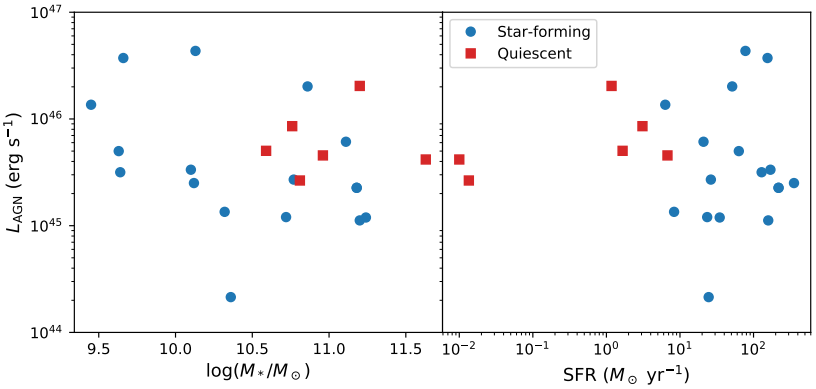

Figure 3.11: Left: AGN bolometric luminosity versus stellar mass. Right: AGN bolometric lumiosity versus SFR. Outflows in star-forming galaxies are shown in blue points, while outflows in quiescent galaxies are shown in red points. There is no significant correlation between L_{AGN} and M_* or SFR in our outflow sample.

For quiescent galaxies, the mass-loading factor is relevant for understanding whether the outflow might keep star formation quenched, but it does not indicate whether the outflows could have initially quenched star formation, since it compares the mass outflow rate with the SFR after quenching has already occurred. To answer the question of whether these outflows could have quenched the star formation initially in these galaxies, it is informative to compare the outflow rate with an approximate past SFR of the host galaxy while it was still forming stars at a high rate. To do this we use the stellar mass of the galaxy and the corresponding SFR of the star-forming

main sequence. We define a re-scaled mass-loading factor $\widetilde{\eta}$ as $\dot{M}_{\rm out}/{\rm SFR}_{\rm MS}$, where ${\rm SFR}_{\rm MS}$ is the SFR the galaxy would have if it was on the star-forming main sequence, given the current stellar mass of the galaxy. This effectively compares the outflow rate with the stellar mass of the host galaxy instead of the current SFR. Such a definition can also eliminate the artifact between η and SFR mentioned above. The lower panel of Figure 3.10 shows the re-scaled mass-loading factor versus $L_{\rm AGN}$, M_*, and SFR.

The re-scaled mass-loading factors are no longer elevated for quiescent galaxies. The re-scaled mass-loading factor is above 0.1 for the majority of the outflows, and has a median of 0.4. The values of $\widetilde{\eta}$ of quiescent galaxies fall along the main trend observed for star-forming galaxies. A correlation between the re-scaled mass-loading factor and AGN luminosity is observed at a p-value of 0.10% for all galaxies and 0.22% for star-forming galaxies only. An analysis combining star-forming and quiescent galaxies yields a best-fit relation of $\widetilde{\eta} \propto L_{\rm AGN}^{1.89\pm0.50}$, consistent with that of star-forming galaxies only, which follows a power of 1.93 ± 0.60.

The artificial correlation between η and SFR is eliminated with the re-scaled definition of $\widetilde{\eta}$. However, this introduces another artificial negative correlation between $\widetilde{\eta}$ and M_*, as the re-scaled mass-loading factor is proportional to the inverse of ${\rm SFR}_{\rm MS}$, which is proportional to M_* by definition. This highlights that extra caution is necessary when interpreting correlations between mass-loading factors and host galaxy properties.

On the other hand, the correlation between mass-loading factor and $L_{\rm AGN}$ is significant both in the standard definition (η) in star-forming galaxies and in the re-scaled definition ($\widetilde{\eta}$) in star-forming and quiescent galaxies. This indicates that the correlation between mass-loading factor and $L_{\rm AGN}$ is a truly physical correlation and is not due to systematic effects. More luminous AGN therefore drive outflows that have greater potential to impact their host galaxy.

The mass-loading factors in ionized gas are greater than 0.1 for 11 out of 17 of the outflows in star forming galaxies. Studies of AGN-driven molecular outflows show that the mass outflow rate in the molecular phase can be comparable to or an order of magnitude greater than that in

the ionized phase in $z \sim 2$ (Vayner et al. 2017; Brusa et al. 2018; Herrera-Camus et al. 2019) AGNs. If 10% of the outflowing mass is ionized, the combined ionized and molecular outflows in these systems would have significant impact on the star formation of the host galaxy. The mass loading factor in star-forming galaxies is positively correlated with $L_{\rm AGN}$, and is capable of exceeding unity at $L_{\rm AGN} \gtrsim 10^{46}$ erg s^{-1}. This shows that more luminous AGNs drive more powerful outflows that have higher impact to the host star-forming galaxy. For outflows in quiescent galaxies, the re-scaled mass loading factor is greater than 0.1 in four out of six detected ionized outflows. This shows that the current outflows in these quiescent galaxies would likely have been sufficient to regulate the past SFR of the host galaxy. Moreover, the current outflows in these quiescent galaxies have mass-loading factor greater than unity, implying that they are capable of keeping star formation quenched in these galaxies. We note that some caution should be exercised when interpreting the impacts of these outflows, considering systematic uncertainties in the outflow rates as discussed above.

3.6.5 Momentum Flux

The momentum flux carried by the outflows can provide useful information for models of AGN-driven winds. Two common models of large-scale AGN-driven winds are momentum-conserving winds driven by radiation pressure on dust (e.g. Thompson et al. 2015; Costa et al. 2018) and energy-conserving winds driven by fast, small-scale winds (e.g. Faucher-Giguère & Quataert 2012; Costa et al. 2014). According to the radiation pressure-driven models, the momentum flux of the outflows is given by

$$\dot{P}_{\rm out} = \tau_{\rm IR} \frac{L_{\rm AGN}}{c}, \tag{3.16}$$

where $\tau_{\rm IR}$ is the optical depth in IR. For energy-driven models, the fast, small-scale winds transport a momentum comparable to $L_{\rm AGN}/c$, and do work to the surrounding material, increasing the

momentum of the large-scale wind. Assuming half of the kinetic energy of the small-scale wind is transferred to the large-scale wind (Faucher-Giguère & Quataert 2012),

$$\frac{\dot{P}_{\rm out}}{\dot{P}_{\rm in}} \approx \frac{1}{2}\frac{v_{\rm in}}{v_{\rm out}}, \tag{3.17}$$

and thus

$$\dot{P}_{\rm out} \approx \frac{1}{2}\frac{v_{\rm in}}{v_{\rm out}}\frac{L_{\rm AGN}}{c}, \tag{3.18}$$

where $\dot{P}_{\rm in} = L_{\rm AGN}/c$ and $v_{\rm in}$ are the momentum flux and velocity of the small-scale wind, respectively, and $v_{\rm out}$ is the velocity of large-scale wind constituted by the swept up material.

In Figure 3.12 we show the ratio of $\dot{P}_{\rm out}$ to $L_{\rm AGN}/c$ versus $v_{\rm max}$. We also show the expected momentum flux ratio for a momentum conserving radiation pressure-driven wind model with $\tau_{\rm IR} = 1$ and for an energy conserving wind model for $v_{\rm in} = 0.03c, 0.1c$, and $0.3c$. These velocities are comparable to those observed in the ultrafast outflows in X-rays reported in Fiore et al. (2017). The typical observed momentum ratios of the outflows are between 0.1 and 10. About 40% of the outflows have momentum ratios above unity, meaning that either an IR optical depth higher than unity is needed for a momentum-conserving wind, or a momentum boost from an energy-conserving wind is required. Three outflows have momentum ratios within the prediction of an energy-conserving wind with $v_{\rm in}$ between $0.01c$ and $0.3c$. This shows that for these outflows, they can be driven by small-scale winds similar to typical X-ray ultrafast outflows. However, the majority of outflows lie below the predicted momentum ratio by energy-conserving winds, such that either these outflows are not strictly energy conserving or some momentum is carried by outflows in other phases, since only ionized outflows are probed here.

Two outflows have momentum ratios higher than the prediction for $v_{\rm in} = 0.3c$. It should be noted that, as $v_{\rm max}$ is used to estimate the 3-dimensional velocity of the outflows from the measured 1-dimensional velocity in general, it may not be strictly accurate for every outflow depending on the actual outflow geometry in each source. Moreover, when calculating outflow

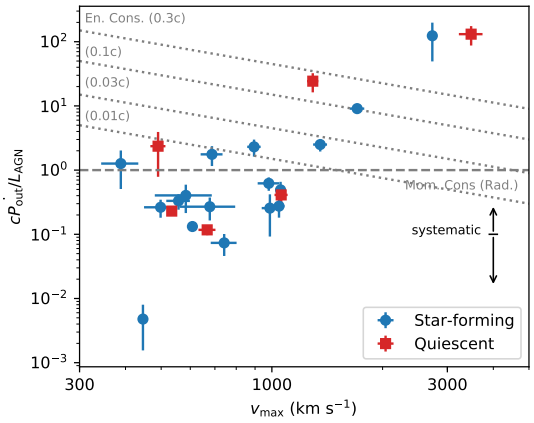

Figure 3.12: The ratio of the momentum flux carried by the outflows to that produced by the radiation of the AGN versus $v_{\rm max}$. Star-forming galaxies are shown in blue while quiescent galaxies are shown in red. The horizontal dashed line shows the predicted momentum ratio for a momentum-conserving wind driven by radiation pressure on dust, with an IR optical depth of unity. The dotted lines show the predicted momentum ratios for an energy-conserving wind driven by a fast, small scale wind with $v_{\rm in} = 0.01c, 0.03c, 0.1c$, and $0.3c$.

rates, a single electron density of $n_e = 150$ cm s^{-1} is assumed for all the outflows in our sample as an average, but the values of n_e in individual sources can vary. For these two outflows, they possibly have smaller actual velocity than $v_{\rm max}$ and/or higher actual electron density than the assumed average, which can lead to overestimation of the momentum ratios and velocities seen in this diagram.

3.7 Conclusions

We use data from the complete MOSDEF survey to analyze the rest-frame optical spectra of a sample of 159 X-ray, IR and/or optical AGNs at $1.4 < z < 3.8$. This dataset triples the previous MOSDEF sample size in Leung et al. (2017) and is the largest uniform sample of AGNs for outflow studies with coverage of multiple important rest-frame optical emission lines at this redshift to date. The AGNs in our sample have bolometric luminosities of 10^{44-47} erg s^{-1} and reside in both quiescent galaxies and star-forming galaxies along and across the star-forming main

sequence, with stellar masses of $10^{9-11.7}\,M_{\odot}$. We identify outflows from additional, typically broadened, kinematic components in the Hβ, [OIII], Hα and [N II] emission line profiles beyond the narrow-line component. Our main findings are as follows:

1. We detect ionized outflows at S/N > 3 in 17% of the 159 AGNs. By contrast, using the same analysis procedures, ionized outflows are detected in emission in only 2.5% out of a mass-matched sample of 1179 inactive MOSDEF galaxies. The ~ 7 times higher incidence of outflows in AGNs strongly suggests that these outflows are AGN-driven. (§3.4.1, §3.4.2)

2. The typical velocity of the outflows is ≈ 940 km s^{-1}, ranging from $400 - 3500$ km s^{-1}. 22 out of the 31 detected outflows are significantly spatially extended, with sizes extending $0.3 - 11.0$ kpc, with a median of 4.5 kpc. These are therefore fast, galaxy-wide outflows. (§3.4.3, §3.4.5)

3. In the BPT diagram, the line ratios of the outflowing gas are shifted towards the AGN region compared to the narrow-line region gas. The [N II]/Hα line ratios of the outflowing gas are not correlated with the velocity dispersion, showing no evidence of shock excitation. The outflowing gas is consistent with being photoionized by the AGN. (§3.4.4)

4. The incidence of outflows is largely uniform in stellar mass and SFR of the host galaxy. While the incidence of outflows *among all galaxies* increases with stellar mass, the incidence of outflows *among detected AGNs* remains constant in stellar mass. The former trend increases at a rate similar to the increasing incidence of AGNs with stellar mass and likely results from the known selection bias of AGNs with stellar mass. The true incidence of outflows is constant with respect to stellar mass. Outflows are detected in both star-forming and quiescent galaxies, reflecting that they exist across different phases of galaxy evolution. (§3.5.1)

5. While the incidence of outflows increases with the [OIII] luminosity of the AGN, it also

increases with the S/N in the [OIII] emission line spectrum, as luminosity and S/N are highly correlated. At a given S/N, there is no difference in the distribution of the offset from the mean $L_{[\mathrm{OIII}]}$ between AGNs with and without outflows. (§3.5.2)

6. The outflow velocity is correlated with $L_{[\mathrm{OIII}]}$, following a power law with $v_{\mathrm{max}} \propto L_{[\mathrm{OIII}]}^{0.27\pm0.09}$, consistent with theoretical models of an energy-conserving outflow. No significant correlation is observed between the outflow size and $L_{[\mathrm{OIII}]}$. As our sample spans $L_{[\mathrm{OIII}]} > 10^{42}$ erg s^{-1}, our results support the existence of an upper limit in outflow size of $\sim 5-10$ kpc above this luminosity. The outflow velocity is inversely correlated with the outflow size. This is consistent with an energy-conserving solution of an expanding outflow, while the momentum-conserving solution underestimates the observed velocities. (§3.6.1)

7. The mass outflow rate and kinetic power of the outflow are positively correlated with L_{AGN}. The kinetic coupling efficiency of the outflow ($\dot{E}_{\mathrm{out}}/L_{\mathrm{AGN}}$) is typically $0.01-1\%$. The luminosity dependence of $\dot{E}_{\mathrm{out}}$ and the similarity of the kinetic coupling efficiency with that at low redshift suggest that outflows can be more energetic at $z \sim 2$, where luminous AGNs are more prevalent. The AGN are energetically sufficient to drive these outflows, while stellar feedback is insufficient. This suggests that these outflows are very likely AGN driven. There is a weak anti-correlation between mass outflow rate and stellar mass for outflows in star-forming galaxies, while the mass outflow rate in quiescent galaxies deviates upwards of this trend. This suggests that at a given stellar mass, outflows in quiescent galaxies are more powerful than those in star-forming galaxies. (§3.6.2, §3.6.3)

8. The mass-loading factor of the outflows is typically between $0.1-1$ and is positively correlated with L_{AGN} *in star-forming galaxies*. This shows that more luminous AGNs drive more powerful outflows that have higher impact to the host star-forming galaxy, capable of producing mass-loading factors larger than unity at $L_{\mathrm{AGN}} \gtrsim 10^{46}$ erg s^{-1}. The mass-loading factor *in quiescent galaxies* is systematically elevated due to the very low SFR of the host

galaxy and can only show whether the outflow may keep the galaxy quenched, but does not indicate the potential role of the outflow in the initial quenching of star formation in the host galaxy. (§3.6.4)

9. The momentum flux of the outflows is typically between $0.1-10$ times the momentum flux output from the radiation pressure of the AGN. This ratio is greater than unity for about 40% of the outflows. For these sources, the outflow can be produced either by a momentum-boost from an energy-conserving wind with an initial velocity of $0.01-0.3c$ or large optical depths at IR wavelengths due to dust around the AGN. (§3.6.5)

Our results provide a census of AGN-driven ionized outflows in the galaxy population at $z\sim1-3$, but much remains to be understood. Key observational challenges remain in terms of determining the electron density of the outflows as well as a simultaneous characterization of the multi-phase content of the outflows. The electron density is crucial in the computation of the outflow rates, but the [S II] emission line ratio from which it is inferred is typically too weak to be significantly detected in outflows at $z\sim2$. The systematic uncertainty in electron density can change the measured outflow rates and mass-loading factors by a factor of a few. While we find that luminous AGNs are capable of producing ionized outflows with mass-loading factors above unity and can potentially bring substantial impact to the host galaxy, a large scatter exists in this trend and the mass-loading factor is modest in most sources. Combined with the uncertainty in electron density, it is unclear whether for the majority of the AGNs the ionized outflows alone are sufficient to quench or only regulate the star formation of the host galaxy. To account for the full impact of the outflows, it is necessary to characterize the multi-phase content of the outflows, including molecular and neutral gas. Only a few examples of molecular AGN outflows currently exist at $z\sim2$ (e.g. Vayner et al. 2017; Brusa et al. 2018; Herrera-Camus et al. 2019). Future progress will greatly benefit from high sensitivity observations of the ionized, neutral and molecular content of AGN-driven outflows in representative samples of galaxies at high redshift.

3.8 Acknowledgements

We thank D. S. Rupke for very useful discussions. We also thank the anonymous referee for helping to improve the paper. This work would not have been possible without the 3D-HST collaboration, who provided us with the spectroscopic and photometric catalogs used to select our targets and to derive stellar population parameters. We acknowledge support from NSF AAG grants AST-1312780, 1312547, 1312764, and 1313171, archival grant AR-13907 provided by NASA through the Space Telescope Science Institute, and grant NNX16AF54G from the NASA ADAP program. JA acknowledges support from an STFC Ernest Rutherford Fellowship, grant code: ST/P004172/1. The data presented herein were obtained at the W.M. Keck Observatory, which is operated as a scientific partnership among the California Institute of Technology, the University of California and the National Aeronautics and Space Administration. The Observatory was made possible by the generous financial support of the W.M. Keck Foundation. The authors wish to recognize and acknowledge the very significant cultural role and reverence that the summit of Mauna Kea has always had within the indigenous Hawaiian community. We are most fortunate to have the opportunity to conduct observations from this mountain.

Chapter 3, in full, is a reprint of the material as it appears in The Astrophysical Journal 2019. Leung, Gene C. K., Coil, A. L., Azadi, M., Aird, J., Shapley, A., Kriek, M., Mobasher, B., Reddy, N., Siana, B., Freeman, W. R., Price, S. H., Sanders, R. L., Shivaei, I. 2019. The dissertation author was the primary investigator and author of this paper.

3.9 Appendix

3.9.1 Emission Line Spectra and Tabulated Data

In this Appendix, we we provide the emission line spectra of the AGN with detected outflows and tabulated data of the AGN, host galaxy and outflow properties in our sample.

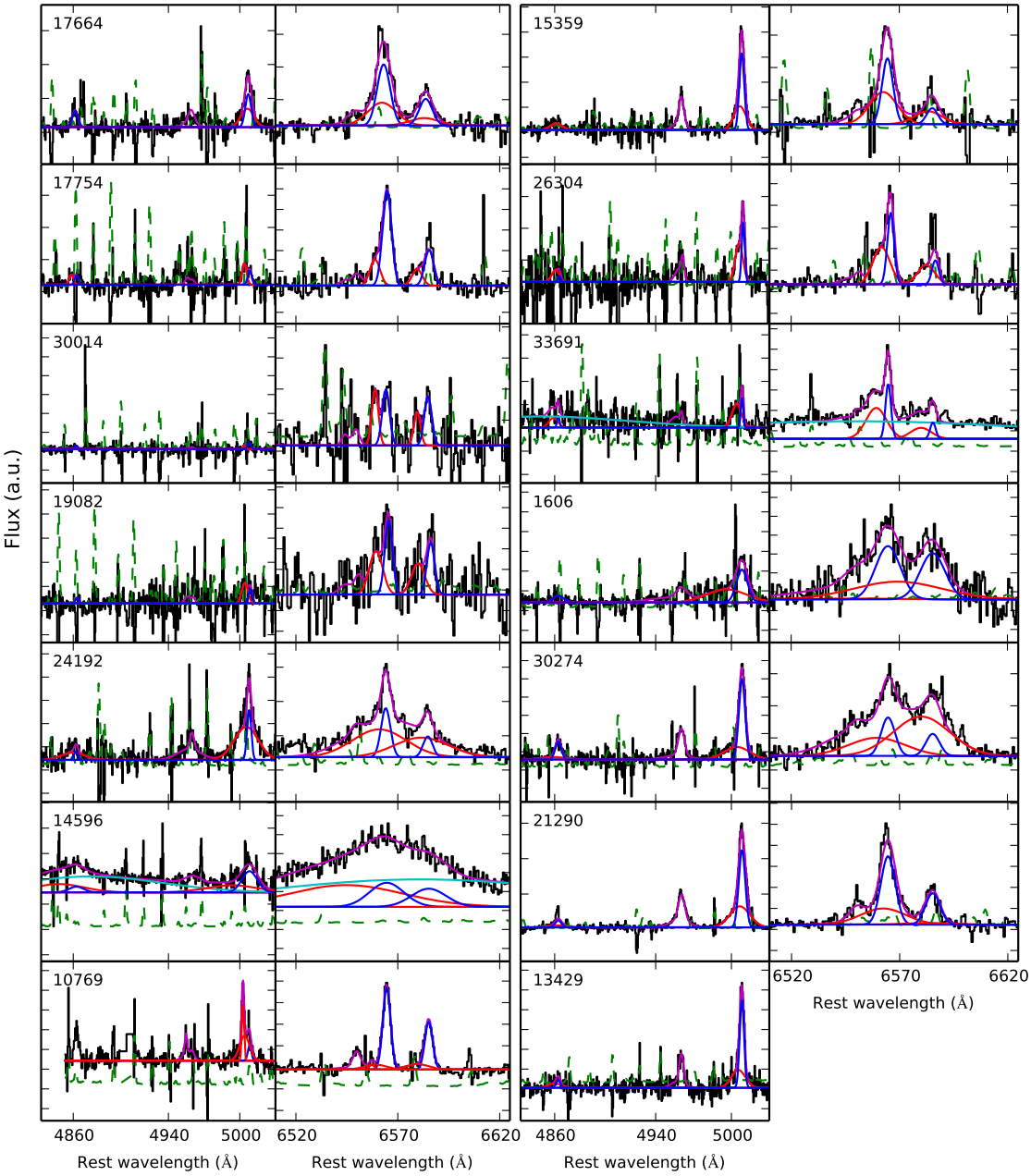

Figure 3.13: Emission line spectra of the AGN with outflows. For each source, the left panel shows the Hβ and [OIII] emission lines while the right panel shows the [N II] and Hα emission lines. The black line shows the observed spectrum and the green dotted line shows the error spectrum. The magenta line shows the best-fit model, while the blue and red lines shows the best-fit narrow-line and outflow components, respectively. Note that the wavelength ranges of the [OIII] and Hα panels are slightly different, so that the widths of the emission lines in the two panels may appear different.

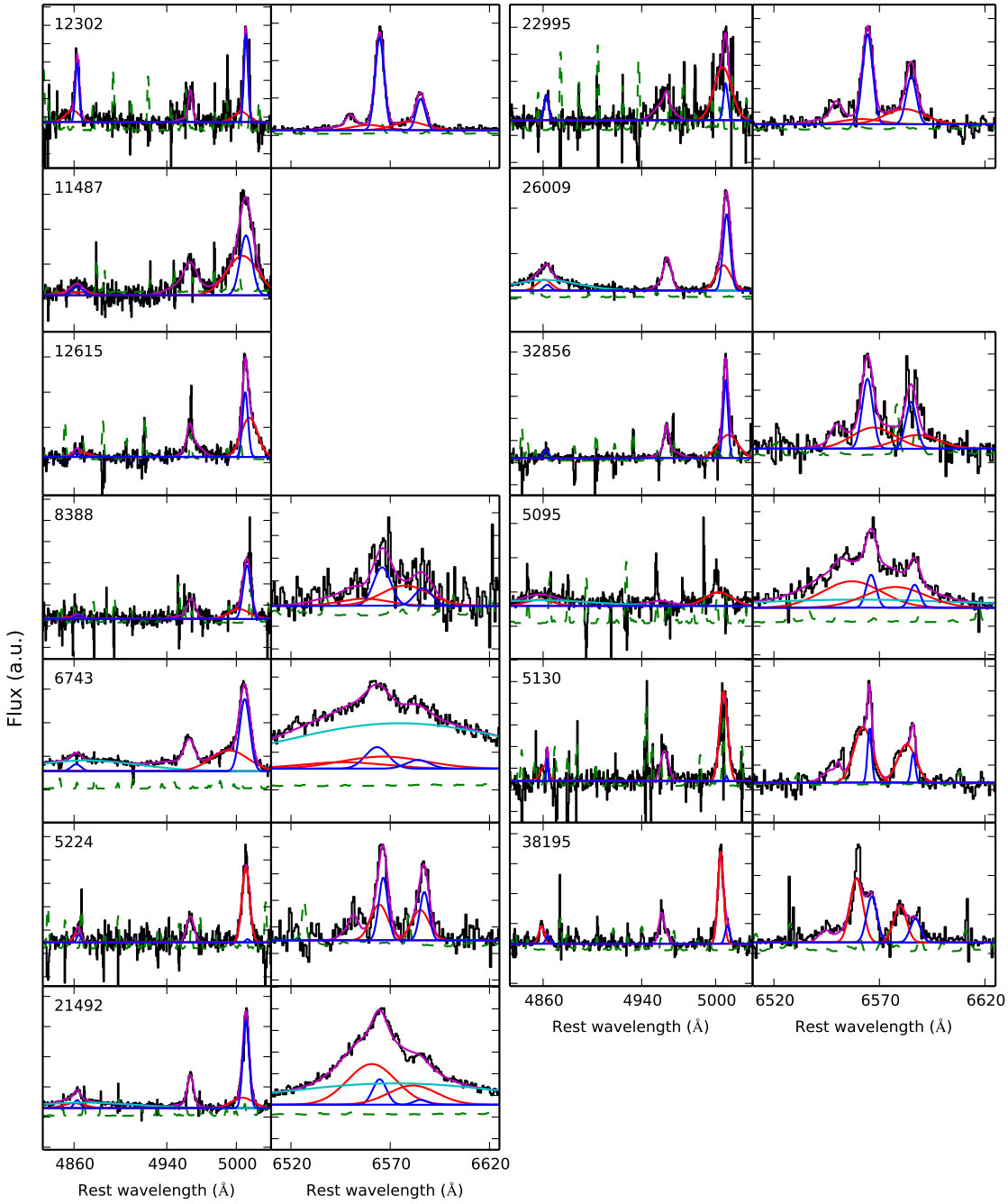

Figure 3.14: Continuation of Figure 3.13.

Table 3.3: AGN, Host Galaxy and Outflow Properties

ID[a]	z	$\log(L_{[OIII]})$ (erg s^{-1})	M_* ($M_\odot$)	SFR ($M_\odot$ yr^{-1})	v_{max} (km s^{-1})	$r_{10,[OIII]}$ (kpc)	$\dot{M}$ ($M_\odot$ yr^{-1})	$\dot{E}$ (erg s^{-1})
1606	2.475	43.04	10.77	105	-2605 ±194	1.66 ±1.33	7.1 ±54.7	$(1.5\pm11.7)\times10^{43}$
5095	2.295	42.62	10.12	355	-1706 ±78	2 ±0.88	60.9 ±7.6	$(5.6\pm1.0)\times10^{43}$
5130	2.377	42.88	10.96	7	-534 ±11	2.02 ±1.74	8.8 ±0.6	$(7.9\pm0.7)\times10^{41}$
5224	2.151	42.65	10.81	<1	-490 ±23	0.28 ±0.17	62.9 ±41.8	$(4.8\pm3.2)\times10^{42}$
6743	2.487	43.79	9.66	155	-2731 ±46	0.06 ±0.03	8050.4 ±4839.2	$(1.9\pm1.1)\times10^{46}$
8388	2.198	42.74	11.03	<1	-1513 ±161	0.05 ±0.34	55.8 ±60.1	$(4.0\pm4.5)\times10^{43}$
10769-1	2.103	42.58	11.18	219	-742 ±60	8.83 ±0.89	1.2 ±0.4	$(2.1\pm0.9)\times10^{41}$
10769-2	2.103	42.58	11.18	219	-446 ±11	11 ±0.3	0.1 ±0.1	$(8.1\pm5.5)\times10^{39}$
11487	3.408	43.62	10.36	6	-1807 ±141	0.09 ±0.1	1973.1 ±2423.2	$(2.0\pm2.5)\times10^{45}$
12302	2.276	42.75	10.10	170	-981 ±66	0.99 ±0.37	11.0 ±2.5	$(3.3\pm1.0)\times10^{42}$
12615	3.179	43.53	10.86	51	1056 ±35	4.5 ±0.37	26.9 ±9.0	$(9.5\pm3.3)\times10^{42}$
13429	3.475	43.36	10.80	87	-816 ±135	0.97 ±2.58	78.5 ±212.6	$(1.6\pm4.5)\times10^{43}$
14596	2.447	42.84	11.63	<1	-3481 ±257	1.34 ±0.36	768.8 ±251.0	$(2.9\pm1.1)\times10^{45}$
15359	1.594	42.92	10.59	2	-667 ±35	4.58 ±0.47	4.4 ±0.7	$(6.2\pm1.4)\times10^{41}$
17664	2.187	42.65	10.77	26	-678 ±117	5.57 ±1.67	5.4 ±1.9	$(7.9\pm4.7)\times10^{41}$
17754	2.297	42.30	11.24	35	-498 ±49	2.63 ±4.71	3.2 ±1.0	$(2.5\pm1.0)\times10^{41}$
19082	2.487	42.27	11.20	158	-583 ±103	9.21 ±4.14	3.6 ±1.6	$(3.8\pm2.5)\times10^{41}$
21290	2.215	43.36	9.45	6	-1046 ±36	3.02 ±0.91	18.4 ±6.2	$(6.4\pm2.2)\times10^{42}$
21492	2.472	43.53	11.20	1	-1292 ±45	0.31 ±0.1	1805.5 ±593.1	$(9.5\pm3.3)\times10^{44}$
22995	2.468	43.01	11.11	21	-988 ±49	2.45 ±1.06	7.9 ±5.0	$(2.4\pm1.6)\times10^{42}$
24192	2.243	42.92	9.63	63	-1353 ±59	2.22 ±1.16	44.4 ±9.6	$(2.6\pm0.6)\times10^{43}$
26009	3.434	43.86	10.13	78	-894 ±38	1.35 ±0.35	361.3 ±106.0	$(9.1\pm2.9)\times10^{43}$
26304	1.632	42.30	10.72	23	-557 ±41	0.53 ±0.47	3.7 ±1.0	$(3.6\pm1.2)\times10^{41}$
30014	2.291	41.55	10.36	25	-388 ±45	1.89 ±1.32	3.4 ±2.0	$(1.6\pm1.1)\times10^{41}$
30274	2.225	43.19	10.47	355	-1432 ±68	1.77 ±3.3	81.8 ±152.8	$(5.3\pm9.9)\times10^{43}$
32856	2.270	43.15	10.76	3	1060 ±43	2.83 ±0.8	16.2 ±5.1	$(5.7\pm1.9)\times10^{42}$
33691	2.243	42.35	10.32	8	-687 ±47	4.38 ±2.3	15.5 ±5.2	$(2.3\pm0.9)\times10^{42}$
38195	1.487	42.72	9.64	129	-608 ±9	8.67 ±0.44	3.4 ±0.2	$(4.0\pm0.3)\times10^{41}$

[a] 3D-HST v4 catalog ID.

Chapter 4

KCWI observations of the extended nebulae in Mrk 273

4.1 Abstract

Ultraluminous infrared galaxies (ULIRGs) represent a critical stage in the merger-driven evolution of galaxies when AGN activity is common and AGN feedback is expected. We present high sensitivity and large field of view intergral field spectroscopy of the ULIRG Mrk 273 using new data from the Keck Cosmic Web Imager (KWCI). The KCWI data captures the complex nuclear region and the two extended nebulae in the northeast (NE) and southwest (SW) to ~ 20 kpc. Kinematics in the nuclear region show that the previously reported nuclear superbubbles extend to ~ 5 kpc, two to three times greater than the previously reported size. The larger scale extended nebulae show fairly uniform kinematics with FWHM ~ 300 km s^{-1} in the SW nebula and FWHM ~ 120 km s^{-1} in the NE nebula. We detect for the first time high ionization [NeV]3426, [OIII]4363 and HeII4684 emission lines in the extended NE nebula. Emission line ratios in the nuclear region correlate with the kinematic structures, with the superbubbles and the less collimated outflow regions showing distinct line ratio trends. Line ratio diagnostics of high

ionization emission lines reveal significant contribution from shock plus precursor ionization in the NE nebula and the nuclear region, mixed with AGN photoionization. We compare our data with theoretical models where kinematically quiescent extended cold gas filaments can form out of the warm phase of an AGN-driven outflow.

4.2 Introduction

A critical unresolved problem in galaxy formation is the co-evolution of supermassive black holes (SMBHs) and their host galaxies. Theoretical models of galaxy formation invoke feedback from active galactic nuclei (AGNs), by means of launching fast gas outflows, to quench star formation in the host galaxy and produce various observed galaxy properties (e.g. Di Matteo et al. 2005; Croton et al. 2006; Hopkins et al. 2006; Kaviraj et al. 2017; Pillepich et al. 2018). In many evolutionary scenarios of galaxies and SMBHs, AGNs represent a key stage following a galaxy merger in an evolutionary sequence (e.g Sanders et al. 1988). In such scenarios, a major merger event triggers a rapid episode of accretion onto the central region of the galaxy, fueling a burst of star formation activity and a dust-obscured AGN. The AGN then drives outflows that couple with the surrounding interstellar medium and eventually removes the obscuring gas and dust in a "blowout", exposing the nucleus resulting in a luminous quasar. These outflows are predicted to be the most powerful in the final stages of the merger, and are potentially sufficient to quench star formation in the environment (e.g Debuhr et al. 2012).

Ultra-luminous infrared galaxies (ULIRGs) are characterized by their extreme far-infrared luminosities exceeding $10^{12} L_{\odot}$, which is believed to originate from dust heated by a starburst and/or AGN in the center of the galaxy (e.g Sanders et al. 1988). Moreover, morphological features consistent with major merging events, such as tidal tails or double nuclei, are almost ubiquitous among ULIRGs (e.g Kim et al. 2002; Veilleux et al. 2002). Therefore, ULIRGs represent a population of galaxies at a critical evolutionary stage when the "blowout" is in action,

and AGN-driven outflows are likely to be powerful. As such, ULIRGs provide an ideal laboratory to observationally test this evolutionary picture, and, in particular, to understand the role of AGN-driven outflows in the evolution of galaxies.

AGN-driven outflows are known to be prevalent in ULIRGs in the ionized (e.g. Harrison et al. 2012; Rodríguez Zaurín et al. 2013; Rupke & Veilleux 2013a, hereafter RV13), molecular (e.g Veilleux et al. 2013; Cicone et al. 2012, 2014; Rupke & Veilleux 2013c; González-Alfonso et al. 2017; Herrera-Camus et al. 2020) and neutral (Rupke & Veilleux 2011, RV13) phases. The physical extent of the outflow is key to quantifying the impact of AGN-driven outflows in ULIRGs, as outflows extending to scales comparable to the size of the galaxy can have substantial impact on the star formation of the host galaxy, and the physical extent is required to determine the mass and energy outflow rate. The physical extent of outflows remains uncertain despite their prevalence. For ionized outflows, integral field unit (IFU) observations in the local Universe have revealed kiloparsec-scale outflows in ULIRGs extending $\sim 2-5$ kpc (e.g. Rupke & Veilleux 2011; RV13), while at high redshift ($z \sim 2$), galaxy-wide outflows in ULIRGs have been observed to reach $\sim 4-14$ kpc (e.g Alexander et al. 2010; Harrison et al. 2012). In contrast, recent long-slit and/or imaging studies of local ULIRGs have revealed more compact outflows with sizes $\lesssim 1.5$ kpc (e.g Rose et al. 2018; Tadhunter et al. 2018; Spence et al. 2018; Tadhunter et al. 2019).

Long-slit spectroscopy can potentially underestimate the size of the outflow, as spatial information is only available along the slit while collimated outflows (e.g. RV13) can be misaligned with the slit orientation. IFU data can reveal the two-dimensional extent, however a critical uncertainty in IFU measurements of outflow extents at low redshift is often the limited field of view (FOV) of the instrument, as outflows often extend across much of the FOV (e.g. RV13). For example, the two-slit mode of the Gemini Multi-Object Spectrograph (GMOS; Allington-Smith et al. 2002; Hook et al. 2004) has a FOV of $5'' \times 7''$, limiting the measurement of the projected galactocentric outflow extent to $\sim 2.5-3.5$ kpc at $z = 0.05$. Therefore, long-slit or FOV-limited IFU measurements of outflow extents in local ULIRGs are in principle lower limits and may

underestimate the true extent.

The commissioning of the Keck Cosmic Web Imager (KCWI; Morrissey et al. 2018) on the Keck II Telescope presents new opportunities to advance the understanding of AGN-driven outflows in galaxy evolution with its large FOV and high throughput. KCWI is a general purpose optical IFU optimized for observations of faint, diffuse objects. In the medium slicer configured, KCWI has a FOV of $16'' \times 20''$, capable of mapping outflowing gas extending to a galactocentric radius of $8-10$ kpc at $z = 0.05$, and covering an area over 9 times larger GMOS in one pointing. In this paper, we present a pilot study of a program to probe the true extent of AGN-driven outflows in low redshift galaxies with KCWI.

Mrk 273, a luminous local ULIRGs and the second closest at $z = 0.0373$, represents a unique target for this study. It has a total star formation rate of 139 $M_\odot$ yr $^{-1}$ (Cicone et al. 2014). It exhibits prominent tidal features which indicate it is a late-stage merger (e.g Kim et al. 2002). It has a complex nuclear structure hosting at least two to possibly three AGNs (see Rodríguez Zaurín et al. 2014, hereafter RZ14; Liu et al. 2019 for recent discussions). The two AGNs detected in X-ray are heavily obscured, with a combined bolometric luminosity of $\sim 5 \times 10^{44}$ erg s^{-1} (Iwasawa et al. 2011, 2018). Mrk 273 is known to host multi-phase high velocity AGN-driven outflows of various scales with a complex kinematic structure in the central ~ 5 kpc region. On the sub-kiloparsec scale, compact molecular outflows have been observed with velocities of > 400 km s^{-1} travelling towards the north up to ~ 600 pc from the nucleus (e.g U et al. 2013; González-Alfonso et al. 2017; Aladro et al. 2018). Long-slit spectroscopy has revealed ionized outflows in the E-W direction about the nucleus with velocity widths (FWHM) > 500 km s^{-1} within a distance of ~ 6 kpc (Rodríguez Zaurín et al. 2013, RZ14; Spence et al. 2016, hereafter S16). IFU observation of the central 4.5×6 kpc shows a separate bipolar superbubble of fast outflowing ionized gas in the N-S direction extending 2 kpc on either side, reaching velocities of ~ 1500 km s^{-1} (RV13).

Apart from the fast ionized outflows in the central region, a striking feature of Mrk 273 are

two extended nebulae of ionized gas stretching > 20 kpc in the NE and SW directions, revealed by ground- and space-based imaging studies combined with long-slit spectroscopy (RZ14; S16). The nature of these extended nebulae is not completely clear. Given the presence of the multiple AGNs and fast central outflows in Mrk 273, it is of interest to determine the relation of the extended nebulae to the AGNs, such as whether they represent present or past episodes of outflows, or gas impacted by such outflows. Long-slit spectroscopy of selected apertures in the extended nebulae by RZ14 and S16 suggests relatively narrow kinematics, which can be associated with tidal debris, but the majority of the nebulae was not sampled. The two extended nebulae are also detected in X-ray (Iwasawa et al. 2011; Liu et al. 2019). Liu et al. (2019) argue that the high temperature and high α/Fe ratio in the SW nebula suggests that it is a reservoir of gas accumulated from past episodes of outflows on a timescale of $\lesssim 0.1$ Gyr, where the turbulence in the gas has dissipated away. IFU observations are required to robustly determine the nature of these extended nebulae, as they can map the full kinematic structure, and yield line ratio maps essential in understanding the physical conditions of the ionized gas.

In this paper, we analyze IFU observations of Mrk 273 using KCWI, with a focus on the nature of the extended nebulae. In Section 4.3, we describe the KCWI observations and the reduction and analysis of the data. In Section 4.4, we present our main results. We discuss the implications of our results in Section 4.5 and summarize our findings in 4.6.

4.3 Observations and Data

4.3.1 KCWI Observations

We observed Mrk 273 with KCWI on the Keck II telescope on June 14 and 15, 2018. We used the blue low-dispersion (BL) grating and medium slicer with KCWI, which provides a spectral resolution of $R = 1800$, a spaxel size of $0.29 \times 0.69''$, and a field of view (FoV) of $20'' \times 16''$ per pointing. We configured the articulating camera to a central wavelength of 4500$\AA$

and used a detector binning of 2×2, yielding wavelength coverage of 3435–5525$\mathring{A}$. The seeing was $0.8''$, corresponding to a projected distance of 0.62 kpc at the redshift of our target. Since the angular size of Mrk 273 exceeds the FoV of the IFU, we defined six pointing areas to cover the galaxy. Each pointing area was observed for 30 to 60 minutes, consisting of individual exposures of 10 minutes for the nuclear region, and 15 minutes for the extended regions. Individual exposures in each pointing area were dithered $0.35''$ along slices to subsample the output spaxels. For the nuclear region, we took a 1-minute exposure for each dither position to sample pixels saturated in the 10-minute exposure.

4.3.2 Data Reduction

We reduced the data using the KCWI Data Extraction and Reduction Pipeline v1.1.0 and the IFSRED library (Rupke 2014a). We first performed a correction to saturated pixels in raw frames of the nuclear region using the routine IFSR_KCWISATCOR. This routine searches for saturated pixels in the 10-minute exposure of the nuclear region, and replaces them with pixels in its corresponding 1-minute exposure after scaling for the exposure time difference. The corrected frames of the nuclear pointing region and raw frames of other pointing regions are then passed to the pipeline. The default wavelength calibration produced large residuals of $\approx 1\mathring{A}$, resulting from a mismatch with the pipeline thorium-argon (ThAr) atlas, so we selected DISPLAY mode 3 to manually accept and reject lines matched by the pipeline. The residuals of the resulting wavelength solutions were reduced to $\approx 0.3\mathring{A}$. Sky subtraction was performed using the pipeline with manual selection of a sky mask region in each frame. For pointings in the nuclear region, where the source occupies the entire FoV, we used a sky frame from a nearby pointing that was observed immediately before or after the nuclear pointing. Following the full pipeline stages, we resampled the data onto $0.29'' \times 0.29''$ spaxel grids using the routine IFSR_KCWIRESAMPLE, and generated a mosaic of the data using the routine IFSR_MOSAIC. The resulting stacked data cube has dimensions of 166×215 spaxels.

4.3.3 Data Analysis

Voronoi Binning

To enhance the signal-to-noise (S/N) for spectroscopic analysis of low surface brightness diffuse emission, we constructed Vorinoi bins (Cappellari & Copin 2003) of the data using the IDL routine VORONOI_2D_BINNING [1]. The Voronoi binning technique is an optimal method to bin two-dimensional data to achieve a minimum S/N in each bin while maximally preserving spatial resolution, and is commonly used in the analysis of IFU data (Cappellari 2009). An emission line flux and error map is required to construct the Voronoi bins. The two strongest emission line features in our data are the [OII]3726,9 doublet and [OIII]5007. We created initial emission line maps of each line by integrating over the emission line and subtracting nearby continuum at wavelengths on either side. The relative emission line strengths of [OIII]5007 and [OII]3726,9 vary widely across different regions of the galaxy. For example, the [OIII]5007 emission line is several times stronger than the [OII]3726,9 doublet in the northeast region of the galaxy, but is several times weaker in the southwest. To minimize binning bias towards one particular emission line, and thus a particular region of the galaxy, we created a combined line map of both emission lines by multiplying the [OII]3726,9 map by two and adding it to the [OIII]5007 map. The factor of two was introduced to avoid bias towards [OIII]5007, which is, on average, approximately two times stronger than [OII]3726,9 across the galaxy. We used the combined line flux and error maps to construct Voronoi bins with a target S/N of 25 and a threshold S/N of 1. The 12184 spaxels above the S/N threshold are grouped into 1588 Voronoi bins, with 1026 unbinned spaxels.

This Voronoi-binned data cube constructed from bright emission lines traces the distribution of ionized gas in the galaxy, but it does not necessarily trace the distribution of the stellar continuum. For example, Voronoi bins in regions with strong line emission but weak continuum emission will have a high S/N in emission lines but low S/N in the continuum. While this is likely

[1] https://www-astro.physics.ox.ac.uk/~mxc/software/#binning

sufficient for obtaining an accurate continuum flux level near emission lines to measure emission line fluxes and kinematics, other continuum parameters such as stellar kinematics may potentially have suboptimal accuracy. Therefore, for the purpose of measuring continuum kinematics only, we constructed a separate set of Voronoi bins using flux and error maps of the continuum with emission lines masked, and a target S/N of 100 and a threshold S/N of 3. A total of 14664 spaxels were above the S/N threshold, among which 1875 Voronoi bins were constructed, with 1204 unbinned spaxels.

Emission-line Fitting

We use the combined [OII] and [OIII] Voronoi-binned data cube for emission line fitting. We modelled the spectrum in each Voronoi bin using the IFSFIT library (Rupke 2014b) in IDL. It uses incorporates PPXF (Cappellari 2012) to fit the stellar continuum, and MPFIT (Markwardt 2009) to fit a user-defined number of Gaussian profiles to the emission lines. IFSFIT first masks emission line regions and fits the stellar continuum, then simultaneously fits the emission lines in the continuum-subtracted spectrum. The continuum spectrum is fit with the González Delgado et al. (2005) high-resolution stellar population synthesis model assuming solar metallicity, and Legendre polynomials to account for residuals from imperfect calibration such as scattered-light or residual sky background. A maximum of three Gaussian components are allowed in each spaxel for each emisison line, where the kinematics of each component is tied to that of [OIII]5007. Model line profiles were convolved with the spectral resolution before fitting. The [OII] doublet is unresolved in our observation, and the [OII]3729/3726 flux ratio is fixed to 1.2, corresponding to an electron density of 400 cm^{-3} (Pradhan et al. 2006). An additional component is included only when it has a significance above 3σ in at least one emission line, and emission lines with a total significance of less than 3σ after fitting are set to zero. From this we created flux and kinematics maps for each emission line.

To measure stellar kinematics, we additionally performed a continuum-only fit to the

continuum Voronoi-binned data cube. Emission lines were masked and the continuum was fit with the same SPS model and Legendre polynomials described above.

4.4 Results

4.4.1 Morphology

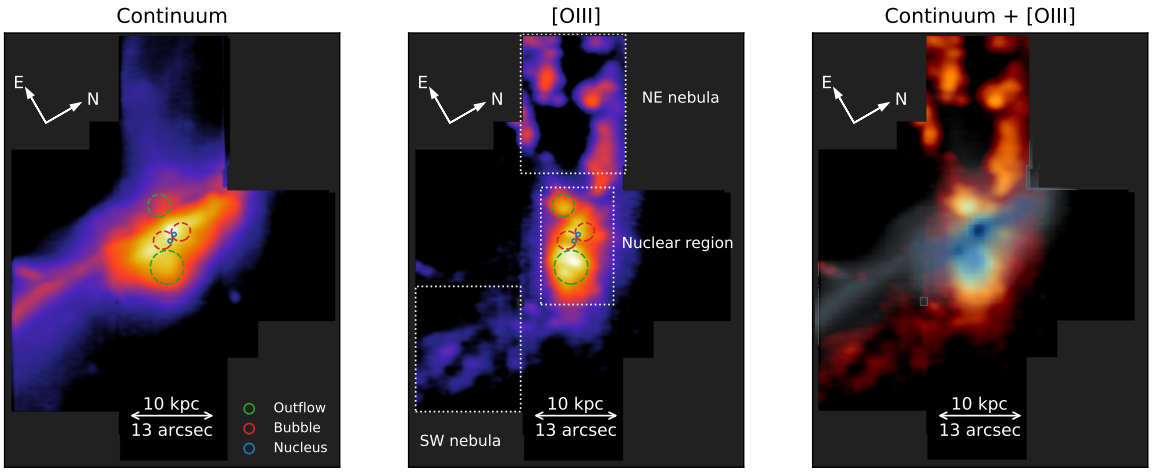

Figure 4.1: Left: Continuum image of Mrk 273 showing stellar emission. A tidal tail extends to the south of the galaxy. Middle: Continuum-subtracted [OIII]4959+5007 image showing emission of ionized gas. Two extended nubulae are observed in the NE and SW directions. The NE nebula contains several bright regions around its edge, and is hollow at the center. Right: Composite image of [OIII]4959+5007 in red and the continuum in blue. In the left and middle panels, the green-dashed circles denote the locations of the outflow regions reported in RZ14, the red-dashed circles denote location of the bipolar superbubble reported in RV13, and the blue circles denote the two AGNs with X-ray detections. In the middle panel, the white-dashed rectangles indicate the regions used in our line ratio analysis for the extended nebulae and the nuclear region in Section 4.4.5.

KCWI has a remarkable capability to map low surface brightness extended emission. The left panel of Figure 4.1 shows the mosaic image of the stellar continuum emission at $3600-5000\AA$ (wavelengths near emission lines have been masked). We also mark the locations of the two known AGNs, the nuclear superbubble in RV13 and the outflow regions in RZ14. A prominent feature is the well-known tidal tail (e.g. Kim et al. 2002; RZ14; S16) extending to the south of

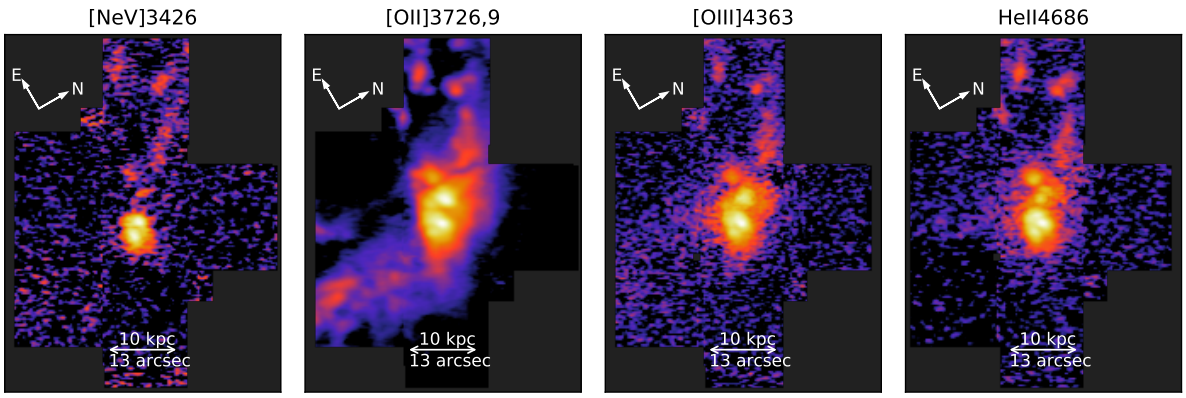

Figure 4.2: From left to right: Continuum-subtracted images of [NeV]3426, [OII]3726,9, [OIII]4363 and HeII4684. High ionization line emission in [NeV]3426, [OIII]4363 and HeII4684 is observed in not only the nuclear region, but also the NE nebula.

the galaxy. This image covers $\sim$ 12 kpc of the tidal tail; the full extent is up to $\sim$ 36 kpc (e.g Kim et al. 2002). We also observe weak diffuse continuum emission in the northeast of the galaxy reported in RZ14.

The middle panel of Figure 4.1 shows the continuum-subtracted [OIII]4959+5007 mosaic image. The emission image was constructed by integrating $\pm$675 km s^{-1}around the doublet and subtracting nearby continuum on both sides. The brightest [OIII] emission is in the central 10 kpc of the galaxy, which we call the nuclear region in this paper. We also detected in [OIII] the two previously-reported extended nebulae (e.g. RZ14; S16). A bright nebula of ionized gas is seen extending at least 20 kpc from the nucleus in the northeast of the galaxy. This NE nebula contains several bright regions around its edge, and is hollow at the center, resembling a bubble or a loop. While it is in the general direction of the diffuse continuum emission, the line and stellar emission regions do not completely overlap, particularly in the northern part of the nebula. Another extended nebula is detected in [OIII] for the first time towards the southwest of the galaxy, west of the tidal tail. This SW nebula extends $\sim$ 20 kpc from the nucleus. It is less luminous in [OIII] compared with the NE nebula. It approximately follows the direction of the

tidal tail, but they are offset by $\sim 1-3$ kpc. A composite continuum and [OIII] image is shown in the right panel of Figure 4.1 for comparison.

4.4.2 Emission Lines

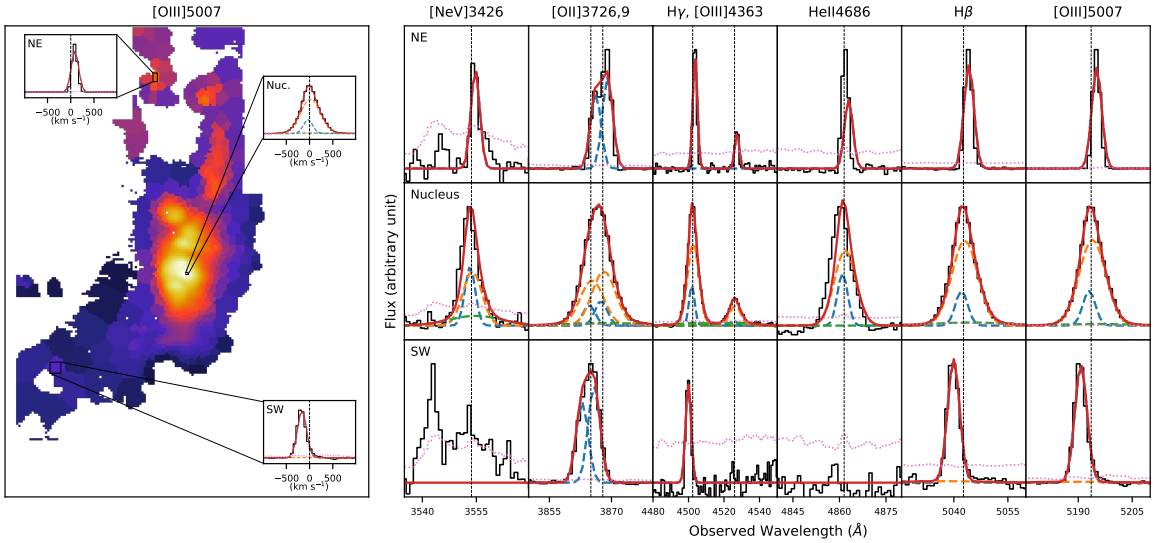

Figure 4.3: Left: Voronoi-binned model flux map of [OIII]5007. [OIII]5007 velocity profiles of representative Voronoi bins in the NE nebula, nuclear region and SW nebula are shown in the insets. Right: Spectra of each representative Voronoi bin from top to bottom. The emission lines are fitted with a maximum of three kinematic components. In the velocity profiles and spectra, the black line is the continuum-subtracted spectrum, the magenta dotted line is the error spectrum, the red line is the total emission line model, the blue, orange and green dashed lines are the emission line models for individual kinematic components. The nuclear bin has the broadest velocity profile, followed by the SW bin, while the NE bin has the narrowest profile.

Our wide-field IFU data allows us to map the flux and spatial distribution of numerous emission lines apart from the [OIII] doublet detected with KCWI. A key result of this paper is the detection and spatial mapping of the faint, high-ionization emission lines [NeV]3426, [OIII]4363 and [HeII]4686, which are useful as shock diagnostics. In addition, we map the emission from the low-ionization [OII]3726,9 doublet. Figure 4.2 shows the continuum-subtracted mosaic images of these emisison lines, integrating $\pm$675 km s^{-1} around the systemic velocity. The high-ionization [NeV]3426, [OIII]4363 and HeII4686 lines show the strongest emission in the nuclear region.

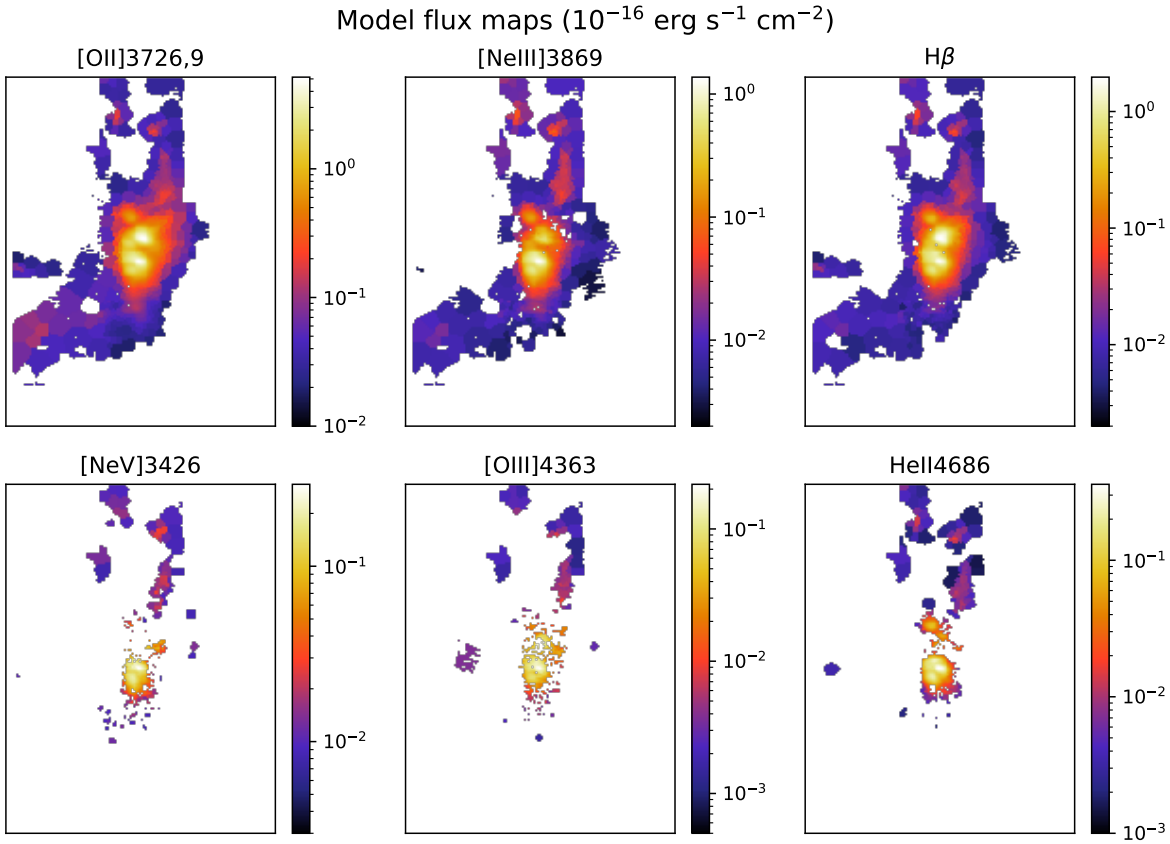

Figure 4.4: Voronoi-binned model flux map of [OII]3726,9, [NeIII]3869, Hβ, [NeV]3426, [OIII]4363 and HeII4684. The color bars show the flux in units of 10^{-16} erg s^{-1} cm^{-2}. The high ionization [NeV]3426, [OIII]4363 and HeII4684 lines are detected in the NE nebula.

Remarkably, these high-ionization lines are all observed to have extended emission in the NE nebula, in regions tracing the emission of the [OIII] doublet, but they are not detected in the SW nebula. On the other hand, the morphology of the low-ionization [OII] doublet emission is similar to that of the [OIII] doublet, but it is enhanced in the SW nebula.

Quantitative measurements of emission line fluxes are obtained using the emission-line fitting procedures on the Voronoi-binned data cube described in Section 4.3.3. The left panel of Figure 4.3 shows the resulting Voronoi-binned model flux map of [OIII]5007, and the velocity profiles of three representative Voronoi bins from the nuclear region, NE nebula, and SW nebula. The nuclear bin has the broadest velocity profile, followed by the SW bin, while the NE bin has the narrowest profile. The detailed kinematic properties of the ionized gas are discussed below in Section 4.4.3. In the right panel of Figure 4.3 we show the emission line spectra and best-fit multi-component models for the [NeV]3426, [OII]3726,9, Hγ, [OIII]4363, HeII4686, Hβ, and [OIII]5007 emission lines. The [OII] doublet, Balmer lines, and [OIII]5007 emission lines are detected in all three spatial bins shown in the left panel, while the higher-ionization [NeV]3426, [OIII]4363 and HeII4686 are only detected in the nuclear and NE bins, and not in the SW bin. For [OIII]5007, three components are required in the nuclear bin, two in the SW bin and one in the NE bin. This is generally true for most Voronoi bins in each region.

In the SW region, large variances are observed in the flux, and the S/N is low, for the wavelengths at the bluest end of the wavelength coverage of our observation, possibly due to differential observing conditions during the exposures in this pointing. The [NeV]3426 emission line, which is within the wavelengths affected, is not detected in the SW bin. Two other high-ionization lines, [OIII]4363 and HeII4686, have lower ionization potentials than [NeV]3426 and are thus potentially more prominent. However, they are also undetected in the SW bin, even though they are not within the affected wavelengths. This forms a consistent picture that high-ionization lines are absent in the SW region. Therefore, the undetection of the [NeV]3426 emission line in the SW bin is likely due to an intrinsic absence of the line rather than the large

flux variance observed in that region.

Figure 4.4 presents a more complete spatial view of each emission line by showing the model flux maps of the [OII]3726,9 doublet, and the [NeIII]3869, Hβ, [NeV]3426, [OIII]4363 and HeII4686 emission lines, using the emission line fits above. The [OII]3726,9 doublet, and the [NeIII]3869 and Hβ emission lines are generally detected in the nuclear, NE and SW regions. However, the high-ionization [NeV]3426, [OIII]4363 and HeII4686 emission liens are detected in only the nuclear and NE regions, and not in the SW region.

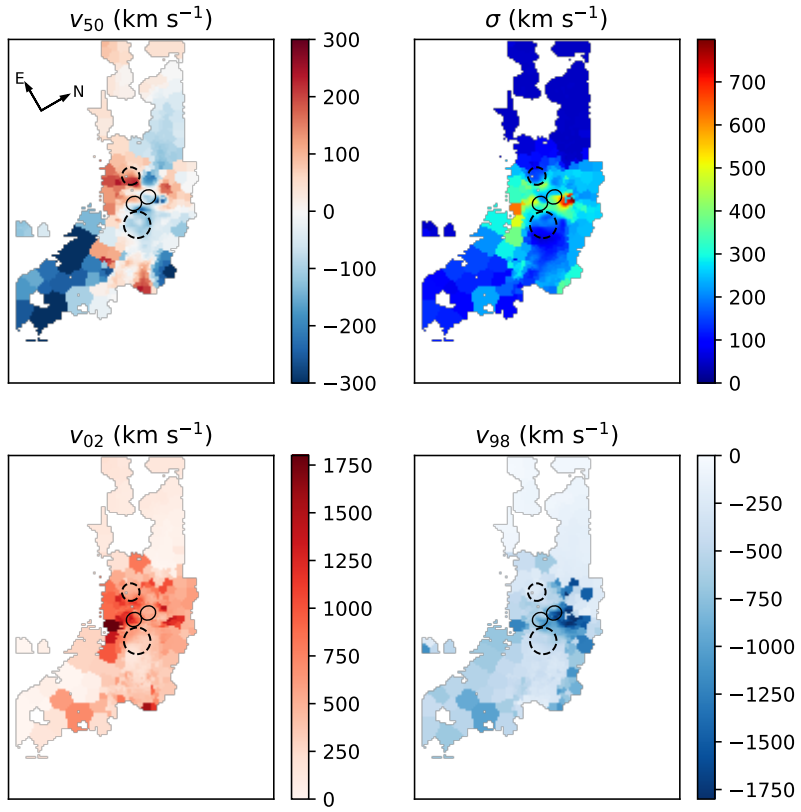

Figure 4.5: The central velocity (v_{50}), velocity dispersion (σ), maximum redshifted velocity (v_{02}) and maximum blueshifted velocity (v_{98}) of [OIII]5007. The black dashed circles show the location of the outflow regions, and the black solid circles show the location of the supperbubble. Regions of high $\sigma > 250$ km s^{-1} are observed along the direction of the bipolar superbubbles, but extend to ~ 5 kpc, approximately two to three times the previously-reported size. Moderately broad emission with $\sigma \sim 150 - 250$ km s^{-1} is observed in the outflow regions extending ~ 5 kpc in the NE and SW directions. The larger scale extended nebulae have fairly uniform velocity dispersion, $\sigma \sim 100 - 150$ km s^{-1} in the SW nebula and $\sigma \sim 50$ km s^{-1} in the NE nebula.

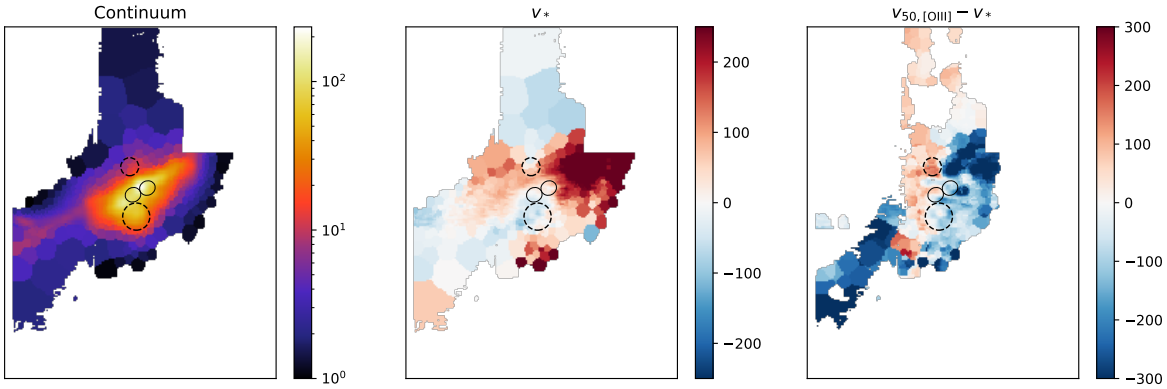

Figure 4.6: Left: Voronoi-binned model flux map for the contiuum. The color bar shows flux in units of 10^{-16} erg s^{-1} cm^{-2}. Middle: Stellar velocity map. Right: Map of [OIII]5007 emission central velocity relative to stellar velocity. The color bars of the middle and right panels show the velocity in km s^{-1}. The black dashed circles show the location of the outflow regions, and the black solid circles show the location of the supperbubbles.

4.4.3 Kinematics

With the integral field KCWI data, we are able to map out the kinematics of the ionized gas in the galaxy and identify distinct kinematic structures within the system. An important result of this paper is the kinematics of the large scale ionized gas, i.e. the NE and SW nebulae. The upper left panel of Figure 4.5 shows the central velocity v_{50}, which is the 50th percentile of the velocity profile, traced by [OIII]5007. The systemic velocity is set to be the central velocity of the stellar continuum. The nuclear region has a complex kinematic structure, with a redshifted region towards the southeast and north of the nucleus, and a blueshifted region towards the west and northeast. The large-scale SW nebula is generally blueshifted by $\sim 200-300$ km s^{-1}. The NE nebula has a mild redshift of $\sim 30-100$ km s^{-1} in the eastern part of the nebula (seen as the left half in the figure), and is mildly blueshifted by $\sim 40-100$ km s^{-1} in the western part (seen as the right half in the figure).

The upper right panel of Figure 4.5 shows the velocity dispersion σ of [OIII]5007 across the galaxy. In the nuclear region, very broad emission with $\sigma > 250$ km s^{-1} is observed along the direction of the bipolar superbubbles in RV13 (marked here as open black circles outlined with a

solid line), but extends to ~ 5 kpc, approximately two to three times the previously-reported size of the superbubbles. The regions with the highest velocity dispersion ($\gtrsim 600$km s^{-1}) lie beyond the known extent superbubbles in the north and east directions. This suggests that the high-velocity outflowing gas in the superbubbles is substantially more extended that previously measured. Moderately broad emission with $\sigma \sim 150-250$ km s^{-1} is observed in the outflow regions defined in RZ14, which extend ~ 5 kpc in both directions perpendicular to the superbubbles (marked here with open circles with dashed outlines). The larger scale extended nebulae have fairly uniform velocity dispersion, with the SW nebula showing $\sigma \sim 100-150$ km s^{-1}and the NE nebula showing a smaller dispersion of $\sigma \sim 50$ km s^{-1}.

The lower left and lower right panels of Figure 4.5 show the "maximum" redshifted and blueshifted velocities v_{02} and v_{98}, which are the velocity that encompasses 2% and 98% of the cumulative velocity distribution, respectively. The southern superbubble contains highly redshifted emission with v_{02} between 800 and 1400 km s^{-1}, while the northern superbubble contains highly blueshifted emission with v_{98} bewteen -1800 and -800 km s^{-1}, consistent with a bipolar superbubble of fast moving outflows. Additionally, fast moving, redshifted gas with $v_{02} \gtrsim 900$ km s^{-1} extends beyond the known superbubble towards a wedge-shaped region in the south up to ~ 5 kpc. Similarly, there is a wedge-shaped region of high-velocity blueshifted gas extending north up to ~ 4 kpc. This, combined with the velocity dispersion map, suggests that fast moving gas from the superbubbles extends two to three times beyond the previously-known extent. On larger scales, the NE nebula has "maximum" velocities up to -200 and 200 km s^{-1}, while the SW nebula generally has velocities between -50 and 500 km s^{-1}.

The kinematics of the stellar emission is measured by fitting the continuum Voronoi-binned data cube described in Section 4.3.3. The left panel of Figure 4.6 shows the resulting model flux map of the continuum, while the middle panel shows the central velocity of the stellar continuum v_*. On large scales, apart from the tidal tail, weak continuum in the NE is also detected. The stellar continuum near the nucleus is redshifted in the north-south direction, and blueshifted

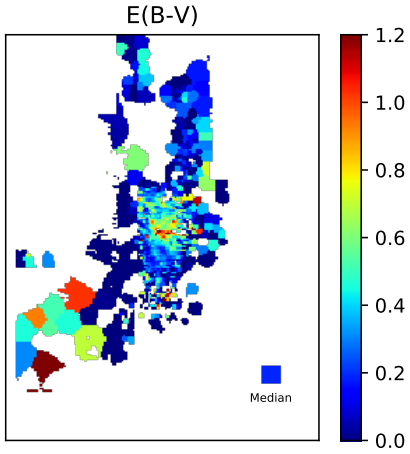

Figure 4.7: Extinction map computed from the Balmer decrement of the Hβ and $H\gamma$ emission lines. The square shows the median extinction value of 0.19. Relatively strong reddening of $E(B-V) \gtrsim 0.5$ is observed in the the SW nebula as well as the inner nuclear region, while the NE nebula has weaker reddening of ~ 0.2.

in the east-west direction. In addition, the weak continuum in the NE is generally blueshifted by ~ 100 km s^{-1}. To quantify how much the kinematics of the ionized gas decouples from the continuum, the right panel of Figure 4.6 shows the central velocity of [OIII]5007 relative to that of the stellar continuum, measured by $v_{50} - v_*$. The ionized gas north of the nucleus is generally blueshifted relative to the stellar continuum, and generally redshifted in the south, despite the complex kinematic structure in [OIII]5007 alone. In addition, the NE nebula is generally redshifted from the stellar continuum by $\sim 50-100$ km s^{-1}, instead of displaying the two distinct redshifted and blueshifted halves as seen in [OIII]5007 alone.

4.4.4 Emission Line Ratio Maps

An important goal of this paper is to investigate the origin of the ionized gas that produces the observed emission. From the numerous emission line maps presented for Mrk 273, one can obtain line ratio maps, which are crucial in diagnosing the physical conditions of the ionized gas in different regions of the galaxy. To obtain accurate line ratios, we first account for extinction across the galaxy. We calculated the reddening $E(B-V)$ in each Voronoi bin from the Balmer

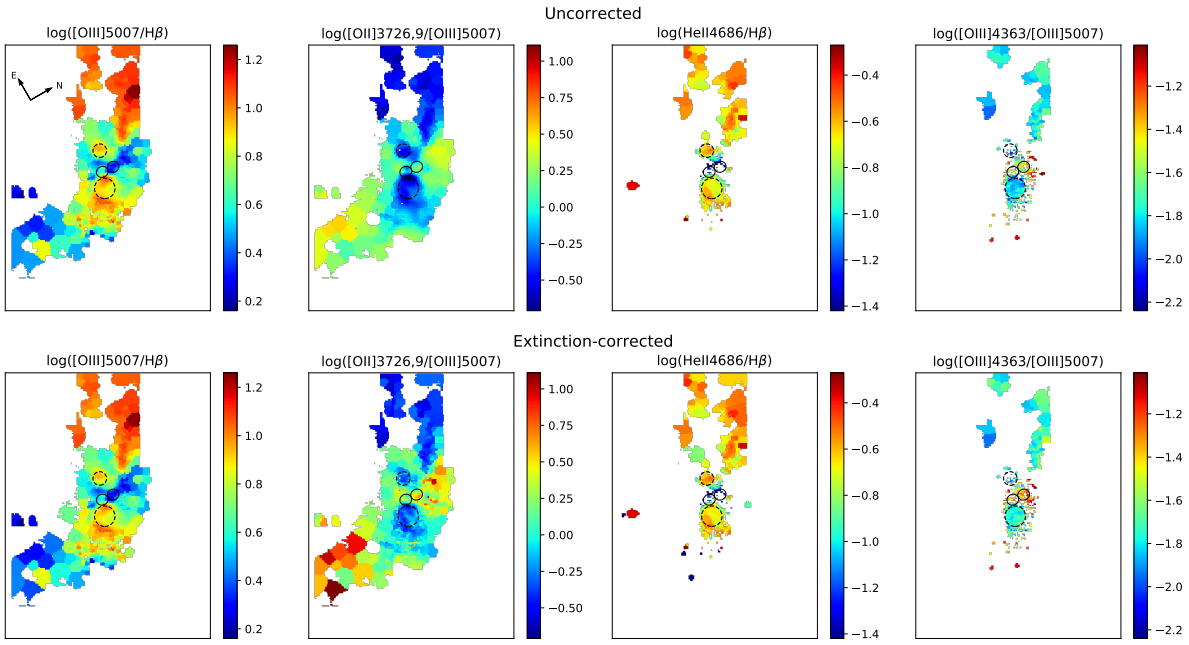

Figure 4.8: Maps of the [OIII]5007/Hβ, [OII]3726,9/[OIII]5007, HeII/Hβ, and [OIII]4363/[OIII]5007 line ratios before (top row) and after (bottom row) extinction correction. Each column shows a line ratio. The black dashed circles show the location of the outflow regions, and the black solid circles show the location of the supperbubbles. The line ratios in the central region differ at the locations of the outflows and superbubbles, with the two regions showing opposite line ratio trends. In the outflow region, high line ratios are measured for [OIII]5007/Hβ and HeII/Hβ. In the superbubbles, high line ratios are measured for [OII]3726,9/[OIII]5007 and [OIII]4363/[OIII]5007. A remarkable feature is that the NE nebula displays similar line ratios as the outflow regions.

decrement of the total Hβ and Hγ emission line fluxes. We assumed Case B recombination at 10^4 K and the Cardelli et al. (1989) extinction curve. The resulting reddening map is shown in Figure 4.7. Relatively strong reddening of $E(B-V) \gtrsim 0.5$ is observed in the the SW nebula as well as the inner nuclear region, while the NE nebula has weaker reddening of ~ 0.2. The median reddening of the galaxy is 0.19.

We constructed maps of line ratios commonly used as diagnostics before and after extinction correction, and show them in Figure 4.8. To correct for extinction, line fluxes in each Voronoi bin are calculated using the reddening map. For Voronoi bins without significant detection of the Balmer lines, the median reddening value across the galaxy is used to calculate the corrected flux. Extinction corrections lead to a median change in the line ratios of [OIII]5007/Hβ, [OII]3726,9/[OIII]5007, HeII/Hβ, and [OIII]4363/[OIII]5007 of -0.01, 0.09, 0.01, and 0.05 dex, respectively. We note that the change in the numerical values of the line ratios are modest, and the spatial trends seen in the line ratio maps are unchanged by extinction correction. Numerical values of line ratios in the rest of this subsection refer to the extinction-corrected values.

The NE nebula has high $\log([\mathrm{OIII}]5007/H\beta)$ line ratios of ~ 1 to 1.2, while these line line ratios are substantially lower in the SW nebula, with values of ~ 0.2 to 0.6. The $\log([\mathrm{OIII}]5007/H\beta)$ line ratios in the nuclear region have a complex structure. An interesting feature is that regions of high $\log([\mathrm{OIII}]5007/H\beta)$ line ratios extend in the northeast and southwest directions, coinciding with the outflow region (dotted circles), while regions of low line ratios extend in the north and south directions, aligning with the axis of the supperbubbles (circles with solid outlines).

The distribution of the $\log([\mathrm{OII}]3726,9/[\mathrm{OIII}]5007)$ line ratio generally displays opposite trends to that of $\log([\mathrm{OIII}]5007/H\beta)$. While this is not entirely unexpected because of the inverse dependence on [OIII]5007 of the two line ratios, the different dynamic range of the line ratios indicates that this is also driven by differences in [OII]3726,9. $\log([\mathrm{OII}]3726,9/[\mathrm{OIII}]5007)$ is the highest in the SW nebula, at ~ 0.5 to 1, and the lowest in the NE nebula, at ~ -0.7 to -0.3.

In the nuclear region, the $\log([\mathrm{OII}]3726,9/[\mathrm{OIII}]5007)$ line ratios are elevated along the direction of the superbubbles, and are lower in the outflow regions.

The $\log(\mathrm{HeII}4686/H\beta)$ line ratio exhibits similar trends to $\log([\mathrm{OIII}]5007/H\beta)$. The NE nebula and the outflow region display enhanced line ratios, while the superbubbles have lower line ratios. The HeII4686 emission line is undetected in the SW nebula. For $\log([\mathrm{OIII}]4363/[\mathrm{OIII}]5007)$, higher line ratios are observed along the superbubbles, and lower line ratios are observed in the outflow region and the NE nebula. The [OIII]4363 emission line is also undetected in the SW nebula.

4.4.5 Ionization Mechanism

In this subsection, we use line ratio diagnostic diagrams to investigate the nature of the ionizing sources of the gas in different regions of Mrk 273. Figures 4.9 to 4.12 show the observed line ratios and predictions of ionization models on diagnostic diagrams. Line ratios are chosen to be either close in wavelength so that extinction effects are minimized, e.g. HeII4686/Hβand [OIII]5007/Hβ, or from the same species so that effects of an unknown metallicity are minimized, e.g. [OII]3726,9/[OIII]5007, [OIII]4363/[OIII5007] and [NeV]3426/[NeIII]3869 (Baldwin et al. 1981). In each diagnostic diagram, we denote line ratios of spaxels in the nuclear region, the NE nebula, and the SW nebula with different colors to analyze the ionization mechanism in each region. When an emission line is undetected in a region, we show the median value of the 3σ upper limit in the spaxels of that region. For line ratios in the nuclear region, we further separate the spaxels in the slow, medium, and fast regions according to their velocity dispersion ($\sigma < 200$ km s^{-1}, 200 km s^{-1} $< \sigma <$ 400 km s^{-1} and $\sigma > 400$ km s^{-1}), and denote them with different colors. In the following, we use the IDL Tool for Emission-line Ratio Analysis (ITERA; Groves & Allen 2010) to explore models of different ionization mechanisms and compare them with the observed line ratios.

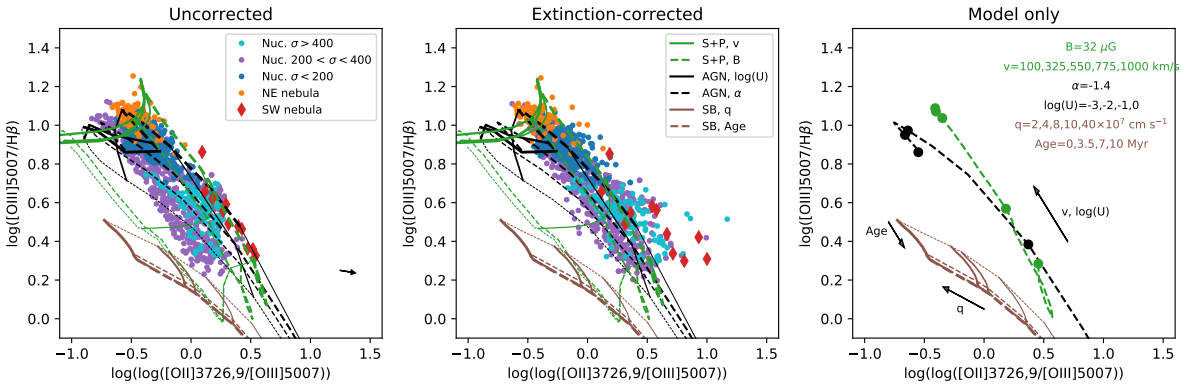

Figure 4.9: Diagnostic diagram of [OIII]5007/Hβ vs. [OII]3726,9/[OIII]5007. Left panel: Line ratios before extinction correction overplotted with model grids. The red diamonds correspond to the SW nebula, the orange points correspond to the NE nebula, the cyan, violet and blue points correspond to the high, medium and low velocity spaxels in the nuclear region. The green grids show a shock+precursor ionization model with solar metallicity and a pre-shock density of 100 cm^{-3}. The solid grid lines correspond to five shock velocity values (100, 325, 550, 775 and 1000 km s^{-1}, thin to thick), while the dashed grid lines correspond to four magnetic field values (0.001, 1, 20 and 100 μG, thin to thick). The black grids show a dusty AGN ionization model with solar metallicity and a density of 100 cm^{-3}. The the solid grid lines correspond to five values of ionization parameter $\log(U)$ (-4, -3, -2, -1 and 0, thin to thick), while dashed grids lines correspond to four values of the power law index (-2, -1.7, -1.4 and -1.2, thin to thick). The brown grids show a starburst ionization model assuming standard mass loss and continuous star formation, with solar metallicity and a density of 100 cm^{-3}. The solid grids lines correspond to five values of ionization parameter q (0.2, 0.4, 0.8, 1 and 4×10^8, thin to thick), while the dashed grid lines correspond to four values of age (0, 3.5, 7 and 10 Myr, thin to thick). The black arrow in the left panel represents the median magnitude and direction of extinction correction on the line ratios. Middle panel: Extinction-corrected line ratios overplotted with model grids. Right panel: To allow for easier visualization of the trends of model parameters, we show model sequences without the observed data. The shock+precursor model is shown at a fixed magnetic field strength of 32 μG, and the AGN photoionization model is shown at a fixed power law index of -1.4. The shock and AGN models overlap with each other, and both align with the observed line ratios. The starburst model cannot reproduce the observed line ratios in any regions of the galaxy.

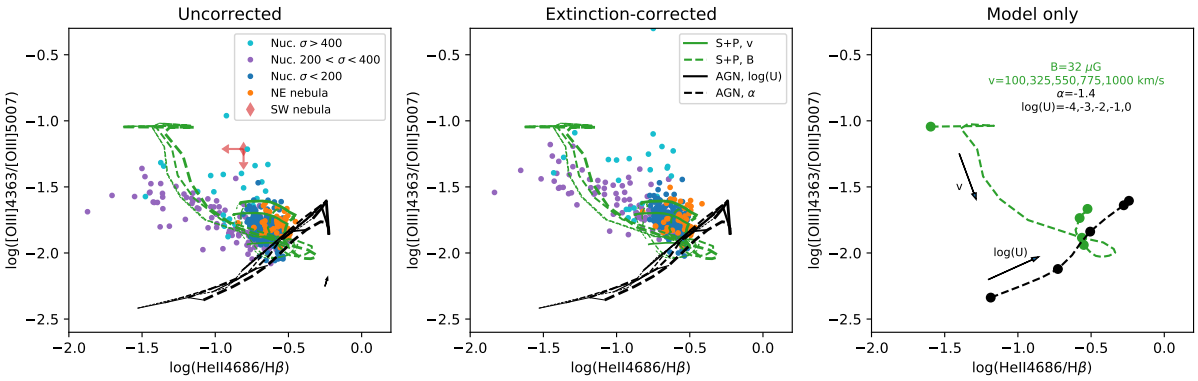

Figure 4.10: Same as Figure 4.9, but for [OIII]4363/[OIII]5007 vs. HeII4686/Hβ line ratios. The shock+precursor model (green grids) successfully reproduces most of the observed line ratios, while the AGN photoionization model fails to account for most of the spaxels in the galaxy. The red arrow shows the median value of the 3σ upper limit in the SW nebula.

Starburst Photoionization

Since ULIRGs are known to have vigorous starburst activity, and Mrk 273 has a SFR of 139 $M_\odot$ yr^{-1}, we first study the possibility of starburst photoionization driving the observed emission. We use the continuous star formation model at standard mass loss rate of Levesque et al. (2010), assuming solar metallicity and an electron density of 100 cm^{-3}. The Levesque et al. (2010) model uses the MAPPINGS III code for radiative transfer, and the Starburst99 code of Vázquez & Leitherer (2005). The free parameters are the age and ionization parameter q , and they vary between $0-10$ Myr and $2-40\times10^7$ cm s^{-1}, respectively. The model grids are overplotted in brown with the observed line ratios in Figure 4.9. The starburst model grids do not overlap with the observed line ratios in any of the regions of Mrk 273. Some of the spaxels in the nuclear regions are the closest to the models, but the predicted model [OIII]5007/Hβ and [OII]3726,9/[OIII]5007 line ratios are at least 0.3 dex lower than observed. For the line ratios of higher ionization lines, the starburst model predicts [OIII]4363/[OIII]5007 line ratios of < -2.4 and HeII4686/Hβ line ratios of < -3.3, while the lowest observed values are $\gtrsim -2.2$ for both line ratios. The model grids are not shown in these diagnostic diagrams since they reside mostly outside of the range of the plot. We also explored the starburst model assuming twice solar

metallicity or a density of 10cm^{-3}, and it resulted in a larger disagreement between the model predictions and the observed data. This rules out starburst photoionization in all spatial regions of Mrk 273, consistent with previous findings using the standard BPT diagram (RZ14; S16).

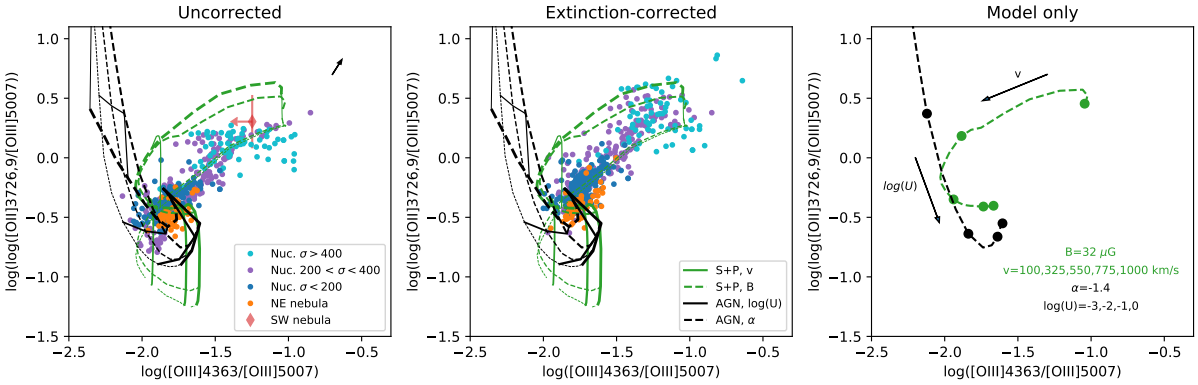

Figure 4.11: Same as Figure 4.9, but for [OII]3726,9/[OIII]5007 vs. [OIII]4363/[OIII]5007 line ratios. The shock plus precursor model grids overlap with most of the observed line ratios in all the regions, while the AGN photoionization model only matches a fraction of the spaxels in the NE nebula and the slow spaxels in the nuclear region.

AGN Photoionization

Since Mrk 273 is known to host at least two AGN in its central region, we next explore the possibility of AGN photoionization. We apply the dusty, radiation pressure dominated AGN model of Groves et al. (2004), assuming solar metallicity and an electron density of 100 cm^{-3}. The model assumes a simple power-law radiation field to represent the AGN ionizing spectrum and a constant gas pressure, and includes dust and the effect of radiation pressure on dust. The free parameters are the AGN power law index (α) and ionization parameter ($\log(U)$), which vary between -2 to -1.2 and -4 to 0, respectively. We overplot the model grids in black with the observed line ratios in Figures 4.9 to 4.12, and in the right panels, plot a model sequence of varying ionization parameter at a fixed power law index of $\alpha = -1.4$ for easier visualization of the model dependence in each line ratio space. We also explore AGN photoionization models with twice solar metallicity and an electron density of 1000 cm^{-3}, holding the other parameter

constant, and find that both models produce a larger disagreement with the observed data.

The AGN model grids reproduce the observed line ratios in all three spatial regions in the [OIII]5007/Hβ vs. [OII]3726,9/[OIII]5007 plane (Figure 4.9). The spaxels in the nuclear region occupy the sequence of model line ratios with ionization parameter ranging from -3 to 0. The fast ($\sigma > 400$ km s^{-1}) spaxels lie in the grids of $\log(U) \sim -3$, while the slow ($\sigma < 200$ km s^{-1}) spaxels reside in those of $\log(U) \sim -2$ to 0. The medium (200 km s^{-1} $< \sigma <$ 400 km s^{-1}) spaxels occupy the entire range of $\log(U) \sim -3$ to 0. The spaxels in the NE nebula occupy model grids at high ionization parameters of $\log(U)$ between -2 and 0, similar to the slow spaxels in the nuclear region. The spaxels in the SW nebula reside in model grids at low ionization parameters of $\log(U) \sim -3$.

However, the AGN model grids cannot reproduce the observed line ratios in the nuclear and NE regions in diagnostics plots involving higher ionization lines. This is the most prominent in Figure 4.10, where the medium and fast spaxels in the nuclear region have high $\log([\text{OIII}]4363/[\text{OIII}]5007)$ line ratios of > -1.5, which are too high to be fit by the AGN model even at the highest ionization parameter. The slow spaxels in the nuclear regions and spaxels in the NE nebula occupy line ratios somewhat closer to the model predictions with $\log(U) \sim -2$, but the majority of the spaxels are still ~ 0.3 dex higher than the model in $\log([\text{OIII}]4363/[\text{OIII}]5007)$. Since both the [OIII]4363 and HeII4686 emission lines are undetected in the SW nebula, only upper limits are available in this diagnostic diagram. We show the median upper limit of the spaxels in the SW region. The upper limit in HeII4686/Hβ in the SW nebula is consistent with AGN photoionization with $\log(U) \sim -3$.

Similar results are observed in Figures 4.11 and 4.12. The fast and medium spaxels in the nuclear region deviate the most from the AGN photoionization model predictions. The slow spaxels in the nuclear region and the spaxels in the NE nebula deviate less from the model predictions, but at least half of these spaxels in Figure 4.11 and the majority of these spaxels in Figure 4.12 cannot be reproduced by the AGN photoionization model. We also show the

median upper limit of [OIII]4363/[OIII]5007 in Figure 4.11, and it is consistent with AGN photoinoization with $\log(U) \sim -3$.

Our results rule out pure AGN photoionization in the fast and medium spaxels in the nuclear region. While the slow nuclear spaxels and the NE spaxels are closer to the predictions of the AGN photoionization model, our results indicate that AGN photoionization can at most produce a minority of the emission, and a significant alternative source of ionization is responsible for most, if not all, of the emission in these regions. Moreover, for these two regions, the model predictions in different diagnostic diagrams suggest somewhat inconsistent values of ionization parameters of -2 to 0, which further disfavors the picture of pure AGN photoionization in these two regions.

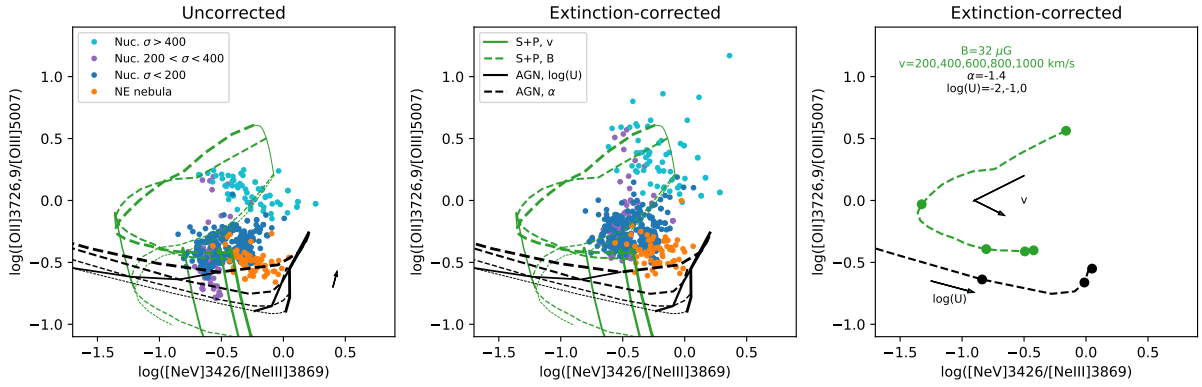

Figure 4.12: Same as Figure 4.9, but for [OII]3726,9/[OIII]5007 vs. [NeV]3426/[NeIII]3869 line ratios and different grid values for the shock velocity. The shock and precursor model grids show five shock velocities of 200, 400, 600, 800 and 1000 km s^{-1}, as model grids for shock velocities below 200 km s^{-1} extend far beyond the axes limits. The shock+precursor model successfully reproduces most of the observed line ratios, while the AGN photoionization model fails to account for most of the spaxels in the galaxy. The red arrow shows the median value of the 3σ upper limit in the SW nebula.

Shock Ionization

An alternative ionization mechanism for the gas in Mrk 273 is radiative shocks. Shocks excitation has been observed in galaxies impacted by galaxy-galaxy interactions and/or outflows

(e.g. Rich et al. 2015). We apply the shock+precursor ionization model of Allen et al. (2008), assuming solar metallicity and a pre-shock electron density of 100 cm^{-3}. The model includes emission from both the post-shock region, where gas is shock-excited, and the pre-shock region, where gas is photoionized by the radiation from the pre-shock region. The free parameters are the shock velocity (v_s) and magnetic field strength (B), which vary between $100-1000$ km s^{-1} and $0.001-100\mu$G, respectively. For a pre-shock density of 100 cm^{-3}, a magnetic field strength of $B\sim 32\mu$G corresponds to equipartition between thermal and magnetic pressures ($B/n^{1/2}\sim 3-5$; Allen et al. 2008). We also explore a shock-only model and find that a high pre-shock density of 1000 cm^{-3} is required to produce satisfactory agreement with the observed data. This would imply a post-shock density of 10000 cm^{-3} (Dopita & Sutherland 1995), which is an extreme assumption. Therefore, the shock and precursor model is preferred and shown here. We overplot the model grids in green with the observed line ratios in Figures 4.9 to 4.12, and in the right panels, plot a model sequence of varying shock velocity at a fixed magnetic field strength of $B=32\mu$G for easier visualization of the models.

All four diagnostic diagrams produces consistent results when comparing the observed line ratios with the shock and precursor model grids. The observed line ratios of spaxels in both the nuclear region and the NE nebula generally reside within the model grids. The medium velocity spaxels in the nuclear region occupy a wide range of model grids along shock velocity values of $100-1000$ km s^{-1}. A peculiar result is that in the nuclear region, the fast spaxels occupy the low shock velocity grids ($v_s\lesssim 300$km s^{-1}), while the slow spaxels occupy the high shock velocity grids ($v_s\gtrsim 300$km s^{-1}). The spaxels in the NE region occupy a similar space in line ratios with the slow spaxels in the nuclear region, in the high v_s grids. For the SW nebula, the line ratios in Figure 4.9 and the upper limits in Figure 4.11 agree with the model grids at $v_s\sim 100-400$km s^{-1}. The upper limits in Figure 4.10 provides a stricter constraint of $v_s\sim 200$km s^{-1}.

Another test relevant for shock ionization is the energy budget of the observed emission.

The self-consistent model of radiative shocks with precursor preionization presented in Dopita & Sutherland (2017) shows that radiative shocks with $v_s \gtrsim 110$km s^{-1} and a preshock density of 100 cm^{-3} can produce emission with Hβ surface brightness of $\sim 7 \times 10^{-15}$ erg cm^{-2} s^{-1} arcsec^{-2}. In Mrk 273, the peak extinction-corrected Hβ surface brightness in the nuclear region, NE nebula and SW nebula are $\sim$ 10, 0.15 and 0.1×10^{-15} erg cm^{-2} s^{-1} arcsec^{-2}, respectively. The observed surface brightness is broadly in agreement with the theoretical predictions, indicating that shocks are an energetically feasible ionization mechanism for the gas in the nuclear region, NE nebula, and SW nebula.

The surface brightness profile of the NE nebula also provides information on its excitation mechanism. For AGN photoionization, a surface brightness profile declining with distance from the nucleus would be expected, as the ionization photons from the AGN decline as r^{-2}. On the other hand, shock emission is produced in-situ, and can produce strong emission at the location of the shock, independent of its distance from the nucleus. The observed surface brightness of the NE nebula is not strongly dependent on the distance from the nucleus, with various clumps with similar peak brightness along the NE direction.

Our results indicate that significant shock and precursor ionization is responsible for the emission in the nuclear region and the NE nebula. The reversed relation between the measured velocity dispersion of spaxels and the shock velocity implied by the model predictions suggests that a combination of ionization mechanisms may be present. As starburst models fail to produce the high line ratios observed, the most likely scenario is the co-existence of shock and AGN ionization in the nuclear region and NE nebula. The larger deviation from the AGN photoionization model predictions of the fast spaxels in the nuclear region suggests a relatively low contribution from AGN photoionization, and a higher contribution from shocks, which is expected from the higher measured velocity dispersion in these spaxels. The slow spaxels in the nuclear region and the spaxels in the NE nebula have a smaller deviation from the AGN model predictions, suggesting a relatively higher AGN contribution and lower shock contribution than

the fast spaxels. Our current observations cannot conclusively determine the contribution of AGN photoionization and shock ionization in the SW region.

4.5 Discussion

One of the most striking features in the KCWI data is the extended NE nebula detected in multiple emission lines spanning over 20 kpc in extent. The NE nebula displays a hollow morphology, which resembles a bubble originating from one of the nuclei. A particularly remarkable result from the line ratio diagnostics presented here is that the slow spaxels in the compact, nuclear region and the spaxels in the extended NE nebula reside in a very similar line ratio space in all of the diagnostic diagrams. Another clear correlation is that not only do both sets of spaxels have similar kinematics ($\sigma < 200$km s^{-1}), they are also located in the same projected physical direction from the nuclei. The slow spaxels in the nuclear region are primarily located in the outflow regions $\sim 1-5$ kpc northeast and southwest of the nucleus. The NE nebula is located $\sim 5-15$ kpc ahead of the NE outflow region northeast of the nucleus. The similar line ratios, kinematics, and physical direction suggest a common source of ionization for the outflow regions and the extended NE nebula.

In the following, we explore a scenario where the NE nebula is produced by the cooling of warm ionized gas driven by AGN outflows. A prominent feature of the NE nebula is its clumpy and filamentary morphology. Filaments of ionized gas extending tens of kpc have been observed in the Perseus Cluster central galaxy NGC 1275 (e.g Conselice et al. 2001; Fabian et al. 2008; Gendron-Marsolais et al. 2018). The NE nebula in Mrk 273 is similar in terms of having filaments with both similar morphology and kinematics of ~ 100 km s^{-1}. Filaments of cold gas extending tens of kiloparsecs from AGN outflows have been explored in radiation-hydrodynamic simulations of AGN feedback (Qiu et al. 2020). In simulations, an AGN drives multiphase outflows containing hot ($T > 10^7$ K), warm ($10^4 < T \leq 10^7$ K), and cold ($T \leq 10^4$ K) gas. As

the outflowing gas travels outwards, the temperature decreases primarily from radiative cooling. The outflows experience ram pressure from the ambient materials, which have a larger effect on the hot gas than the warm gas, as the latter has a shorter cooling timescale leading to a decreased cross section. As a result, outflows in the hot phase are confined in the central ~ 2 kpc, while outflows in the warm phase are confined in the region between $2-4$ kpc. Cold gas forming out of the warm outflows due to radiative cooling is least affected by ram pressure can travel beyond distances of 20 kpc. As a result, ram pressure promotes the formation of cold filaments over tens of kpc from warm outflows.

In the KCWI data of Mrk 273, outflows with $\sigma \sim 200$ km s^{-1} are observed in the outflow regions spanning the NE and SW directions for ~ 5 kpc. The NE nebula, with $\sigma \sim 50$ km s^{-1}, lies ahead of the NE outflow region and extends ~ 20 kpc. The kinematic distribution of the outflow region and the NE nebula is similar to the extended Hα filaments observed in NGC 1275, where the gas dislpays a velocity dispersion of ~ 200 km s^{-1} in the central few kpc, and declines to $\lesssim 100$ km s^{-1} beyond ~ 10 kpc (Gendron-Marsolais et al. 2018). The NE outflow region could represent the initial warm outflows launched by the AGN. The outflow regions and the NE nebula both display similar line ratios suggesting a mixing of shock and AGN ionization. The shocks can result from the interaction between the warm outflows and the ambient materials, when ram pressure gradually suppresses the warm outflows while dynamically less turbulent, cooler gas survives and forms the NE nebula.

4.6 Conclusions

In this paper we present new KCWI observations of the ULIRG Mrk 273. We analyze the morphology, kinematics, and ionization of the ionized gas in the system. We examine the properties of the ionized gas in three regions: the nuclear region, the NE nebula and the SW nebula. We detect emission in multiple emission lines in the two extended nebulae up to ~ 20

kpc from the center of the galaxy. Our main findings are summarized below:

1. We detect high ionization [NeV]3426, [OIII]4363, and HeII4684 emission in the NE nebula, tracing the morphology of the nebula as seen in [OIII]5007 emission. These high ionization lines are not detected in the SW nebula.

2. In the center of the galaxy we detect high velocity gas with $\sigma > 250$ km s^{-1} along the direction of the previously-detected bipolar superbubbles, but to a distance of ~ 5 kpc, approximately two to three times the previously-reported size. Moderately broad emission with $\sigma \sim 150 - 250$ km s^{-1} is observed in the previously reported outflow regions, extending ~ 5 kpc in the NE and SW directions.

3. The larger scale extended nebulae have fairly uniform velocity dispersion, $\sigma \sim 100 - 150$ km s^{-1} in the SW nebula and $\sigma \sim 50$ km s^{-1} in the NE nebula.

4. The ratios of various emission lines within the nuclear region are correlated with the kinematic structures. In the outflow region, high line ratios are measured for [OIII]5007/Hβ and HeII/Hβ. In the superbubbles, high line ratios are measured for [OII]3726,9/[OIII]5007 and [OIII]4363/[OIII]5007.

5. Line ratio diagnostics of high ionization emission lines show significant shock plus precursor excitation in the NE nebula and the nuclear region. There appears to be mixing between AGN photoionization and shock excitation in both regions. Stronger shock contribution is observed in the nuclear superbubbles, while relatively strong AGN photoionzation is observed in the outflow regions and the NE nebula.

6. The NE outflow region and NE nebula display similarity in kinematics and line ratios, and are spatially connected.

7. We explore a possible scenario in which the warm ($10^4 - 10^7$ K) gas in the AGN-driven outflows in the outflow regions cools and forms extended filaments of kinematically quiescent

gas in the NE nebula on scales of ~ 20 kpc.

Mrk 273 is a unique source at a critical stage of evolution with potentially powerful feedback in action. Our results present new observations with extensive spatial and wavelength coverage of Mrk 273. We reveal in detail the complex two-dimensional kinematics in the nuclear region as well as in the extended large-scale nebulae. Maps of multiple high ionization emission lines allow for spatially-resolved diagnostics of ionized gas in the galaxy. Our results demonstrate the power of IFU observations in uncovering the complex features of ULIRGs and AGN-driven outflows, vital to our understanding of the process of mergers and feedback in the evolution of galaxies.

4.7 Acknowledgements

The data presented herein were obtained at the W. M. Keck Observatory, which is operated as a scientific partnership among the California Institute of Technology, the University of California and the National Aeronautics and Space Administration. The Observatory was made possible by the generous financial support of the W. M. Keck Foundation. The authors wish to recognize and acknowledge the very significant cultural role and reverence that the summit of Maunakea has always had within the indigenous Hawaiian community. We are most fortunate to have the opportunity to conduct observations from this mountain.

Chapter 4, in full, is currently being prepared for submission for publication of the material. Leung, Gene C. K., Coil, A. L., Rupke, D. S. N. and Perrotta, S. The dissertation author was the primary investigator and author of this paper.

Chapter 5

Conclusions and Future Work

In this dissertation, I use results from large surveys as well as detailed observations of individual objects to study the properties, demographics and impact of AGN-driven outflows in the early and contemporary Universe.

In Chapter 2, I present a study using data from the first two years of the MOSDEF survey, focusing on the incidence and physical properties AGN-driven outflows at $z \sim 2$. I use this dataset to lead one of the first efforts to systematically identify and characterize AGN-driven ionized outflows at $z \sim 2$. I first determine the prevalence of AGN outflows at $z \sim 2$. I show that ionized outflows in emission are common in AGN at $z \sim 2$, with an incidence rate of 17%, at least as high as in similar datasets in the local Universe. I find that there is a seven-fold increase in the incidence rate of outflows in AGN than in a stellar mass-matched control sample of inactive galaxies, showing that these outflows are driven by AGN activity. Moreover, I find that these outflows are fast ($\sim$ 1000 km s^{-1}) and extended ($\sim$ 5 kpc), reaching similar scales as their host galaxies. By comparing the observed kinematics and physical extent of these outflows with analytic solutions, I show that these outflows are in the energy-conserving phase, while the momentum-conserving solutions underestimate the observed velocities . I determine the excitation mechanisms of the outflows using rest-frame optical emission line ratio diagnostics,

showing that the outflowing gas has enhanced photonionization contribution from AGN relative to star formation, and that shock excitation is unlikely. This is consistent with the picture of negative AGN feedback, in which AGN outflows regulate or quench star formation, and shows that the impact of positive AGN feedback, in which AGN outflows stimulate star formation, is not prominent on galaxy scales.

In Chapter 3, I present a study using the full dataset of the MOSDEF survey, focusing on the demographics of AGN-dricen outflows and the relation between outflows and the galaxy and AGN populations. With the statistical AGN sample and uniform galaxy sample in the MOSDEF survey, I show that, after accounting for the common AGN observational selection bias in M_*, AGN-driven outflows occur equally frequently in virtually all galaxies probed by MOSDEF, independent of M_* and SFR, in both star-forming and quiescent galaxies. This shows that AGN-driven outflows are a widespread phenomenon that occur uniformly among galaxies both along and across the SF main sequence, and across different phases of galaxy evolution. I show that the kinetic power of the outflows at $z \sim 2$ are $\sim 0.01 - 1\%$ of the AGN bolometric luminosity ($L_{\rm AGN}$), similar to that found in the local Universe. Moreover, I show for the first time in a uniform sample of AGN at $z \sim 2$ that the mass and energy outflow rates depends most strongly on the $L_{\rm AGN}$ but not significantly on M_* or SFR. Since the power of the outflows is primarily determined by $L_{\rm AGN}$ and the kinetic coupling efficiency is largely unchanged over cosmic time, AGN-driven outflows are more energetic at $z \sim 2$, where luminous AGN are the most prevalent. The mass outflow rate observed is typically a substantial fraction of, or comparable to, the SFR of the host galaxy, and increases with $L_{\rm AGN}$. This shows that luminous AGN are capable of driving powerful outflows that at least regulate, and may quench, star formation in their host galaxies.

In Chapter 4, I present high sensitivity and large field of view IFU observations of the ULIRG and AGN Mrk 273 using KCWI. This study focuses on the fast outflows near the AGN, as well as the properties and origin extended nebulae of ionized gas on scales of $\gtrsim 20$ kpc. I show that the previously reported nuclear superbubbles extend to ~ 5 kpc, two to three times greater

than the previously reported size. High ionization [NeV]3426, [OIII]4363 and HeII4684 emission lines are detected in the extended NE nebula for the first time. Analysis of flux ratios of high ionization emission lines reveal significant contribution from shock plus precursor ionization in the NE nebula and the nuclear region, mixed with AGN photoionization. I discuss the KCWI data and its relation to theoretical models where the warm phase of an AGN-driven outflow can lead to the formation of extended and kinematically quiescent cold gas at scales of tens of kpc. The data suggests that AGNs are capable of ejecting gas to large distances through the cooling of outflows during the critical ULIRG phase of galaxy evolution.

5.1 Unveiling the Impact of Molecular AGN-Driven Outflows at $z \sim 2$

In the local Universe ($z \sim 0.1$), outflows in AGNs have been observed to be ubiquitous and extend to kpc scales in both ionized and molecular phases (e.g. Mullaney et al. 2013; Cicone et al. 2014). In order to ascertain the importance of AGN outflows, however, it is crucial to study them at $z \sim 2$, when both galaxies and SMBHs are undergoing peak growth, and when AGN outflows should be the most prevalent, powerful, and impactful. Unfortunately, observations of molecular outflows at this crucial epoch are sorely lacking, with current studies including only a few sources (e.g. Vayner et al. 2017; Herrera-Camus et al. 2019). Studies at lower redshift (e.g. Fiore et al. 2017) have revealed large and massive molecular outflows that carry gas roughly 10 times more massive and 3 times more extended than the ionized outflows in these sources. As such, tracing the outflows in the ionized phase alone can substantially underestimate the full impact of the outflow on the host galaxy. To fully quantify the impact of AGN outflows, it is crucial to simultaneously characterize their multi-phase content, which includes both molecular and ionized gas. This can be achieved at $z \sim 2$ by combining new observations from the Atacama Large Millimeter Array (ALMA) with existing rest-frame optical spectra, observed at NIR wavelengths.

In the future, I aim to capitalize on the success of the MOSDEF survey, in which I lead one of the first efforts to systematically identify and characterize AGN-driven ionized outflows at $z \sim 2$. A key measure of the impact of AGN-driven outflows is the mass-loading factor $\eta = \dot{M}/\mathrm{SFR}$. I show in this dissertation that η of these ionized outflows observed is typically $\sim 0.1 - 1$. It is currently unclear from these modest η values whether these ionized outflows alone can fully quench star formation in their host galaxies or only regulate it. Observations of molecular outflows is the missing link in determining the full impact of AGN outflows to the evolution of their host galaxy in these systems. The unique MOSDEF dataset provides a statistical sample of known ionized outflows with robust kinematic, spatial, energetic, and mass measurements in a representative sample of AGNs at $z \sim 2$.

I plan to select targets from this ideal parent sample for ALMA observations to identify and characterize molecular outflows, obtain robust constraints on the total outflow mass in these systems, and quantify their full impact on galaxy evolution at the peak of galaxy and AGN growth. The AGN in this parent sample mostly reside in the star-forming main sequence, providing a sample that is representative of the typical star-forming galaxy population. Unlike in previous ALMA observations of molecular outflows in AGN at $z \sim 2$, which were focused on the most luminous quasars, the AGN in the MOSDEF parent sample span a wide luminosity range which is largely unexplored territory in the literature. This will result in the first uniform statistical sample of AGN-driven outflows with simultaneous measurements of their ionized and molecular contents at $z \sim 2$. The sample will cover a comprehensive range of AGN, galaxy, and outflow properties, providing superb laboratories for studying the impact of AGN-driven molecular outflows on the evolution of galaxies in a broader context at $z \sim 2$.

5.2 Revealing the Full Physical Extent of AGN Outflows

An actively-debated question in studies of AGN-driven outflows is how far they extend. The physical extent is key to understanding the impact outflows have on their host galaxies, as it determines the mass and energy outflow rates, and whether the outflowing gas escapes the host dark matter halos, populating not only the CGM but also the IGM. While I have shown in this dissertation that at $z \sim 2$, similar to that in the local Universe, AGN-driven outflows can extend to the galaxy disk scale length (1-10 kpc), these extents are lower limits, restricted by instrument sensitivity to low surface brightness emission as well as the FOV of existing IFS. However, it has been observed that substantial outflowing gas mass often resides in low density, and thus low surface brightness, regions of outflows that account for a substantial fraction of the known physical extent (Mingozzi et al. 2019), such that current measurements likely underestimate the actual mass in outflows.

The new Keck/KCWI IFS provides has an order of magnitude increase in sensitivity and FOV compared to previous instruments. In the pilot program presented in this dissertation, I used KCWI to observe outflows in a nearby IR-luminous, obscured quasar, Mrk 273. In collaboration with Prof. David Rupke and Prof. Alison Coil, I have obtained KCWI data on eight more nearby quasars with known ionized outflows. I plan to to use this statistical sample of quasar outflows to robustly determine the physical extent as well as spatially-resolved kinematics and ionization of outflows in AGN. I will compare the robustly measurements of physical extents from new observations with those from existing observations, and establish a relation between the two as a function of the depth of the observations, as well as AGN properties. This will allow us to estimate the actual physical extents of the wealth of existing measurements of AGN outflows, potentially updating our understanding of the impact of the outflows in galaxy evolution. Moreover, the driving mechanism of AGN outflows are currently hotly debated, with contradicting evidence supporting a radiation-driven momentum-conserving wind scenario and

an energy-conserving wind scenario with a momentum boost. Such an inconsistency is likely due to the large uncertainty in the measured outflowing momentum flux obtained from physical extent measurements of heterogeneous observation depths or instrumental limits. I will use these new observations to construct a homogeneous sample of AGN-driven outflows with reliable measurements, and determine the driving mechanism of these outflows. Such detailed studies are required to robustly determine the importance of AGN-driven outflows in galaxy evolution and the origin of AGN-driven outflows.

5.3 Quantifying AGN-driven Outflows with Very Large Samples

To reveal the role of AGN-driven outflows in galaxy evolution and determine their physical characteristics in the context of the galaxy and AGN populations, it is necessary to have a statistical sample of AGN selected from a uniform sample of galaxies. In this dissertation, I use the full MOSDEF dataset and construct the largest uniform spectroscopic sample of AGN at $z \sim 2$ to study the relation between outflows and the galaxy and AGN populations. I show that, after accounting for the common AGN observational selection bias in M_*, AGN-driven outflows occur equally frequently in virtually all galaxies probed by MOSDEF, independent of M_* and SFR. This shows that careful treatment of selection biases are crucial in such statistical studies in order to make correct conclusions about the sample. Moreover, I show for the first time in a uniform sample of AGN at $z \sim 2$ that the mass and energy outflow rates depend primarily on $L_{\rm AGN}$ but not significantly on M_* or SFR.

While this dissertation presented a census of AGN-driven outflows with the largest sample at $z \sim 2$, studies at high redshift are inevitably limited in terms of signal-to-noise ratio (S/N) and sample size compared with those in the local Universe. The local Universe provides an ideal testing ground for studying outflow incidence or properties and host galaxy or AGN properties,

benefiting from a wealth of spectroscopic data available in very large surveys such as the SDSS, where $\sim 10^4$ AGN have been observed. Such a large sample is currently unachievable at high redshift.

In the future, I plan to take advantage of the very large samples of AGN in SDSS to robustly determine which galaxies or AGN host outflows and the major deciding factor of outflow properties. While many successful studies of AGN-driven outflows have been conducted using SDSS data (e.g. Mullaney et al. 2013; Woo et al. 2016; Perna et al. 2017b,a), these studies study AGN samples only, and the relation between outflows and the host galaxy population has not been examined. I will use sources in the public catalog of multicomponent emission line fits of over 20,000 optical SDSS AGN in presented in Mullaney et al. (2013), which provides the outflow velocity and mass from the [OIII] and Hβ emission lines, while obtaining host galaxy properties from the MPA-JHU catalog. With this sample, I will disentangle the complex convolution among galaxy and AGN properties, as well as observational biases due to S/N, which is not currently possible using relatively small samples at high redshift. Only such a sample enables one to answer the critical open question of what drives both the incidence and impact of AGN outflows within the galaxy population.

Bibliography

Aird J., Coil A. L., Georgakakis A. 2018, X-rays across the galaxy population - II. The distribution of AGN accretion rates as a function of stellar mass and redshift., MNRAS, 474, 1225, doi: 10.1093/mnras/stx2700

Aird J., Coil A. L., Georgakakis A. 2019, X-rays across the galaxy population - III. The incidence of AGN as a function of star formation rate, MNRAS, 484, 4360, doi: 10.1093/mnras/stz125

Aird J., Coil A. L., Georgakakis A., Nandra K., Barro G., Pérez-González P. G. 2015, The evolution of the X-ray luminosity functions of unabsorbed and absorbed AGNs out to z$\sim$ 5, MNRAS, 451, 1892, doi: 10.1093/mnras/stv1062

Aird J., Nandra K., Laird E. S., Georgakakis A., Ashby M. L. N., Barmby P., Coil A. L., Huang J. S., Koekemoer A. M., Steidel C. C., Willmer C. N. A. 2010, The evolution of the hard X-ray luminosity function of AGN, MNRAS, 401, 2531, doi: 10.1111/j.1365-2966.2009.15829.x

Aird J., Coil A. L., Moustakas J., Blanton M. R., Burles S. M., Cool R. J., Eisenstein D. J., Smith M. S. M., Wong K. C., Zhu G. 2012, PRIMUS: The Dependence of AGN Accretion on Host Stellar Mass and Color, ApJ, 746, 90, doi: 10.1088/0004-637X/746/1/90

Aladro R., König S., Aalto S., González-Alfonso E., Falstad N., Martín S., Muller S., García-Burillo S., Henkel C., van der Werf P., Mills E., Fischer J., Costagliola F., Krips M. 2018, Molecular gas in the northern nucleus of Mrk 273: Physical and chemical properties of the disc and its outflow, A&A, 617, A20, doi: 10.1051/0004-6361/201833338

Alexander D. M., Swinbank A. M., Smail I., McDermid R., Nesvadba N. P. H. 2010, Searching for evidence of energetic feedback in distant galaxies: a galaxy wide outflow in a z ~2 ultraluminous infrared galaxy, MNRAS, 402, 2211, doi: 10.1111/j.1365-2966.2009.16046.x

Allen M. G., Groves B. A., Dopita M. A., Sutherland R. S., Kewley L. J. 2008, The MAPPINGS III Library of Fast Radiative Shock Models, ApJS, 178, 20, doi: 10.1086/589652

Allington-Smith J., Murray G., Content R., Dodsworth G., Davies R., Miller B. W., Jorgensen I., Hook I., Crampton D., Murowinski R. 2002, Integral Field Spectroscopy with the Gemini Multiobject Spectrograph. I. Design, Construction, and Testing, PASP, 114, 892, doi: 10.1086/341712

Antonucci R. 1993, Unified models for active galactic nuclei and quasars., ARA&A, 31, 473, doi: 10.1146/annurev.aa.31.090193.002353

Antonuccio-Delogu V., Silk J. 2010, AGN Feedback in Galaxy Formation, doi: 10.1017/CBO9780511761386

Arnouts S., Schiminovich D., Ilbert O., Tresse L., Milliard B., Treyer M., Bardelli S., Budavari T., Wyder T. K., Zucca E., Le Fèvre O., Martin D. C., Vettolani G., Adami C., Arnaboldi M., Barlow T., Bianchi L., Bolzonella M., Bottini D., Byun Y. I., Cappi A., Charlot S., Contini T., Donas J., Forster K., Foucaud S., Franzetti P., Friedman P. G., Garilli B., Gavignaud I., Guzzo L., Heckman T. M., Hoopes C., Iovino A., Jelinsky P., Le Brun V., Lee Y. W., Maccagni D., Madore B. F., Malina R., Marano B., Marinoni C., McCracken H. J., Mazure A., Meneux B., Merighi R., Morrissey P., Neff S., Paltani S., Pellò R., Picat J. P., Pollo A., Pozzetti L., Radovich M., Rich R. M., Scaramella R., Scodeggio M., Seibert M., Siegmund O., Small T., Szalay A. S., Welsh B., Xu C. K., Zamorani G., Zanichelli A. 2005, The GALEX VIMOS-VLT Deep Survey Measurement of the Evolution of the 1500 Å Luminosity Function, ApJ, 619, L43, doi: 10.1086/426733

Azadi M., Aird J., Coil A. L., Moustakas J., Mendez A. J., Blanton M. R., Cool R. J., Eisenstein D. J., Wong K. C., Zhu G. 2015, PRIMUS: The Relationship between Star Formation and AGN Accretion, ApJ, 806, 187, doi: 10.1088/0004-637X/806/2/187

Azadi M., Coil A. L., Aird J., Reddy N., Shapley A., Freeman W. R., Kriek M., Leung G. C. K., Mobasher B., Price S. H., Sanders R. L., Shivaei I., Siana B. 2017, The MOSDEF Survey: AGN Multi-wavelength Identification, Selection Biases, and Host Galaxy Properties, ApJ, 835, 27, doi: 10.3847/1538-4357/835/1/27

Azadi M., Coil A., Aird J., Shivaei I., Reddy N., Shapley A., Kriek M., Freeman W. R., Leung G. C. K., Mobasher B., Price S. H., Sanders R. L., Siana B., Zick T. 2018, The MOSDEF Survey: The Nature of Mid-infrared Excess Galaxies and a Comparison of IR and UV Star Formation Tracers at $z \sim 2$, ApJ, 866, 63, doi: 10.3847/1538-4357/aad3c8

Bae H.-J., Woo J.-H. 2016, The Prevalence of Gas Outflows in Type 2 AGNs. II. 3D Biconical Outflow Models, ApJ, 828, 97, doi: 10.3847/0004-637X/828/2/97

Baldry I. K., Glazebrook K., Brinkmann J., Ivezić Ž., Lupton R. H., Nichol R. C., Szalay A. S. 2004, Quantifying the Bimodal Color-Magnitude Distribution of Galaxies, ApJ, 600, 681, doi: 10.1086/380092

Baldry I. K., Glazebrook K., Budavári T., Eisenstein D. J., Annis J., Bahcall N. A., Blanton M. R., Brinkmann J., Csabai I., Heckman T. M., Lin H., Loveday J., Nichol R. C., Schneider D. P. 2005, The Sloan Digital Sky Survey u-band Galaxy Survey: luminosity functions and evolution, MNRAS, 358, 441, doi: 10.1111/j.1365-2966.2005.08799.x

Baldry I. K., Driver S. P., Loveday J., Taylor E. N., Kelvin L. S., Liske J., Norberg P., Robotham A. S. G., Brough S., Hopkins A. M., Bamford S. P., Peacock J. A., Bland-Hawthorn J.,

Conselice C. J., Croom S. M., Jones D. H., Parkinson H. R., Popescu C. C., Prescott M., Sharp R. G., Tuffs R. J. 2012, Galaxy And Mass Assembly (GAMA): the galaxy stellar mass function at z ¡ 0.06, MNRAS, 421, 621, doi: 10.1111/j.1365-2966.2012.20340.x

Baldwin J. A., Phillips M. M., Terlevich R. 1981, Classification parameters for the emission-line spectra of extragalactic objects., PASP, 93, 5, doi: 10.1086/130766

Baron D., Netzer H. 2019a, Discovering AGN-driven winds through their infrared emission - I. General method and wind location, MNRAS, 482, 3915, doi: 10.1093/mnras/sty2935

Baron D., Netzer H. 2019b, Discovering AGN-driven winds through their infrared emission - II. Mass outflow rate and energetics, MNRAS, 486, 4290, doi: 10.1093/mnras/stz1070

Becker R. H., White R. L., Helfand D. J. 1995, The FIRST Survey: Faint Images of the Radio Sky at Twenty Centimeters, ApJ, 450, 559, doi: 10.1086/176166

Behroozi P. S., Wechsler R. H., Conroy C. 2013a, On the Lack of Evolution in Galaxy Star Formation Efficiency, ApJ, 762, L31, doi: 10.1088/2041-8205/762/2/L31

Behroozi P. S., Wechsler R. H., Conroy C. 2013b, The Average Star Formation Histories of Galaxies in Dark Matter Halos from z = 0-8, ApJ, 770, 57, doi: 10.1088/0004-637X/770/1/57

Bennert N., Falcke H., Schulz H., Wilson A. S., Wills B. J. 2002, Size and Structure of the Narrow-Line Region of Quasars, ApJ, 574, L105, doi: 10.1086/342420

Benson A. J., Bower R. G., Frenk C. S., Lacey C. G., Baugh C. M., Cole S. 2003, What Shapes the Luminosity Function of Galaxies?, ApJ, 599, 38, doi: 10.1086/379160

Bicknell G. V., Sutherland R. S., van Breugel W. J. M., Dopita M. A., Dey A., Miley G. K. 2000, Jet-induced Emission-Line Nebulosity and Star Formation in the High-Redshift Radio Galaxy 4C 41.17, ApJ, 540, 678, doi: 10.1086/309343

Blanton M. R., Hogg D. W., Bahcall N. A., Baldry I. K., Brinkmann J., Csabai I., Eisenstein D., Fukugita M., Gunn J. E., Ivezić Ž., Lamb D. Q., Lupton R. H., Loveday J., Munn J. A., Nichol R. C., Okamura S., Schlegel D. J., Shimasaku K., Strauss M. A., Vogeley M. S., Weinberg D. H. 2003, The Broadband Optical Properties of Galaxies with Redshifts 0.02¡z¡0.22, ApJ, 594, 186, doi: 10.1086/375528

Borch A., Meisenheimer K., Bell E. F., Rix H. W., Wolf C., Dye S., Kleinheinrich M., Kovacs Z., Wisotzki L. 2006, The stellar masses of 25 000 galaxies at $0.2 \leq z \leq 1.0$ estimated by the COMBO-17 survey, A&A, 453, 869, doi: 10.1051/0004-6361:20054376

Bouché N., Dekel A., Genzel R., Genel S., Cresci G., Förster Schreiber N. M., Shapiro K. L., Davies R. I., Tacconi L. 2010, The Impact of Cold Gas Accretion Above a Mass Floor on Galaxy Scaling Relations, ApJ, 718, 1001, doi: 10.1088/0004-637X/718/2/1001

Brammer G. B., van Dokkum P. G., Franx M., Fumagalli M., Patel S., Rix H.-W., Skelton R. E., Kriek M., Nelson E., Schmidt K. B., Bezanson R., da Cunha E., Erb D. K., Fan X., Förster Schreiber N., Illingworth G. D., Labbé I., Leja J., Lundgren B., Magee D., Marchesini D., McCarthy P., Momcheva I., Muzzin A., Quadri R., Steidel C. C., Tal T., Wake D., Whitaker K. E., Williams A. 2012, 3D-HST: A Wide-field Grism Spectroscopic Survey with the Hubble Space Telescope, ApJS, 200, 13, doi: 10.1088/0067-0049/200/2/13

Brandt W. N., Alexander D. M. 2015, Cosmic X-ray surveys of distant active galaxies. The demographics, physics, and ecology of growing supermassive black holes, A&A Rev., 23, 1, doi: 10.1007/s00159-014-0081-z

Brennan R., Pandya V., Somerville R. S., Barro G., Taylor E. N., Wuyts S., Bell E. F., Dekel A., Ferguson H. C., McIntosh D. H., Papovich C., Primack J. 2015, Quenching and morphological transformation in semi-analytic models and CANDELS, MNRAS, 451, 2933, doi: 10.1093/mnras/stv1007

Brusa M., Zamorani G., Comastri A., Hasinger G., Cappelluti N., Civano F., Finoguenov A., Mainieri V., Salvato M., Vignali C., Elvis M., Fiore F., Gilli R., Impey C. D., Lilly S. J., Mignoli M., Silverman J., Trump J., Urry C. M., Bender R., Capak P., Huchra J. P., Kneib J. P., Koekemoer A., Leauthaud A., Lehmann I., Massey R., Matute I., McCarthy P. J., McCracken H. J., Rhodes J., Scoville N. Z., Taniguchi Y., Thompson D. 2007, The XMM-Newton Wide-Field Survey in the COSMOS Field. III. Optical Identification and Multiwavelength Properties of a Large Sample of X-Ray-Selected Sources, ApJS, 172, 353, doi: 10.1086/516575

Brusa M., Bongiorno A., Cresci G., Perna M., Marconi A., Mainieri V., Maiolino R., Salvato M., Lusso E., Santini P., Comastri A., Fiore F., Gilli R., La Franca F., Lanzuisi G., Lutz D., Merloni A., Mignoli M., Onori F., Piconcelli E., Rosario D., Vignali C., Zamorani G. 2015, X-shooter reveals powerful outflows in z $\sim$ 1.5 X-ray selected obscured quasi-stellar objects, MNRAS, 446, 2394, doi: 10.1093/mnras/stu2117

Brusa M., Cresci G., Daddi E., Paladino R., Perna M., Bongiorno A., Lusso E., Sargent M. T., Casasola V., Feruglio C., Fraternali F., Georgiev I., Mainieri V., Carniani S., Comastri A., Duras F., Fiore F., Mannucci F., Marconi A., Piconcelli E., Zamorani G., Gilli R., La Franca F., Lanzuisi G., Lutz D., Santini P., Scoville N. Z., Vignali C., Vito F., Rabien S., Busoni L., Bonaglia M. 2018, Molecular outflow and feedback in the obscured quasar XID2028 revealed by ALMA, A&A, 612, A29, doi: 10.1051/0004-6361/201731641

Bunker A. J., Stanway E. R., Ellis R. S., McMahon R. G. 2004, The star formation rate of the Universe at z~6 from the Hubble Ultra-Deep Field, MNRAS, 355, 374, doi: 10.1111/j.1365-2966.2004.08326.x

Burbidge E. M., Burbidge G. R. 1965, Optical Evidence Suggesting the Occurrence of a Violent Outburst in NGC 1275., ApJ, 142, 1351, doi: 10.1086/148421

Calzetti D., Armus L., Bohlin R. C., Kinney A. L., Koornneef J., Storchi-Bergmann T. 2000, The Dust Content and Opacity of Actively Star-forming Galaxies, ApJ, 533, 682, doi: 10.1086/308692

Cano-Díaz M., Maiolino R., Marconi A., Netzer H., Shemmer O., Cresci G. 2012, Observational evidence of quasar feedback quenching star formation at high redshift, A&A, 537, L8, doi: 10.1051/0004-6361/201118358

Cappellari M. 2009, Voronoi binning: Optimal adaptive tessellations of multi-dimensional data, arXiv e-prints, arXiv:0912.1303. https://arxiv.org/abs/0912.1303

Cappellari M. 2012, pPXF: Penalized Pixel-Fitting stellar kinematics extraction. http://ascl.net/1210.002

Cappellari M., Copin Y. 2003, Adaptive spatial binning of integral-field spectroscopic data using Voronoi tessellations, MNRAS, 342, 345, doi: 10.1046/j.1365-8711.2003.06541.x

Cardelli J. A., Clayton G. C., Mathis J. S. 1989, The Relationship between Infrared, Optical, and Ultraviolet Extinction, ApJ, 345, 245, doi: 10.1086/167900

Chabrier G. 2003, Galactic Stellar and Substellar Initial Mass Function, PASP, 115, 763, doi: 10.1086/376392

Cicone C., Feruglio C., Maiolino R., Fiore F., Piconcelli E., Menci N., Aussel H., Sturm E. 2012, The physics and the structure of the quasar-driven outflow in Mrk 231, A&A, 543, A99, doi: 10.1051/0004-6361/201218793

Cicone C., Maiolino R., Sturm E., Graciá-Carpio J., Feruglio C., Neri R., Aalto S., Davies R., Fiore F., Fischer J., García-Burillo S., González-Alfonso E., Hailey-Dunsheath S., Piconcelli E., Veilleux S. 2014, Massive molecular outflows and evidence for AGN feedback from CO observations, A&A, 562, A21, doi: 10.1051/0004-6361/201322464

Ciliegi P., Zamorani G., Hasinger G., Lehmann I., Szokoly G., Wilson G. 2003, A deep VLA survey at 6 cm in the Lockman Hole, A&A, 398, 901, doi: 10.1051/0004-6361:20021721

Ciliegi P., Zamorani G., Bondi M., Pozzetti L., Bolzonella M., Gregorini L., Garilli B., Iovino A., McCracken H. J., Mellier Y., Radovich M., de Ruiter H. R., Parma P., Bottini D., Le Brun V., Le Fèvre O., Maccagni D., Picat J. P., Scaramella R., Scodeggio M., Tresse L., Vettolani G., Zanichelli A., Adami C., Arnaboldi M., Arnouts S., Bardelli S., Cappi A., Charlot S., Contini T., Foucaud S., Franzetti P., Guzzo L., Ilbert O., Marano B., Marinoni C., Mathez G., Mazure A., Meneux B., Merighi R., Merluzzi P., Paltani S., Pollo A., Zucca E., Bongiorno A., Busarello G., Gavignaud I., Pellò R., Ripepi V., Rizzo D. 2005, The VVDS-VLA deep field. II. Optical and near infrared identifications of VLA $S_{1.4GHz}$ ¿ 80 μ Jy sources in the VIMOS VLT deep survey VVDS-02h field, A&A, 441, 879, doi: 10.1051/0004-6361:20042204

Coatman L., Hewett P. C., Banerji M., Richards G. T., Hennawi J. F., Prochaska J. X. 2019, Kinematics of C IV and [O III] emission in luminous high-redshift quasars, MNRAS, 486, 5335, doi: 10.1093/mnras/stz1167

Coil A. L., Aird J., Reddy N., Shapley A. E., Kriek M., Siana B., Mobasher B., Freeman W. R., Price S. H., Shivaei I. 2015, The MOSDEF Survey: Optical Active Galactic Nucleus Diagnostics at z ~2.3, ApJ, 801, 35, doi: 10.1088/0004-637X/801/1/35

Conroy C., Gunn J. E., White M. 2009, The Propagation of Uncertainties in Stellar Population Synthesis Modeling. I. The Relevance of Uncertain Aspects of Stellar Evolution and the Initial Mass Function to the Derived Physical Properties of Galaxies, ApJ, 699, 486, doi: 10.1088/0004-637X/699/1/486

Conselice C. J., Gallagher John S. I., Wyse R. F. G. 2001, On the Nature of the NGC 1275 System, AJ, 122, 2281, doi: 10.1086/323534

Costa T., Rosdahl J., Sijacki D., Haehnelt M. G. 2018, Driving gas shells with radiation pressure on dust in radiation-hydrodynamic simulations, MNRAS, 473, 4197, doi: 10.1093/mnras/stx2598

Costa T., Sijacki D., Haehnelt M. G. 2014, Feedback from active galactic nuclei: energy- versus momentum-driving, MNRAS, 444, 2355, doi: 10.1093/mnras/stu1632

Crenshaw D. M., Kraemer S. B., George I. M. 2003, Mass Loss from the Nuclei of Active Galaxies, ARA&A, 41, 117, doi: 10.1146/annurev.astro.41.082801.100328

Croton D. J., Springel V., White S. D. M., De Lucia G., Frenk C. S., Gao L., Jenkins A., Kauffmann G., Navarro J. F., Yoshida N. 2006, The many lives of active galactic nuclei: cooling flows, black holes and the luminosities and colours of galaxies, MNRAS, 365, 11, doi: 10.1111/j.1365-2966.2005.09675.x

Debuhr J., Quataert E., Ma C.-P. 2012, Galaxy-scale outflows driven by active galactic nuclei, MNRAS, 420, 2221, doi: 10.1111/j.1365-2966.2011.20187.x

Di Matteo T., Springel V., Hernquist L. 2005, Energy input from quasars regulates the growth and activity of black holes and their host galaxies, Nature, 433, 604, doi: 10.1038/nature03335

Donley J. L., Koekemoer A. M., Brusa M., Capak P., Cardamone C. N., Civano F., Ilbert O., Impey C. D., Kartaltepe J. S., Miyaji T., Salvato M., Sanders D. B., Trump J. R., Zamorani G. 2012, Identifying Luminous Active Galactic Nuclei in Deep Surveys: Revised IRAC Selection Criteria, ApJ, 748, 142, doi: 10.1088/0004-637X/748/2/142

Dopita M. A., Sutherland R. S. 1995, Spectral Signatures of Fast Shocks. II. Optical Diagnostic Diagrams, ApJ, 455, 468, doi: 10.1086/176596

Dopita M. A., Sutherland R. S. 2017, Effects of Preionization in Radiative Shocks. II. Application to the Herbig-Haro Objects, ApJS, 229, 35, doi: 10.3847/1538-4365/aa6542

Dubois Y., Gavazzi R., Peirani S., Silk J. 2013, AGN-driven quenching of star formation: morphological and dynamical implications for early-type galaxies, MNRAS, 433, 3297, doi: 10.1093/mnras/stt997

Dutton A. A., van den Bosch F. C., Dekel A. 2010, On the origin of the galaxy star-formation-rate sequence: evolution and scatter, MNRAS, 405, 1690, doi: 10.1111/j.1365-2966.2010.16620.x

Faber S. M., Willmer C. N. A., Wolf C., Koo D. C., Weiner B. J., Newman J. A., Im M., Coil A. L., Conroy C., Cooper M. C., Davis M., Finkbeiner D. P., Gerke B. F., Gebhardt K., Groth E. J., Guhathakurta P., Harker J., Kaiser N., Kassin S., Kleinheinrich M., Konidaris N. P., Kron R. G., Lin L., Luppino G., Madgwick D. S., Meisenheimer K., Noeske K. G., Phillips A. C., Sarajedini V. L., Schiavon R. P., Simard L., Szalay A. S., Vogt N. P., Yan R. 2007, Galaxy Luminosity Functions to z~1 from DEEP2 and COMBO-17: Implications for Red Galaxy Formation, ApJ, 665, 265, doi: 10.1086/519294

Fabian A. C., Johnstone R. M., Sanders J. S., Conselice C. J., Crawford C. S., Gallagher J. S. I., Zweibel E. 2008, Magnetic support of the optical emission line filaments in NGC 1275, Nature, 454, 968, doi: 10.1038/nature07169

Faucher-Giguère C.-A., Quataert E. 2012, The physics of galactic winds driven by active galactic nuclei, MNRAS, 425, 605, doi: 10.1111/j.1365-2966.2012.21512.x

Feain I. J., Papadopoulos P. P., Ekers R. D., Middelberg E. 2007, Dressing a Naked Quasar: Star Formation and Active Galactic Nucleus Feedback in HE 0450-2958, ApJ, 662, 872, doi: 10.1086/518027

Ferrarese L., Merritt D. 2000, A Fundamental Relation between Supermassive Black Holes and Their Host Galaxies, ApJ, 539, L9, doi: 10.1086/312838

Fiore F., Feruglio C., Shankar F., Bischetti M., Bongiorno A., Brusa M., Carniani S., Cicone C., Duras F., Lamastra A., Mainieri V., Marconi A., Menci N., Maiolino R., Piconcelli E., Vietri G., Zappacosta L. 2017, AGN wind scaling relations and the co-evolution of black holes and galaxies, A&A, 601, A143, doi: 10.1051/0004-6361/201629478

Fontana A., Santini P., Grazian A., Pentericci L., Fiore F., Castellano M., Giallongo E., Menci N., Salimbeni S., Cristiani S., Nonino M., Vanzella E. 2009, The fraction of quiescent massive galaxies in the early Universe, A&A, 501, 15, doi: 10.1051/0004-6361/200911650

Förster Schreiber N. M., Übler H., Davies R. L., Genzel R., Wisnioski E., Belli S., Shimizu T., Lutz D., Fossati M., Herrera-Camus R., Mendel J. T., Tacconi L. J., Wilman D., Beifiori A., Brammer G. B., Burkert A., Carollo C. M., Davies R. I., Eisenhauer F., Fabricius M., Lilly S. J., Momcheva I., Naab T., Nelson E. J., Price S. H., Renzini A., Saglia R., Sternberg A., van Dokkum P., Wuyts S. 2019, The KMOS^{3D} Survey: Demographics and Properties of Galactic Outflows at z = 0.6-2.7, ApJ, 875, 21, doi: 10.3847/1538-4357/ab0ca2

Freeman W. R., Siana B., Kriek M., Shapley A. E., Reddy N., Coil A. L., Mobasher B., Muratov A. L., Azadi M., Leung G., Sanders R., Shivaei I., Price S. H., DeGroot L., Kereš D. 2019, The MOSDEF Survey: Broad Emission Lines at z = 1.4-3.8, ApJ, 873, 102, doi: 10.3847/1538-4357/ab0655

Gabor J. M., Bournaud F. 2014, Active galactic nuclei-driven outflows without immediate quenching in simulations of high-redshift disc galaxies, MNRAS, 441, 1615, doi: 10.1093/mnras/stu677

Gaibler V., Khochfar S., Krause M., Silk J. 2012, Jet-induced star formation in gas-rich galaxies, MNRAS, 425, 438, doi: 10.1111/j.1365-2966.2012.21479.x

Gebhardt K., Bender R., Bower G., Dressler A., Faber S. M., Filippenko A. V., Green R., Grillmair C., Ho L. C., Kormendy J., Lauer T. R., Magorrian J., Pinkney J., Richstone D., Tremaine S. 2000, A Relationship between Nuclear Black Hole Mass and Galaxy Velocity Dispersion, ApJ, 539, L13, doi: 10.1086/312840

Gendron-Marsolais M., Hlavacek-Larrondo J., Martin T. B., Drissen L., McDonald M., Fabian A. C., Edge A. C., Hamer S. L., McNamara B., Morrison G. 2018, Revealing the velocity structure of the filamentary nebula in NGC 1275 in its entirety, MNRAS, 479, L28, doi: 10.1093/mnrasl/sly084

Genzel R., Förster Schreiber N. M., Rosario D., Lang P., Lutz D., Wisnioski E., Wuyts E., Wuyts S., Bandara K., Bender R., Berta S., Kurk J., Mendel J. T., Tacconi L. J., Wilman D., Beifiori A., Brammer G., Burkert A., Buschkamp P., Chan J., Carollo C. M., Davies R., Eisenhauer F., Fabricius M., Fossati M., Kriek M., Kulkarni S., Lilly S. J., Mancini C., Momcheva I., Naab T., Nelson E. J., Renzini A., Saglia R., Sharples R. M., Sternberg A., Tacchella S., van Dokkum P. 2014, Evidence for Wide-spread Active Galactic Nucleus-driven Outflows in the Most Massive z ~1-2 Star-forming Galaxies, ApJ, 796, 7, doi: 10.1088/0004-637X/796/1/7

Georgakakis A., Pérez-González P. G., Fanidakis N., Salvato M., Aird J., Messias H., Lotz J. M., Barro G., Hsu L.-T., Nandra K., Rosario D., Cooper M. C., Kocevski D. D., Newman J. A. 2014, Investigating evidence for different black hole accretion modes since redshift z $\sim$ 1, MNRAS, 440, 339, doi: 10.1093/mnras/stu236

González-Alfonso E., Fischer J., Spoon H. W. W., Stewart K. P., Ashby M. L. N., Veilleux S., Smith H. A., Sturm E., Farrah D., Falstad N., Meléndez M., Graciá-Carpio J., Janssen A. W., Lebouteiller V. 2017, Molecular Outflows in Local ULIRGs: Energetics from Multitransition OH Analysis, ApJ, 836, 11, doi: 10.3847/1538-4357/836/1/11

González Delgado R. M., Cerviño M., Martins L. P., Leitherer C., Hauschildt P. H. 2005, Evolutionary stellar population synthesis at high spectral resolution: optical wavelengths, MNRAS, 357, 945, doi: 10.1111/j.1365-2966.2005.08692.x

Greene J. E., Zakamska N. L., Ho L. C., Barth A. J. 2011, Feedback in Luminous Obscured Quasars, ApJ, 732, 9, doi: 10.1088/0004-637X/732/1/9

Grogin N. A., Kocevski D. D., Faber S. M., Ferguson H. C., Koekemoer A. M., Riess A. G., Acquaviva V., Alexander D. M., Almaini O., Ashby M. L. N., Barden M., Bell E. F., Bournaud F., Brown T. M., Caputi K. I., Casertano S., Cassata P., Castellano M., Challis P., Chary R.-R., Cheung E., Cirasuolo M., Conselice C. J., Roshan Cooray A., Croton D. J., Daddi E., Dahlen T., Davé R., de Mello D. F., Dekel A., Dickinson M., Dolch T., Donley J. L., Dunlop J. S., Dutton A. A., Elbaz D., Fazio G. G., Filippenko A. V., Finkelstein S. L., Fontana A., Gardner J. P., Garnavich P. M., Gawiser E., Giavalisco M., Grazian A., Guo Y., Hathi N. P., Häussler B., Hopkins P. F., Huang J.-S., Huang K.-H., Jha S. W., Kartaltepe J. S., Kirshner R. P., Koo D. C., Lai K., Lee K.-S., Li W., Lotz J. M., Lucas R. A., Madau P., McCarthy P. J., McGrath E. J., McIntosh D. H., McLure R. J., Mobasher B., Moustakas L. A., Mozena M., Nandra K., Newman J. A., Niemi S.-M., Noeske K. G., Papovich C. J., Pentericci L., Pope A., Primack J. R., Rajan A., Ravindranath S., Reddy N. A., Renzini A., Rix H.-W., Robaina A. R., Rodney S. A., Rosario D. J., Rosati P., Salimbeni S., Scarlata C., Siana B., Simard L., Smidt J., Somerville R. S., Spinrad H., Straughn A. N., Strolger L.-G., Telford O., Teplitz H. I., Trump J. R., van der Wel A., Villforth C., Wechsler R. H., Weiner B. J., Wiklind T., Wild V., Wilson G., Wuyts S., Yan H.-J., Yun M. S. 2011, CANDELS: The Cosmic Assembly Near-infrared Deep Extragalactic Legacy Survey, ApJS, 197, 35, doi: 10.1088/0067-0049/197/2/35

Groves B. A., Allen M. G. 2010, ITERA: IDL tool for emission-line ratio analysis, NewA, 15, 614, doi: 10.1016/j.newast.2010.02.005

Groves B. A., Dopita M. A., Sutherland R. S. 2004, Dusty, Radiation Pressure-Dominated Photoionization. I. Model Description, Structure, and Grids, ApJS, 153, 9, doi: 10.1086/421113

Hainline K. N., Hickox R., Greene J. E., Myers A. D., Zakamska N. L. 2013, SALT Long-slit Spectroscopy of Luminous Obscured Quasars: An Upper Limit on the Size of the Narrow-line Region?, ApJ, 774, 145, doi: 10.1088/0004-637X/774/2/145

Hainline K. N., Hickox R. C., Greene J. E., Myers A. D., Zakamska N. L., Liu G., Liu X. 2014, Gemini Long-slit Observations of Luminous Obscured Quasars: Further Evidence for an Upper Limit on the Size of the Narrow-line Region, ApJ, 787, 65, doi: 10.1088/0004-637X/787/1/65

Harrison C. M., Alexander D. M., Mullaney J. R., Swinbank A. M. 2014, Kiloparsec-scale outflows are prevalent among luminous AGN: outflows and feedback in the context of the overall AGN population, MNRAS, 441, 3306, doi: 10.1093/mnras/stu515

Harrison C. M., Costa T., Tadhunter C. N., Flütsch A., Kakkad D., Perna M., Vietri G. 2018, AGN outflows and feedback twenty years on, Nature Astronomy, 2, 198, doi: 10.1038/s41550-018-0403-6

Harrison C. M., Alexander D. M., Swinbank A. M., Smail I., Alaghband-Zadeh S., Bauer F. E., Chapman S. C., Del Moro A., Hickox R. C., Ivison R. J., Menéndez-Delmestre K., Mullaney J. R., Nesvadba N. P. H. 2012, Energetic galaxy-wide outflows in high-redshift ultraluminous

infrared galaxies hosting AGN activity, MNRAS, 426, 1073, doi: 10.1111/j.1365-2966.2012.21723.x

Harrison C. M., Alexander D. M., Mullaney J. R., Stott J. P., Swinbank A. M., Arumugam V., Bauer F. E., Bower R. G., Bunker A. J., Sharples R. M. 2016, The KMOS AGN Survey at High redshift (KASHz): the prevalence and drivers of ionized outflows in the host galaxies of X-ray AGN, MNRAS, 456, 1195, doi: 10.1093/mnras/stv2727

Heckman T. M., Armus L., Miley G. K. 1990, On the Nature and Implications of Starburst-driven Galactic Superwinds, ApJS, 74, 833, doi: 10.1086/191522

Heckman T. M., Best P. N. 2014, The Coevolution of Galaxies and Supermassive Black Holes: Insights from Surveys of the Contemporary Universe, ARA&A, 52, 589, doi: 10.1146/annurev-astro-081913-035722

Herrera-Camus R., Tacconi L., Genzel R., Förster Schreiber N., Lutz D., Bolatto A., Wuyts S., Renzini A., Lilly S., Belli S., Übler H., Shimizu T., Davies R., Sturm E., Combes F., Freundlich J., García-Burillo S., Cox P., Burkert A., Naab T., Colina L., Saintonge A., Cooper M., Feruglio C., Weiss A. 2019, Molecular and Ionized Gas Phases of an AGN-driven Outflow in a Typical Massive Galaxy at z $\approx$ 2, ApJ, 871, 37, doi: 10.3847/1538-4357/aaf6a7

Herrera-Camus R., Sturm E., Graciá-Carpio J., Veilleux S., Shimizu T., Lutz D., Stone M., González-Alfonso E., Davies R., Fischer J., Genzel R., Maiolino R., Sternberg A., Tacconi L., Verma A. 2020, Molecular gas inflows and outflows in ultraluminous infrared galaxies at $z \sim 0.2$ and one QSO at z = 6.1, A&A, 633, L4, doi: 10.1051/0004-6361/201937109

Hickox R. C., Mullaney J. R., Alexander D. M., Chen C.-T. J., Civano F. M., Goulding A. D., Hainline K. N. 2014, Black Hole Variability and the Star Formation-Active Galactic Nucleus Connection: Do All Star-forming Galaxies Host an Active Galactic Nucleus?, ApJ, 782, 9, doi: 10.1088/0004-637X/782/1/9

Ho I. T., Kewley L. J., Dopita M. A., Medling A. M., Allen J. T., Bland-Hawthorn J., Bloom J. V., Bryant J. J., Croom S. M., Fogarty L. M. R., Goodwin M., Green A. W., Konstantopoulos I. S., Lawrence J. S., López-Sánchez Á. R., Owers M. S., Richards S., Sharp R. 2014, The SAMI Galaxy Survey: shocks and outflows in a normal star-forming galaxy, MNRAS, 444, 3894, doi: 10.1093/mnras/stu1653

Holt J., Tadhunter C. N., Morganti R., Emonts B. H. C. 2011, The impact of the warm outflow in the young (GPS) radio source and ULIRG PKS 1345+12 (4C 12.50), MNRAS, 410, 1527, doi: 10.1111/j.1365-2966.2010.17535.x

Hook I. M., Jørgensen I., Allington-Smith J. R., Davies R. L., Metcalfe N., Murowinski R. G., Crampton D. 2004, The Gemini-North Multi-Object Spectrograph: Performance in Imaging, Long-Slit, and Multi-Object Spectroscopic Modes, PASP, 116, 425, doi: 10.1086/383624

Hopkins A. M., Beacom J. F. 2006, On the Normalization of the Cosmic Star Formation History, ApJ, 651, 142, doi: 10.1086/506610

Hopkins P. F., Cox T. J., Kereš D., Hernquist L. 2008, A Cosmological Framework for the Co-Evolution of Quasars, Supermassive Black Holes, and Elliptical Galaxies. II. Formation of Red Ellipticals, ApJS, 175, 390, doi: 10.1086/524363

Hopkins P. F., Hernquist L., Cox T. J., Di Matteo T., Robertson B., Springel V. 2006, A Unified, Merger-driven Model of the Origin of Starbursts, Quasars, the Cosmic X-Ray Background, Supermassive Black Holes, and Galaxy Spheroids, ApJS, 163, 1, doi: 10.1086/499298

Hopkins P. F., Quataert E., Murray N. 2012, Stellar feedback in galaxies and the origin of galaxy-scale winds, MNRAS, 421, 3522, doi: 10.1111/j.1365-2966.2012.20593.x

Hubble E. P. 1926, Extragalactic nebulae., ApJ, 64, 321, doi: 10.1086/143018

Husemann B., Scharwächter J., Bennert V. N., Mainieri V., Woo J. H., Kakkad D. 2016, Large-scale outflows in luminous QSOs revisited. The impact of beam smearing on AGN feedback efficiencies, A&A, 594, A44, doi: 10.1051/0004-6361/201527992

Inskip K. J., Villar-Martín M., Tadhunter C. N., Morganti R., Holt J., Dicken D. 2008, PKS2250-41: a case study for triggering, MNRAS, 386, 1797, doi: 10.1111/j.1365-2966.2008.13171.x

Ishibashi W., Fabian A. C. 2012, Active galactic nucleus feedback and triggering of star formation in galaxies, MNRAS, 427, 2998, doi: 10.1111/j.1365-2966.2012.22074.x

Ishibashi W., Fabian A. C., Canning R. E. A. 2013, Can AGN feedback-driven star formation explain the size evolution of massive galaxies?, MNRAS, 431, 2350, doi: 10.1093/mnras/stt333

Ivezić Ž., Menou K., Knapp G. R., Strauss M. A., Lupton R. H., Vand en Berk D. E., Richards G. T., Tremonti C., Weinstein M. A., Anderson S., Bahcall N. A., Becker R. H., Bernardi M., Blanton M., Eisenstein D., Fan X., Finkbeiner D., Finlator K., Frieman J., Gunn J. E., Hall P. B., Kim R. S. J., Kinkhabwala A., Narayanan V. K., Rockosi C. M., Schlegel D., Schneider D. P., Strateva I., SubbaRao M., Thakar A. R., Voges W., White R. L., Yanny B., Brinkmann J., Doi M., Fukugita M., Hennessy G. S., Munn J. A., Nichol R. C., York D. G. 2002, Optical and Radio Properties of Extragalactic Sources Observed by the FIRST Survey and the Sloan Digital Sky Survey, AJ, 124, 2364, doi: 10.1086/344069

Iwasawa K., U V., Mazzarella J. M., Medling A. M., Sanders D. B., Evans A. S. 2018, Testing a double AGN hypothesis for Mrk 273, A&A, 611, A71, doi: 10.1051/0004-6361/201731662

Iwasawa K., Mazzarella J. M., Surace J. A., Sand ers D. B., Armus L., Evans A. S., Howell J. H., Komossa S., Petric A., Teng S. H., U V., Veilleux S. 2011, The location of an active nucleus and a shadow of a tidal tail in the ULIRG Mrk 273, A&A, 528, A137, doi: 10.1051/0004-6361/201015872

Kakkad D., Groves B., Dopita M., Thomas A. D., Davies R. L., Mainieri V., Kharb P., Scharwächter J., Hampton E. J., Ho I. T. 2018, Spatially resolved electron density in the narrow line region of z ¡ 0.02 radio AGNs, A&A, 618, A6, doi: 10.1051/0004-6361/201832790

Kang D., Woo J.-H. 2018, Unraveling the Complex Structure of AGN-driven Outflows. III. The Outflow Size-Luminosity Relation, ApJ, 864, 124, doi: 10.3847/1538-4357/aad561

Karouzos M., Woo J.-H., Bae H.-J. 2016a, Unraveling the Complex Structure of AGN-driven Outflows. I. Kinematics and Sizes, ApJ, 819, 148, doi: 10.3847/0004-637X/819/2/148

Karouzos M., Woo J.-H., Bae H.-J. 2016b, Unravelling the Complex Structure of AGN-driven Outflows. II. Photoionization and Energetics, ApJ, 833, 171, doi: 10.3847/1538-4357/833/2/171

Kauffmann G., Heckman T. M. 2009, Feast and Famine: regulation of black hole growth in low-redshift galaxies, MNRAS, 397, 135, doi: 10.1111/j.1365-2966.2009.14960.x

Kauffmann G., Heckman T. M., White S. D. M., Charlot S., Tremonti C., Peng E. W., Seibert M., Brinkmann J., Nichol R. C., SubbaRao M., York D. 2003a, The dependence of star formation history and internal structure on stellar mass for 10^5 low-redshift galaxies, MNRAS, 341, 54, doi: 10.1046/j.1365-8711.2003.06292.x

Kauffmann G., Heckman T. M., Tremonti C., Brinchmann J., Charlot S., White S. D. M., Ridgway S. E., Brinkmann J., Fukugita M., Hall P. B., Ivezić Ž., Richards G. T., Schneider D. P. 2003b, The host galaxies of active galactic nuclei, MNRAS, 346, 1055, doi: 10.1111/j.1365-2966.2003.07154.x

Kaviraj S., Laigle C., Kimm T., Devriendt J. E. G., Dubois Y., Pichon C., Slyz A., Chisari E., Peirani S. 2017, The Horizon-AGN simulation: evolution of galaxy properties over cosmic time, MNRAS, 467, 4739, doi: 10.1093/mnras/stx126

Kelly B. C. 2007, Some Aspects of Measurement Error in Linear Regression of Astronomical Data, ApJ, 665, 1489, doi: 10.1086/519947

Kennicutt Robert C. J. 1998, Star Formation in Galaxies Along the Hubble Sequence, ARA&A, 36, 189, doi: 10.1146/annurev.astro.36.1.189

Kewley L. J., Dopita M. A., Leitherer C., Davé R., Yuan T., Allen M., Groves B., Sutherland R. 2013a, Theoretical Evolution of Optical Strong Lines across Cosmic Time, ApJ, 774, 100, doi: 10.1088/0004-637X/774/2/100

Kewley L. J., Maier C., Yabe K., Ohta K., Akiyama M., Dopita M. A., Yuan T. 2013b, The Cosmic BPT Diagram: Confronting Theory with Observations, ApJ, 774, L10, doi: 10.1088/2041-8205/774/1/L10

Kim D. C., Veilleux S., Sanders D. B. 2002, Optical and Near-Infrared Imaging of the IRAS 1 Jy Sample of Ultraluminous Infrared Galaxies. I. The Atlas, ApJS, 143, 277, doi: 10.1086/343843

King A. R., Zubovas K., Power C. 2011, Large-scale outflows in galaxies, MNRAS, 415, L6, doi: 10.1111/j.1745-3933.2011.01067.x

Koekemoer A. M., Faber S. M., Ferguson H. C., Grogin N. A., Kocevski D. D., Koo D. C., Lai K., Lotz J. M., Lucas R. A., McGrath E. J., Ogaz S., Rajan A., Riess A. G., Rodney S. A., Strolger L., Casertano S., Castellano M., Dahlen T., Dickinson M., Dolch T., Fontana A., Giavalisco M., Grazian A., Guo Y., Hathi N. P., Huang K.-H., van der Wel A., Yan H.-J., Acquaviva V., Alexander D. M., Almaini O., Ashby M. L. N., Barden M., Bell E. F., Bournaud F., Brown T. M., Caputi K. I., Cassata P., Challis P. J., Chary R.-R., Cheung E., Cirasuolo M., Conselice C. J., Roshan Cooray A., Croton D. J., Daddi E., Davé R., de Mello D. F., de Ravel L., Dekel A., Donley J. L., Dunlop J. S., Dutton A. A., Elbaz D., Fazio G. G., Filippenko A. V., Finkelstein S. L., Frazer C., Gardner J. P., Garnavich P. M., Gawiser E., Gruetzbauch R., Hartley W. G., Häussler B., Herrington J., Hopkins P. F., Huang J.-S., Jha S. W., Johnson A., Kartaltepe J. S., Khostovan A. A., Kirshner R. P., Lani C., Lee K.-S., Li W., Madau P., McCarthy P. J., McIntosh D. H., McLure R. J., McPartland C., Mobasher B., Moreira H., Mortlock A., Moustakas L. A., Mozena M., Nandra K., Newman J. A., Nielsen J. L., Niemi S., Noeske K. G., Papovich C. J., Pentericci L., Pope A., Primack J. R., Ravindranath S., Reddy N. A., Renzini A., Rix H.-W., Robaina A. R., Rosario D. J., Rosati P., Salimbeni S., Scarlata C., Siana B., Simard L., Smidt J., Snyder D., Somerville R. S., Spinrad H., Straughn A. N., Telford O., Teplitz H. I., Trump J. R., Vargas C., Villforth C., Wagner C. R., Wand ro P., Wechsler R. H., Weiner B. J., Wiklind T., Wild V., Wilson G., Wuyts S., Yun M. S. 2011, CANDELS: The Cosmic Assembly Near-infrared Deep Extragalactic Legacy Survey—The Hubble Space Telescope Observations, Imaging Data Products, and Mosaics, ApJS, 197, 36, doi: 10.1088/0067-0049/197/2/36

Koratkar A., Blaes O. 1999, The Ultraviolet and Optical Continuum Emission in Active Galactic Nuclei: The Status of Accretion Disks, PASP, 111, 1, doi: 10.1086/316294

Kormendy J., Ho L. C. 2013, Coevolution (Or Not) of Supermassive Black Holes and Host Galaxies, ARA&A, 51, 511, doi: 10.1146/annurev-astro-082708-101811

Kormendy J., Richstone D. 1995, Inward Bound—The Search For Supermassive Black Holes In Galactic Nuclei, ARA&A, 33, 581, doi: 10.1146/annurev.aa.33.090195.003053

Kriek M., van Dokkum P. G., Labbé I., Franx M., Illingworth G. D., Marchesini D., Quadri R. F. 2009, An Ultra-Deep Near-Infrared Spectrum of a Compact Quiescent Galaxy at z = 2.2, ApJ, 700, 221, doi: 10.1088/0004-637X/700/1/221

Kriek M., Shapley A. E., Reddy N. A., Siana B., Coil A. L., Mobasher B., Freeman W. R., de Groot L., Price S. H., Sanders R., Shivaei I., Brammer G. B., Momcheva I. G., Skelton R. E., van Dokkum P. G., Whitaker K. E., Aird J., Azadi M., Kassis M., Bullock J. S., Conroy C., Davé R., Kereš D., Krumholz M. 2015, The MOSFIRE Deep Evolution Field (MOSDEF) Survey: Rest-frame Optical Spectroscopy for ~1500 H-selected Galaxies at 1.37 ¡ z ¡ 3.8, ApJS, 218, 15, doi: 10.1088/0067-0049/218/2/15

Lacy M., Storrie-Lombardi L. J., Sajina A., Appleton P. N., Armus L., Chapman S. C., Choi P. I., Fadda D., Fang F., Frayer D. T., Heinrichsen I., Helou G., Im M., Marleau F. R., Masci

F., Shupe D. L., Soifer B. T., Surace J., Teplitz H. I., Wilson G., Yan L. 2004, Obscured and Unobscured Active Galactic Nuclei in the Spitzer Space Telescope First Look Survey, ApJS, 154, 166, doi: 10.1086/422816

Laird E. S., Nandra K., Georgakakis A., Aird J. A., Barmby P., Conselice C. J., Coil A. L., Davis M., Faber S. M., Fazio G. G., Guhathakurta P., Koo D. C., Sarajedini V., Willmer C. N. A. 2009, AEGIS-X: the Chandra Deep Survey of the Extended Groth Strip, ApJS, 180, 102, doi: 10.1088/0067-0049/180/1/102

Le Floc'h E., Papovich C., Dole H., Bell E. F., Lagache G., Rieke G. H., Egami E., Pérez-González P. G., Alonso-Herrero A., Rieke M. J., Blaylock M., Engelbracht C. W., Gordon K. D., Hines D. C., Misselt K. A., Morrison J. E., Mould J. 2005, Infrared Luminosity Functions from the Chandra Deep Field-South: The Spitzer View on the History of Dusty Star Formation at 0 ¡~z ¡~1, ApJ, 632, 169, doi: 10.1086/432789

Leung G. C. K., Coil A. L., Azadi M., Aird J., Shapley A., Kriek M., Mobasher B., Reddy N., Siana B., Freeman W. R., Price S. H., Sanders R. L., Shivaei I. 2017, The MOSDEF Survey: The Prevalence and Properties of Galaxy-wide AGN-driven Outflows at $z \sim 2$, ApJ, 849, 48, doi: 10.3847/1538-4357/aa9024

Levesque E. M., Kewley L. J., Larson K. L. 2010, Theoretical Modeling of Star-Forming Galaxies. I. Emission-Line Diagnostic Grids for Local and Low-Metallicity Galaxies, AJ, 139, 712, doi: 10.1088/0004-6256/139/2/712

Liu G., Zakamska N. L., Greene J. E., Nesvadba N. P. H., Liu X. 2013a, Observations of feedback from radio-quiet quasars - I. Extents and morphologies of ionized gas nebulae, MNRAS, 430, 2327, doi: 10.1093/mnras/stt051

Liu G., Zakamska N. L., Greene J. E., Nesvadba N. P. H., Liu X. 2013b, Observations of feedback from radio-quiet quasars - II. Kinematics of ionized gas nebulae, MNRAS, 436, 2576, doi: 10.1093/mnras/stt1755

Liu W., Veilleux S., Iwasawa K., Rupke D. S. N., Teng S., U V., Tombesi F., Sanders D., Max C. E., Meléndez M. 2019, Elliptical Galaxy in the Making: The Dual Active Galactic Nuclei and Metal-enriched Halo of Mrk 273, ApJ, 872, 39, doi: 10.3847/1538-4357/aafdfc

Luo B., Brandt W. N., Xue Y. Q., Brusa M., Alexand er D. M., Bauer F. E., Comastri A., Koekemoer A., Lehmer B. D., Mainieri V., Rafferty D. A., Schneider D. P., Silverman J. D., Vignali C. 2010, Identifications and Photometric Redshifts of the 2 Ms Chandra Deep Field-South Sources, ApJS, 187, 560, doi: 10.1088/0067-0049/187/2/560

Lynden-Bell D. 1969, Galactic Nuclei as Collapsed Old Quasars, Nature, 223, 690, doi: 10.1038/223690a0

Lynden-Bell D., Rees M. J. 1971, On quasars, dust and the galactic centre, MNRAS, 152, 461, doi: 10.1093/mnras/152.4.461

Madau P., Dickinson M. 2014, Cosmic Star-Formation History, ARA&A, 52, 415, doi: 10.1146/annurev-astro-081811-125615

Madau P., Ferguson H. C., Dickinson M. E., Giavalisco M., Steidel C. C., Fruchter A. 1996, High-redshift galaxies in the Hubble Deep Field: colour selection and star formation history to z~4, MNRAS, 283, 1388, doi: 10.1093/mnras/283.4.1388

Magorrian J., Tremaine S., Richstone D., Bender R., Bower G., Dressler A., Faber S. M., Gebhardt K., Green R., Grillmair C., Kormendy J., Lauer T. 1998, The Demography of Massive Dark Objects in Galaxy Centers, AJ, 115, 2285, doi: 10.1086/300353

Marconi A., Risaliti G., Gilli R., Hunt L. K., Maiolino R., Salvati M. 2004, Local supermassive black holes, relics of active galactic nuclei and the X-ray background, MNRAS, 351, 169, doi: 10.1111/j.1365-2966.2004.07765.x

Markwardt C. B. 2009, in Astronomical Society of the Pacific Conference Series, Vol. 411, Astronomical Data Analysis Software and Systems XVIII, ed. D. A. Bohlender, D. Durand, P. Dowler, 251. https://arxiv.org/abs/0902.2850

Matthews T. A., Sandage A. R. 1963, Optical Identification of 3C 48, 3C 196, and 3C 286 with Stellar Objects., ApJ, 138, 30, doi: 10.1086/147615

McElroy R., Croom S. M., Pracy M., Sharp R., Ho I. T., Medling A. M. 2015, IFU observations of luminous type II AGN - I. Evidence for ubiquitous winds, MNRAS, 446, 2186, doi: 10.1093/mnras/stu2224

McLean I. S., Steidel C. C., Epps H., Matthews K., Adkins S., Konidaris N., Weber B., Aliado T., Brims G., Canfield J., Cromer J., Fucik J., Kulas K., Mace G., Magnone K., Rodriguez H., Wang E., Weiss J. 2010a, in Society of Photo-Optical Instrumentation Engineers (SPIE) Conference Series, Vol. 7735, Ground-based and Airborne Instrumentation for Astronomy III, 77351E, doi: 10.1117/12.856715

McLean I. S., Steidel C. C., Epps H., Matthews K., Adkins S., Konidaris N., Weber B., Aliado T., Brims G., Canfield J., Cromer J., Fucik J., Kulas K., Mace G., Magnone K., Rodriguez H., Wang E., Weiss J. 2010b, in Society of Photo-Optical Instrumentation Engineers (SPIE) Conference Series, Vol. 7735, Ground-based and Airborne Instrumentation for Astronomy III, 77351E, doi: 10.1117/12.856715

Meléndez M., Heckman T. M., Martínez-Paredes M., Kraemer S. B., Mendoza C. 2014, Theoretical modelling of emission-line galaxies: new classification parameters for mid-infrared and optical spectroscopy, MNRAS, 443, 1358, doi: 10.1093/mnras/stu1242

Mingozzi M., Cresci G., Venturi G., Marconi A., Mannucci F., Perna M., Belfiore F., Carniani S., Balmaverde B., Brusa M., Cicone C., Feruglio C., Gallazzi A., Mainieri V., Maiolino R., Nagao T., Nardini E., Sani E., Tozzi P., Zibetti S. 2019, The MAGNUM survey: different gas properties in the outflowing and disc components in nearby active galaxies with MUSE, A&A, 622, A146, doi: 10.1051/0004-6361/201834372

Momcheva I. G., Brammer G. B., van Dokkum P. G., Skelton R. E., Whitaker K. E., Nelson E. J., Fumagalli M., Maseda M. V., Leja J., Franx M., Rix H.-W., Bezanson R., Da Cunha E., Dickey C., Förster Schreiber N. M., Illingworth G., Kriek M., Labbé I., Ulf Lange J., Lundgren B. F., Magee D., Marchesini D., Oesch P., Pacifici C., Patel S. G., Price S., Tal T., Wake D. A., van der Wel A., Wuyts S. 2016, The 3D-HST Survey: Hubble Space Telescope WFC3/G141 Grism Spectra, Redshifts, and Emission Line Measurements for ~100,000 Galaxies, ApJS, 225, 27, doi: 10.3847/0067-0049/225/2/27

Morrissey P., Matuszewski M., Martin D. C., Neill J. D., Epps H., Fucik J., Weber B., Darvish B., Adkins S., Allen S., Bartos R., Belicki J., Cabak J., Callahan S., Cowley D., Crabill M., Deich W., Delecroix A., Doppman G., Hilyard D., James E., Kaye S., Kokorowski M., Kwok S., Lanclos K., Milner S., Moore A., O'Sullivan D., Parihar P., Park S., Phillips A., Rizzi L., Rockosi C., Rodriguez H., Salaun Y., Seaman K., Sheikh D., Weiss J., Zarzaca R. 2018, The Keck Cosmic Web Imager Integral Field Spectrograph, ApJ, 864, 93, doi: 10.3847/1538-4357/aad597

Mullaney J. R., Alexander D. M., Fine S., Goulding A. D., Harrison C. M., Hickox R. C. 2013, Narrow-line region gas kinematics of 24 264 optically selected AGN: the radio connection, MNRAS, 433, 622, doi: 10.1093/mnras/stt751

Murray N., Quataert E., Thompson T. A. 2005, On the Maximum Luminosity of Galaxies and Their Central Black Holes: Feedback from Momentum-driven Winds, ApJ, 618, 569, doi: 10.1086/426067

Nandra K., Laird E. S., Aird J. A., Salvato M., Georgakakis A., Barro G., Perez-Gonzalez P. G., Barmby P., Chary R. R., Coil A., Cooper M. C., Davis M., Dickinson M., Faber S. M., Fazio G. G., Guhathakurta P., Gwyn S., Hsu L. T., Huang J. S., Ivison R. J., Koo D. C., Newman J. A., Rangel C., Yamada T., Willmer C. 2015, AEGIS-X: Deep Chandra Imaging of the Central Groth Strip, ApJS, 220, 10, doi: 10.1088/0067-0049/220/1/10

Nesvadba N. P. H., De Breuck C., Lehnert M. D., Best P. N., Collet C. 2017, The SINFONI survey of powerful radio galaxies at z 2: Jet-driven AGN feedback during the Quasar Era, A&A, 599, A123, doi: 10.1051/0004-6361/201528040

Nesvadba N. P. H., Lehnert M. D., De Breuck C., Gilbert A. M., van Breugel W. 2008, Evidence for powerful AGN winds at high redshift: dynamics of galactic outflows in radio galaxies during the "Quasar Era", A&A, 491, 407, doi: 10.1051/0004-6361:200810346

Nesvadba N. P. H., Lehnert M. D., Eisenhauer F., Gilbert A., Tecza M., Abuter R. 2006, Extreme Gas Kinematics in the z=2.2 Powerful Radio Galaxy MRC 1138-262: Evidence for Efficient Active Galactic Nucleus Feedback in the Early Universe?, ApJ, 650, 693, doi: 10.1086/507266

Nesvadba N. P. H., Polletta M., Lehnert M. D., Bergeron J., De Breuck C., Lagache G., Omont A. 2011, The dynamics of the ionized and molecular interstellar medium in powerful obscured quasars at z$\geq$ 3.5, MNRAS, 415, 2359, doi: 10.1111/j.1365-2966.2011.18862.x

Netzer H. 2015, Revisiting the Unified Model of Active Galactic Nuclei, ARA&A, 53, 365, doi: 10.1146/annurev-astro-082214-122302

Newman S. F., Genzel R., Förster-Schreiber N. M., Shapiro Griffin K., Mancini C., Lilly S. J., Renzini A., Bouché N., Burkert A., Buschkamp P., Carollo C. M., Cresci G., Davies R., Eisenhauer F., Genel S., Hicks E. K. S., Kurk J., Lutz D., Naab T., Peng Y., Sternberg A., Tacconi L. J., Vergani D., Wuyts S., Zamorani G. 2012, The SINS/zC-SINF Survey of z ~2 Galaxy Kinematics: Outflow Properties, ApJ, 761, 43, doi: 10.1088/0004-637X/761/1/43

Newman S. F., Buschkamp P., Genzel R., Förster Schreiber N. M., Kurk J., Sternberg A., Gnat O., Rosario D., Mancini C., Lilly S. J., Renzini A., Burkert A., Carollo C. M., Cresci G., Davies R., Eisenhauer F., Genel S., Shapiro Griffin K., Hicks E. K. S., Lutz D., Naab T., Peng Y., Tacconi L. J., Wuyts S., Zamorani G., Vergani D., Weiner B. J. 2014, Nebular Excitation in z ~2 Star-forming Galaxies from the SINS and LUCI Surveys: The Influence of Shocks and Active Galactic Nuclei, ApJ, 781, 21, doi: 10.1088/0004-637X/781/1/21

Osterbrock D. E., Ferland G. J. 2006, Astrophysics of gaseous nebulae and active galactic nuclei

Perna M., Lanzuisi G., Brusa M., Cresci G., Mignoli M. 2017a, An X-ray/SDSS sample. II. AGN-driven outflowing gas plasma properties, A&A, 606, A96, doi: 10.1051/0004-6361/201730819

Perna M., Lanzuisi G., Brusa M., Mignoli M., Cresci G. 2017b, An X-ray/SDSS sample. I. Multi-phase outflow incidence and dependence on AGN luminosity, A&A, 603, A99, doi: 10.1051/0004-6361/201630369

Perna M., Brusa M., Cresci G., Comastri A., Lanzuisi G., Lusso E., Marconi A., Salvato M., Zamorani G., Bongiorno A., Mainieri V., Maiolino R., Mignoli M. 2015, Galaxy-wide outflows in z ~1.5 luminous obscured quasars revealed through near-IR slit-resolved spectroscopy, A&A, 574, A82, doi: 10.1051/0004-6361/201425035

Pillepich A., Springel V., Nelson D., Genel S., Naiman J., Pakmor R., Hernquist L., Torrey P., Vogelsberger M., Weinberger R., Marinacci F. 2018, Simulating galaxy formation with the IllustrisTNG model, MNRAS, 473, 4077, doi: 10.1093/mnras/stx2656

Polletta M., Tajer M., Maraschi L., Trinchieri G., Lonsdale C. J., Chiappetti L., Andreon S., Pierre M., Le Fèvre O., Zamorani G., Maccagni D., Garcet O., Surdej J., Franceschini A., Alloin D., Shupe D. L., Surace J. A., Fang F., Rowan-Robinson M., Smith H. E., Tresse L. 2007, Spectral Energy Distributions of Hard X-Ray Selected Active Galactic Nuclei in the XMM-Newton Medium Deep Survey, ApJ, 663, 81, doi: 10.1086/518113

Pradhan A. K., Montenegro M., Nahar S. N., Eissner W. 2006, [OII] line ratios, MNRAS, 366, L6, doi: 10.1111/j.1745-3933.2005.00119.x

Qiu Y., Bogdanović T., Li Y., McDonald M., McNamara B. R. 2020, The formation of dusty cold gas filaments from galaxy cluster simulations, Nature Astronomy, doi: 10.1038/s41550-020-1090-7

Reddy N. A., Kriek M., Shapley A. E., Freeman W. R., Siana B., Coil A. L., Mobasher B., Price S. H., Sanders R. L., Shivaei I. 2015, The MOSDEF Survey: Measurements of Balmer Decrements and the Dust Attenuation Curve at Redshifts z ~1.4-2.6, ApJ, 806, 259, doi: 10.1088/0004-637X/806/2/259

Rich J. A., Kewley L. J., Dopita M. A. 2015, Galaxy Mergers Drive Shocks: An Integral Field Study of GOALS Galaxies, ApJS, 221, 28, doi: 10.1088/0067-0049/221/2/28

Rodríguez Zaurín J., Tadhunter C. N., Rose M., Holt J. 2013, The importance of warm, AGN-driven outflows in the nuclear regions of nearby ULIRGs, MNRAS, 432, 138, doi: 10.1093/mnras/stt423

Rodríguez Zaurín J., Tadhunter C. N., Rupke D. S. N., Veilleux S., Spoon H. W. W., Chiaberge M., Ramos Almeida C., Batcheldor D., Sparks W. B. 2014, Extended warm gas in the ULIRG Mrk273: Galactic outflows and tidal debris, A&A, 571, A57, doi: 10.1051/0004-6361/201423540

Rose M., Tadhunter C., Ramos Almeida C., Rodríguez Zaurín J., Santoro F., Spence R. 2018, Quantifying the AGN-driven outflows in ULIRGs (QUADROS) - I: VLT/Xshooter observations of nine nearby objects, MNRAS, 474, 128, doi: 10.1093/mnras/stx2590

Rupke D. S., Veilleux S., Sanders D. B. 2005, Outflows in Infrared-Luminous Starbursts at z ¡ 0.5. II. Analysis and Discussion, ApJS, 160, 115, doi: 10.1086/432889

Rupke D. S. N. 2014a, IFSRED: Data Reduction for Integral Field Spectrographs. http://ascl.net/1409.004

—. 2014b, IFSFIT: Spectral Fitting for Integral Field Spectrographs. http://ascl.net/1409.005

Rupke D. S. N., Gültekin K., Veilleux S. 2017, Quasar-mode Feedback in Nearby Type 1 Quasars: Ubiquitous Kiloparsec-scale Outflows and Correlations with Black Hole Properties, ApJ, 850, 40, doi: 10.3847/1538-4357/aa94d1

Rupke D. S. N., Veilleux S. 2011, Integral Field Spectroscopy of Massive, Kiloparsec-scale Outflows in the Infrared-luminous QSO Mrk 231, ApJ, 729, L27, doi: 10.1088/2041-8205/729/2/L27

Rupke D. S. N., Veilleux S. 2013a, The Multiphase Structure and Power Sources of Galactic Winds in Major Mergers, ApJ, 768, 75, doi: 10.1088/0004-637X/768/1/75

Rupke D. S. N., Veilleux S. 2013b, The Multiphase Structure and Power Sources of Galactic Winds in Major Mergers, ApJ, 768, 75, doi: 10.1088/0004-637X/768/1/75

Rupke D. S. N., Veilleux S. 2013c, Breaking the Obscuring Screen: A Resolved Molecular Outflow in a Buried QSO, ApJ, 775, L15, doi: 10.1088/2041-8205/775/1/L15

Salpeter E. E. 1964, Accretion of Interstellar Matter by Massive Objects., ApJ, 140, 796, doi: 10.1086/147973

Sanders D. B., Soifer B. T., Elias J. H., Madore B. F., Matthews K., Neugebauer G., Scoville N. Z. 1988, Ultraluminous Infrared Galaxies and the Origin of Quasars, ApJ, 325, 74, doi: 10.1086/165983

Sanders R. L., Shapley A. E., Kriek M., Reddy N. A., Freeman W. R., Coil A. L., Siana B., Mobasher B., Shivaei I., Price S. H., de Groot L. 2016, The MOSDEF Survey: Electron Density and Ionization Parameter at z ~2.3, ApJ, 816, 23, doi: 10.3847/0004-637X/816/1/23

Schaye J., Crain R. A., Bower R. G., Furlong M., Schaller M., Theuns T., Dalla Vecchia C., Frenk C. S., McCarthy I. G., Helly J. C., Jenkins A., Rosas-Guevara Y. M., White S. D. M., Baes M., Booth C. M., Camps P., Navarro J. F., Qu Y., Rahmati A., Sawala T., Thomas P. A., Trayford J. 2015, The EAGLE project: simulating the evolution and assembly of galaxies and their environments, MNRAS, 446, 521, doi: 10.1093/mnras/stu2058

Schmidt M. 1963, 3C 273 : A Star-Like Object with Large Red-Shift, Nature, 197, 1040, doi: 10.1038/1971040a0

Schmitt H. R., Donley J. L., Antonucci R. R. J., Hutchings J. B., Kinney A. L., Pringle J. E. 2003, A Hubble Space Telescope Survey of Extended [O III] λ5007 Å Emission in a Far-Infrared-Selected Sample of Seyfert Galaxies: Results, ApJ, 597, 768, doi: 10.1086/381224

Seyfert C. K. 1943, Nuclear Emission in Spiral Nebulae., ApJ, 97, 28, doi: 10.1086/144488

Shapley A. E., Reddy N. A., Kriek M., Freeman W. R., Sanders R. L., Siana B., Coil A. L., Mobasher B., Shivaei I., Price S. H., de Groot L. 2015, The MOSDEF Survey: Excitation Properties of $z \sim 2.3$ Star-forming Galaxies, ApJ, 801, 88, doi: 10.1088/0004-637X/801/2/88

Sharples R., Bender R., Agudo Berbel A., Bezawada N., Castillo R., Cirasuolo M., Davidson G., Davies R., Dubbeldam M., Fairley A., Finger G., Förster Schreiber N., Gonte F., Hess A., Jung I., Lewis I., Lizon J. L., Muschielok B., Pasquini L., Pirard J., Popovic D., Ramsay S., Rees P., Richter J., Riquelme M., Rodrigues M., Saviane I., Schlichter J., Schmidtobreick L., Segovia A., Smette A., Szeifert T., van Kesteren A., Wegner M., Wiezorrek E. 2013, First Light for the KMOS Multi-Object Integral-Field Spectrometer, The Messenger, 151, 21

Shivaei I., Reddy N. A., Shapley A. E., Kriek M., Siana B., Mobasher B., Coil A. L., Freeman W. R., Sanders R., Price S. H., de Groot L., Azadi M. 2015, The MOSDEF Survey: Dissecting the Star Formation Rate versus Stellar Mass Relation Using Hα and Hβ Emission Lines at z ∼ 2, ApJ, 815, 98, doi: 10.1088/0004-637X/815/2/98

Shivaei I., Reddy N. A., Siana B., Shapley A. E., Kriek M., Mobasher B., Freeman W. R., Sanders R. L., Coil A. L., Price S. H., Fetherolf T., Azadi M., Leung G., Zick T. 2018, The MOSDEF Survey: Direct Observational Constraints on the Ionizing Photon Production Efficiency, ξ_{ion}, at $z \sim 2$, ApJ, 855, 42, doi: 10.3847/1538-4357/aaad62

Silk J. 2005, Ultraluminous starbursts from supermassive black hole-induced outflows, MNRAS, 364, 1337, doi: 10.1111/j.1365-2966.2005.09672.x

Silk J., Rees M. J. 1998, Quasars and galaxy formation, A&A, 331, L1. https://arxiv.org/abs/astro-ph/9801013

Silva L., Maiolino R., Granato G. L. 2004, Connecting the cosmic infrared background to the X-ray background, MNRAS, 355, 973, doi: 10.1111/j.1365-2966.2004.08380.x

Skelton R. E., Whitaker K. E., Momcheva I. G., Brammer G. B., van Dokkum P. G., Labbé I., Franx M., van der Wel A., Bezanson R., Da Cunha E., Fumagalli M., Förster Schreiber N., Kriek M., Leja J., Lundgren B. F., Magee D., Marchesini D., Maseda M. V., Nelson E. J., Oesch P., Pacifici C., Patel S. G., Price S., Rix H.-W., Tal T., Wake D. A., Wuyts S. 2014, 3D-HST WFC3-selected Photometric Catalogs in the Five CANDELS/3D-HST Fields: Photometry, Photometric Redshifts, and Stellar Masses, ApJS, 214, 24, doi: 10.1088/0067-0049/214/2/24

Spence R. A. W., Tadhunter C. N., Rose M., Rodríguez Zaurín J. 2018, Quantifying the AGN-driven outflows in ULIRGs (QUADROS) III: measurements of the radii and kinetic powers of eight near-nuclear outflows, MNRAS, 478, 2438, doi: 10.1093/mnras/sty1046

Spence R. A. W., Zaurín J. R., Tadhunter C. N., Rose M., Cabrera-Lavers A., Spoon H., Muñoz-Tuñón C. 2016, No evidence for large-scale outflows in the extended ionized halo of ULIRG Mrk273, MNRAS, 459, L16, doi: 10.1093/mnrasl/slw033

Steidel C. C., Erb D. K., Shapley A. E., Pettini M., Reddy N., Bogosavljević M., Rudie G. C., Rakic O. 2010, The Structure and Kinematics of the Circumgalactic Medium from Far-ultraviolet Spectra of z ~= 2-3 Galaxies, ApJ, 717, 289, doi: 10.1088/0004-637X/717/1/289

Stern D., Eisenhardt P., Gorjian V., Kochanek C. S., Caldwell N., Eisenstein D., Brodwin M., Brown M. J. I., Cool R., Dey A., Green P., Jannuzi B. T., Murray S. S., Pahre M. A., Willner S. P. 2005, Mid-Infrared Selection of Active Galaxies, ApJ, 631, 163, doi: 10.1086/432523

Strateva I., Ivezić Ž., Knapp G. R., Narayanan V. K., Strauss M. A., Gunn J. E., Lupton R. H., Schlegel D., Bahcall N. A., Brinkmann J., Brunner R. J., Budavári T., Csabai I., Castander F. J., Doi M., Fukugita M., Győry Z., Hamabe M., Hennessy G., Ichikawa T., Kunszt P. Z., Lamb D. Q., McKay T. A., Okamura S., Racusin J., Sekiguchi M., Schneider D. P., Shimasaku K., York D. 2001, Color Separation of Galaxy Types in the Sloan Digital Sky Survey Imaging Data, AJ, 122, 1861, doi: 10.1086/323301

Sun A.-L., Greene J. E., Zakamska N. L. 2017, Sizes and Kinematics of Extended Narrow-line Regions in Luminous Obscured AGN Selected by Broadband Images, ApJ, 835, 222, doi: 10.3847/1538-4357/835/2/222

Tadhunter C., Holden L., Ramos Almeida C., Batcheldor D. 2019, Quantifying the AGN-driven outflows in ULIRGs (QUADROS) IV: HST/STIS spectroscopy of the sub-kpc warm outflow in F14394+5332, MNRAS, 488, 1813, doi: 10.1093/mnras/stz1755

Tadhunter C., Rodríguez Zaurín J., Rose M., Spence R. A. W., Batcheldor D., Berg M. A., Ramos Almeida C., Spoon H. W. W., Sparks W., Chiaberge M. 2018, Quantifying the AGN-driven outflows in ULIRGs (QUADROS) - II. Evidence for compact outflow regions from HST [O III] imaging observations, MNRAS, 478, 1558, doi: 10.1093/mnras/sty1064

Thompson T. A., Fabian A. C., Quataert E., Murray N. 2015, Dynamics of dusty radiation-pressure-driven shells and clouds: fast outflows from galaxies, star clusters, massive stars, and AGN, MNRAS, 449, 147, doi: 10.1093/mnras/stv246

Tonry J. L. 1984, Evidence for a central mass concentration in M 32., ApJ, 283, L27, doi: 10.1086/184326

Tonry J. L. 1987, A Central Black Hole in M32, ApJ, 322, 632, doi: 10.1086/165758

U V., Medling A., Sanders D., Max C., Armus L., Iwasawa K., Evans A., Kewley L., Fazio G. 2013, The Inner Kiloparsec of Mrk 273 with Keck Adaptive Optics, ApJ, 775, 115, doi: 10.1088/0004-637X/775/2/115

Ueda Y., Akiyama M., Ohta K., Miyaji T. 2003, Cosmological Evolution of the Hard X-Ray Active Galactic Nucleus Luminosity Function and the Origin of the Hard X-Ray Background, ApJ, 598, 886, doi: 10.1086/378940

Vayner A., Wright S. A., Murray N., Armus L., Larkin J. E., Mieda E. 2017, Galactic-scale Feedback Observed in the 3C 298 Quasar Host Galaxy, ApJ, 851, 126, doi: 10.3847/1538-4357/aa9c42

Vázquez G. A., Leitherer C. 2005, Optimization of Starburst99 for Intermediate-Age and Old Stellar Populations, ApJ, 621, 695, doi: 10.1086/427866

Veilleux S., Cecil G., Bland-Hawthorn J. 2005, Galactic Winds, ARA&A, 43, 769, doi: 10.1146/annurev.astro.43.072103.150610

Veilleux S., Kim D. C., Sanders D. B. 2002, Optical and Near-Infrared Imaging of the IRAS 1 Jy Sample of Ultraluminous Infrared Galaxies. II. The Analysis, ApJS, 143, 315, doi: 10.1086/343844

Veilleux S., Osterbrock D. E. 1987, Spectral Classification of Emission-Line Galaxies, ApJS, 63, 295, doi: 10.1086/191166

Veilleux S., Meléndez M., Sturm E., Gracia-Carpio J., Fischer J., González-Alfonso E., Contursi A., Lutz D., Poglitsch A., Davies R., Genzel R., Tacconi L., de Jong J. A., Sternberg A., Netzer H., Hailey-Dunsheath S., Verma A., Rupke D. S. N., Maiolino R., Teng S. H., Polisensky E. 2013, Fast Molecular Outflows in Luminous Galaxy Mergers: Evidence for Quasar Feedback from Herschel, ApJ, 776, 27, doi: 10.1088/0004-637X/776/1/27

Weedman D. W. 1970, High-Velocity Gas Motions in Galactic Nuclei, ApJ, 159, 405, doi: 10.1086/150318

Woo J.-H., Bae H.-J., Son D., Karouzos M. 2016, The Prevalence of Gas Outflows in Type 2 AGNs, ApJ, 817, 108, doi: 10.3847/0004-637X/817/2/108

Yang G., Brandt W. N., Vito F., Chen C. T. J., Trump J. R., Luo B., Sun M. Y., Xue Y. Q., Koekemoer A. M., Schneider D. P., Vignali C., Wang J. X. 2018, Linking black hole growth with host galaxies: the accretion-stellar mass relation and its cosmic evolution, MNRAS, 475, 1887, doi: 10.1093/mnras/stx2805

Yu Q., Tremaine S. 2002, Observational constraints on growth of massive black holes, MNRAS, 335, 965, doi: 10.1046/j.1365-8711.2002.05532.x

Zakamska N. L., Greene J. E. 2014, Quasar feedback and the origin of radio emission in radio-quiet quasars, MNRAS, 442, 784, doi: 10.1093/mnras/stu842

Zakamska N. L., Strauss M. A., Krolik J. H., Ridgway S. E., Schmidt G. D., Smith P. S., Heckman T. M., Schneider D. P., Hao L., Brinkmann J. 2006, Type II Quasars from the Sloan Digital Sky Survey. V. Imaging Host Galaxies with the Hubble Space Telescope, AJ, 132, 1496, doi: 10.1086/506986

Zel'dovich Y. B. 1964, The Fate of a Star and the Evolution of Gravitational Energy Upon Accretion, Soviet Physics Doklady, 9, 195